# Alma Mater Studiorum – Università di Bologna

## DOTTORATO DI RICERCA IN
*Ingegneria Elettronica, Telecomunicazioni e Tecnologie dell'Informazione*

### Ciclo XXVI

**Settore Concorsuale di afferenza: 09/F1 – CAMPI ELETTROMAGNETICI**

**Settore Scientifico disciplinare: ING–INF/02 – CAMPI ELETTROMAGNETICI**

# Design and experimental characterization of antennas and wireless systems for innovative wearable and implantable ultra low–power applications

Presentata da:  MARTINO ALDRIGO

| | |
|---|---|
| **Coordinatore Dottorato** | **Relatore** |
| Prof. Alessandro Vanelli Coralli | Chiar.mo Prof. Vittorio Rizzoli |
| | **Correlatori** |
| | Prof. Alessandra Costanzo |

Esame finale anno 2014

*To Sorin Ş.*

*"Watch your thoughts, for they become words.*
*Watch your words, for they become actions.*
*Watch your actions, for they become habits.*
*Watch your habits, for they become your character.*
*Watch your character, for it becomes your destiny.*
*What we think we become."*

*And what I feel makes me a better man.*
*Thank you.*

## Acknowledgement

I want to thank all the people who have been close to me so far, in a professional and human sense: Chiar.mo Prof. Vittorio Rizzoli for his recognized talent in stimulating an acute approach to even complex problems; Prof. Alessandra Costanzo for her continuous support and spur to a constant personal improvement; Ing. Diego Masotti for his precious suggestions, help, competence, company and whatever one could desire from one of his professors; all my colleagues who have been following me during the last years: Ing. Francesco Donzelli, Ing. Giacomo Bichicchi, Ing. Nicola Arbizzani, Ing. Manuel Faccioli, Ing. Massimo Del Prete, Ing. Ramona Rosini, Ing. Gaia Leli and Ing. Piero Orlandi; I want to thank warmly Prof. Mircea Dragoman and all the nice people at IMT (Bucharest) for the great opportunity to work with such skilled and kind scientists, in particular I would like to thank Ing. Alexandra Stefanescu for her exquisite company during my stay in Bucharest; I want to thank Prof. Apostolos Georgiadis for his useful suggestions in reviewing my PhD thesis; I want to thank, of course, my family: no need to say how important you all are for me; last, but not least, I want to thank two special persons who have been, are and will be the most important ones in my life: there is no rhetoric in saying that you, Mattia, and you, Sorin, have enriched my life more than whoever could have done, and could do…

"Zwei Dinge erfüllen das Gemüt mit immer neuer und zunehmenden Bewunderung und Ehrfurcht, je öfter und anhaltender sich das Nachdenken damit beschäftigt:
*der bestirnte Himmel über mir, und das moralische Gesetz in mir.*
Beide darf ich nicht als in Dunkelheiten verhüllt, oder im Überschwenglichen, außer meinem Gesichtskreise, suchen und bloß vermuten;
ich sehe sie vor mir und verknüpfe sie unmittelbar mit dem Bewußtsein meiner Existenz."

"Due cose riempiono l'animo di ammirazione e venerazione sempre nuova e crescente, quanto più spesso e più a lungo la riflessione si occupa di esse:
*il cielo stellato sopra di me, e la legge morale in me.*
Queste due cose io non ho bisogno di cercarle e semplicemente supporle come se fossero avvolte nell'oscurità, o fossero nel trascendente fuori del mio orizzonte; io le vedo davanti a me e le connetto immediatamente con la coscienza della mia esistenza."

Immanuel Kant, Kritik der praktischen Vernunft

# LIST OF ACRONYMS

- ACPR: Adjacent–Channel Power Ratio
- AF: Array Factor
- AM: Air Mass
- ANN: Artificial Neural Network
- AWGN: Additive White Gaussian Noise
- BAN: Body Area Network
- BAP: Battery Assisted Passive
- BER: Bit Error Rate
- CAD: Computer–Aided Design
- CPA: Coplanar Patch Antenna
- CPW: CoPlanar Waveguide
- CVD: Chemical Vapour Deposition
- DUT: Device Under Test
- EIRP: Effective Isotropic Radiated Power
- EM: Electro–Magnetic
- EVM: Error Vector Magnitude
- FMR: Ferro–Magnetic Resonance
- HB: Harmonic Balance
- HIS: High Impedance Surface
- IR: Infra–Red
- ISM: Industrial Scientifical Medical
- MD: Magneto–Dielectric
- MHB: Modulated Harmonic Balance
- MIMO: Multi–Input Multi–Output
- MOM: Metal–Oxide–Metal
- MW: Microwave
- NLOS: Non–Line–Of–Sight
- OD: Only–Dielectric
- PCB: Printed Circuit Board
- PDA: Personal Digital Assistant
- PEC: Perfect Electric Conductor
- PMC: Perfect Magnetic Conductor
- QED: Quantum Electro–Dynamics
- QHE: Quantum Hall Effect
- RF: Radio Frequency
- RFID: Radio Frequency IDentification
- RIS: Reactive Impedance Surface
- RT: Ray Tracing
- SAR: Specific Absorption Rate
- SEM: Scanning Electron Microscope
- SISO: Single–Input Single–Output
- SNR: Signal–to–Noise Ratio
- UV: Ultra–Violet
- VSS: Virtual System Simulator
- WKB: Wentzel–Kramers–Brillouin
- WLAN: Wireless Local Area Network
- WSN: Wireless Sensor Network
- VSWR: Voltage Standing Wave Ratio

# TABLE OF CONTENTS

# INTRODUCTION

Wireless applications have become one of the most important challenges for modern communication systems. Since Marconi's first experiments and discoveries, the interest in such an engineering field has been growing without a break and going hand in hand with theoretical and applied research. This has lead to a wide panorama of significant achievements in the scientific community and, furthermore, to interesting outlooks as to their exploitation for off–the–shelf consumer items.

The need for combining enhanced computational capabilities and portability in modern RF devices has its main counterpart and, at the same time, drawback in an increasing miniaturization process of all components, so as to accomplish their integration in small volumes (on the order of some $cm^3$ or even less). A key requirement in such systems is the energy consumption, which can affect dramatically the design process and, in the worst case, become an insurmountable constraint. Nowadays, the research in the field of low–power or energetically autonomous applications focuses the efforts of several scientists involved in a wide range of topics: physics, chemistry, materials science, telecommunication engineering, computer science, etc.

Upon the afore–mentioned considerations, an important role for distributed and pervasive wireless systems applications is played by the so–called *BANs*: *BANs* could be considered as a particular realization of *WSNs* but with a coverage limited to the space surrounding a human body, hence restricted to some meters. By means of *ad hoc* designed sensors, these telecommunication systems allow to monitor the desired vital/environmental parameters and correlate the gathered data, in order to provide the required information for the appropriate interventions. Two simple examples of *BANs* are shown in Fig. 1: the monitoring of health parameters in an athlete and a wearable sensor network.
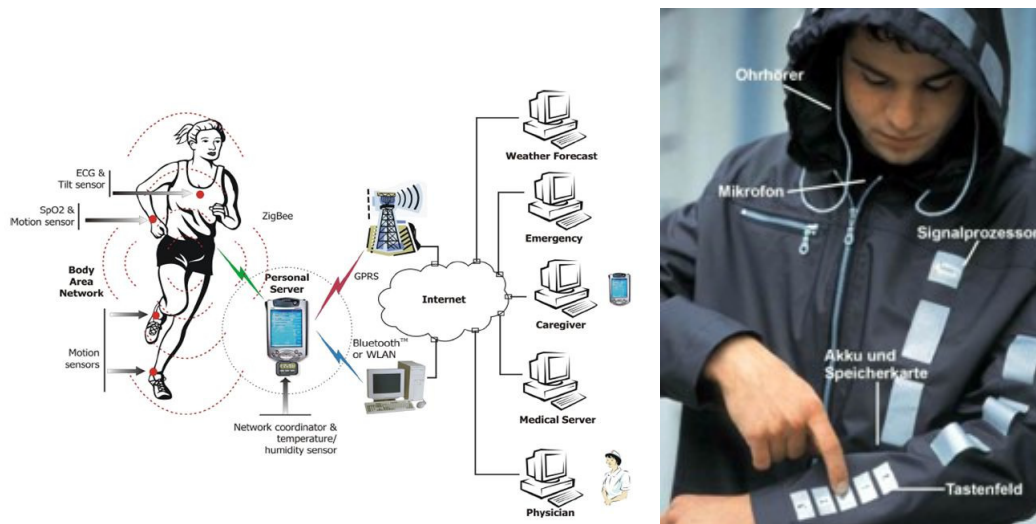


Fig. 1.  Examples of *BANs*.

My research as a PhD student has been aimed at the development of innovative wireless micro– and nano–devices to be deployed in wearable and, in perspective, implantable *BANs* and other future telecommunication systems. A particular attention has been directed to the issues regarding energy consumption and renewable energy sources, which is a key requirement for modern low–environmental impact engineering applications.

It is every (potential) scientist's desire to give one's contribute to the enhancement of everyday life. He who is writing hopes to have succeeded in giving, *cum grano salis* and at least to a small degree, a little help in scientific knowledge improvement.

## Plan of the present PhD thesis

Starting point of the present PhD thesis is the exploitation of the design skills I have been improving since my master thesis' research. A brief description of the chapters' content follows.

- Chapter 1: the simulation of a complete *front–end* is a very complex problem and, in particular, is the basis upon which the prediction of the overall performance of the system is possible. By means of a commercial EM simulation tool (CST MICROWAVE STUDIO®) and a rigorous nonlinear/EM circuit co–simulation based on the Reciprocity Theorem, the above–mentioned prediction can be achieved and exploited for wireless links characterization. This will represent the theoretical basics of the entire present thesis and will be supported by two RF applications.
- Chapter 2: an extensive dissertation about Magneto–Dielectric (MD) materials will be presented, together with their peculiar characteristics as substrates for antenna miniaturization purposes. A designed and tested device for RF on–body applications will be described in detail. Finally, future research will be discussed.
- Chapter 3: this chapter will deal with the issue regarding the exploitation of renewable energy sources for low–energy consumption devices. Hence the problem related to the so–called *energy harvesting* will be tackled and a first attempt to deploy THz solar energy in an innovative way will be presented and discussed. Future research will be proposed as well.
- Chapter 4: graphene is a very promising material for devices to be exploited in the RF and THz frequency range for a wide range of engineering applications, including those ones marked as the main research goal of the present thesis. This chapter will present the results obtained during my research period at the National Institute for Research and Development in Microtechnologies (IMT) in Bucharest, Romania. It will concern the design and manufacturing of antennas and diodes made in graphene–based technology for detection/rectification purposes.
- Final conclusions.
- List of publications.

# CHAPTER 1

## NONLINEAR/EM CIRCUIT CO–SIMULATION: A THEORETICAL BASIS FOR THE PREDICTION OF HIGH–FREQUENCY WIRELESS SYSTEMS PERFORMANCE

Traditional approach in simulating RF links is based upon *functional* system blocks, for which a behavioral description fulfills the desired computational requirements. Hence the afore–mentioned blocks can be considered as "black boxes" disregarding their inside circuit topology, thus enhancing the numerical capabilities of the algorithms at the expense of an accurate prediction of the overall performance of the wireless system under consideration.

In order to overcome the latter constraints, my research group at Department of Electrical, Electronic, and Information Engineering "Guglielmo Marconi" – DEI of University of Bologna, Italy, was deeply involved in the past years in the field of the nonlinear/EM circuit co–simulation: this new approach allows to rigorously compute all the potential interference and/or nonlinear effects occurring in modern wireless communication systems. In the matter in question:

- modern *front–ends* comprise a variety of strongly nonlinear components, such as power amplifiers, mixers, oscillators etc., which need a proper characterization in the design process;
- nonlinear interactions have to be taken into account among the different subsystems in which a *front–end* can be decomposed. Complexity due to a high number of components/subsystems is a key issue in evaluating all the potential nonlinear effects;
- EM couplings occur between *front–ends* and antennas;
- EM coupling among adjacent antennas have to be considered if no array configuration is possible due to technological constraints;
- fading and distortions due to attenuation and multipath can affect significantly the received power level;
- many wireless communication systems work in the same frequency band: this requires an accurate planning of the spectrum usage in order to avoid potentially destructive interferences and other nonlinear effects (i.e. co– or inter–channel inter–modulations);
- etc.

The first RF application that will be discussed in detail regards the characterization of a MIMO link operating at 2.437 GHz.

In order to achieve the purpose of a rigorous computation of the system performance, each part of the link was studied by exploiting the most suitable simulation tool (commercial or customized, as will be apparent in the following): various techniques were adopted for best prediction of the behavior of a specific component, i.e. circuit (linear and nonlinear), EM and propagation. In the following, a brief description of the afore–mentioned approach is given.

- EM techniques: the circuit matrices of the antennas (scattering, impedance and admittance matrices) were extracted by means of CST MICROWAVE STUDIO®. These matrices were subsequently exploited in the nonlinear and propagation simulation tools.
- Circuit techniques: the simulation of the transceivers was carried out using NONLIN, a customized tool (developed by my research group) that takes into account the linear

and nonlinear effects of circuits and implements the HB (= Harmonic Balance) technique, which describes the *linear* components in the frequency domain.

- Propagation techniques: a 3D RT (= Ray Tracing) algorithm was used to calculate the ray paths connecting each transmitter to each receiver. The computation relies upon a specific *realistic* propagation scenario in order to offer an effective prediction of the co–simulation capabilities.

Other simulation tools were deployed to complete in an exhaustive way the link characterization, namely:

- VSS (= Virtual System Simulator), i.e. a system simulator inside *AWR Design Environment*, was used to calculate the BER (= Bit Error Rate) at the output ports of the multi–receiver;
- Spectre (Cadence® proprietary) was exploited to simulate, for the sake of comparison, the entire MIMO link in the time domain.

Finally, an ANN (= Artificial Neural Network) model was deployed to expand the (by default) short sequence of the output samples generated by the nonlinear simulations: this way, a more accurate prediction of the BER is possible and, at the same time, a reduction of the computation time can be achieved.

The second application of the CAD approach which will be exploited throughout the present PhD thesis is the design and experimental testing of an 868 MHz–RFID mobile device for a civil application on behalf of an Italian electronic factory.


## 1.1. FIRST APPLICATION: OVERVIEW OF A MIMO SYSTEM

MIMO systems are largely used in many modern wireless communications systems for their capability of improving link capacity and BER performance by exploiting *spatial diversity* and *multipath propagation*. In many cases of practical interest, due to space limitations they require compact antenna arrays with reduced spacing between radiators [1]. This entails that both i) near–field coupling effects between antenna elements and ii) far–field radiating behavior of the antenna array for a specific channel scenario are of primary importance. The former are needed to accurately describe port mismatch and power transfer effects between the antenna elements and the nonlinear subsystems, as well as the dependence of antenna impedances on frequency [2,3]. The latter are needed for a realistic computation of the channel transfer matrix and hence of the MIMO system capacity [4]. The purpose of the nonlinear/EM co–simulation is to systematically handle the nonlinear interactions of the transmitter and receiver subsystems through the transmitting/receiving antenna array couplings in conjunction with a realistic, fully 3D propagation scenario. The basic ideas were introduced for the first time in [5] and their accomplishments were limited to the analysis of a reference MIMO system, by optimizing the transmitter side only. In the following, the method capabilities of simultaneously accounting for the impact of dissimilar design variables affecting different domains of interest will be discussed. In particular:
i) I will introduce the new capabilities for the link optimization with respect to receiving antennas spacing, which is needed in practical MIMO link planning activities;
ii) an optimization and a significant acceleration of the RT algorithm were obtained, by separating the computation of geometrical aspects from the frequency–dependent ones;
iii) finally I will provide a validation of the entire approach by comparing the results with those computed by a completely different simulation technique, such as a time–domain

analysis, which shows similar results but at the expense of a more intensive computation time.

A block diagram of the simulation procedure is shown in

Fig. 2. The detailed meanings of the symbols are explained in the discussion presented in the following Sections.
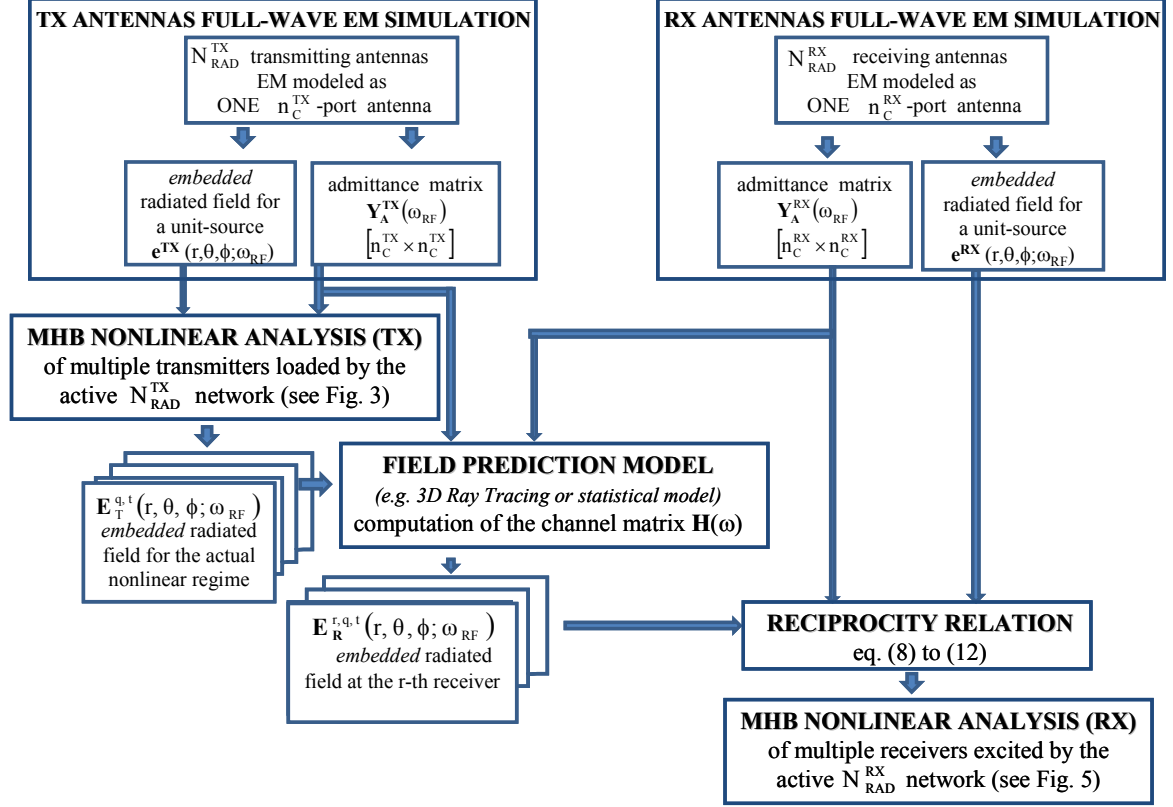


Fig. 2. Block diagram of the integrated multi–domain simulation flux for the end–to–end MIMO link analysis.

### 1.1.1. MULTI–ELEMENT ANTENNA ARRAYS EXCITATIONS AND FAR–FIELDS

Fig. 3 shows a block representation of a MIMO transmitter including the antenna array. The multiple RF/MW transmitter *front–ends* are described as a *unique* nonlinear system consisting of an arbitrary set of nonlinear devices interconnected by a linear sub–network. Making use of the piecewise HB technique, the circuit is partitioned into a linear and a nonlinear sub–network connected through $n_D^{TX}$ device ports, where:

$$n_D^{TX} = \sum_{t=1}^{N^{TX}} n_D^t \tag{1}$$

In Eq. (1) $N^{TX}$ is the number of transmitters and $n_D^t$ is the number of device ports belonging to the *t*–th transmitter. The linear sub–network is referred to as $N_{NORAD}^{TX}$ in Fig. 3, and can be treated by conventional circuit analysis algorithms or full–wave EM simulations, depending on the frequency and/or the circuit layout under exam. The antenna array is referred to as $N_{RAD}^{TX}$ in Fig. 3. It is described layout–wise and analyzed as a linear multiport radiating system by full–wave EM simulation [6] through the Finite Integration Technique. This analysis simultaneously provides the antenna scattering matrix $\mathbf{S}$ and the three–dimensional far–field

radiation pattern **E** at all frequencies of interest. The $N_{NORAD}^{TX}$ ports may be grouped into three sets, as shown again in Fig. 3, namely $n_D^{TX}$ ports for nonlinear device connection, $n_E^{TX}$ excitation ports and $n_C^{TX}$ ports for connection to the $N_{RAD}^{TX}$ network.
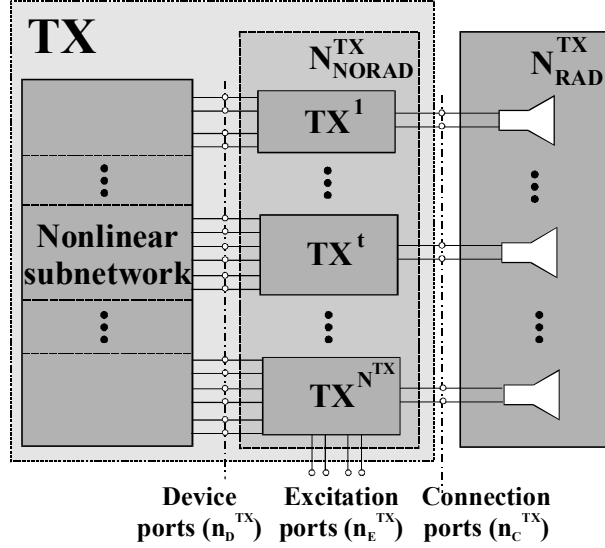


Fig. 3. Block diagram of a MIMO transmitter.

The voltages or currents at the connection ports represent the antenna array excitation. The latter can be computed by exploiting the customized nonlinear simulator, hence the HB technique, which allows to determine the large–signal regime of each transmitter *front–end*. This regime is quasi–periodic with spectral lines at all the inter–modulation products given as follows:

$$\Omega_{\overline{k}}^{TX} = k_1 \omega_{IF}^{TX} + k_2 \omega_{LO}^{TX} \qquad \overline{k} = \begin{bmatrix} k_1 & k_2 \end{bmatrix}^{tr} \tag{2}$$

In Eq. (2) the $k_i$'s are integer harmonic numbers, $\omega_{IF}^{TX}$ is the (angular) frequency of a sinusoidal IF signal exciting each transmitter *front–end* and $\omega_{LO}^{TX}$ is the (angular) frequency of a sinusoidal local oscillator (LO). A multi–tone HB analysis was carried out by well–known algorithms to compute the $n_D^{TX}$–vectors of the voltage harmonics $\overline{X}_{\overline{k}}^{TX}$ at all the transmitter device ports and at all discrete lines defined by (2). For some $\overline{k}$, say $\overline{k} = s$, we obtained from (2) the spectral line corresponding to the RF frequency $\omega_{RF}$ ($\omega_{RF} = \Omega_s^{TX}$). Let us now define: i) $\underline{Y}_{DT}^{TX}$, i.e. the ($n_D^{TX} \times n_C^{TX}$) admittance sub–matrix of the $N_{NORAD}^{TX}$ network; ii) $\underline{Y}_{TT}^{TX}$, i.e. the ($n_C^{TX} \times n_C^{TX}$) admittance sub–matrix seen from the connection ports; iii) $\overline{X}_s^{TX}$, i.e. the voltage harmonics vector at the RF frequency; iv) $\overline{V}_s^{TX}$, i.e. the vector of voltage phasors at the connection ports at the RF frequency. By means of the latter assumptions, the complex phasors of the currents flowing out of the $n_C^{TX}$ ports may be expressed as follows:

$$-\overline{I}_s^{TX} = \underline{Y}_{DT}^{TX}(\omega_{RF})\overline{X}_s^{TX} + \underline{Y}_{TT}^{TX}(\omega_{RF})\overline{V}_s^{TX} \tag{3}$$

Be $\underline{Y}_A^{TX}$ the ($n_C^{TX} \times n_C^{TX}$) admittance matrix of the multi–element antenna resulting from the EM analysis carried out by means of CST MICROWAVE STUDIO®, then we have:

$$\overline{I}_s^{TX} = \underline{Y}_A^{TX}(\omega_{RF})\overline{V}_s^{TX} \tag{4}$$

Finally, combining Eqs. (3) and (4) we get Eq. (5):

$$-\overline{V}_s^{TX} = \left[\underline{Y}_A^{TX}(\omega_{RF}) + \underline{Y}_{TT}^{TX}(\omega_{RF})\right]^{-1}\underline{Y}_{DT}^{TX}(\omega_{RF})\overline{X}_s^{TX} \tag{5}$$

Fig. 4 shows the reference systems for the propagation of the generic $q$–th ray from the generic $t$–th transmitter.
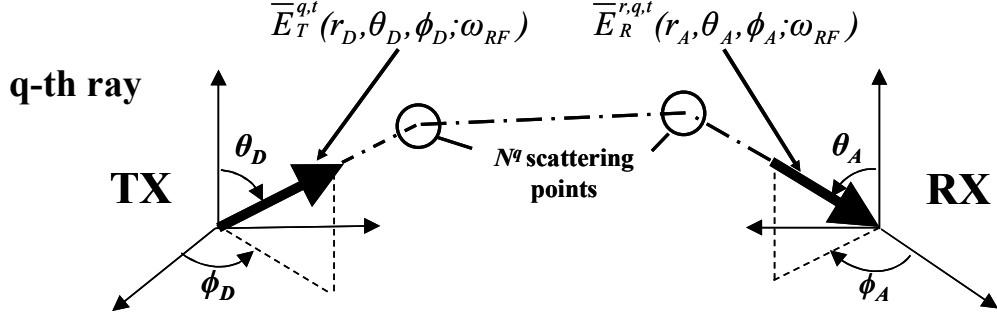


Fig. 4. Reference systems for the propagation of the generic ray from the generic transmitter. Subscript "$D$" denotes the departure, whereas subscript "$A$" denotes the arrival.

Be $A_\theta^t$ and $A_\phi^t$ the scalar components of the normalized field radiated by the $t$–th antenna at $\omega_{RF}$ in a spherical coordinate system with origin in the phase center $O_T$ of the transmitting array. Such components are generated by EM simulation of the antenna array [6] with a unit–voltage sinusoidal source of angular frequency $\omega_{RF}$ connected to the $t$–th port (of the $t$–th transmitter) and the remaining ports short–circuited. This way, the *actual* frequency–dependent array admittance and the *embedded radiation pattern* of each array element become available and can be combined with any desired channel description tool. By assuming free–space propagation, for the $t$–th array element the total radiated field $\overline{E}_T^t$ at $\omega_{RF}$ can be expressed as follows [7]:

$$\overline{E}_T^t(r,\theta,\phi;\omega_{RF}) = \frac{\exp(-j\beta r)}{r}\left[A_\theta^t(\theta,\phi;\omega_{RF})\hat{\theta} + A_\phi^t(\theta,\phi;\omega_{RF})\hat{\phi}\right]\overline{V}_s^{TX,t} \tag{6}$$

It has to be stressed that, due to the nonlinearity of the whole MIMO system (in particular, of the mixers and the power amplifiers), each transmitter cannot be described by a Thévenin equivalent circuit, i.e. as a voltage source in series with a constant impedance connected to each array port, because a Thévenin equivalent is only available for *linear* circuits. This is a crucial point, since the performance of a power amplifier designed for a nominal 50 $\Omega$ load impedance will change greatly as a function of the actual load, and thus of the inter–element couplings by which the load itself is affected. In order to account for such effects, a full nonlinear analysis of the entire set of transmitters loaded by the multiport antenna array is the only available way. A further consequence of the circuit nonlinearity is the increased spread of the output signal constellation due to nonlinear distortion, which gives a significant contribution to BER.

Fig. 5 displays a block representation of a MIMO receiver including the antenna array. The sub–system definition is exactly the same as the transmitter multi–array topology defined above and shown in Fig. 3, where the superscripts "TX" have been replaced by "RX".
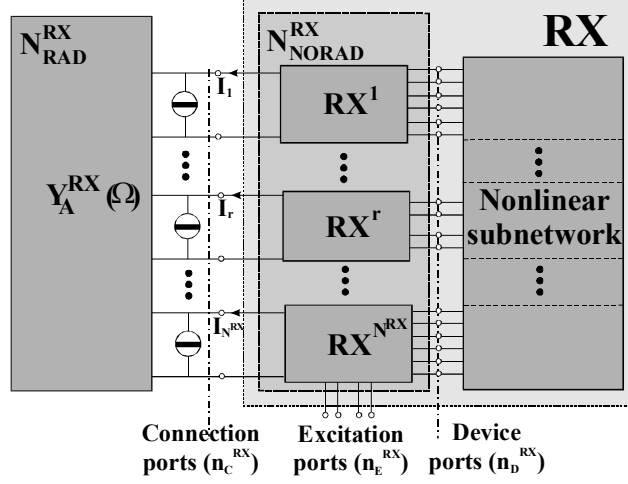


Fig. 5. Block diagram of a MIMO receiver.

Let us consider the $q$–th ray radiated by the $t$–th element of the transmitting antenna: it will excite voltages and currents in the receiver array. In such conditions $N_{RAD}^{RX}$ is a (linear) active network and may be represented by a Norton equivalent circuit as in Fig. 5, which leads to the following circuit equation:

$$\overline{I}_{s}^{RX,q,t} = \underline{Y}_{A}^{RX}\left(\omega_{RF}\right)\overline{V}_{s}^{RX,q,t} + \overline{J}_{s}^{RX,q,t} \tag{7}$$

In Eq. (7) $\overline{J}_{s}^{RX,q,t}$ is the vector of the unknown Norton equivalent current sources at the $n_{C}^{RX}$ ports, representing the circuit equivalent of the incident field associated with the $q$–th ray radiated by the $t$–th element of the transmitting antenna. In order to find $\overline{J}_{s}^{RX,q,t}$, for each array port a two–step procedure based on the Reciprocity Theorem was used: this allows a rigorous computation of the Norton current sources on the base of EM considerations. In the first step the incident $q$–th ray is suppressed, and the receiving array operates in a transmitting mode. The array is now fed by a unit voltage source connected to the $r$–th port, and all remaining ports are short–circuited. In such conditions the normalized radiated far–field $\overline{E}_{RN}^{r}\left(\theta_{A}^{'},\phi_{A}^{'};\omega_{RF}\right)$ (i.e., the physical field multiplied by r·exp(jβr)) and the input admittance parameters $Y_{TT}^{r}$ are computed by EM analysis, $\left(\theta_{A}^{'},\phi_{A}^{'}\right)$ are the angular coordinates of the $q$–th ray direction of arrival in a receiver–referred spherical reference frame. In the second step the incident field is reintroduced and all the antenna ports are short–circuited, so that by (7) the entries of $\overline{J}_{s}^{RX,q,t}$ coincide with the port currents. Such currents may then be expressed by a straightforward application of the Reciprocity Theorem. Specifically, for the $q$–th ray radiated by the $t$–th element, the $r$–th entry of $\overline{J}_{s}^{RX,q,t}$ (namely $J_{s}^{r,q,t}$) may be expressed in the form:

$$J_{s}^{r,q,t} = j\frac{2}{\eta}\lambda\, Y_{TT}^{r}\,\overline{E}_{RN}^{r}\left(\theta_{A}^{'},\phi_{A}^{'};\omega_{RF}\right)\bullet\overline{E}_{R}^{r,q,t}\left(r_{A},\theta_{A},\phi_{A};\omega_{RF}\right) \qquad \left(1\le r\le N^{RX}\right) \tag{8}$$

where $\bullet$ denotes the scalar product and $\overline{E}_R^{r,q,t}$ is the field incident on the phase center of the receiving array and referred to the position of its $r$–th element. In particular, $\overline{E}_R^{r,q,t}$ is given by the following expression:

$$\overline{E}_R^{r,q,t}(r_A,\theta_A,\phi_A;\omega_{RF}) = \Gamma^{q,t}(s_1^q,...,s_i^q,...,s_{N^q}^q)\underline{\underline{A}}\,\overline{E}_T^{q,t}(r_D,\theta_D,\phi_D;\omega_{RF})\exp(\pm j\beta d^{r,q,t}) \quad (9)$$

In Eq. (9):

1. $\overline{E}_R^{r,q,t}$ is described in a reference frame local to the receiver;
2. $(\theta_A,\phi_A)$ represents the direction of arrival of the $q$–th ray, whereas $r_A$ is the distance at which $\overline{E}_R^{r,q,t}$ is evaluated;
3. $\Gamma^{q,t}$ is the *scalar spreading factor* accounting for the natural attenuation of the field as it propagates along the ray. The $q$–th ray is a piecewise straight line consisting of $N^q$ cascaded segments, and $s_\ell^q$ is the length of the $\ell$–th part of such segments. The exponential factor accounts for the phase shift along the $q$–th ray between the $t$–th transmitting and the $r$–th receiving antenna element. The distance $d^{r,q,t}$ is the overall ray length taking into account the antenna element positions referred to their respective phase centers;
4. $(\theta_D,\phi_D)$ is the initial (departure) direction of the $q$–th ray with respect to a local reference system on the transmitter side;
5. $\overline{E}_T^{q,t}$ is the far–field radiated by the $t$–th antenna on the $q$–th ray at a reference distance $r_D$ (conventionally chosen as 1 m) in the direction $(\theta_D,\phi_D)$ and is computed by means of Eq. (6);
6. $\underline{\underline{A}}$ is a dyadic accounting for the effect of ray interactions (reflections, diffractions, etc.), which may be cast in the following form:

$$\underline{\underline{A}} = \left[\prod_{\ell=\min\{1,N^{q,t}\}}^{N^q}\underline{\underline{A}}_\ell^q\right] \quad (10)$$

where $\underline{\underline{A}}_\ell^q$ is an appropriate dyadic which decomposes the field into orthogonal components at the $\ell$–th interaction point and incorporates the proper interaction coefficients [8].

A superposition of the contributions (8), spanning all the incoming rays, finally yields the current source at the $r$–th port:

$$J_s^r = \sum_{t=1}^{N^{TX}}\sum_{q=1}^{N_{RAY}^t}J_s^{r,q,t} \quad (11)$$

where $N_{RAY}^t$ is the number of rays originating from the $t$–th transmitter element.

Combining Eqs. (6), (8), (9) and (11) each current $J_s^r$ ($1 \le r \le N^{RX}$) can be expressed now as a linear combination of the voltages $V_s^t$ ($1 \le t \le N^{TX}$). This allows to establish a linear map between the vector $\overline{J}_s^{RX}$ of the receiver excitation currents at the receiving antenna ports and the vector $\overline{V}_s^{TX}$ of the transmitting antenna excitation voltages. This map can be cast in the following form:

$$\overline{J}_s^{RX} = \underline{H}(\omega_{RF})\overline{V}_s^{TX} \tag{12}$$

In Eq. (12) $\underline{H}(\omega_{RF})$ is the ($N^{RX} \times N^{TX}$) complex matrix representing the channel transfer matrix.

In Eqs. (13) a 2x2 MIMO link with only two NLOS rays (one for each transmitter) will be presented as a simple example of application of Eq. (12), which takes on the following form:

$$\begin{bmatrix} J_s^{r1} \\ J_s^{r2} \end{bmatrix} = \begin{bmatrix} H_{11} & H_{12} \\ H_{21} & H_{22} \end{bmatrix} \begin{bmatrix} V_s^{t1} \\ V_s^{t2} \end{bmatrix}$$

$$H_{11} = j\frac{2}{\eta}\lambda\, Y_{TT}^{r1}(\omega_{RF})\,\Gamma^{I,t1}\exp(\pm j\beta d^{r1,I,t1})\overline{E}_{RN}^{r1}(\theta_A^I,\phi_A^I;\omega_{RF}) \bullet \left[\underline{\underline{A}}\,\overline{E}_T^{I,t1}\right]V_s^{t1}$$

$$H_{12} = j\frac{2}{\eta}\lambda\, Y_{TT}^{r1}(\omega_{RF})\,\Gamma^{II,t2}\exp(\pm j\beta d^{r1,II,t2})\overline{E}_{RN}^{r1}(\theta_A^{II},\phi_A^{II};\omega_{RF}) \bullet \left[\underline{\underline{A}}\,\overline{E}_T^{II,t2}\right]V_s^{t2} \tag{13}$$

$$H_{21} = j\frac{2}{\eta}\lambda\, Y_{TT}^{r2}(\omega_{RF})\,\Gamma^{I,t1}\exp(\pm j\beta d^{r2,I,t1})\overline{E}_{RN}^{r2}(\theta_A^I,\phi_A^I;\omega_{RF}) \bullet \left[\underline{\underline{A}}\,\overline{E}_T^{I,t1}\right]V_s^{t1}$$

$$H_{22} = j\frac{2}{\eta}\lambda\, Y_{TT}^{r2}(\omega_{RF})\,\Gamma^{II,t2}\exp(\pm j\beta d^{r2,II,t2})\overline{E}_{RN}^{r2}(\theta_A^{II},\phi_A^{II};\omega_{RF}) \bullet \left[\underline{\underline{A}}\,\overline{E}_T^{II,t2}\right]V_s^{t2}$$

In Eq. (13) superscripts $^{t1},^{t2}$ and $^{r1},^{r2}$ are the transmitted and incident rays indexes.

The channel transfer matrix $\underline{H}(\omega_{RF})$ defined by Eq. (12) simultaneously accounts for selective fading due to 3D multipath propagation in the channel, for all electromagnetic couplings existing between the transmitting and receiving antennas, and for polarization mismatches between incident field and receiving antennas. The latter are due to power transfer between cross polarizations taking place in the channel and possibly to different antenna structures.

At this stage, the receiver $N_{NORAD}^{RX}$ equations can be written in a way similar to Eq. (3):

$$-\overline{I}_s^{RX} = \underline{Y}_{DT}^{RX}(\omega_{RF})\overline{X}_s^{RX} + \underline{Y}_{TT}^{RX}(\omega_{RF})\overline{V}_s^{RX} \tag{14}$$

where the superscript "RX" stands for "receiver", and the meanings of all quantities are otherwise identical to those appearing in Eq. (3). Eqs. (7) and (14) and the nonlinear sub–network equations may now be handled by well–known algorithms [7] to produce a full nonlinear analysis of the receiver under modulated–RF drive.

## 1.1.2. 3D RT ALGORITHM: AN EFFECTIVE EVALUATION OF MIMO PERFORMANCE

RT algorithms are among the most accurate field prediction tools for the study and planning of radio systems in realistic propagation environments. Until now, the main obstacle to the widespread use of RT models has been the need for a detailed 3D database of the environment. However, this requirement has become even less critical thanks to the nowadays availability of digitized maps provided by City Authorities or of commercially available urban maps obtained through aerophotogrammetry. RT models provide effective computation capabilities to predict the multipath pattern and thus the time– and angle–dispersion of the radio signal: this is especially useful for studying MIMO systems, which exploit such

phenomena to increase the transmission capacity of the radio channel [9]. For the present case of study, a 3D RT model [10] was considered and adapted to MIMO radio channel characterization. A fully 3D vector approach with an embedded diffuse scattering model [11] was adopted to pursue a realistic description of multipath propagation. A coherent representation of the transmitted electric field corresponding to each radio path is provided, as is necessary for MIMO channel characterization. Therefore, the electric field of each radio path (ray) is represented by a complex vector, which depends on the travelled distance and on the interactions (reflections, diffractions, etc.) experienced by the propagating wave.

The so called *narrowband array* assumption is considered as well: the multipath pattern is assumed to be unique for a given couple of transmit/receive phase–center positions. By tracing all the rays between the two radio terminals a multidimensional characterization of the array–dependent MIMO channel matrix was derived.

The peculiar feature of the adopted RT tool, empowered by the embedded diffuse scattering model, is its ability to accurately describe the multipath nature of the radio link, including its angular spreading which is fundamental for MIMO performance. Such ability is assessed in [12,13] where the model is validated against multidimensional MIMO measurements performed at the Helsinki University of Technology. Furthermore, the adopted RT algorithm showed to yield realistic results in terms of MIMO maximum transmission capacity, as reported in [14].

### 1.1.3. 2x2 MIMO LINK SIMULATION: A RIGOROUS APPROACH FOR BEST PERFORMANCE PREDICTION

For the present PhD thesis I will consider a 2x2 MIMO link designed for a WLAN application at 2.437 GHz. The transmitter consists of two single–conversion *front–ends* with a total of 196 device ports and 2,370 internal nodes. The receiver consists of two image–rejection *front–ends* with 416 device ports and 2,490 nodes. The antennas are two parallel groundless half–wavelength dipoles built on Taconic RF–60 substrate ($\varepsilon_r$ = 6.15, tan$\delta$ = 0.0028), and are analyzed by [6]. The array is depicted in Fig. 6. The results, in terms of scattering parameters of the array and of the radiation pattern of each element in the presence of the other one, are plotted in Fig. 7a and Fig. 7b, respectively, and are compared with similar quantities for the standalone dipole.
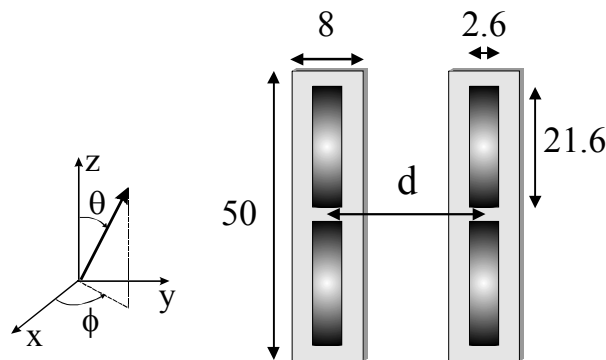


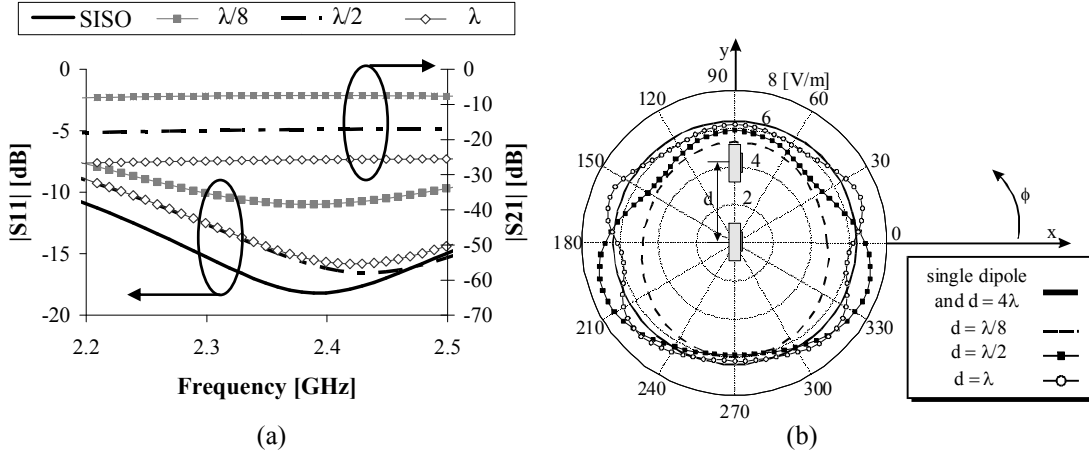Fig. 6. Printed dipole array (dimensions are in mm).

Fig. 7. (a) Scattering parameters of the two–port transmitting antenna for different dipoles spacing d and for the standalone dipole (SISO); (b) H–plane radiation pattern of a standalone dipole and of one dipole in the presence of the other for different inter–element spacing. The antennas are displayed from the top view (along the z > 0 direction) according to the reference system of Fig. 6.

The reflection coefficients exhibit resonance frequency shifts up to 2%, and a mutual coupling up to −10 dB is observed. The latter produces a remarkable deformation of the H–plane radiation pattern with respect to the standalone dipole, as is evident from Fig. 7b. These results clearly show that theoretical approaches to MIMO analysis based on the assumption of isolated antennas do not represent a valid description of real–world compact systems. Antenna interactions are significant even at distances d comparable with the wavelength. In turn, transmitter performance is strongly dependent on couplings between antennas. Indeed due to couplings transmitter loads are a function of antenna distance, and so is the transmitter performance. This effect is demonstrated in Fig. 8, where the far–field radiated power density $\overline{E}_T \bullet \overline{E}_T^*/2\eta$ evaluated by Eq. (6) is plotted against IF input power as a function of dipoles spacing. For the sake of comparison, the same analysis is repeated for an identical standalone transmitter. The transmitter gain compression curve is found to be strongly influenced by the presence of neighboring array elements.
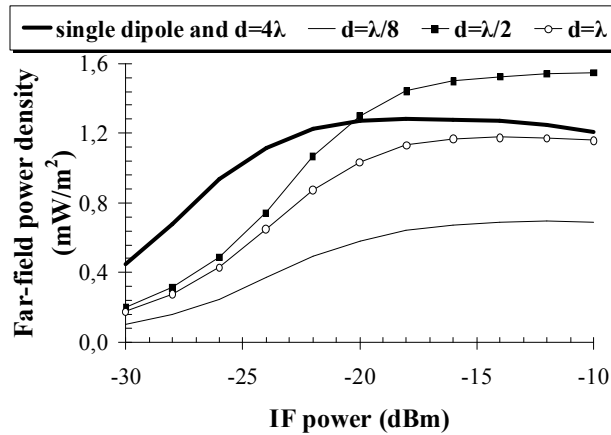


Fig. 8. Transmitter gain compression curve for different dipoles spacing.

Frequency–dependent antenna interactions have a primary influence on MIMO channel capacity [2,4]; furthermore, they also play an essential role in determining the linear and nonlinear transmitter performance, as is apparent in Fig. 8 [15]. Indeed such performance may

be enhanced or degraded with respect to the SISO case depending on antennas spacing, which plays en essential role in the overall design of the system.

As regards the effects of the receiving antennas spacing on the channel transfer matrix in a rich scattering propagation scenario, the first analysis was carried out under RF sinusoidal excitation at 2.437 GHz *without modulation*. The transmitting antenna elements were kept at a fixed distance of 6.16 cm, corresponding to half a wavelength. The channel scenario needed more than 3,000 propagation rays. Fig. 9 shows the magnitudes of the entries of the channel transfer matrix $\overline{H}(\omega_{RF})$ for receiving antennas spacing of $3\lambda/8$ (Fig. 9a) and $\lambda/8$ (Fig. 9b), respectively. From the two plots it is apparent that, for the chosen propagation scenario, selective fading may be effectively compensated by suitable receiving antennas spacing, since larger values of the $\overline{H}(\omega_{RF})$ entries automatically result in a channel capacity improvement [2,4].
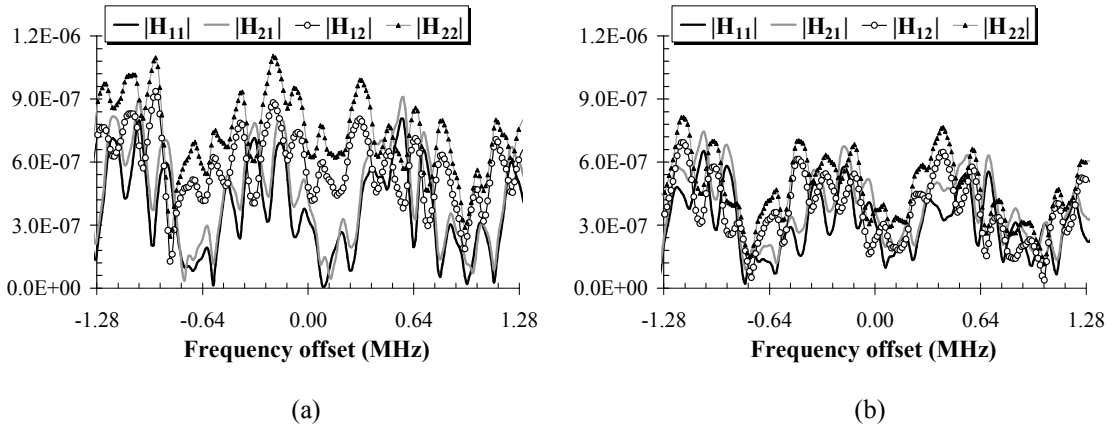


Fig. 9. Magnitudes of the channel transfer matrix entries for: (a) $3\lambda/8$ dipoles spacing; (b) $\lambda/8$ dipoles spacing (receiver side).

The next step was the optimization of the receiving antennas spacing for the given channel scenario and for an effective digitally–modulated signal. The selected modulation format was the 16–QAM at a bit rate of 1.28 Mb/sec. The system output signal was computed by in–phase combining the output signals of the two receivers (*equal–gain combining* technique). The considered performance index is the BER in the presence of thermal noise described by an AWGN model. The noise calculation was based on the assumption that the noise received by the antenna is the dominant noise contribution. According to the well–known theory of linear network noise, this contribution was modeled by a set of equivalent noise current sources connected in parallel to the receiving antenna ports, and thus to the current sources $J_s^r$ given by Eq. (11), representing the useful signal. The noise sources have Gaussian statistics, and their correlation matrix is proportional to the real part of the multiport receiving antenna admittance matrix trough an equivalent antenna noise temperature [16]. BER evaluation was carried out at the circuit level by the same technique introduced in [7] for the SISO case. Once all the system parameters were specified, the input modulating signal is described as a random sequence of bits, and the output sequence is evaluated by the envelope–transient technique in a time slot of finite length, say a few hundreds of bits. This I/O information generated by simulation is used to train an ANN model of the link in the given operating conditions. The ANN model is then used to cheaply generate an output sequence of several millions of bits that is used to compute the BER by direct comparison with the input sequence [7,17]. Note that a full frequency–domain noise analysis for nonlinear circuits including the LO noise contribution in receiver *front–ends* was previously

demonstrated [16,18]. However, handling LO noise inside a rigorous nonlinear circuit–level BER analysis of the kind outlined above is not straightforward. Fig. 10 shows the results obtained for a fixed SNR of 10 dB at the receiver input. Such results are based on a sequence of 1,600,000 samples generated by an ANN link model trained by a sequence of 512 simulated samples. For the propagation scenario under consideration the optimum antennas spacing ($d \approx \lambda/4$) results in a BER reduction of about two orders of magnitude with respect to the SISO case. Note that the optimum performance is acceptable in spite of the low SNR. It has to be stressed that we can expect the MIMO curve to converge to the SISO curve for large values of antennas spacing, since the EM interactions among the various elements become negligible and each antenna acts a standalone dipole. As an alternative to the BER, an evaluation of the EVM could be provided to test the system performance.
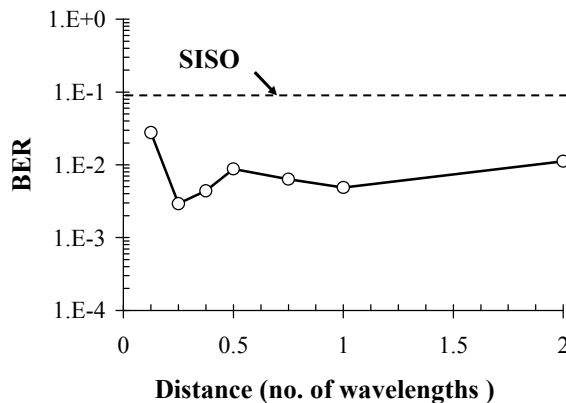


Fig. 10.  Estimated BER of a MIMO link as a function of receiving dipoles spacing.

These results are visually confirmed by comparison of the output signal constellations of the MIMO link with optimal $\lambda/4$ (Fig. 11a) and non–optimal $\lambda/8$ (Fig. 11b) receiving antennas spacing.



(a)                                                                (b)
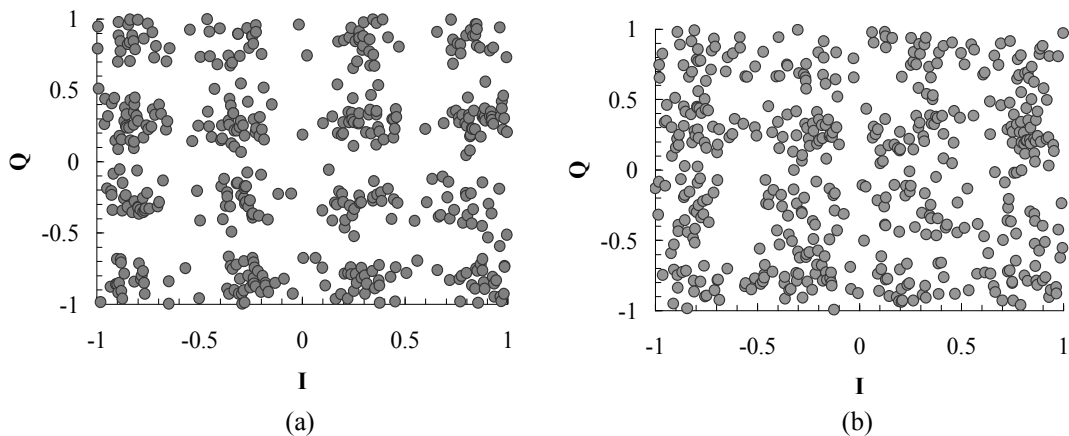
Fig. 11.  Output signal constellation of the MIMO link with: (a) optimal receiving antennas spacing ($d \approx \lambda/4$); (b) non–optimal antennas spacing ($d \approx \lambda/8$).

The two main sources of the signal corruption observed in Fig. 11 are noise and in–band linear distortion. Nonlinear distortion is also somewhat improved by the MIMO arrangement with respect to the corresponding SISO system (same circuits and channel), but the effect is not as dramatic as for BER. This is evident by comparison of Fig. 12a and Fig. 12b, where the

input and output signal spectra are shown (in the absence of noise) for the MIMO system with optimal antennas spacing and for the corresponding SISO system, respectively. The ACPR is reduced by about 4 dB in the MIMO case. Furthermore, for a MIMO system nonlinear distortion is almost independent of antennas spacing. As an example, the output spectrum reported in Fig. 12c for a case of non–optimal antennas spacing (d ≈ λ/8) exhibits a distortion level quite similar to that observed in Fig. 12a (the change in ACPR is less than 1 dB). A full nonlinear/electromagnetic multi–tone analysis of the 2x2 MIMO link requires about 100 minutes of CPU time on a 2.8 GHz PC. Within this budget, about 40% of the time is taken by the EM simulation of the transmitting and receiving antenna arrays, about 45% by the computation of the RT–based field prediction model, and the remaining 15% by the nonlinear analysis of the transmitter and receiver *front–ends*.
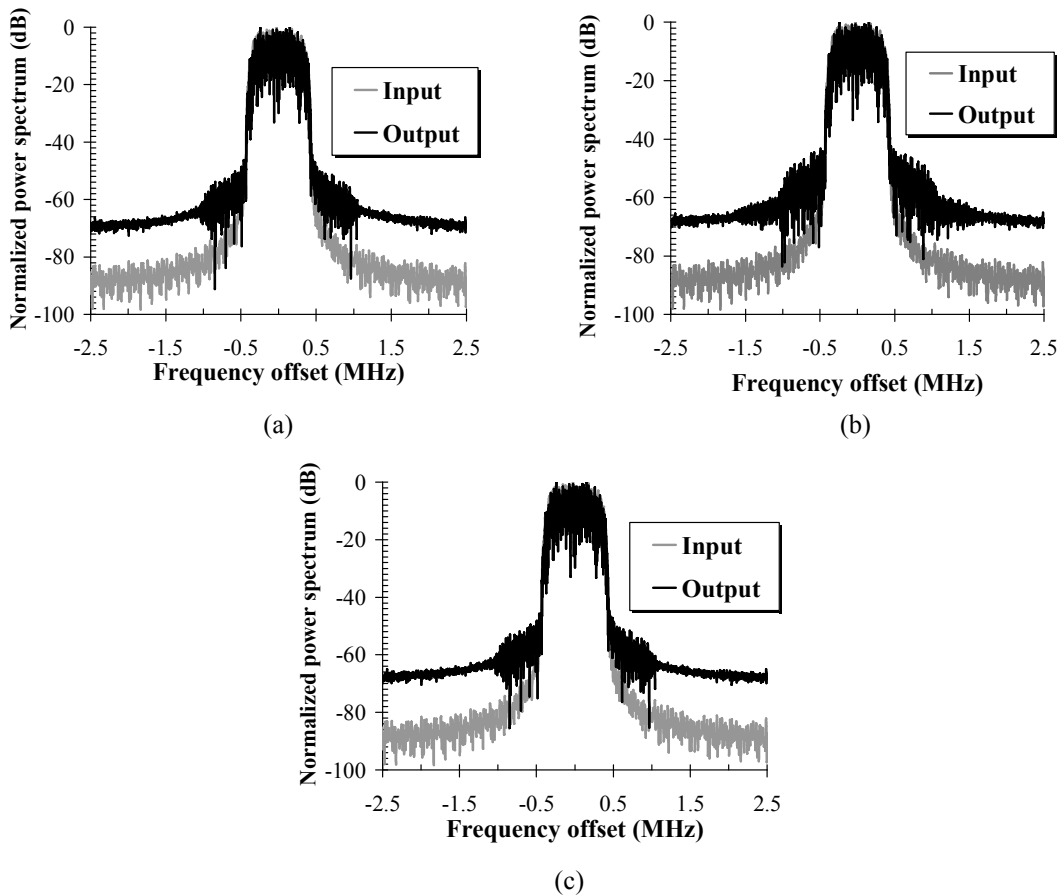


(a)



(b)



(c)

Fig. 12. Normalized power spectra for: (a) a MIMO link with optimal dipoles spacing (ACPR is about –50.1 dBc); (b) the SISO link corresponding to Fig. 12a (ACPR is about –46.2 dBc); (c) a MIMO link with non–optimal dipoles spacing (d ≈ λ/8) (ACPR is about –49.2 dBc).

In the following I will present a comparison of the MIMO link analysis results produced by the technique explained so far with those generated by time–domain analysis making use of Spectre HDL [9]. For this purpose, the frequency–domain channel model was converted into a time–domain user–defined component in Spectre HDL format according to the technique discussed in [19]. This procedure was very demanding in terms of CPU time since it basically relies upon a time–domain convolution. The other bottleneck is the slow (1.28 Mb/sec) modulation of the 2.437 GHz RF carrier, which generates the need for an unreasonably large number of time–domain integration steps. Hence it was necessary to work out a tradeoff between accuracy and CPU time by limiting the number of frequency–domain sampling points for the entries of the channel transfer matrix, and of time–domain sampling points in

the integration process. Even so, the CPU time required to compute the results reported in Fig. 13 and Fig. 14 by time–domain analysis was about 22,000 times longer than by the CAD procedure discussed before. The benchmark quantity used for comparison is the Norton equivalent current source $J_s^1$ defined by Eq. (11). The analysis was limited to a 64–bit time slot. Fig. 13 provides a visual comparison of the time–domain waveforms of this current computed in the presence of digital modulation. More quantitative comparisons are provided in Fig. 14a and Fig. 14b, showing the in–phase (a) and quadrature (b) components of the complex envelope. In all cases the agreement may be considered very satisfactory, which provides a reliable validity check for the presented MHB analysis procedure.
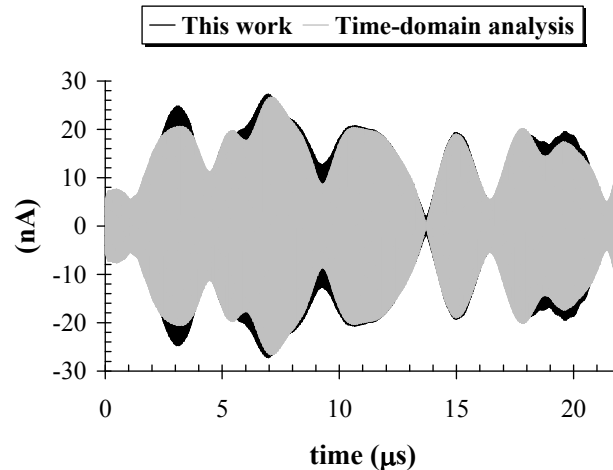


Fig. 13. Time–domain waveform of the modulated current source $J_s^1$ for a 2x2 MIMO link with optimal receiving dipoles spacing (64–bit time slot).
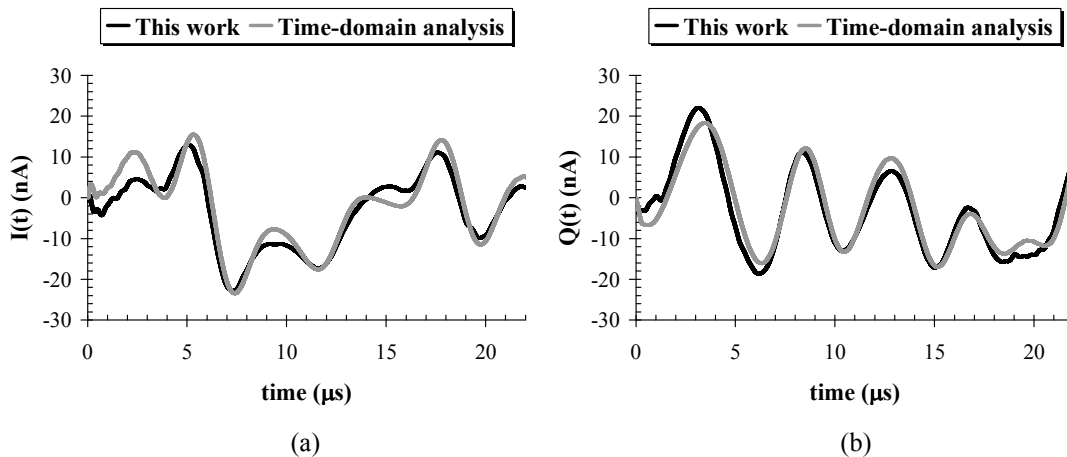


Fig. 14. In–phase (a) and quadrature (b) component of the complex envelope for the modulated current source $J_s^1$.

Finally, in order to validate the BER computation procedure, results similar to those reported in Fig. 10 were tried to be generated by means of a commercial software. Again, a 16–QAM modulated input signal was considered, with a bit rate of 1.28 Mb/sec and a 10 dB SNR at the receiver ports. This turned out to be an awkward task, because a direct time–domain approach was found to be impossible due to impractically large CPU time requirements. Thus the investigation was resorted to a system simulator. In order to get the best accuracy within the capabilities of system–oriented software, each transmitter and

receiver was described by a behavioral model derived by HB analysis, and the channel description was input as a user–defined component characterized by the Eq. (12) at the data entry level. In this way, the results provided by the system simulator were found to agree with those reported in Fig. 10 with a maximum discrepancy of $\pm 10\%$ for $d \geq \lambda$. However, for closely spaced antennas the commercial simulator was unable to reproduce the dependence of the transmitter performance on antenna couplings and the BER results were grossly in error.

## 1.2.  SECOND APPLICATION: INTEGRATED DESIGN AND TESTING OF AN 868 MHZ–RFID MOBILE DEVICE

The assigned task was the development of an *ad hoc* antenna (possibly in array configuration) operating at 868 MHz for a commercial RFID application, taking into account the embedded multi–mode RFID chip. Many constraints were mandatory as regarded area occupation and interactions with the underlying circuitry, whose design was outside the requested assignment. Nevertheless the integration of an efficient radiating system into a pre–defined housing with specific requests in terms of radiation pattern and efficiency was a formidable problem, which required a deep study of several possible configurations. The bottleneck of the project was the feeding network which should satisfy the following requirements:

1.    designed for a balanced bi–dimensional antenna array (dipoles)
2.    connected to an UHF chip
3.    matching to two chip state impedances
4.    maximum power transfer to the antenna array
5.    easy fabrication and mechanical robustness

Furthermore, in the opposite direction of the RFID link a low back–radiation and a low value of SAR were unavoidable constraints for the design of the device: this turned out to be a challenging task, since it was necessary to consider the presence of the digital circuitry in the back part of the housing. An original and "smart" solution was then investigated and, at a later stage, manufactured in order to be tested.

After a brief introduction, the design details and the characterization of the device will be provided in order to demonstrate that an accurate (in this case, *linear*) CAD model is a starting point for any other successive step in the project of an off–the–shelf wireless system.

### 1.2.1. MOTIVATION OF THE DESIGN TASK

In the last years there has been an increasing interest in exploiting metal planes in PCBs of PDA devices. A PDA device is a handheld device combining computing, telephone/fax, Internet and networking features. A typical PDA can function as a cellular phone, fax sender, web browser and personal organizer. Unlike portable computers, most PDAs began as pen–based, using a stylus rather than a keyboard for input. This means that they also incorporated handwriting recognition features. Some PDAs can also react to voice input by using voice recognition technologies. PDAs of today are available in either a stylus or keyboard version.

The aim of the afore–mentioned integration of PCB ground planes in PDAs is the enhancement of antenna performance. According to the EM behavior of a meander line configuration, slotted meandered metal planes may be used as electrically longer, even though their physical size is unchanged. Usually this is exploited for increasing the operating bandwidth or for generating new operating frequencies [20,21], while keeping the antenna volume inside the requirements of small PDAs. These solutions provide significant

advantages with respect to operating frequency bands but they generally do not perform satisfactorily from the point of view of antenna efficiency and radiation reduction in undesired directions [22]. These requirements are mandatory when applications based on passive or semi–passive RFIDs are concerned because of the twofold need of: i) long range coverage; ii) low–power consumption. Furthermore, it is well known that the design of an RFID antenna on a PCB still presents many problems, because solid metal planes, traces and electronic components may dramatically reduce the read distance.

### 1.2.2. PSEUDO YAGI–UDA BI–DIMENSIONAL ARRAY DESIGN

In agreement with the assigned task, in order to obtain a *broadside* radiation in the desired direction (z > 0) a bi–dimensional, linearly–polarized antenna array was designed: it consists of two driven dipoles, acting as directors, and two passive ones, acting as reflectors, according to the Yagi–Uda concept. Dipoles are printed on different PCB slides stacked inside a customized PDA. The radiation direction of the array was required to be orthogonal to the dipoles plane, in the z > 0 half–space. Fig. 15 shows the PCB layers housing the bi–dimensional dipole array. The side view of the multilayer PCB is also displayed together with the main dimensions of the PDA case.
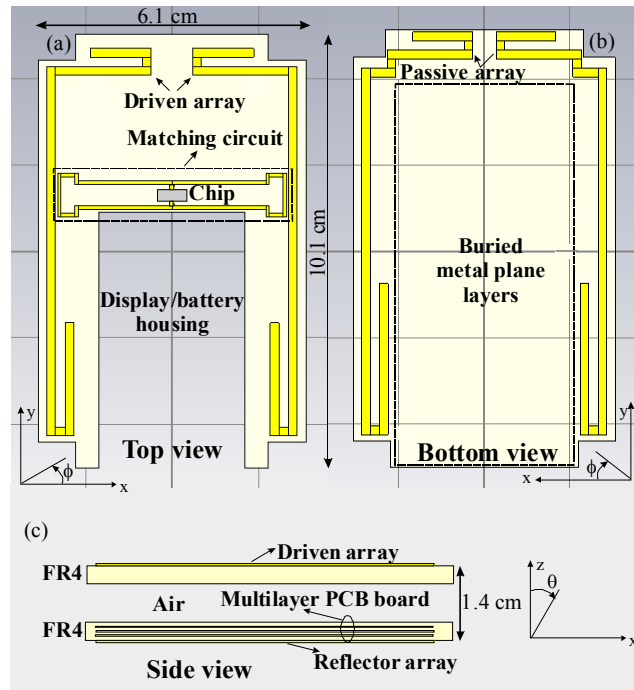


Fig. 15. Geometry of the stacked bi–dimensional array: (a) top view; (b) bottom view; (c) side view.

The requested device should operate as a fingerprint detector for disabled–oriented easy–access capabilities in cities equipped with traffic–controlled passages. The top view faces the vehicle windscreen, whereas the bottom view is in the direction of the disabled user. Purpose of the system is to allow the vehicle entrance into the surveillance camera–controlled city center only in the effective presence of the PDA holder in the vehicle itself, hence avoiding (unfortunately very common) inappropriate usage of disabled–oriented facilities. By means of the fingerprint, the digital circuitry (inside the "multilayer PCB board" in the side view of Fig. 15) certifies the identity of the PDA holder and activates the antenna array with a signal which authorizes the vehicle to pass under the controlled access. It is apparent in Fig. 15 that

restrictive space constraints were mandatory to fulfill customer's needs in terms of electric and electronic components displacement, in particular:

1. dipole antennas should not be located at the border of the substrate(s) in order to leave enough space for rivets;
2. the lower part of the upper substrate (with the "driven dipoles" in the top view of Fig. 15) is empty since it houses the batteries;
3. the upper part of the upper substrate is dedicated to the fingerprint detector, hence this space could not be exploited for driven dipoles design;
4. the multilayer PCB board ("side view" in Fig. 15) houses the digital circuitry with multiple buried metal plane layers, the latter being very close to the passive dipole array necessary to obtain the *end–fire* radiation in the desired direction (according to the Yagi–Uda antenna array concept);
5. the space between the two substrates is filled with air and the distance between the two FR4 layers (consistent with the PDA height along the z–direction) is only 1.4 cm, which corresponds to about $\lambda_0/25$, where $\lambda_0$ is the free–space wavelength and $\lambda_0 \approx 34.56$ cm at 868 MHz. This entails that a CAD optimization was mandatory to investigate the best antenna topology and hence achieve the goal of a *pseudo* Yagi–Uda array (for which a spacing of about $\lambda_0/4$ between driven and passive dipoles is the key issue to obtain the wanted radiation pattern).

The proposed solution satisfied all the afore–mentioned requirements (hence it does not interfere with the space allocated for all the other subsystems) by exploiting meandered dipole antennas and meandered ground. In particular the latter allows to almost remove the undesired bi–directional radiation at the reflectors side, since they behave as a slow–wave structure with minimal area removal. This solution gets rid of cavity–like enclosures which can degrade the performance of the antenna while increasing complexity in manufacturing, volume and weight. The antenna design was carried out by combining EM simulation [6] with advanced optimization techniques [23] simultaneously accounting for the RFID chip matching in back–scattering operation.

A low–cost FR4 substrate ($\varepsilon_r = 4.75$, $\tan\delta = 0.025$) was used for both stack layers shown in Fig. 15, whereas all the metallization (dipoles and ground planes) are made of copper. On the borders of the top layer two half–wavelength driven dipoles were *symmetrically* placed in order to enhance the *broadside* radiation (along the z–direction). The latter was required for wireless communication, nevertheless the radiation in the z < 0 space was undesired for both maximizing the reading distance and preventing radiation to closely–located people and to RF/digital circuitry. Fig. 15 shows that the driven dipoles are connected to the RFID chip ports through an inductively–coupled matching network designed to operate in the 868 MHz band. Two significant advantages of the proposed design procedure can be highlighted: i) the dipoles lengths and the RFID chip matching network were optimized simultaneously, thus accounting for different operating states and power conditions [23]; ii) the reading range was preserved from being reduced due to antenna–chip mismatch. In order to avoid radiation in the z < 0 half–space, on the back side of the multilayered PCB two passive dipoles, having longer lengths to act as reflectors, were considered aligned with the director ones. This is equivalent to the design of a *pseudo* Yagi–Uda antenna array, since:

1. each couple made of a driven dipole and a passive one along the z–direction acts as a Yagi–Uda antenna array;
2. the distance between the two elements of each Yagi–Uda antenna array is not equal to about $\lambda_0/4$, hence a *pseudo* Yagi–Uda can be defined accordingly;

3. finally, the combination of two *pseudo* Yagi–Uda antenna arrays along the x–direction allow to enhance the broadside pattern avoiding asymmetrical radiation along the z–direction.

   In order to fit into the case dimensions, the optimal electrical lengths were reached by meandering the dipoles metallization along the space allowed by the case shape. To preserve the linear polarization, which is usually required for RFID–enable applications, the majority of the dipoles physical length was kept along the case major dimension. The air gap between director and reflector dipoles was optimized for the best coupling to maximize the directivity of the resulting bi–dimensional array, consistent with the PDA height. In the absence of other metallization, the final array configuration satisfied the design specifications with excellent performance. In Fig. 16 the simulated E–plane and H–plane radiation patterns are superimposed on the same polar plot. A gain of 3.9 dB was realized with a front–to–back ratio better than –8 dB.
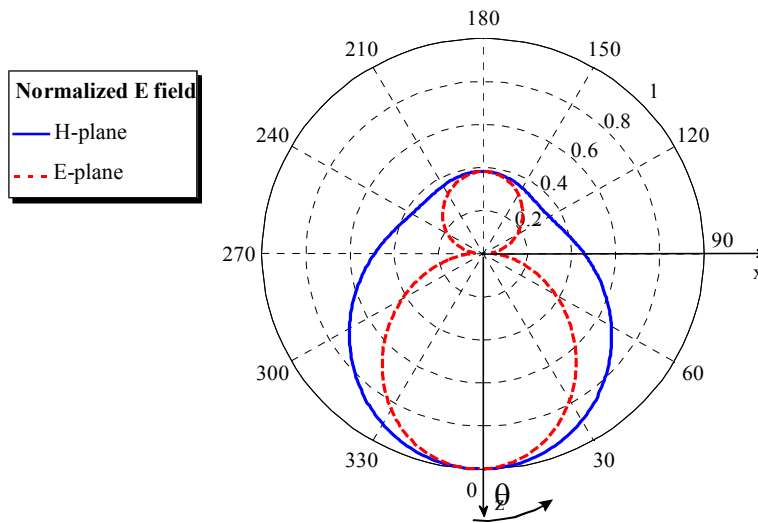


Fig. 16. E–plane and H–plane radiation pattern of the bi–dimensional dipole array made of dipoles printed on a standard FR4 substrate.

## 1.2.3. EFFECT OF THE MEANDERED BURIED GROUND PLANES

   In realistic applications, only the areas under the dipoles can be designed without ground planes, whereas the remaining ones consist of multilayer structures, including metal planes, to manage electronic components placement and powering. For the present study case, 4x9 cm$^2$ metal planes were buried inside the bottom substrate in Fig. 15 for ground reference and battery supply. They are almost coplanar with the reflector dipoles and are only 0.6 cm (i.e. less than $\lambda_0/50$) far from them. In this situation a strong coupling with the array was observed such that the ground planes themselves act as director elements. This is proven to be true for ground planes whose length is up to 35% shorter than those of driven dipoles, which are 14.5 cm long. The ground planes influence on array behavior is clearly demonstrated by simulated E–plane and H–plane radiation patterns of Fig. 17: radiation along the $\theta = 0°$ direction is still present but the major power density is now concentrated towards the opposite one. This may strongly affect RFID systems reading range. Thus, in order to effectively skip the influence of the ground planes, their length should be shorter than 7.5 cm (less than 50% of dipoles length), but this would entail a too small area left for components placement.
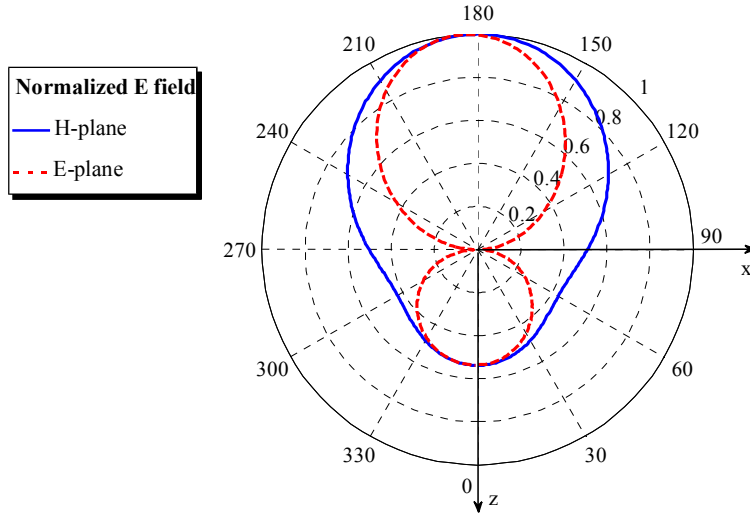
Fig. 17. E–plane and H–plane radiation pattern of the bi–dimensional dipole array made of dipoles printed on multilayered FR4 substrate, including ground planes.

In order to reduce the back–radiation in the z < 0 direction, an optimization based on meandered PCB ground planes was carried out as to provide equivalent electrical lengths far longer than the physical ones. Several ground layouts were investigated to reach the required radiation performance while preserving the PCB from being full of large slots. This way dense placement of electronic components, typical of current multi–purpose PDAs, was not compromised. Narrow rectangular cuts (300 μm–wide) were made on the metal layers. By properly adjusting their dimensions and relative positions, reduced back–radiation was achieved at the desired operating frequency (i.e. 868 MHz). The chosen shape of the ground plane layout is drawn in Fig. 18a: the number of metal–plane cuts ($n_c$), the cuts length ($L_c$) and the distance between adjacent cuts ($L_d$) were chosen as the design parameters to provide a current path along the ground planes acting as a slow–wave at the frequency of interest. In order to have a preliminary idea of the first resonance introduced by the ground plane, corresponding to $L_{eq} = \lambda/2$, an equivalent length may be roughly computed as:

$$L_{eq} = L_c \cdot 2 + (L_c - L_d) \cdot (n_c - 2) \qquad (15)$$

The more the number of cuts is low, the more Eq. (15) is valid. For the present design $n_c = 8$, $L_c = 3.1$ cm and $L_d = 0.97$ cm, which brings the ground plane resonant frequency to be 661 MHz, quite far from the operating one. Fig. 18b reports the EM–simulated current pattern on the optimized ground plane shape at 661 MHz: the current distribution, with a maximum in the middle and zeros on the edges, confirm the half–wavelength dipole behavior of the plane at this frequency. The final arrangement of the array provides the radiation performance shown in Fig. 19. A comparison with Fig. 16 allows to conclude that the considered approach choice has a twofold advantage: i) the preservation of most of the area for circuitry placing; ii) the assurance of the best operation of the bi–dimensional array with extremely low back–radiation and SAR in the opposite (unwanted) direction of the RFID link.
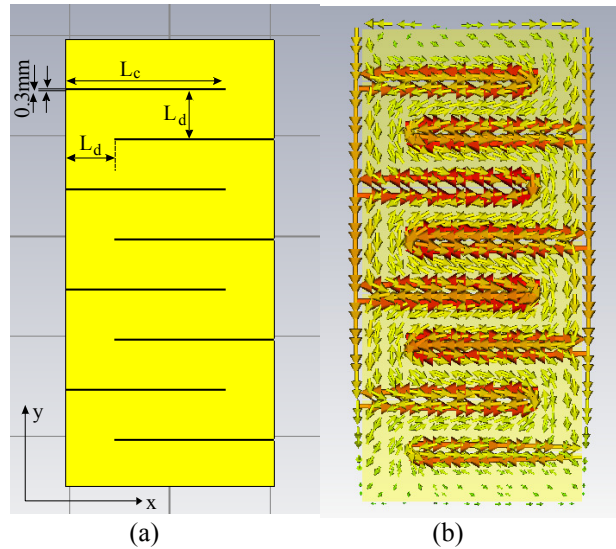
Fig. 18. (a) Meandered metal plane geometry; (b) its current pattern at the ground plane resonant frequency (661 MHz).
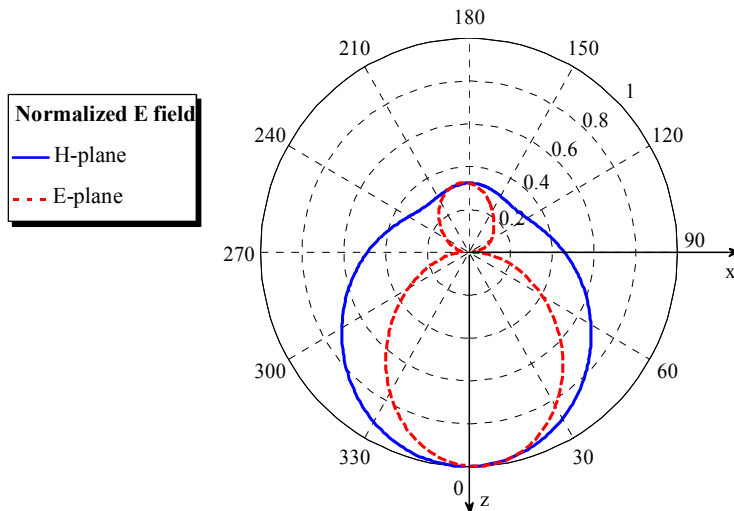


Fig. 19. E–plane and H–plane radiation pattern of the bi–dimensional dipole array made of dipoles printed on a multi–layer FR4 substrate, including meandered ground planes.

Table I summarizes the array performance for the different layouts which have been studied so far. The computed directivity is considered in the wanted direction ($\theta = 0°$ or $z > 0$ half–space). While the radiation efficiency was preserved in all designs, the directivity was improved with the meandered ground planes and strongly degraded with uniform ground planes, as it was expected. Furthermore, the front–to–back ratio provided by the meandered solution was slightly improved with respect to the stand–alone array, since the electrically–long ground plane increased the reflecting action of the parasitic dipoles, thus allowing to extend the RFID link reading range.

Table I.  Array performance for the various layouts.

| | Directivity (dB) | Efficiency (%) | Front–to–back ratio (dB) |
|---|---|---|---|
| **Stand–alone array** | 6.2 | 59 | −8.4 |
| **Array with uniform ground planes** | 0.1 | 62 | +5.4 |
| **Array with meandered ground planes** | 6.5 | 58 | −9.8 |

The antenna array matching network, of the inductively–coupled type shown in Fig. 15, was optimized by EM simulation for connection to an UHF chip. The EM4325 chip manufactured by EM Microelectronic–Marin SA operating with back–scattering modulation was chosen and the matching to both chip states was carried out. Fig. 20 shows the predicted reflection coefficient at the antenna input port for the complete PDA. The curves correspond to the two operating modes of the EM4325 chip: passive mode and BAP (= Battery Assisted Passive) mode or semi–passive mode. Therefore the reflection coefficient was evaluated by combining the values of the antenna input impedance at the balanced port with the provided chip impedance values at 868 MHz (kept fixed all over the band of interest). The latter are: i) 19–j188 Ω in passive mode; ii) 11–j164 Ω in BAP mode. Fig. 20 shows that matching requirements are better than –20 dB around the chip operating frequency in a 25–MHz and in a 190–MHz band in passive mode and in BAP mode, respectively. For the same array the far–field polarization was investigated, too: an axial ratio bigger than 20 dB is guaranteed in all the half–space of interest ($-90° \le \theta \le 90°$), as shown in Fig. 21.
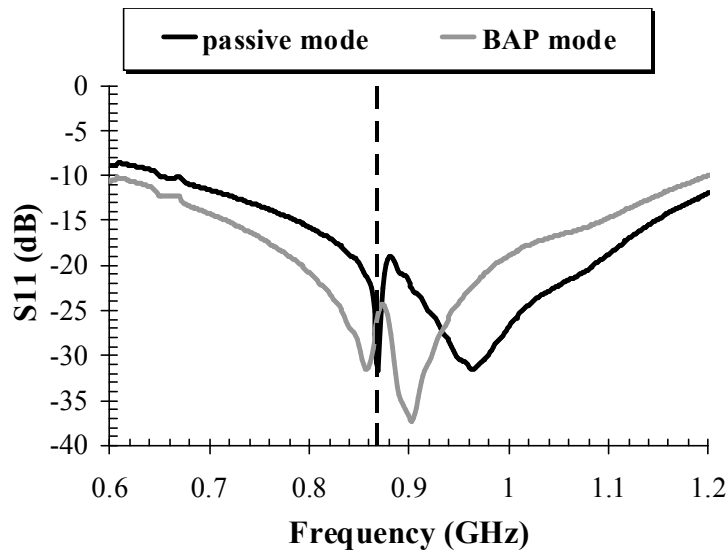


Fig. 20.  Simulated reflection coefficient for the complete PDA for the two chip states.
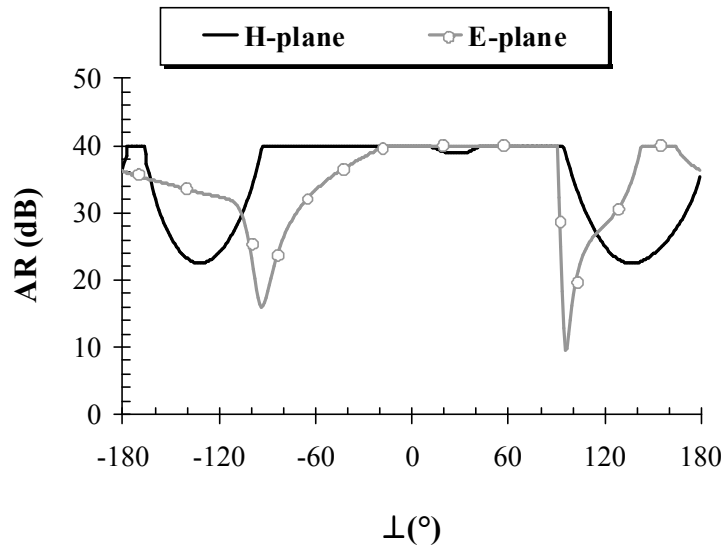
Fig. 21.  Predicted axial ratio behavior of the complete PDA.

A prototype of the entire system discussed above was then manufactured.

Fig. 22 shows the upper part of the prototype with the experimental setup developed to measure the antenna differential impedance [25]: this is a key issue in order to make a comparison between the predicted (simulated) and the effective (measured) impedance matching by taking into account the balanced port at each driven dipole. The RF impedance measurement system consist simply of two short coaxial cables with a length of about 6 cm, corresponding to about $\lambda/4$ at 868 MHz.



Fig. 22.  Complete PDA prototype with $S_{11}$ measurement set–up.

Fig. 23 shows the circuit technique deployed to measure a differential impedance: it is based upon a straightforward application of the equivalence between the differential antenna input impedance $Z_d$ and the two–port impedance matrix $\underline{Z}$, according to the following Eqs. (16):

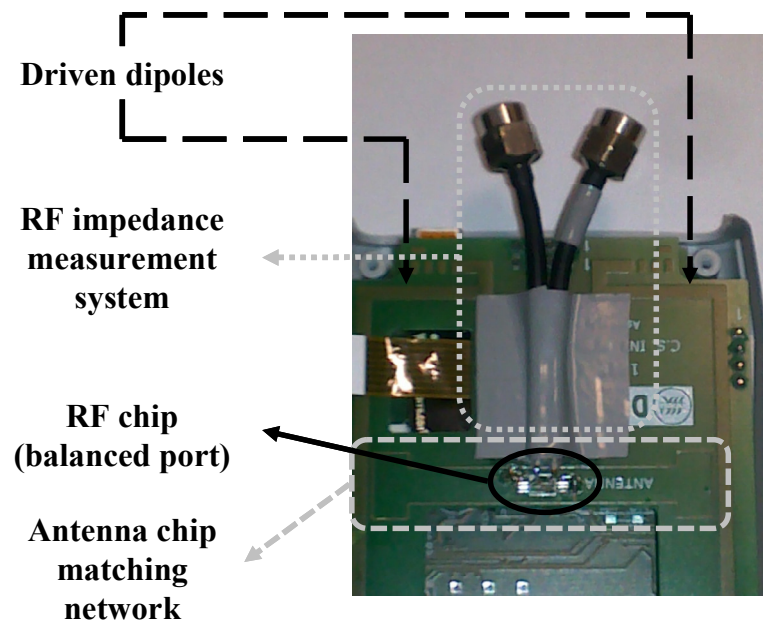$$\begin{bmatrix} V_1 \\ V_2 \end{bmatrix} = \underline{Z} \bullet \begin{bmatrix} I_1 \\ I_2 \end{bmatrix} = Z_d \bullet \begin{bmatrix} I_d \\ -I_d \end{bmatrix}$$

$$Z_d = \frac{V_d}{I_d} = \frac{V_1 - V_2}{I_d} = Z_{11} - Z_{21} - Z_{12} + Z_{22}$$

(16)
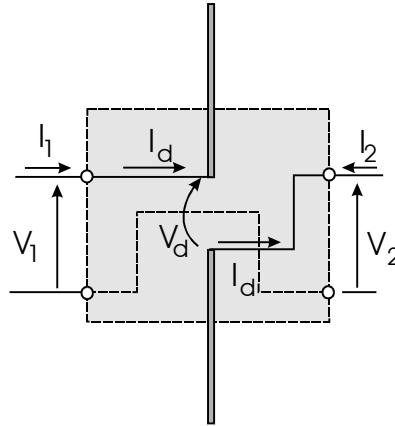


Fig. 23. Schematic view of the circuit technique exploited to measure a differential impedance.

Finally, Fig. 24 shows the simulated (with coaxial cables) and measured (by means of a Vector Spectrum Analyzer) values of the absolute values of the reflection coefficient $|S_{11}|$ dB all over the band of interest. A very good agreement is apparent for both chip states (passive mode and BAP mode). Furthermore, it is evident the meandered ground planes resonance at 661 MHz, thus giving a direct proof of the accurate EM modeling carried out for the design of the whole RFID system.
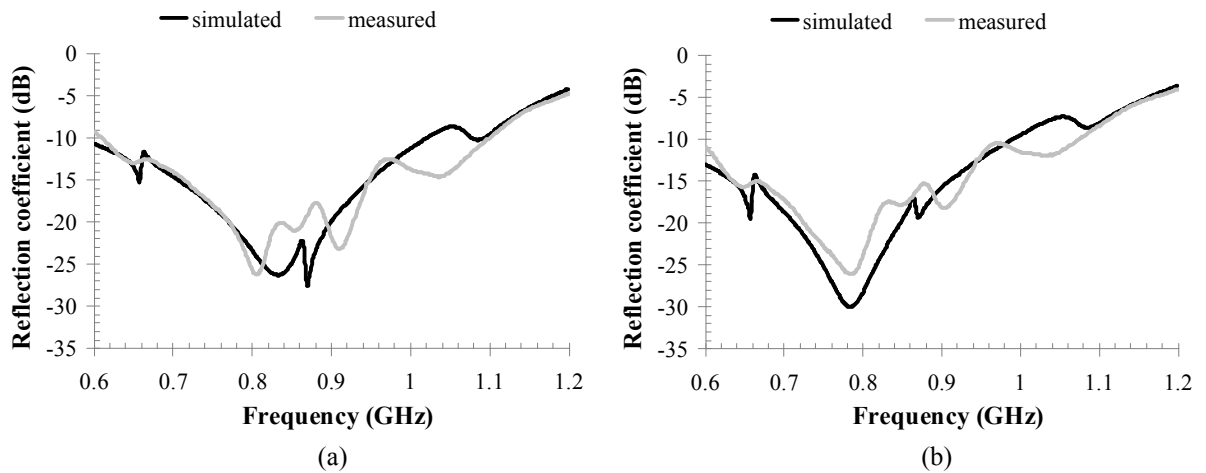


Fig. 24. Simulated and measured values of $|S_{11}|$ dB for the whole RFID system with meandered ground planes and coaxial cables for the two chip states: (a) passive mode; (b) BAP mode. It is evident the ground planes resonance at 661 MHz.

31

## 1.2.4. READING RANGE PREDICTION

Let us now consider a system comparison in terms of the maximum reading range of the designed solutions analyzed so far. By means of the well–known Friis equation, assuming ideal polarization and impedance matching, the maximum distance may be approximately predicted by:

$$d_{\max} = \frac{\lambda}{4\pi} \cdot \sqrt{\frac{P_{reader} \cdot G_{reader} \cdot G_{tag}}{P_{tag}}}$$

(17)

In Eq. (17) $P_{reader}$ is the power transmitted by the reader; $P_{tag}$ is the power received by the dipole array; $G_{reader}$ is the reader antenna gain; $G_{tag}$ is the array gain. Usually the *Effective Isotropic Radiated Power* (*EIRP* = $P_{reader}$ $G_{reader}$) is considered to characterize the reader. Typical values for maximum *EIRP* is 3.2 Watt in Europe, corresponding to 35 dBm, as established by the Electronic Communications Committee (ECC) within the European Conference of Postal and Telecommunications Administrations (CEPT). In the proposed design $G_{tag}$ is variable with the ground planes shape in the array arrangement and $P_{tag}$ is the activation threshold, i.e. the RF power level above which the chip starts operating. For the two different operating modes of the selected chip these are $P_{tag} = -12$dBm, in passive mode and $P_{tag} = -29$ dBm in BAP mode. In Table II, the predicted values of $d_{\max}$ are listed for all the antenna topologies discussed above and for all the possible operating modes of the selected chip.

Table II.  RFID link reading range.

|  | Broadside gain (dB) | Passive mode range $d_{\max}$ (m) | BAP mode range $d_{\max}$ (m) |
|---|---|---|---|
| **Stand–alone array** | 3.9 | ~ 9.6 | ~ 68.1 |
| **Array with uniform ground planes** | −1 | ~ 5.5 | ~ 38.9 |
| **Array with meandered ground planes** | 4.1 | ~ 9.9 | ~ 69.9 |

Table II demonstrates that the proposed bi–dimensional array, with meandered ground planes, allows a longer available reading range (both in passive and BAP modes) with respect to the same type of antenna with no ground planes or with standard ground plane. This result could be very meaningful as it allows RFID–system designers to account for a tag–antenna connection directly performed in a PCB. This is possible by suitably modifying ground planes shape, preserving at the same time the antenna characteristics and, consequently, the maximum reading distance of the whole system. A further analysis of the entire antenna–chip assembly embedded in the plastic case, which houses batteries and other peripherals, was carried out by EM simulation. As expected a slight detuning of the operating frequency was observed and promptly adjusted by varying the dipole lengths.

## CONCLUSIONS

The CAD simulation of a complete MIMO link is a very complex problem, which is normally tackled by a set of simplifying assumptions whose combined impact on the overall analysis accuracy may be difficult to predict. The biggest difficulties in the link modeling are encountered when antennas must be placed in close proximity of each other, e.g., due to space limitations as in modern wireless telecommunication systems. In such cases antenna couplings may critically affect the overall system performance. The proposed approach is based upon the combination of both state–of–the–art software tools and basic EM theory in order to systematically handle all the subsystems, as well as the interactions among them, in a very general and rigorous way. Key aspects are the EM characterization of the transmit/receive arrays, the analysis of transmit/receive *front–ends* by nonlinear CAD methods, the RT–based channel model and the description of the EM fields as the actual physical link between the transmitter and receiver side. Several aspects still have to be improved or developed: for example, time–domain statistical channel models may be the way to go for mobile MIMO links, and will have to be interfaced with the other analysis tools taking advantage of the hybrid time–frequency domain representation already used to describe digitally–modulated signals.

The design of a customized RFID device could be a great challenge as well, especially if several restrictive constraints have to be taken into account. In particular, the presence of a big number of digital/RF components in modern PDAs could not provide enough space to place an antenna array with satisfying radiation performance and robustness against interferences with the circuitry itself. When modeling such a system by using a CAD simulation tool, great accuracy has to be dedicated to the materials characterization and to the proper displacement of all components within the device, in order to consider as best as possible all the potential interactions among the various parts inside the PDA. This is a key issue for the prototype manufacturing, since it allows to achieve the best agreement between predicted (simulated) and measured performance of the device.

## REFERENCES

[1] C. Waldschmidt, S. Schultieis, W. Wiesbeck, "Complete RF System Model for Analysis of Compact MIMO Arrays", *IEEE Trans. Vehicular Tech.,* Vol. 53, No.3, pp. 579–586, May 2004.
[2] K. Rosengreen and P. S. Kildal, "Radiation efficiency, correlation, diversity gain and capacity of a six–monopole antenna array for a MIMO system: theory, simulation and measurement in reverberation chamber", *Proc. IEEE, Microw. Antennas and Prop.,* Vol. 152, No.1, pp. 7–16, Feb. 2005.
[3] H. Kanj, S. Ali, P. Lusina, and F. Kohandani, "A Modeling Approach for Simulating MIMO Systems with Near–Field Effects", *Proc. Europ. Conf. on Wireless Tech.*, pp. 143–146, Oct. 2008.
[4] J. W. Wallace and M. A. Jensen, "Mutual coupling in MIMO wireless systems: a rigorous network theory analysis," *IEEE Trans. Wireless Commun.,* Vol. 3, No. 4, pp. 1317–1326, July 2004.
[5] V. Rizzoli et al., "A CAD Procedure for MIMO Link Estimation by the Combination of Nonlinear, Electromagnetic and Propagation Analysis Techniques", *2008 IEEE MTT–S Int. Microw. Symp. Dig.*, pp. 927–930, June 2008.
[6] CST Microwave Studio 2009.
[7] V. Rizzoli, A. Costanzo, D. Masotti, P. Spadoni, "Prediction of the End–to–End Performance of a Microwave/RF Link by means of Nonlinear/Electromagnetic Co–Simulation", *IEEE Trans. Microwave Theory Tech.,* Vol. 54, pp. 4149–4160, Dec. 2006.
[8] C. A. Balanis, Advanced Engineering Electromagnetics, New York: Wiley, 1989.

[9] A. J. Paulraj, D. A. Gore, R. U. Nabar, H. Bolcskei, "An Overview of MIMO Communications – A Key to Gigabit Wireless", *Proc. IEEE,* Vol. 92, No. 2, pp. 198–218, Feb. 2004.

[10] V. Degli Esposti et al., "An advanced field prediction model including diffuse scattering", *IEEE Trans. Antennas Prop.*, Vol. 52, pp. 1717–1728, July 2004.

[11] V. Degli Esposti, "A diffuse scattering model for urban propagation prediction", *IEEE Trans. Antennas and Propagation,* Vol. 49, No. 7, pp. 1111–1113, July 2001.

[12] K. Kalliola, H. Laitinen, P. Vainikainen, M. Toeltsch, J. Laurila, E. Bonek, "3–D double directional radio channel characterization for urban macrocellular applications", *IEEE Trans. Antennas and Propagation*, Vol. 51, No. 11, pp. 3122–3133, November 2003.

[13] F. Fuschini, H. El–Sallabi, V. Degli Esposti, L. Vuokko, D. Guiducci, P. Vainikainen, "Analysis of multipath propagation in urban environment through multidimensional measurements and advanced ray tracing simulation," *IEEE Trans. Antennas and Propagation*, Vol. 56, No. 3, pp. 848–857, Mar. 2008.

[14] E. M. Vitucci, V. Degli Esposti, F. Fuschini, "MIMO channel characterization through ray tracing simulation" *European Conference on Antennas and Propagation EUCAP 2006*, Nice (Fr), Nov. 2006.

[15] V. Rizzoli, A. Costanzo, D. Masotti, P. Spadoni, "Computer–Aided Design of Ultra–Wideband Active Antenna by Means of a new Figure of Merit", *IEEE Microwave and Wireless Comp. Lett.,* Vol. 8, pp. 290–292, Apr. 2008.

[16] V. Rizzoli, F. Mastri, and D. Masotti, "General noise analysis of nonlinear microwave circuits by the piecewise harmonic–balance technique", *IEEE Trans. Microwave Theory Tech.*, Vol. 42, pp. 807–819, May 1994.

[17] AWR–VSS Design Environment.

[18] V. Rizzoli, A. Costanzo, D. Masotti, and F. Mastri, "Computer–aided noise analysis of near–carrier noise in RF–microwave frequency converters", *Int. Journal RF and Microwave Computer–Aided Eng.*, Vol. 9, pp. 449–467, Nov. 1999.

[19] V. Rizzoli, A. Costanzo, F. Mastri, A. Neri, "A general SPICE model for arbitrary linear dispersive multiport components described by frequency–domain data", *2003 IEEE MTT–S Int. Microw. Symp. Dig.,* Vol. 1, pp. 9–12, June 2003.

[20] M. F. Abedin and M. Ali, "Modifying the ground plane and its effect on planar inverted–F antennas (PIFAs) for mobile phone handsets", *IEEE Antennas and Wireless Propagation Lett.*, Vol. 2, No. 1, pp. 226–229, 2003.

[21] A. Cabedo, J. Anguera, C. Picher, M. Ribo, and C. Puente, "Multiband Handset Antenna Combining a PIFA, Slots, and Ground Plane Modes", *IEEE Trans. Antennas and Propagation*, Vol. 57, No. 9, pp. 2526–2533, 2009.

[22] Q. Rao, T. A. Denidni, and R. H. Johnston, "A single–substrate microstrip–fed slot antenna array with reduced back radiation", *IEEE Antennas and Wireless Propagation Lett.*, Vol. 3, No. 1, pp. 265–268, 2004.

[23] V. Rizzoli, A. Costanzo, D. Masotti, A. Lipparini, and F. Mastri, "Computer–aided optimization of nonlinear microwave circuits with the aid of electromagnetic simulation", *IEEE Trans. Microwave Theory Tech.*, Vol. 52, pp. 362–377, Jan. 2004.

[24] V. Rizzoli, A. Costanzo, M. Rubini, and D. Masotti, "Investigation Of Interactions Between Passive RFid Tags By Means Of Nonlinear/EM Co–Simulation", *Proc. 36th European Microwave Conference*, pp. 722–725, Sept. 2006.

[25] K. D. Palmer and M. W. Van Rooyen, "Simple broadband measurements of balanced loads using a network analyzer", *IEEE Trans. Instrum. Meas.*, Vol. 55, No. 2, pp. 266–272, Feb. 2006.

# CHAPTER 2

## MAGNETO–DIELECTRIC MATERIALS: A PATH TOWARDS SMART MINIATURIZATION OF ANTENNAS

As demonstrated in Chapter 1, modern wireless telecommunication systems are based upon very complex *front–ends* that comprise a huge number of digital/RF components. The increasing demand for integration of all the afore–mentioned components in small volumes represents a great technological challenge, since many problems and constraints have to be tackled in order to achieve satisfying performance of the devices in terms of reliability, lifetime and mechanical robustness. From the EM point of view, the close proximity of one or more antennas to other parts within the same enclosure can affect dramatically their radiation properties, hence an as accurate as possible design is necessary to avoid destructive interferences. Furthermore, in the last ten years a growing interest in wearable and implantable devices has been shown, since they can be exploited for applications in *BANs*. As already stated in the Introduction, *BANs* are of great importance for real–time monitoring of health parameters, e.g. blood pressure, breathing rate, etc.

One of the biggest challenges in the development of integrated RF systems is the miniaturization of all components, since this is a mandatory requirement in order to build easy–to–wear or implantable devices. The drawback is that miniaturization affects the antenna radiation behavior and a trade–off between antenna reduced dimensions and performance needs to be reached. A largely exploited solution is given by the so–called *electrically small* antennas, i.e. antennas whose physical length is very small compared to the free–space wavelength (at least less than $\lambda_0/4$). This type of antennas, although mandatory in portable devices (like mobile phones), exhibit strong limitations on the bandwidth and on the radiation efficiency: the former are due to the theoretical minimum Quality Factor $Q$ as a function of the size (according to Chu [1], Harrington, McLean [2] and Collin), the latter are due to the theoretical maximum gain again as a function of the size (according to Harrington). A brief description of the afore–mentioned limitations will be presented in the following as an introduction to the proposed MD antenna for an UHF–RFID wearable application.

### 2.1. ELECTRICALLY SMALL ANTENNAS: MAIN CHARACTERISTICS

As regards the bandwidth limitations, the *Field Method* [2] can be applied to calculate the $Q$ of (for example) an electric dipole with its axis aligned along the z–direction, hence an antenna characterized by linear polarization. In particular, an *electrically small* antenna is defined as an antenna that fulfills the condition that $k{\cdot}a < 1$, where

- $k$ is the wavenumber in free–space;
- $a$ is the radius of the *minimum* sphere that encloses the antenna (*radian–sphere*).

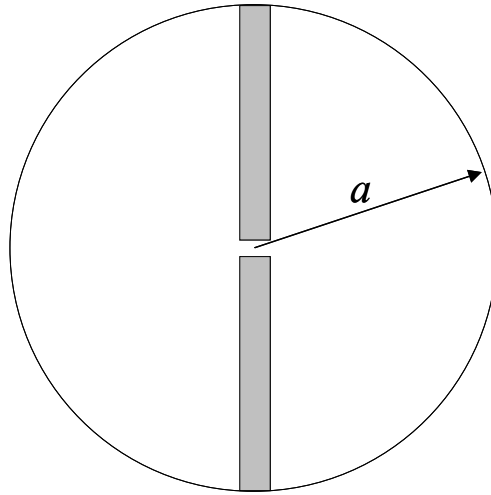Fig. 25 shows the above–mentioned minimum sphere.

Fig. 25. Dipole antenna enclosed in a sphere with minimum radius *a*.

The following steps are needed in the *Field Method*:

1. fields due to the antenna are expanded in spherical waves;
2. the total energy due to traveling waves and reactive fields are calculated;
3. radiated energy is obtained from the field components as functions of $1/r$;
4. non–propagating energy is obtained by subtracting the radiated energy from the total energy.

After some cumbersome calculations, the *minimum Q* can be expressed as follows [2]:

$$Q_{min} = \frac{1}{(k \cdot a)^3} + \frac{1}{k \cdot a}$$ (1)

Eq. (1) is valid for *lossless electrically small* antennas with linear polarization and coincides with the so–called *Chu's limit*. Some conclusions can be now inferred:

1. an *electrically small* antenna should have $Q > Q_{min}$;
2. the antenna $Q$ increases as the size of the antenna itself decreases;
3. the biggest challenge in designing *electrically small* antennas is approaching *Chu's limit* as much as possible;
4. the derivation of $Q$ does not consider the stored EM energy inside the volume $r < a$, hence for wire–like antennas *Chu's limit* must be increased by a factor of $1.5 \div 3$.

Two antenna examples will be now provided to explain the effect of their $Q$:

1. *convoluted electrically small* wire antennas can be self–resonant but the obtained $Q$ is about one order of magnitude (10 times) larger than *Chu's limit*;
2. *planar* antennas (like patches) have worse performance than *volume* antennas due to their inefficient use of the available volume. The use of dielectric materials in the construction of the antenna increases the stored energy and in consequence the $Q$. A safe approximation is to consider that the $Q$ of a *planar electrically small* antenna will be about one order of magnitude larger than *Chu's limit*.

Now let's define the radiation Quality Factor $Q_{rad}$:

$$Q_{rad} = \omega_r \frac{W_{stored}}{P_{rad}} \tag{2}$$

where $\omega_r$ is the resonance (angular) frequency, $W_{stored}$ is the energy stored in the antenna volume and $P_{rad}$ is the power radiated by the antenna. Be $\eta_{rad}$ the radiation efficiency of the antenna; $Q_{rad}$ is the quantity limited by *Chu's limit* but the total observed $Q_T$ at the antenna input terminals is:

$$Q_T = Q_{rad} \cdot \eta_{rad} \tag{3}$$

Eq. (3) summarizes a very important result to achieve when designing an *electrically small* antenna: a trade–off between $Q_{rad}$ and $\eta_{rad}$ has to be reached in order to satisfy the required constraints given by project. Indeed it is well–known that, given the upper $f_{up}$, lower $f_{low}$ and center $f_c$ frequency of the band of interest, the $Q$ is also defined as:

$$\frac{1}{Q} = \frac{f_{up} - f_{low}}{f_c} \tag{4}$$

Eq. (4) entails that the higher the $Q$, the narrower the bandwidth $BW = f_{up} - f_{low}$ of the considered antenna.
In order to miniaturize antennas, several techniques could be deployed, such as:

1. antenna loading (with lumped elements or high–permittivity/permeability materials): *electrically small* antennas are difficult to be matched and non–resonant due to a small radiation resistance and to a strong reactive part of the input impedance. This requires a matching network;
2. making some part of the antenna virtual (using ground planes or short circuits);
3. optimizing the geometry;
4. environment exploitation: i) the metallic parts of the case can be used in a constructive way; ii) the maximum available volume should be deployed; iii) the human body acts as a natural ground plane;
5. multi–frequency antennas.

As regards the gain limitations, constraining to $N$ the number of modes (wave functions) radiated by the antenna, the maximum antenna gain $G$ can be roughly expressed as [3]:

$$G = N^2 + 2N \tag{5}$$

Hence increasing the number of radiated modes, antenna gain increases.
Potential causes for the gain limitation are:

1. possibility to manufacture an antenna radiating many propagating modes;
2. losses (higher order modes usually have higher losses);
3. bandwidth (the more the radiated modes, the narrower the bandwidth).

The maximum value of $G$ for a practical bandwidth $BW$ is:

$$G_{BW} = (k \cdot a)^2 + 2k \cdot a \tag{6}$$

It is apparent from Eqs. (1) and (6) that a trade–off between an acceptably–low value of $Q_{min}$ and the desired value of $G_{BW}$ is necessary, thus the best miniaturizing technique needs to be investigated to obtain an *electrically small* antenna with satisfying performance.

## 2.2. MAGNETO–DIELECTRIC MATERIALS

A solution to build miniaturized and non–invasive antennas that has been highly exploited so far is the patch antenna mounted on a dielectric substrate, thanks to its low–profile (this characteristic is very important when integrating the radiating system in a portable device). Several solutions have been proposed for the reduction of the patch size [4], but not sufficient to fulfill wearable/implantable applications requirements. A further miniaturization could be achieved by adopting *ceramic* substrates with high values of relative permittivity $\varepsilon_r$. In this case a significant reduction of the radiation resistance is observed, which causes a decay in the radiation efficiency. In fact, radiation efficiency $\eta_{rad}$ is defined as [5]:

$$\eta_{rad} = \frac{R_r}{R_r + R_L} \tag{7}$$

where $R_r$ is the radiation resistance and $R_L$ represents the conduction–dielectric losses of the antenna. It can be stated that part of the power delivered to the antenna is radiated through the mechanism provided by $R_r$ and the other is dissipated as heat through $R_L$. A decreasing of $R_r$ has another drawback, i.e. a too low antenna input impedance is obtained, difficult to match. Indeed antenna input impedance $Z_A$ is defined as follows:

$$Z_A = R_A + jX_A = R_r + R_L + jX_A \tag{8}$$

In many cases of practical interest, a good assumption is that $R_L \approx 0$.

For patch antennas on high–permittivity substrates, the reduced effective wavelength $\lambda_g$ due to high values of $\varepsilon_r$ is obtained at the expense of a strong reduction in the well–known *field fringing effect*, i.e. the mechanism upon which patch antenna operation relies. The main effects of such a phenomenon are:

1. an increased coupling between the patch metallization and the ground plane, which lowers the radiation efficiency (since a considerable part of EM energy is stored inside the substrate);
2. be $\eta_0$ the free–space intrinsic impedance, then the substrate intrinsic impedance $\eta_i$ is defined as follows:

$$\eta_i = \frac{\eta_0}{\sqrt{\varepsilon_r}} \tag{9}$$

   It is apparent that an increasing of $\varepsilon_r$ decreases $\eta_i$, hence (as already stated previously) a difficult impedance matching has to be taken into account;
3. a higher Quality Factor $Q$ of the resonant patch is observed, thus a narrower bandwidth has to be considered. In fact, be $RL$ the return loss and $BW_{max}$ the maximum bandwidth; according to Fano's limit, $BW_{max}$ can be expressed as follows:

$$BW_{max} = \frac{27}{Q \cdot RL} \tag{10}$$

Hence fixing $RL$ and varying $Q$ a smaller value of $BW_{max}$ can be achieved.

By means of MD materials, antenna dimensions can be further reduced by exploiting relative magnetic permeability $\mu_r$ greater than unit and keeping $\varepsilon_r$ at reasonable values. This way the same miniaturization factor can be obtained without affecting the above mentioned performance, since the refraction index $n$ is defined as:

$$n = \sqrt{\varepsilon_r \cdot \mu_r} \quad \Rightarrow \quad \lambda_g = \frac{\lambda_0}{\sqrt{\varepsilon_r \cdot \mu_r}} \tag{11}$$

In particular, the substrate intrinsic impedance $\eta_i$ can be kept in a range allowing easy antenna matching, since:

$$\eta_i = \eta_0 \sqrt{\frac{\mu_r}{\varepsilon_r}} \tag{12}$$

Furthermore, a radiating performance improvement, due to the increased radiation resistance, and a wider bandwidth can be observed.

MD materials can be classified into two main groups: meta–materials and composite materials. When using, for example, *Embedded–Circuit Mediums* as meta–materials [6,7], one has to carefully take account of some crucial issues, such as properly embedding high–$Q$ resonant loops in low–permittivity substrates and mutual couplings among embedded loops. Furthermore, mutual couplings between loops and antenna metallization inductance affect the permittivity of the dielectric substrate.

On the other hand, composite materials such as ferrites [8] have natural magnetic properties, which can be optimized during the synthesis process, thus allowing the desired trade–off between high values of $\mu_r$ and the Ferro–Magnetic Resonance at higher frequencies with respect to meta–materials. The most significant shortcoming of ferrites is represented by high magnetic losses at microwave frequencies, which have to be taken into account for best performance prediction of devices designed on such composite substrates.

Hereinafter I will always refer to the *complex* relative permittivity $\varepsilon_r$ and permeability $\mu_r$:

$$\varepsilon_r = \varepsilon' - j\varepsilon'' \quad \text{and} \quad \mu_r = \mu' - j\mu'' \tag{13}$$

Eqs. (13) allow to define a dielectric and a magnetic loss tangent taking into account the dielectric and magnetic losses, respectively:

$$\tan\delta_\varepsilon = \frac{\varepsilon''}{\varepsilon'} \quad \text{and} \quad \tan\delta_\mu = \frac{\mu''}{\mu'} \tag{14}$$

Ferrites are promising candidates for their deployment as MD *ceramic* materials, since they have both magnetic and dielectric properties that, in principle, can be engineered separately; moreover, raw materials are low–cost and easily available. To achieve low magnetic loss tangent, the materials obtained should have a resonance frequency far beyond the desired frequency band of interest for antenna designs, as will be explained in detail in the next paragraphs. In particular, three types of ferrites can be considered:

1. spinels
2. garnets
3. hexaferrites

The resonance frequencies of composites based on ferrites of the type 1 and 2 exhibit resonance frequencies from tens to hundreds of MHz, whereas ferrites of type 3 have resonance frequencies in the microwave band. It is therefore possible to use spinel or garnet ferrites for low–frequency applications and hexaferrites for microwave devices.

As regards the present PhD thesis, the synthesis of an MD material (barium–strontium hexaferrite) to use as the substrate for the design of a small patch antenna with an overall size suitable for wearable applications [9,10] will be presented. The material was prepared at CNR–ISTEC (= Istituto di Scienza e TEcnologia dei materiali Ceramici), Faenza, Italy and permittivity and permeability measurements of the material were carried out at the Faculty of Physics of University "Al. Ioan Cuza", Iaşi, Romania by standard instrumentation with reference samples. Then the characterization was repeated by means of resonance methods [11] while preparing the antenna layout and therefore using the actual antenna dimensions with the engineered MD substrate.

When using MD materials for antenna miniaturization purposes, one has to take into account two main problems:

1. not negligible magnetic losses (hence high $\tan\delta_\mu$) in the microwave frequency band
2. $\mu_r$ is close to the initial (static) permeability $\mu_i'$ at frequencies up to the so–called *Ferro–Magnetic Resonance* (*FMR*) frequency.

A detailed description of hexaferrites characteristics will be now provided in order to give the theoretical basics for the entire following treatise.

## 2.3. HEXAFERRITE COMPOSITES: PHYSICS, MANUFACTURING AND CHARACTERIZATION

### A. PHYSICS OF MD MATERIALS

Hexaferrites show a magnetoplumbite–similar crystal structure (i.e. cubic–hexagonal) [8], with high magneto–crystalline anisotropy and a preferred direction of magnetization (a magnetoplumbite is "a mineral $(Pb,Mn)(Fe,Mn,Ti)_6O_{10}(?)$ consisting of an oxide of ferric iron with lead, manganese, and titanium occurring in acute black metallic hexagonal pyramids"). Different correlations between crystal and magnetic properties give rise to a further classification into S, M, W, Y, Z, X types, which are characterized by: i) a high coercive field, typical of "hard" permanent magnets; ii) magnetic losses damping the *FMR* frequency, as a consequence of the anisotropy of single–crystals structure, where the shift of the resonance frequency depends on the orientation of the applied field with respect to the principal crystal axes. The resonance band is broadened especially in polycrystalline materials, with randomly–oriented crystals. In polycrystalline materials, further contributions to the band broadening derive from grain boundaries, porosity or in–homogeneities. The advantage in using hexaferrites consists in their high–frequency *FMR* due to moderate values of relative permittivity and permeability, large anisotropy field and low eddy–current losses (eddy currents are generated in electrically–conductive materials when a dynamic magnetic field is applied).

In particular, the present research concentrated on M–type hexaferrites ($MFe_{12}O_{19}$ with M = Ba, Sr or Pb): they are important ferromagnetic oxides with hexagonal magnetoplumbite (M–type) structure of space group P63/mmc and strong anisotropy. The latter allows to extend the frequency limit expressed by the Snoek's law, i.e. a higher *FMR* frequency can be observed as a large anisotropy (elliptically–polarized) field $H_K$. The modified Snoek's law is expressed by Eq. (15) for M–type hexaferrite specimen s with *planar* geometry:

$$\omega_r^{\min} \cdot \mu_i' = \gamma \cdot 4\pi M_S \cdot \sqrt{\frac{H_{K\theta}}{H_{K\phi}}} \qquad (15)$$

where $\omega_r^{\min}$ is the minimum (angular) FMR frequency, $\mu_i'$ is the static permeability (i.e. the initial value of $\mu'$, which is assumed to be constant up to the FMR), $\gamma = 1.76 \times 10^6$ rad/sec·Oe is the gyromagnetic constant, $M_S$ is the saturation magnetization and $H_{K\theta}$, $H_{K\phi}$ are the cross–polar and co–polar components of $H_K$ (respectively) with respect to the easy–plane of magnetization. It is of primary importance to utilize the MD substrate below the FMR frequency, in order to avoid strong energy absorption and highly–dispersive behavior of permeability values. In practical applications, such materials exhibit non–negligible magnetic losses in the microwave frequency band (most MDs have the FMR in the UHF band). In particular, $\omega_r^{\min}$ and $\mu_i'$ depend on the composition, the manufacturing process, the heat treatment and the presence of impurities in the raw–materials admixture, whereas $M_S$ depends only on the composition, hence it can be considered as a figure of merit for all materials with magnetic properties.

Fig. 26 [12] highlights the interactions between alternating magnetic drive field $H_{ac}$ and magnetization vector $M$: it is apparent the difference between a relaxation and a FMR behavior of the magnetic material under consideration. In particular, up to the frequency range where non–resonant relaxation damping occurs, the initial permeability $\mu_i'$ is determined by the facility of magnetization rotation within the randomly oriented single–domains driven by the longitudinal interaction $H_{ac} \cdot M$. At frequencies approaching the microwave band, transverse coupling begins to occur through the gyromagnetic interaction $H_{ac} \times M$. In Fig. 26, $\omega_\tau$ is the non–resonant relaxation rate, $\tau$ is the effective spin–lattice relaxation time and $\omega_r$ is the resonance frequency. If the magnetic material is not fully magnetized, the magnetization can be divided into *domains*: in each of these domains $M$ is aligned according to local crystallographic "easy" axes (of magnetization). In polycrystalline composites like hexaferrites $M$ vectors can be distributed as individual single–domain grains (if the latter are too small to support the formation of domain walls).
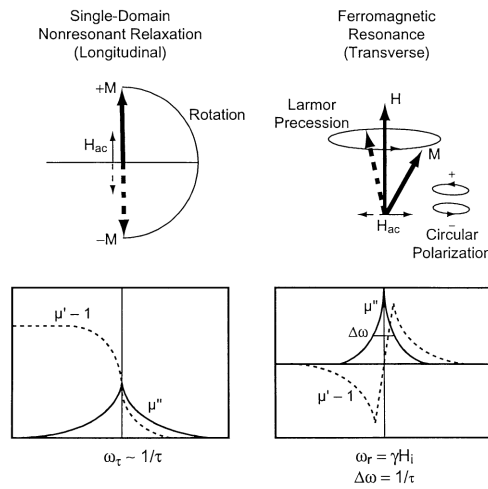


Fig. 26. Physical origins and permeability effects of longitudinal and transverse interactions between alternating magnetic drive field $H_{ac}$ and magnetization vector $M$ [9].

As depicted in Fig. 27a [12], the anisotropy fields $H_K$ define the directions of the saturation magnetization vectors $M_S$ and are set by the orientation of the grains themselves, in presence or not of domain walls. There is no reference direction by which longitudinal and transverse

drive fields $H_{ac}$ can be distinguished, because there is no resultant of the combined $M_S$ vectors in an unsaturated state. In particular, $H_{ac}$ can exceed the coercive field $H_c$, which allows domain wall movement to increase the longitudinal susceptibility, if low anisotropy and ideal microstructure provide negligible impediments to reversible wall movement. Furthermore, domain walls can resonate as damped forced harmonic oscillators at a characteristic frequency related to the spin–lattice relaxation rate. At frequencies in the microwave range, gyromagnetism occurs through transverse coupling about internal demagnetizing fields that originate in part from magnetic poles on the surfaces of the walls. A result of this frequency dependence is that absorption occurs beginning at about 1 MHz from longitudinal components of drive fields and can be significant in the GHz range for the transverse components, as it is apparent in Fig. 26. Finally, Fig. 27b [12] shows a schematic of the frequency–dependent relaxation and resonance phenomena that characterize magnetic materials: $\omega_w$ is the natural undamped wall oscillation frequency and $\tau_w$ is the wall damping time constant.
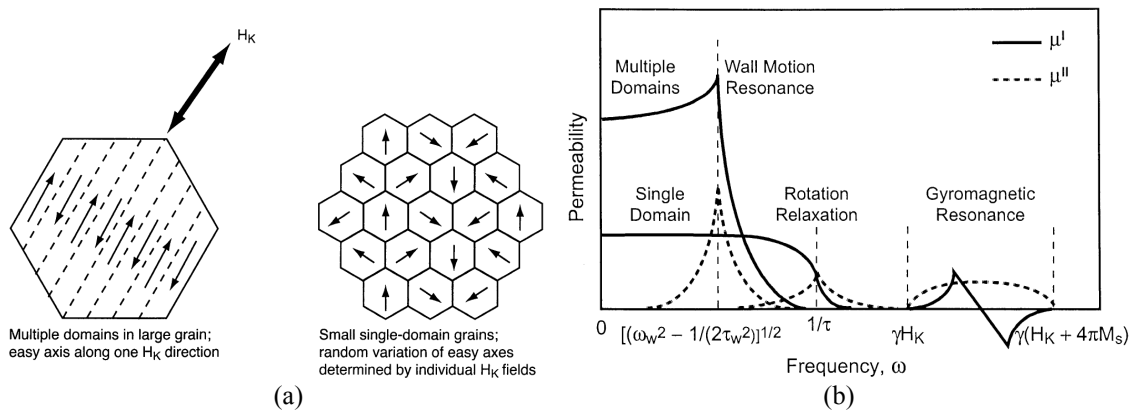


Fig. 27. (a) Magnetization vectors $M$ in a large grain with multiple domains (left) and an aggregate of small single–domain grains under the influence of local $H_K$ fields; (b) frequency–dependent permeability variations due to various magnetic damping actions [9].

Polycrystalline M–type hexaferrites are categorized as "hard" magnets due to their large coercive field $H_c$ resulting from high values of $H_{K\theta}$ (in the order of tens of kOe). Furthermore, hexaferrite specimens of planar geometry are single–domain composites or comprise crystallographically–oriented single–domain particles with magnetization vectors $M$ and domain rotation confined to the plane (of magnetization), hence for this type of MD materials in Fig. 27b the curve for $\mu'$ relative to the single–domain case has to be considered (as will be shown in the following with respect to the measured values of complex relative permeability). Another advantage in using hexaferrites relies exactly upon their high effective internal magnetic anisotropy: the latter contributes to the permanent bias, since for high–frequency applications the permanent part of magnetic bias should be as high as possible. Generally, this requires large permanent magnets, hence relatively–large size and high–cost microwave passive components. Indeed such self–biased materials remain magnetized even after removing the external applied magnetic field.

The main goal of the present PhD thesis is the research for new MD materials with high performance by moving the *FMR* as far as possible towards higher frequencies, in order to exploit the engineered substrates for antenna miniaturization in the *entire* UHF band (for example in the so–called ISM band). This could be achieved only by taking into account simultaneously:

1. the limit imposed by Eq. (15), which means that a trade–off between $\omega_r^{min}$ and $\mu_i'$ has to

be reached, even if more favorable thanks to the presence of the supplementary term $\sqrt{H_{K\theta}/H_{K\phi}}$ with respect to Snoek's law valid for other non–hexaferrite–type magnetic materials. In practical applications, $\mu_i'$ cannot be increased as required;

2. hexaferrites have a complex polycrystalline structure which has to be carefully controlled during the synthesis process.

## B. HEXAFERRITE MANUFACTURING

The first synthesized material for the band of interest was a *barium–strontium* hexaferrite with the composition $Ba_{0.75}Sr_{0.25}Fe_{12}O_{19}$ (BSFO) [10]. BSFO–based components have great importance for the modern society because they are deployed in a variety of electronic devices used for magnetic recording, communication, generation and distribution of electric energy, automotive and medical equipments. Furthermore, they can be used as magnets in purifiers of water (i.e. to eliminate undesired metallic impurities) and in particles accelerators. BSFO presents properties strongly related to its microstructure and morphology, whereas the decrease in the size of the particles results in advantages such as high $H_c$ values, high–frequency applicability, low–cost, great resistance to the heat and high resistance to the corrosion, in comparison to other materials that carry out the same function.

The substrate was produced by ceramic processing: the raw materials $BaCO_3$, $SrCO_3$, $Fe_2O_3$ were ball milled in stoichiometric amount and the solid solution was produced via the *Mixed Oxide* synthesis method by calcination at different temperatures and soaking times: among those the optimal one resulted to be the heating at 900 °C for 12 hours. The obtained powder was then attrition milled, sieved and cold consolidated by die pressing at 400 kg/cm$^2$, followed by cold isostatic pressing at 3000 kg/cm$^2$. Heat treatment at 1250 °C for 5 hours resulted into sintered bodies with the highest final relative density of about 96%. The SEM morphology of the sintered material is shown in Fig. 28; the *average* grain size was verified to be in the range 1 ÷ 2 μm. It has to be stressed out that even significant changes in the values of $\varepsilon_r$ and $\mu_r$ can occur due to porosity and grain dimensions, hence an optimization of the overall synthesis process is mandatory to obtain high–performance materials.
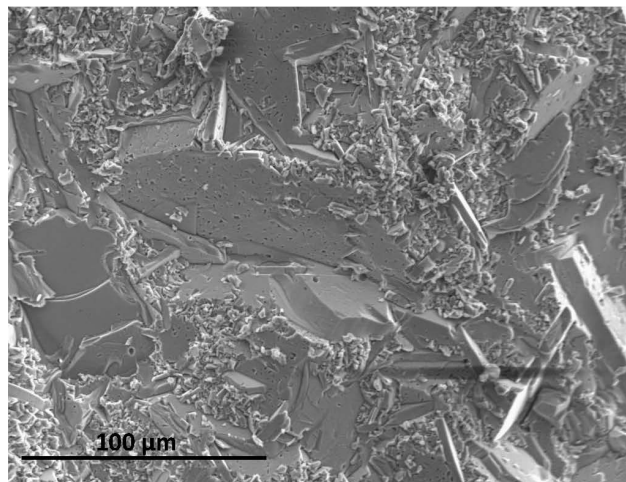


Fig. 28. SEM morphology of the sintered BSFO material.

Disks of different diameter and thickness were prepared for both permittivity and permeability measurements and for the prototype antenna (Fig. 29). The sintered samples (Fig. 29a) were grinded and punched (Fig. 29b). Metallization were put on the top and bottom surfaces of the sample and connected by screen printing a silver paste, followed by heating at
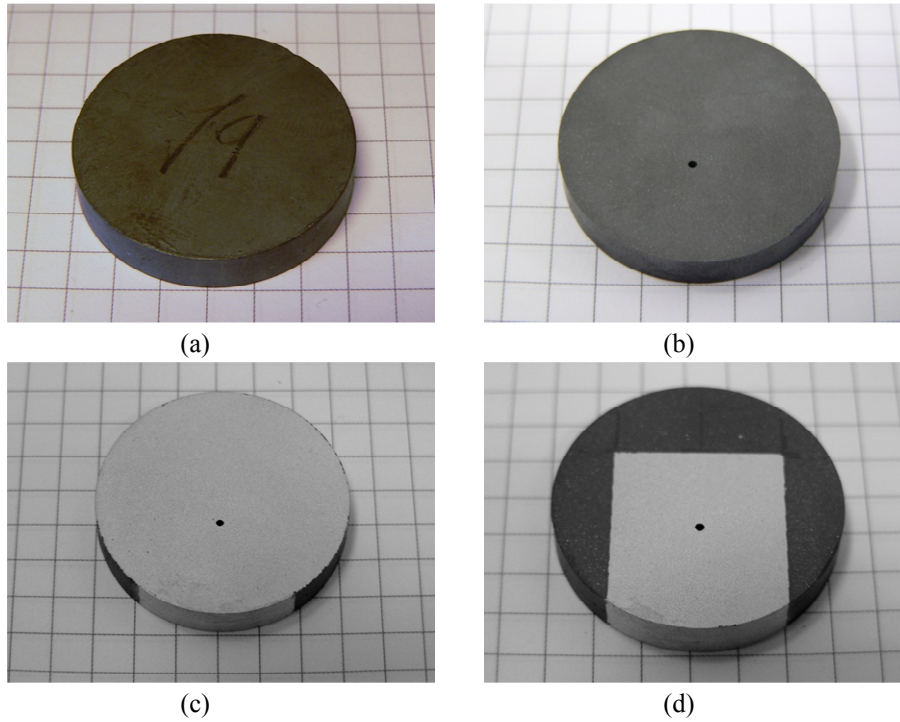
750 °C (Fig. 29c and Fig. 29d):



(a)

(b)

(c)

(d)

Fig. 29. BSFO sample: (a) after sintering; (b) after grinding and punching; (c)–(d) after deposition of silver metallization on both sides (via–hole is clearly visible).

## C. ELECTRICAL PARAMETERS CHARACTERIZATION

Two different set–ups where used for the permittivity and the permeability measurements. In this section, I will refer to the sample as Device Under Test (DUT). For the permittivity characterization, a disk of the BSFO material was deployed, with diameter of 12.7 mm and thickness of 1.3 mm. The measurement procedure was based on two instruments: a *Solartron 1296 Dielectric Interface* in the band 1 Hz – 1 MHz (Fig. 30a) and an *Agilent E4991A RF Impedance/Material Analyzer* in the band 1 MHz – 1 GHz (Fig. 30b and Fig. 30c) [13], to double validate measurements at 1 MHz.

At low frequencies, the dielectric measurements were carried out by recording the complex impedance of a fixture with parallel metallic plates filled with the DUT: in Fig. 30a, the "Hi" electrode position is adjustable by means of a micrometer, whereas the "Lo" electrode position is fixed. The holder is equipped with a guard ring to ensure the electric field homogeneity and prevent from *fringing* effects at the edge of the DUT. In these conditions the structure is modeled as a capacitor and the complex permittivity is computed by taking account of the structure geometrical parameters.

At high frequencies, the impedance/material analyzer with dielectric holder *Agilent 16453A* shown in Fig. 30b was used, with the overall structure still configured as a parallel–plate capacitor. The dispersive $G_p - C_p$ parallel circuit (where $G_p(\omega)$ is the equivalent parallel conductance representing dielectric losses, and $C_p(\omega)$ is the equivalent parallel capacitance) is used to derive the complex permittivity from the measurements over a pre–established frequency band:

$$Y_c = G_p + j\omega C_p = j\omega \left( \frac{C_p}{C_0} - j\frac{G_p}{\omega C_0} \right) C_0 \tag{16}$$

where $Y_c$ is the measured complex admittance of the equivalent circuit and $C_0$ is the capacitance when using air as DUT, then we have:

$$\varepsilon' = \frac{C_p}{C_0} \tag{17}$$

$$\varepsilon'' = \frac{G_p}{\omega C_0} \tag{18}$$

For the permeability characterization, a toroid–shaped DUT of the same BSFO material, 1.3 mm–thick with inner $d_{DUT}$ and outer $D_{DUT}$ diameter of 3.3 mm and 12.4 mm (respectively), was adopted. The permeability measurements were carried out by the same network analyzer: a conductive shield surrounding the central conductor and terminating in a short–circuit test fixture TF (*Agilent 16454A*, referred to as "Magnetic Holder" in Fig. 30c) holds the toroid–shaped magnetic DUT. The central conductor is rolled once around the DUT and relative permeability is calculated from the inductance values at the end of the DUT itself. The magnetic field generated by the current flowing through the central wire is perpendicular to any cross section of the toroidal DUT. The short–circuit configuration ensures a maximum magnetic field and a minimum electric field near the DUT. The magnetic permeability is derived from the input impedance of the holder with and without the DUT. The complex impedance $Z_c$ of a simple $R_s - L_s$ series circuit can be used to model the measurement set–up: $R_s$ is the equivalent series resistance that represents magnetic losses, and $L_s$ is the equivalent series self–inductance of the measurement circuit. We also define: i) the self–inductance $L_{s0}$ when a DUT is not mounted in the TF; ii) the thickness $h$ of the DUT; iii) the radius $r$ of the central wire; iv) the radius $r_0$ of the TF; v) the height $h_0$ of the TF, then we have:

$$Z_c = R_s + j\omega L_s = j\omega \left( \frac{R_s}{j\omega} + L_s \right) \tag{19}$$

$$\mu_r = \frac{2\pi(Z_c - j\omega L_{s0})}{j\omega \mu_0 h \ln\left( \dfrac{D_{DUT}}{d_{DUT}} \right)} + 1 \quad \Rightarrow \quad \mu' = \mathrm{Re}\{\mu_r\},\ \mu'' = \mathrm{Im}\{\mu_r\} \tag{20}$$

$$L_{s0} = \frac{\mu_0}{2\pi} h_0 \ln\left( \frac{r_0}{r} \right) \tag{21}$$
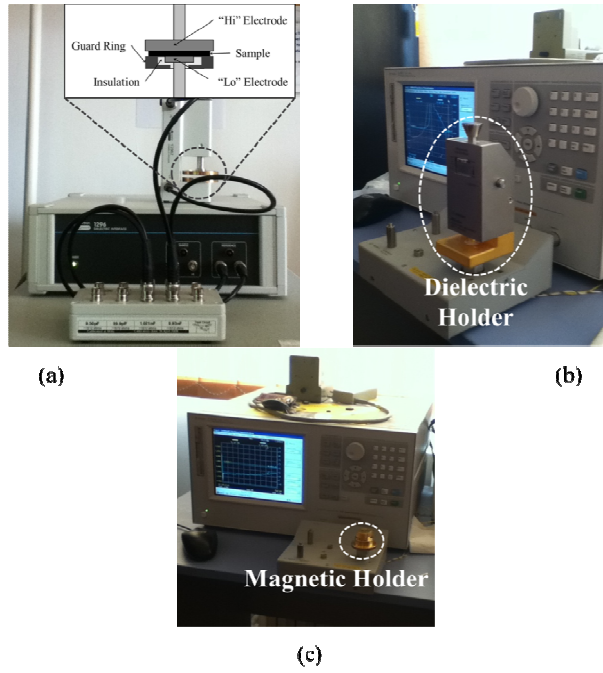
Fig. 30. (a) Low–frequency complex permittivity measurement set–up by the *Solartron 1296 Dielectric Interface*; high–frequency measurement set–up by the *Agilent E4991A RF Impedance/Material Analyzer* for (b) complex permittivity with dielectric holder *Agilent 16453* and for (c) complex permeability with magnetic holder *Agilent 16454A*.

The dielectric and magnetic measurements were performed using the Agilent E4991A–002 software that provides direct readout of material parameters such as permittivity and permeability up to 1 GHz.

From the measured material characteristics, no effective *FMR* is visible up to 1 GHz. On the contrary, just a relaxation phenomenon around 200 MHz is visible in the curves relative to $\mu_r$: this gave a proof of the single–domain crystallographic structure of the synthesized hexaferrite specimen, as stated in paragraph A. This is apparent in Fig. 31b, whereas Fig. 31a shows the frequency–dependent dispersive behavior of $\varepsilon_r$.

For the antenna design the measured behavior of the permittivity and permeability in the frequency range 1 MHz – 1 GHz was exploited to build the material model inside the EM simulation tool [14]. Indeed an *ad hoc* piecewise polynomial approximation was deployed to implement a customized model, since no satisfactory pre–defined model was available. The accuracy of this choice is clearly shown in Fig. 32: a relatively–small band (750–1000 MHz) was considered to guarantee the best matching between the EM tool Lorentz dispersive model and the measured values for $\varepsilon'$, $\varepsilon''$, $\mu'$ and $\mu''$. As expected, considerable magnetic losses can be observed, nevertheless this aspect was improved in a second material fabrication by means of the optimization of the grain synthesis process. On the contrary the dielectric losses show an acceptable behavior all over the measured band. At the design frequency of 868 MHz, the BSFO sample exhibits a value of $\varepsilon' \approx 12$ and a value of $\mu' \approx 2$, with dielectric loss tangent $\varepsilon''/\varepsilon' \approx 0.01$ and magnetic loss tangent $\mu''/\mu' \approx 0.38$. This results in a refraction index of about 5, hence the reduced effective wavelength is $\lambda_g \approx \lambda_0/5$ (where $\lambda_0$ is the free–space wavelength).
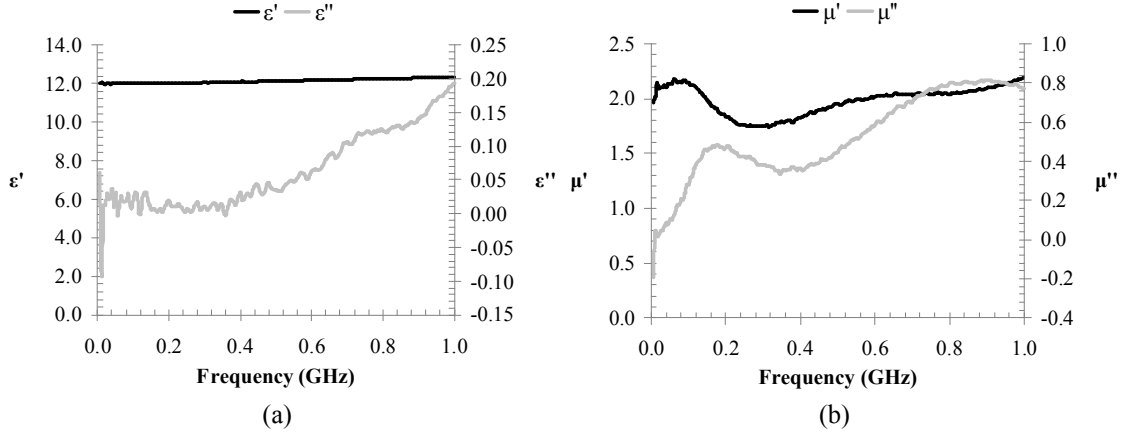
Fig. 31. Measured values of (a) relative permittivity and (b) permeability in the band 1 Hz – 1 GHz.
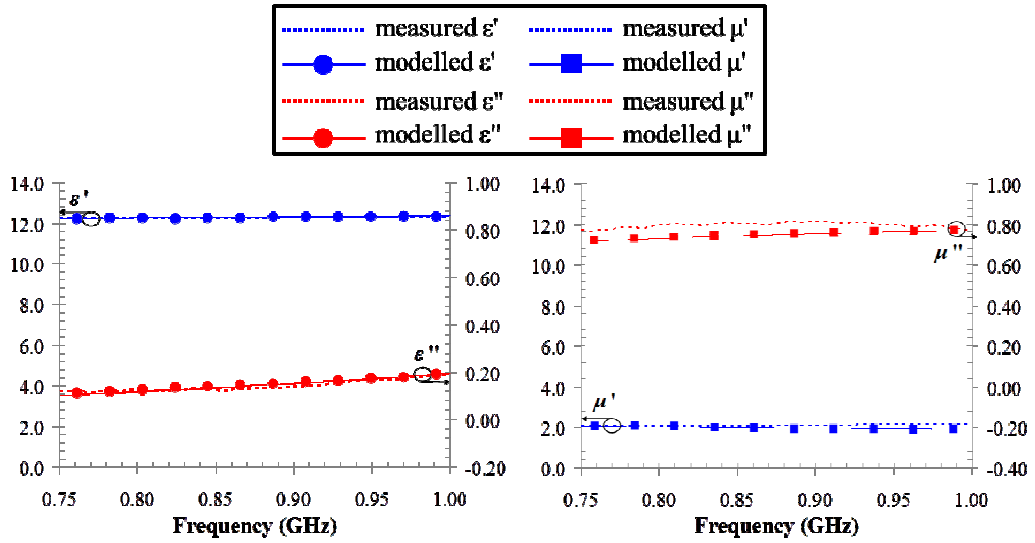


Fig. 32. Comparison between measured and modeled values of relative permittivity (left) and permeability (right) in the band 750 MHz – 1 GHz.

## D.    BSFO MAGNETIZATION PROPERTIES AND *FMR* PREDICTION

Once the whole characterization at high–frequency was performed, the BSFO sample was broken in small pieces, one of which (of weight $w \approx 32.12$ mg) was used to measure the magnetic hysteresis loop $m$(H), shown in Fig. 33, where $m$ is the magnetic moment (in emu) and H is the magnitude of the applied magnetic field (in Oe). Since $m$ is an extensive property mainly depending on the mass of the sample, in order to compare different samples it is necessary to use magnetization $M$, either mass magnetization $M_m$ (measured in emu/g) or volume magnetization $M_V$ (measured in emu/cm$^3$) by calculating $m/w$ or $m/V$, respectively. For the BSFO under test, the magnetic hysteresis loop, measured at room temperature, revealed a typical hysteresis for materials with random anisotropies. A coercive field $H_c$ of about 2,577 Oe, (mass) saturation magnetization $M_{m,S}$ of about 60 emu/g (saturation is reached for $m \approx 1.84$ emu), (mass) remaining magnetization $M_{m,R}$ of about 34.11 emu/g and a squareness ratio $SR$ ($SR = M_{m,R}/M_{m,S}$) of about 0.57 were registered. The latter values are in agreement with the ones experimentally determined for other BSFO materials [10]. As already stated in paragraph A, because of the large $H_c$ hexaferrites can be categorized as "hard" permanent magnets, since the non–zero value of $m$ for H = 0 Oe means a permanent magnetization of the material.

47

Considering that BSFO structure is equivalent to a magnetic system consisting of magnetic entities with randomly–distributed magneto–crystalline anisotropy, from the value of $H_c$ an approximate value of the anisotropy field $H_K$ of about 5053 Oe is obtained, since

$$H_c \approx 0.51 \cdot H_K \quad \text{and} \quad H_K = \frac{2K}{M_{m,S}} \tag{22}$$

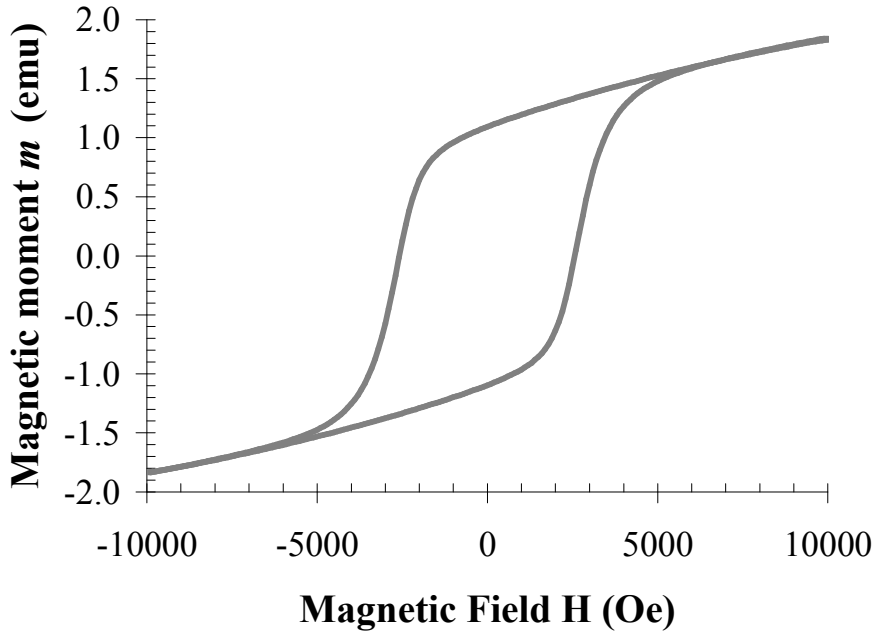where $K$ is the magneto–crystalline anisotropy constant.



Fig. 33. Magnetic hysteresis loop for BSFO at room temperature (1 emu = $10^{-3}$ A·m², 1 Oe = $10^3/4\pi$ A/m).

To characterize the material with respect to its *FMR* and thus to establish the maximum feasible operating frequency, the magnetic losses at 10 GHz were experimentally investigated, therefore well above the selected frequency band of interest (the 10–GHz reference frequency was selected as the highest possible one compatible with the available instrumentation). A cavity with and without the BSFO sample was placed between two magnets and the magnetic field intensity was varied up to 9,037.6 Oe, corresponding to a maximum value for magnetic induction B of 1 T. In the absence of the sample, no shift of the cavity resonance frequency was observed. When the cavity was filled with the sample, a resonance frequency shift and an attenuation of the specific reflection coefficient intensity $|S_{22}|$ were observed (see Fig. 34), demonstrating that magnetic losses are non–negligible but not high enough to significantly degrade $|S_{22}|$. In fact, the maximum value of $|S_{22}|$ is about –13.6 dB for an applied magnetic field of intensity 1,460.8 Oe: this corresponds to a maximum of magnetic energy absorption in the cavity, due to a weak ferromagnetic resonance that is not clearly visible, since the overall losses of the material are low. Moreover, the range of values for $|S_{22}|$ is only about 1.8 dB wide for the sample under test. Increases in the losses have to be taken into account if bigger samples are analyzed.

The latter results allowed to conclude that at 10 GHz the material losses are far from varying strongly and rapidly, which is the typical behavior around the *FMR* frequency. The missing of the *FMR* peak at 10 GHz was expected for the BSFO, because for materials with a

high value of $H_K$ the resonance frequency $f_{res,Hk}$, which corresponds to the gyromagnetic lower limit of the absorption band [10], is expressed by Eq. (23):

$$f_{res,Hk} = \frac{\gamma}{2\pi} H_K \quad \Rightarrow \quad f_{res,Hk} \approx 14.15 \, \text{GHz} \tag{23}$$

and, consequently, the maximum magnetic energy absorption is expected to be at a frequency higher than 10 GHz.

The magnetic permeability measurements were performed for samples in saturated/demagnetized state. It has to be stressed that the radiation properties of the antenna are related very closely to the magnetic permeability, which is a tensor for magnetic materials. Modifying the magnetization direction and amplitude, i.e. the magnetization state of the MD substrate, the overall radiation performance is changed accordingly.
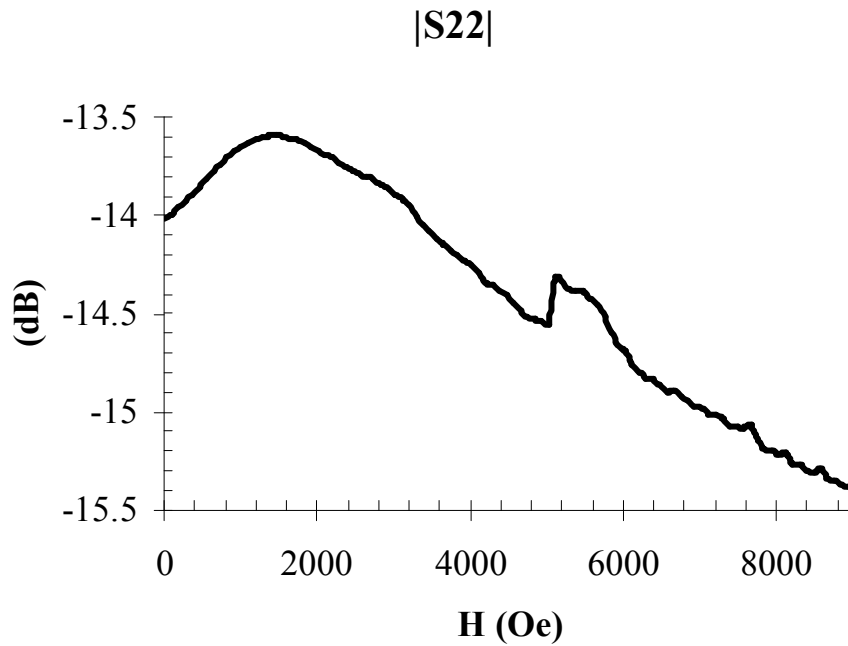
**|S22|**



Fig. 34. $|S_{22}|$ dB for the hexaferrite under test as a function of the applied magnetic field H (Oe).

## 2.4. ANTENNA DESIGN, PROTOTYPING AND TESTING: VALIDATION OF THE NUMERICAL APPROACH AND ON–BODY EXPERIMENTAL SET–UP

### A. DESIGN AND MANUFACTURING

As reported in [15,16], antennas with equivalent surface magnetic currents $\mathbf{J}_{ms}$ (such as patch antennas) are more suitable to be exploited with MD substrates, since the electric field $\mathbf{E}$ is the principal responsible of the radiation. The application of the Lowe's field equivalence principle allows to replace the volume source of the transmitting antenna mainly with the equivalent magnetic surface currents only (which are not affected by $\mu_r$):

$$\mathbf{J}_{ms} = \mathbf{E} \times \widehat{\mathbf{n}} \tag{24}$$

This allows to reach antenna miniaturization and, at the same time, an overall size as stated in Eq. (11) with no significant reduction of the radiation performance. Hence under the assumption of negligible magnetic losses, the two main advantages in using the proposed MD material are: i) preserving radiation efficiency; ii) increasing in bandwidth (due to a lower Quality Factor $Q$). According to [17,18], an 868 MHz patch antenna was designed to test the engineered substrate, as this is a much exploited frequency for RFID applications in the UHF band in Europe. The BSFO sample used for the prototype was a disk, since round in shape devices are more suitable for wearable applications thanks to the absence of sharp edges. To further enhance the antenna miniaturization, a shorting–plate solution was adopted, thus providing a $\lambda_g/4$–patch antenna: $\lambda_0 \approx 345.62$ mm at 868 MHz, hence $\lambda_g/4 \approx 18$ mm. The diameter for the disk was chosen equal to 33 mm in order to provide a substrate large enough for the patch antenna aperture. Finally, two drawbacks needed to be tackled:

1. the fragility of the ceramic composite when drilling a hole in the sample for the antenna feeding;
2. the high dielectric permittivity of the material, which could degrade the radiating properties of the antenna.

The best trade–off between robustness against mechanical stress and EM behavior (in terms of both magnetic losses and radiation performance) of the antenna was reached by choosing a substrate thickness of 5 mm. The curved shorting–plate was mounted on the top of the substrate: this turned out to be an easy–to–make solution preserving antenna radiating properties, since the radiating aperture faces a bigger portion of substrate with respect to a centered patch. The patch, the shorting–plate and the ground plane were made of a 4 μm–thick silver film. The penetration depth of silver at resonance frequency is about 2.152 μm, hence metal thickness of the antenna is about two times the penetration depth, which is the minimum acceptable limit to avoid thin–conductor loss effects. The antenna feeding was realized by inserting a micro–coaxial cable U.FL–LP–088 (50 Ω) into a via.

An image exported from the EM simulator and reporting the parameters used for the design is shown in Fig. 35, together with the final prototype of the antenna: the metallization dimensions of the patch are $L = 19.15$ mm (length) and $W = 17.65$ mm (width), the distance $d$ between the via and the lower edge of the patch is 9.57 mm and the feeding–point radius is 440 μm. The overall weight of the final prototype is about 20 g.

The broadside radiation performance was enhanced by extending the ground plane area of the BSFO–based patch. For this purpose, a 254 μm–thick EMC–shielding conductive fabric, with conductivity $\sigma = 1 \times 10^7$ S/m, was attached to the patch ground plane [19]. This turned out to be an excellent choice to be exploited for any wearable application, since it provides even more reduced interactions with human body and thus guarantees the compliance of healthy safety rules in terms of SAR.
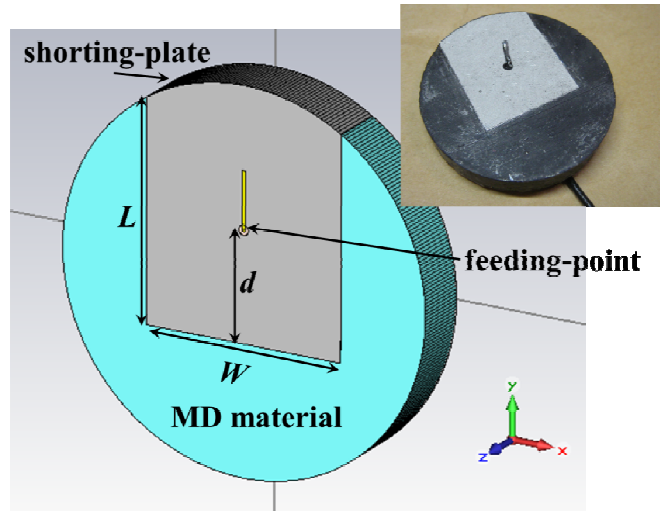
Fig. 35. Button–shaped patch antenna: EM model (left) and view of the prototype (upper–right corner).

## B. EXPERIMENTAL CHARACTERIZATION AND ON–BODY MEASUREMENTS

In the following, an extensive comparison between simulated and measured results will be provided. In Fig. 36 the surface currents plot is considered at the resonance frequency of 868 MHz. It clearly demonstrates that the designed antenna acts as a quarter–wavelength patch: the current nulls occur in correspondence of the lower radiating slot, and the current maxima are at the shorting–plate section. This also provides a proof of the accuracy of the material characterization.
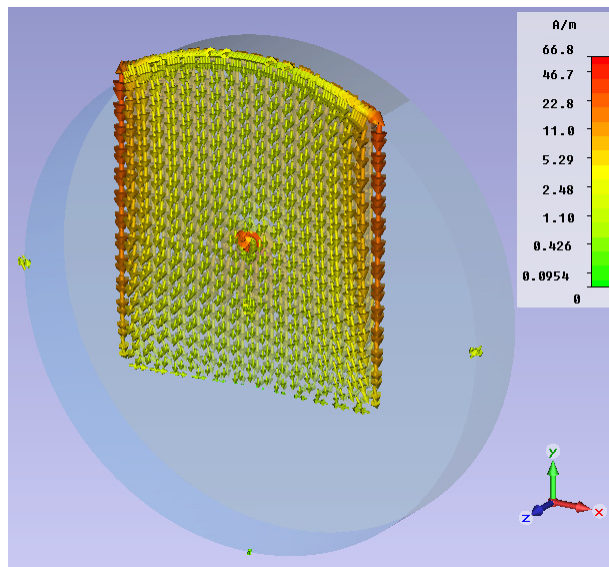


Fig. 36. Surface currents plot of the wearable patch antenna at the resonance frequency of 868 MHz.

In Fig. 37a, a very good agreement between simulated and measured values of the reflection coefficient is demonstrated. In the band 750 MHz – 1 GHz the two curves exhibit a $|S_{11}|$ lower than –10 dB all over the band: this corresponds to a relative bandwidth of 29%, which is the result of the designed substrate properties, whereas a typical characteristic of patch antennas is being narrow–band (about 4% of relative bandwidth in most cases). This could be considered a great advantage in terms of: i) robustness of the antenna against mechanical tolerances; ii) different RFID standard applications; iii) compatibility with standard feeding

techniques. For comparison the same patch antenna printed on an Only–Dielectric (OD) substrate was characterized: the dielectric has a permittivity $\varepsilon_{r,OD}$ providing the same refraction index of the proposed MD antenna. Be $\varepsilon_{r,MD}$ and $\mu_{r,MD}$ the EM properties of the MD material, then $\varepsilon_{r,OD}$ can be defined by Eq. (25) as follows:

$$\sqrt{\varepsilon_{r,OD}} = \sqrt{\varepsilon_{r,MD} \cdot \mu_{r,MD}} \tag{25}$$

In Fig. 37b the simulated values of $|S_{11}|$ for the new substrate are shown as well: good matching conditions cannot be obtained in this case neither by varying the feeding point of the patch antenna (see distance $d$ in Fig. 35): as discussed above this behavior is due to the very low intrinsic impedance provided by the OD material.
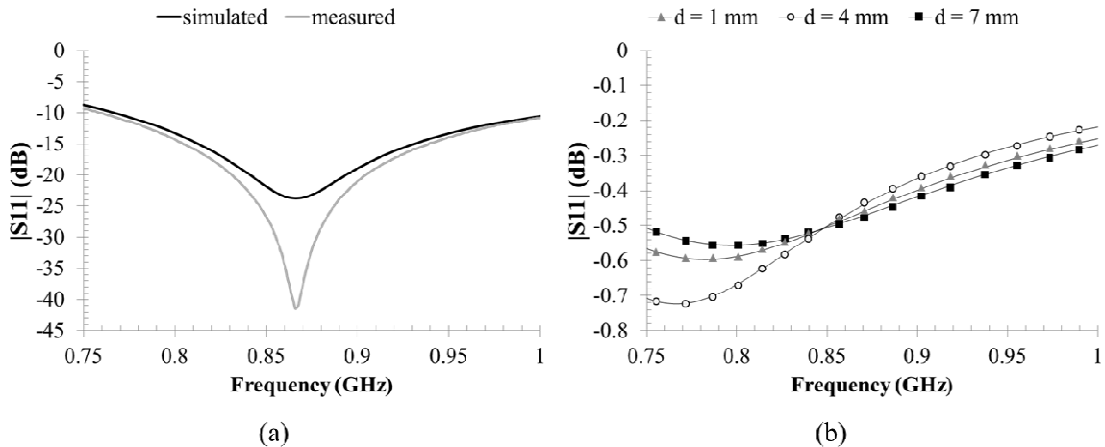


Fig. 37. (a) Simulated and measured magnitudes of the reflection coefficient in the band 750 MHz – 1 GHz for the proposed MD antenna; (b) simulated magnitude of the reflection coefficient in the band 750 MHz – 1 GHz for the Only–Dielectric (OD) antenna for some values of the distance $d$.

In Fig. 38, the E–plane (yz) and the H–plane (xz) simulated (blue solid line) and measured (red dotted line) normalized radiation patterns of the E–field at 868 MHz are plotted in polar coordinates, respectively, with the antenna mounted on the conductive fabric. A very good correspondence can be observed in both two planes. The computed maximum directivity is about 6.4 dBi with a half–power beam width on the xz plane of about 82°, whereas the radiation efficiency is 1.5%. The latter low value is mainly due to the magnetic losses and to the *electrically small* characteristics required by our application purposes: in fact, the total length of the patch in $L \approx \lambda_0/20$. However, the bandwidth–gain product is enhanced with respect to *electrically small* antennas on pure high–$\varepsilon_r$ dielectric substrates. In turn the overall antenna size is compatible with a jacket button (see Fig. 35). Furthermore, matching and radiating properties of the whole system, i.e. antenna and wearable substrate, are independent of the presence of human body which the system itself is attached to. This is the consequence of using the conductive shielding fabric which enhances the antenna radiation performance and ensures EM compatibility at the same time. This is apparent in Fig. 38, where a very low front–to–back ratio is observed (the minimum measured value is −16.34 dB), thus ensuring negligible interactions between antenna and human body. Anyway the antenna alone, directly placed on the human body without the conductive fabric, still guarantees a fairly good behavior. This is shown in Fig. 38 where the E–plane (yz) and the H–plane (xz) (green circles line) radiation patterns at 868 MHz computed in this situation are superimposed to those obtained for the antenna–on–conductive–fabric system. The maximum directivity is about 4.8 dBi, with a half–power beam width on the xz plane of about 117° and a front–to–back ratio of

about −8.5 dB. This entails two main results: i) the idea of adopting a conductive fabric allows an easy–to–embed solution, but the skin itself acts as an extended ground plane which preserves the broadside radiation behavior of the antenna; ii) the (computed) directivity is only 1.5 dBi lower and the back–radiation still exhibits a negligible value for potential interactions with human tissues.

The radiation patterns in Fig. 38 have been measured at a 3–meters distance from the antenna: the good correspondence between measurements and far–field simulations performance confirms that the far–field approximation is valid for the experimental set–up.
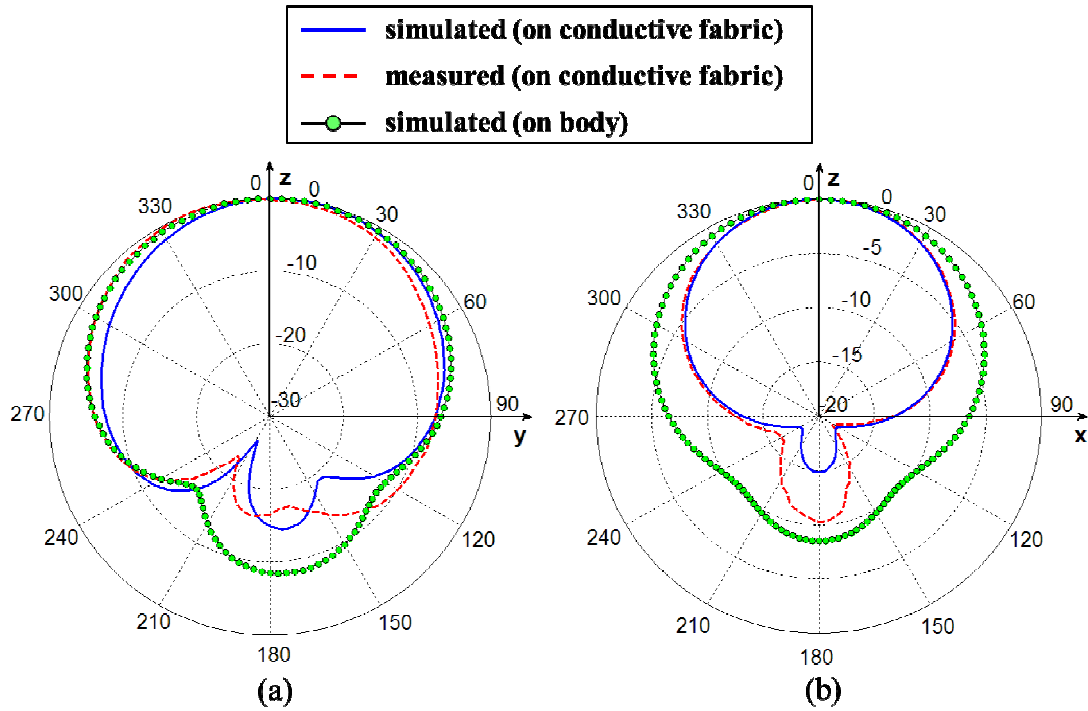


Fig. 38.  (a) E–plane and (b) H–plane simulated and measured normalized radiation patterns of the proposed MD–based button antenna at 868 MHz, on a conductive fabric and placed directly on the body skin.

In order to demonstrate that magnetic losses have a predominant role on antenna efficiency, the effect of silver thickness was also investigated. As stated before, metal thickness of the antenna is about two times the penetration depth. Simulations with increasing values of the silver thickness up to 35 μm were carried out, showing that no significant improvement of the radiation efficiency could be achieved and hence giving an indirect proof of magnetic losses prevalence.

Finally, the feasibility of the proposed solution for wearable applications in indoor spaces was investigated. For this purpose, first the power received by a 5 dB–gain antenna located at 1 m–distance ($r = 1$ m) from the MD button–type patch was measured, with an emitted power $P_E$ of −10 dBm (this was the input power at the antenna terminals): the experimental set–up is schematically shown in Fig. 39. The space was kept free of obstacles and the receiving antenna was placed in the focus of a parabolic reflector in order to deal with reduced fading– and multipath effects. A received power $P_{RX}$ of −44 dBm was measured, in good agreement with the results of the corresponding Friis calculations (−46.1 dBm); at a 3 m–distance ($r = 3$ m) the same quantity decreased to about −55.6 dBm (Table III summarizes the latter results).These received power levels allowed to suppose that the proposed solution is well suitable for being exploited in indoor scenarios with links extension of few meters, typical requirement of civil or healthcare spaces. For example, assuming a receiver sensitivity of −85 dBm, a 30 dB margin is preserved for potential scattering attenuation.
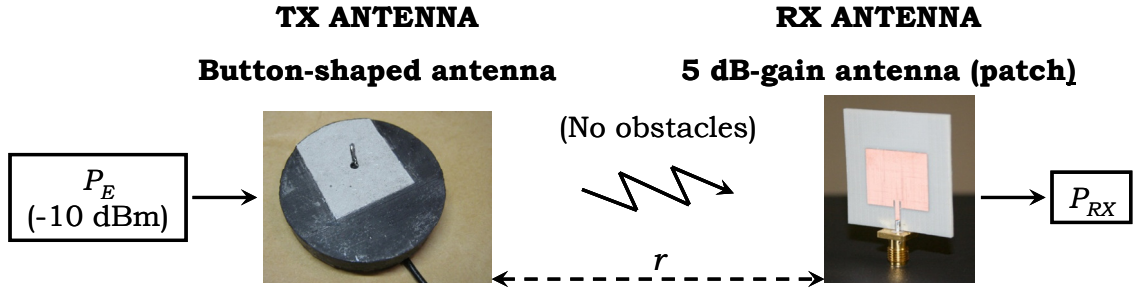
**TX ANTENNA**

**Button-shaped antenna**

**RX ANTENNA**

**5 dB-gain antenna (patch)**

(No obstacles)

$P_E$ (-10 dBm)

$P_{RX}$

$r$

Fig. 39. Schematic view of the experimental set–up for link–budget measurements. *r* is the distance between antennas.

Table III. Link–budget measurements for the experimental set–up displayed in Fig. 39.

| Distance from RX antenna | Emitted power $P_E$ (dBm) | Friis–calculated $P_{RX}$ (dBm) | Measured $P_{RX}$ (dBm) |
|---|---|---|---|
| 1 m | −10 | −46.1 | −44 |
| 3 m | −10 | −55.7 | −55.6 |

Then, in order to validate the link performance in a realistic rich–scattering indoor environment, power measurements with the on–body (worn) configuration (shown in Fig. 40) and with the off–body (not worn) one were carried out. In the two set–ups, the overall radiating system (button–shaped antenna and conductive fabric) was excited with $P_E = −10$ dBm and kept at various distances from a 6 dB–gain circularly–polarized patch antenna connected to a Spectrum Analyzer in order to measure $P_{RX}$. The environment surrounding the measurement set–up (see Fig. 40) was characterized by many different obstacles which could be seen as "scatterers", thus representing a realistic operating mode of the device under test. The radiating performance of the button–shaped antenna were expected not to change significantly in the two situations (on–body and off–body) thanks to the conductive fabric attached to the patch ground plane. The experimental results are summarized in Table IV: a good agreement between the two set–ups can be observed, thus providing a proof of the device reliability in terms of radiating performance and EM compatibility.
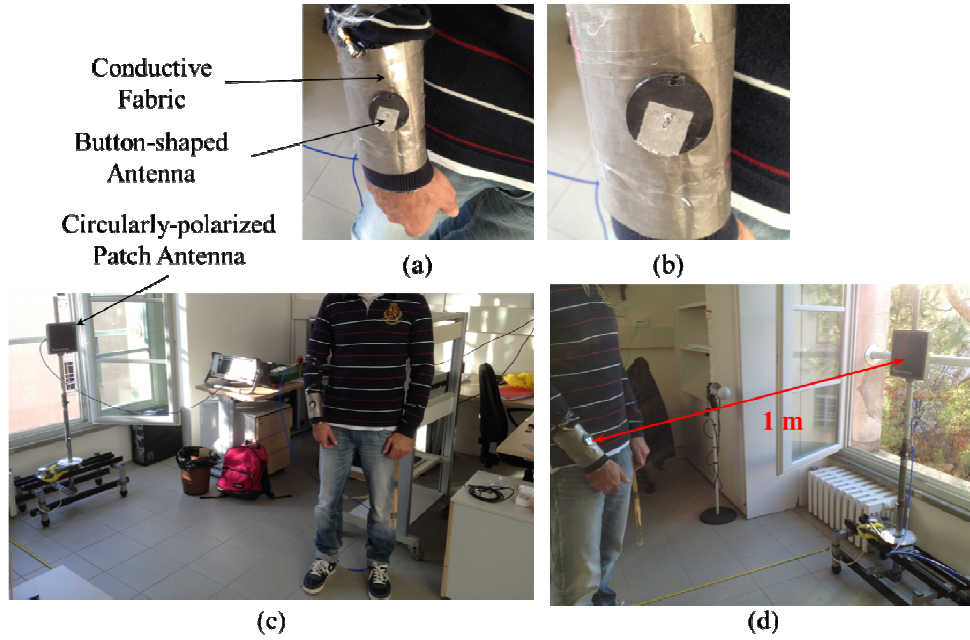
Fig. 40. Measurement set–up for the on–body (worn) solution: (a) overall radiating system worn on right arm; (b) detail of button–shaped antenna attached to conductive fabric; (c) measurement environment; (d) measurement example at 1 m–distance.

Table IV. Link–budget measurements for on– and off–body solution in a realistic propagation scenario.

| Distance from RX antenna | Emitted power $P_E$ (dBm) | On–body solution $P_{RX}$ (dBm) | Off–body solution $P_{RX}$ (dBm) |
|---|---|---|---|
| 1 m | −10 | −51.1 | −53.4 |
| 2 m | −10 | −57 | −57.1 |
| 3 m | −10 | −62.4 | −64.3 |

## CONCLUSIONS

In the present chapter, the synthesis and the detailed physical–EM characterization of an innovative MD material (barium–strontium hexaferrite, BSFO) have been presented. Aim of the research was the development of a new family of substrates to be adopted for the design of *electrically small* patch antennas for wearable applications in the 868–MHz band. First an investigation on state–of–the–art MD materials was carried out in order to select the best ferrite composite with enhanced magnetic properties in terms of high–frequency *FMR*. To reach this goal, a hexaferrite was chosen since it exhibited an *FMR* at a very high frequency thanks to its intrinsic physical characteristics, i.e. large anisotropy field and low eddy–current losses. In cooperation with ISTEC (Faenza, Italy), a set of BSFO samples was produced and then characterized in detail at the Faculty of Physics of University "Al. Ioan Cuza" (Iaşi, Romania). The CAD design of an *electrically small* patch antenna was then carried out and a prototype of the antenna was manufactured by ISTEC. The measured EM properties (reflection coefficient, radiation patterns and efficiency) showed a very good agreement with the predicted (simulated) performance. Finally, a handful of measurements of RF–link power budget were carried out by means of a realistic on–body set–up: this way, a proof of the effective capabilities of the overall system performance was given. Major results of this research are:

1. the engineered BSFO has an *FMR* well above the operating frequency (i.e. 868 MHz), thus it could be exploited in the entire UHF band;
2. the value of relative permeability is doubled all over the band of interest, which allows a reduction of the effective wavelength of about 30%;
3. a standard feeding technique by means of a 50 Ω coaxial cable inserted into a via was adopted with a very good simulated and measured matching at the desired operating frequency;
4. a relative bandwidth of 29% was achieved, hence more than 7 times the relative bandwidth of a standard on–high–permittivity–substrate patch antenna;
5. as expected, the radiation efficiency of the overall system is low due to high magnetic losses and *electrically small* characteristics. However, the bandwidth–gain product is enhanced with respect to *electrically small* antennas on pure high–relative–permittivity dielectric substrates;
6. simulated and measured radiation patterns on an EMC–shielding conductive fabric show a very good agreement;
7. simulations of the antenna using human skin as ground plane instead of the afore–mentioned EMC–shielding conductive fabric demonstrated the effective wearable capabilities of the proposed system thanks to limited back–radiation phenomena;
8. measurements of RF–link power budget in a realistic rich–scattering indoor scenario demonstrated that the designed antenna offers satisfying performance at some meters of distance from the receiving antenna even in presence of potentially–dangerous scatterers;
9. the overall size of the proposed patch antenna is suitable for a wearable application thanks to its easy–to–embed button–shape.

Future research in the field of MD materials comprise:

1. ceramic processing optimization to increase the value of relative permeability and decrease the value of relative permittivity;
2. theoretical model of the correlation between grain dimensions and MD properties;
3. new MD materials (composites and multilayer structures), also for wearable/implantable applications in the 2.4 GHz ISM band;
4. MD materials with $\mu_r \geq \varepsilon_r$ and reduced magnetic losses to enhanced radiation efficiency, matching and bandwidth;
5. new antenna layouts;
6. new techniques for low–cost and fast EM characterization of MD materials at microwave frequencies.

The present research can be considered as a starting point of new investigations for a further reduction of antenna size in the modern wireless telecommunication systems. Several other issues need to be addressed, especially when embedding such MD materials inside human body for implantable applications, hence a close integration with material processing techniques and biological compatibility tests have to be taken into account to achieve high–performance and health–safe radiating systems.

## REFERENCES

[1] L. J. Chu, "Physical limitations on omni–directional antennas," *J. Appl. Phys.*, Vol. 19, pp. 1163–1175, Dec. 1948.

[2] J. S. McLean, "A re–examination of the fundamental limits on the radiation Q of electrically small antennas", *IEEE Trans. on AP*, Vol. 44, pp. 672–675, May 996.

[3] R. F. Harrington, "On the gain and beamwidth of directional antennas", *IRE Trans. on AP*, Vol. 6, pp. 219–225, 1958.

[4] R. B. Waterhouse, S. D. Targonski, D. M. Kokotoff, "Design and performance of small printed antennas", *IEEE Trans. on Antennas and Propagation*, Vol. 46, No. 11, pp. 1629–1633, 1998.

[5] C. A. Balanis, Antenna Theory, Wiley, 2005.

[6] H. Mosallaei, K. Sarabandi, "Engineered meta–substrates for antenna miniaturization", *URSI International Symposium on Electromagnetic Theory*, Pisa (Italy), May 2004.

[7] H. Mosallaei, K. Sarabandi, "Design and Modeling of Patch Antenna Printed on Magneto–Dielectric Embedded–Circuit Metasubstrate", *IEEE Trans. on Antennas and Propagation*, Vol. 55, No. 1, pp. 45–52, 2007.

[8] U. Ozgur, Y. Alivov, H. Morkoc, "Microwave ferrites, part 1: fundamental properties", *J Mater Sci: Mater Electron*, Vol. 20, No. 9, pp. 789–834, 2009.

[9] M. Aldrigo, A. Costanzo, D. Masotti, C. Galassi, "Exploitation of a novel magneto–dielectric substrate for miniaturization of wearable UHF antennas", *Elsevier Materials Letters*, Vol. 87, pp. 127–130, 2012.

[10] F. M. M. Pereira, M. R. P. Santos, R. S. T. M. Sohn, J. S. Almeida, A. M. L. Medeiros, M. M. Costa, A. S. B. Sombra, "Magnetic and dielectric properties of the M–type barium–strontium hexaferrite ($Ba_xSr_{1-x}Fe_{12}O_{19}$) in the RF microwave (MW) frequency range", *J Mater Sci: Mater Electron*, Vol. 20, pp. 408–417, 2009.

[11] V. Rizzoli, "Resonance Measurement of Single– and Coupled–Microstrip Propagation Constants", *IEEE Trans. on Microwave Theory and Techniques*, Vol. 25, No. 2, 1977.

[12] G. F. Dionne, "Magnetic Relaxation and Anisotropy Effects on High–Frequency Permeability", *IEEE Trans. on Magnetics*, Vol. 39, No. 5, 2003.

[13] C. E. Ciomaga, I. Dumitru, L. Mitoseriu, C. Galassi, A. R. Iordan, M. Airimioaei, M. N. Palamaru, "Magnetoelectric ceramic composites with double–resonant permittivity and permeability in GHz range: A route towards isotropic materials", *Scripta Materialia*, Vol. 62, No. 8, 2010.

[14] CST Microwave Studio 2011, www.cst.com.

[15] A. O. Karilainen, P. M. T. Ikonen, C. R. Simovski, S. A. Tretyakov, "Choosing Dielectric or Magnetic Material to Optimize the Bandwidth of Miniaturized Resonant Antennas", *IEEE Trans. on Antennas and Propagation*, Vol. 59, No. 11, pp. 3991–3998, 2011.

[16] A. Pacini, "Studio di topologie d'antenne su substrati magneto–dielettrici", B. Sc. thesis, Faculty of Engineering of Bologna, Cesena Campus, Oct. 2012.

[17] R. C. Hansen, M. Burke, "Antennas with magneto–dielectrics", *Microwave Opt. Tech. Lett.*, Vol. 26, No. 2, pp. 75–78, 2000.

[18] M. Aldrigo, D. Bianchini, A. Costanzo, D. Masotti, C. Galassi, L. Mitoseriu, "New broadband button–shaped antenna on innovative magneto–dielectric material for wearable applications", *Proc. EuMW 2012*, Amsterdam (NL), 28 Oct.–2 Nov. 2012.

[19] A. Costanzo, F. Donzelli, D. Masotti, V. Rizzoli, "Rigorous design of RF multi–resonator power harvesters", *Proc. European Conf. Antennas and Propagation EUCAP 2010*, Barcelona (Spain), April 2010.

# CHAPTER 3

## ENERGY–HARVESTING FOR SOLAR ENERGY EXPLOITATION: AN INNOVATIVE APPROACH FOR "GREEN" TECHNOLOGY ISSUES

The "Industrial Revolution" in 19$^{th}$ century represented a milestone for the entire humankind. Since several new technologies arose starting from the first steam machines, factory facilities have been improving by leaps and bounds in terms of sophisticated and efficient mechanical and electrical–electronic equipments. In this field, one of the most important discoveries was the oil refining, which requires invasive revenue plants. Furthermore, no need to talk about the well–known consequences of hydrocarbon combustion on the environment.

For the afore–mentioned reasons, *green* (i.e. environmentally–friendly) technologies started to play a crucial role in preserving environment integrity from diffuse pollution when the effects of the diffused industrialization began to go out of control and to put in danger the survival itself of humanity. Hence the research in the field of *alternative* energy sources contributes to the investment in a more sustainable world, where engineering processes are already facing a plethora of problems in developing innovative techniques to exploit new natural resources. Among the latter, EM energy can be considered the most pervasive one, since it reveals itself in a set of different ways, i.e. from TV and mobile phone signals to IR and UV radiation etc. In particular, it is well–known that the solar spectrum is divided in many portions, which need different technologies to be properly deployed: photovoltaic panels are probably the most important application for industrial and homely–customized power supply systems. For such installations, conversion efficiency $\eta$ is a key requirement: its average value for common silicon cells is no more than 15% and higher values have been obtained only in laboratory solutions. Solar panels exploit mostly the visible light and UV regions, so that they are transparent to THz/IR radiation, which represents more than 40% of the total energy radiated by the sun and covers the frequencies up to about 400 THz. Moreover, photovoltaic technology suffers from some intrinsic limitations, such as: i) raw–material cost; ii) area occupation; iii) sensitivity to visible light and UV radiation only upon direct illumination; iv) strong influence of atmospheric effects on panels performance; v) maintenance cost.

According to a common engineering classification, THz–frequency band and IR–frequency band can be defined as follows:

1. THz–frequency band: 0.3 ÷ 30 THz;
2. IR–frequency band: 30 ÷ 400 THz.

State–of–the–art IR applications comprise infrared detection and sensors, spectroscopy and imaging techniques but not energy–harvesting systems. The latter could represent an interesting solution for the supply of low–consumption electronic devices, e.g. in wearable wireless applications. As will be discussed in the following, the exploitation of IR solar energy has some unavoidable shortcomings, mainly due to the scarce amount of available power. For this reason, the same technology could be usefully applied to the deployment of dedicated IR sources for indoor energy–scavenging systems, e.g. power supply of RFID tags from IR lasers. Two of the most challenging issues in developing IR energy–harvesters are:

1. the peculiar behavior of antenna metallization at infrared frequencies;
2. the limited rectification properties of the tunnel Metal–Oxide–Metal (MOM) diodes to

use for the IR–DC conversion. This technology has been the most exploited so far to achieve rectification capabilities at such THz–frequencies for reasons that will be explained in the following.

## 3.1. THE SOLAR IRRADIANCE: A MOTIVATION FOR USING AN ANTENNA ARRAY

Several solutions are already present in literature, but they all suffer from some limitations: in [1,2] important approximations are introduced in the description of both the materials and the rectifying diode at IR frequencies; in [3] the actual conversion efficiency is not predicted. The research carried out during my last year of the PhD course aimed to bridge this gap by means of an accurate nonlinear/EM approach. For this purpose, I will present an original solution to deploy IR power for potential energy–harvesting applications by means of innovative bow–tie antenna arrays. This will be done first by motivating the choice of an antenna array and second by an in–depth description of the rectification performance offered by a whole energy–harvester. At the end, technological enhancements and future research of the proposed solution will be provided together with a practical off–the–shelf application to tackle the problem of the low–level input power even under direct solar illumination.

Let us define the *angular diameter* or *apparent size* of a generic astronomic object: it is the ratio between the object diameter and the distance of the object from the observer. Hence the sun angular diameter (as it can be seen on earth) is about 0.5° or, equivalently, $8.7 \times 10^{-3}$ rad as is shown in Fig. 41:
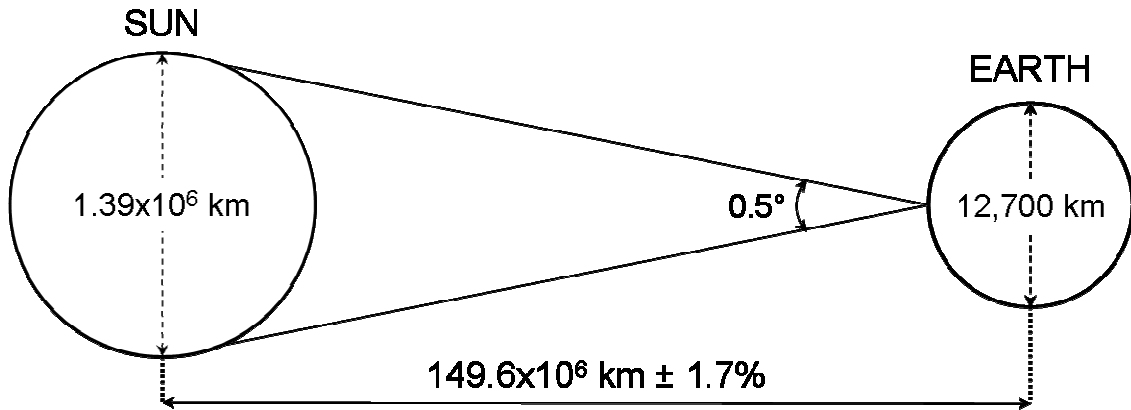


Fig. 41. Schematic view of the sun–earth astronomic system.

Since the earth angular speed is about $7.3 \times 10^{-5}$ rad/sec, the time needed to cover 0.5° is about 2 min., thus the exploitation of an antenna array with a half–power beam width in the angular range 20° ÷ 30° allows to keep a solar energy–harvesting system in a fixed position for about 80 ÷ 120 min., respectively. This way a better exploitation of the available IR solar radiation is guaranteed disregarding mobility and exposure time, since IR spectrum is less sensitive to atmospheric effects and phenomena than visible light/UV spectrum. The typical value of sun power density (which will be referred to as "solar constant") is about 1,000 W/m$^2$ at ground level. The sun can be also modeled as a "black body" which radiates at a surface temperature of about 5,800 K, according to the Planck's law:

$$E_\lambda = 2\pi c \frac{1}{\lambda^5} \frac{hc}{\exp\left(\frac{hc}{\lambda K_B T_K}\right) - 1} \tag{1}$$

In Eq. (1) $E_\lambda$ is the *spectral emitting power* (in W/m²·λ), $h$ is the Planck's constant, $c$ is the light speed (in vacuum), λ is the wavelength in free–space, $K_B$ is the Boltzmann's constant and $T_K$ is the temperature in Kelvin degrees. Fig. 42 shows the well–known curve of $E_\lambda$ (in W/m²·λ) as a function of λ (in μm) in the band 77 ÷ 1500 THz (corresponding to the wavelength interval 0.2 ÷ 3.89 μm) for the sun surface temperature of about 5,800 K:

## Sun spectral emitting power
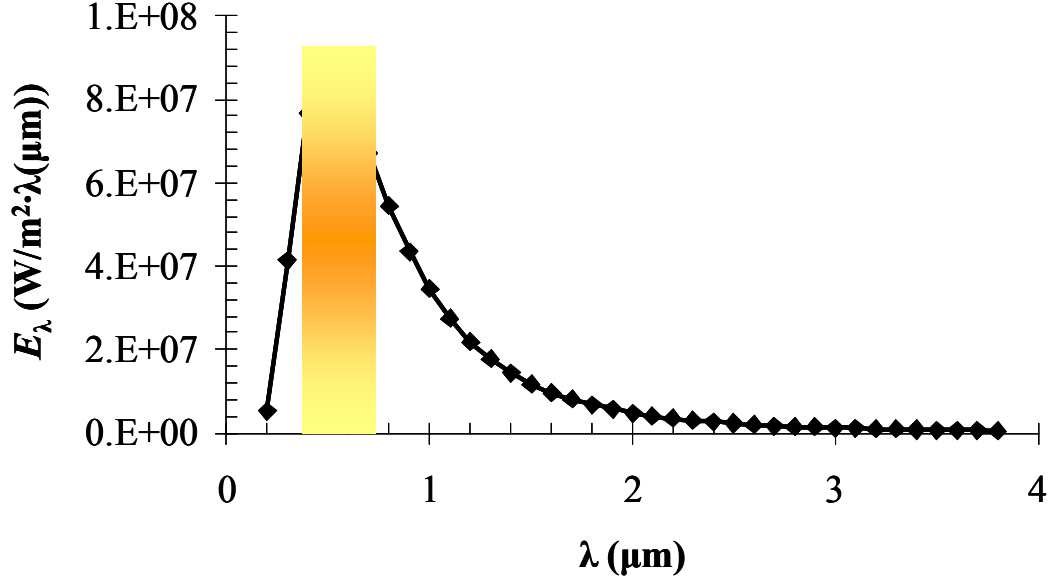


Fig. 42. Sun spectral emitting power as a function of wavelength for $T_K \approx 5,800$ K. The colored area represents the visible spectrum.

At a given temperature, $E_\lambda$ increases with λ till it reaches a maximum value $E_{\lambda,\max}$, after which it decreases monotonically. In particular, let us define the first derivative of $E_\lambda$ as follows:

$$\xi = {hc}\big/{\lambda K_B T_K}$$
$$\frac{dE_\lambda}{d\lambda} = 0 \quad \Leftrightarrow \quad \frac{\xi}{5} + \exp(-\xi) = 1 \tag{2}$$

An analytical solution of Eq. (2) gives $\xi_{\max} = 4.9651$, hence the value of wavelength corresponding to $E_{\lambda,\max}$ is $\lambda_{\max}$ such that:

$$\lambda_{\max} \cdot T_K = b \tag{3}$$

Eq. (3) is the Wien's displacement law and $b = 2.898 \times 10^{-3}$ m·K is a constant of proportionality called Wien's displacement constant. Eq. (3) states that the peak spectral emitting power $E_{\lambda,\max}$ can be observed in correspondence of a shorter wavelength when increasing the temperature $T_K$ of the black body. As is apparent in Fig. 42, at about 5,800 K $\lambda_{\max} \approx 500$ nm (yellow light). This means that the sun emits its maximum power in the visible spectrum, i.e. in the frequency band 400 ÷ 790 THz (corresponding to the wavelength interval

380 ÷ 750 nm as can be seen from the colored area in Fig. 42).

A very important quantity is the black body *emitting power* $E_{\lambda_1,\lambda_2}$ in a certain interval of wavelengths $[\lambda_1,\lambda_2]$ (in W/m$^2$) which can be obtained by integrating Eq. (1) over $[\lambda_1,\lambda_2]$:

$$C_1 = 2\pi hc^2 = 3.742 \times 10^{-16} \text{ W} \cdot \text{m}^2$$
$$C_2 = hc\Big/ K_B = 1.439 \times 10^{-2} \text{ m} \cdot \text{K} \tag{4}$$
$$E_{\lambda_1,\lambda_2} = \int_{\lambda_1}^{\lambda_2} E_\lambda \, d\lambda = \frac{C_1 T_K^4}{C_2^4} \int_{\lambda_1}^{\lambda_2} \frac{\xi^3}{\exp(\xi)-1} \, d\xi$$

For the present case of study, $\lambda_1 = 2.44$ μm (123 THz) and $\lambda_2 = 3.89$ μm (77 THz), since it is the band of the considered bow–tie base–antenna exploited for the nano–scale energy–harvester (as will be shown in the following).

Because of its spherical shape, incoming solar radiation impinging onto earth surface is characterized by an effective *emitting power* $E_{\lambda_1,\lambda_2}^{eff}$ which can be obtained by Eq. (4) as follows:

$$E_{\lambda_1,\lambda_2}^{eff} = E_{\lambda_1,\lambda_2} \left( \frac{r_{solar}^{av}}{d_{sun-earth}^{av}} \right)^2$$
$$r_{solar}^{av} = 6.95 \times 10^8 \text{ m} \tag{5}$$
$$d_{sun-earth}^{av} = 1.49 \times 10^{11} \text{ m}$$

Referring to Fig. 41 $r_{solar}^{av}$ is the average solar radius and $d_{sun-earth}^{av}$ is the average sun–earth distance.

Let us now define the so–called Air Mass (AM): the Air Mass takes into account the effect of terrestrial atmosphere on sun light and corresponds to the relative length of the path of direct solar radiation through the atmosphere. Mathematically, it can be defined as the ratio between the path effectively covered by sun rays through the atmosphere and the minimum value of the path itself. For example:

1. outside terrestrial atmosphere, sun at zenith point: AM = 0 (AM0);
2. at sea level with crystal clear sky and air pressure $P_0 = 1.013$ bar (760 mm Hg), sun at zenith point: AM = 1 (AM1);
3. in general:

$$\text{AM} = \frac{P}{P_0} \cdot \frac{1}{\sin\theta} \tag{6}$$

where $P$ is the local pressure of air (in bar), $P_0 = 1.013$ bar and $\theta$ is the solar elevation angle, i.e. the angle from which the sun can be seen with respect to the zenith point.

Increasing AM entails an increasing attenuation of solar radiation due to atmospheric effects, which depend on latitude, season and day time. AM = 1.5 (AM1.5) corresponds to the solar spectrum with $\theta = 48.2°$ and is the value (taken as a reference by the Commission of the European Community) conventionally chosen for lab tests of photovoltaic components. Indeed the curve of Fig. 42 was calculated with the assumption AM = AM1.5.

Finally, the real *emitting power* $E_{\lambda_1,\lambda_2}^{real}$ takes into account also the atmospheric effects:

$$E_{\lambda_1,\lambda_2}^{real} = E_{\lambda_1,\lambda_2}^{eff} k(\text{AM}) = E_{\lambda_1,\lambda_2} \left( \frac{r_{solar}^{av}}{d_{sun-earth}^{av}} \right)^2 k(\text{AM})$$

$$0 < k(\text{AM}) < 1 \tag{7}$$

where $k(\text{AM})$ is an attenuation factor depending on AM.

Eq. (7) will be used to calculate the *emitting power* $E_{\lambda_1,\lambda_2}^{real}$ in the band of interest of the proposed nano–harvester for solar radiation deployment.

## 3.2. BASE–ANTENNA DESIGN: TECHNOLOGICAL AND COMPUTATIONAL CHALLENGES

First of all an array solution with a single diode was addressed, instead of a multi–element antenna with multiple diodes (one for each antenna), in order to achieve the highest THz–DC conversion efficiency [4] due to the highly–directive array behavior As reported in literature [5,6], the bow–tie antenna as base–element of the proposed THz array was chosen, since like the dipole antenna it exhibits a high radiation efficiency (more than 90%) which is a key issue to maximize the power transferred to the diode. With respect to resonant dipoles, bow–ties have the main advantage to offer a wider relative bandwidth. The frequency band of interest was first selected in the range 77 ÷ 123 THz around the central frequency of 100 THz ($\lambda_0 \approx 3$ μm – a typical IR frequency of solar spectrum) to verify the feasibility of the proposed solution. Then, the material characteristics at THz frequencies were investigated:

1. for the substrate a 200 nm–thick silicon dioxide ($SiO_2$) layer was chosen, since it largely exploited in its crystalline form at optical and sub–optical frequencies;
2. for the metallization a 35 nm–thick gold layer was considered.

The starting point of the CAD design was the modeling of the afore–mentioned materials at the selected operating frequency: $SiO_2$ has negligible losses around 100 THz [7], whereas gold has highly–dispersive characteristics similar to other metals exploited at such IR frequencies. In particular, free electrons inside metals experience a relaxation movement making the AC conductivity a complex number $\sigma = \sigma'-j\sigma''$ with imaginary part $\sigma''$ of the same order of magnitude as real part $\sigma'$: this introduces further losses in the metal structure affecting the overall system performance. The above–mentioned losses are due for most to a plasma of electrons oscillating on the metal surface, which gives rise to an inductive component of the metal surface impedance bigger than the resistive one.

In order to deal with the appropriate materials model inside the EM analysis tool [8], according to [9] in the frequency band of interest the measured values of complex refraction index $n_c = n-j\kappa$ [7] were exploited for both $SiO_2$ and gold, and converted them into complex values of relative permittivity $\varepsilon_r = \varepsilon'-j\varepsilon''$ in the following way:

$$n_c = \sqrt{\varepsilon_r} \quad \Rightarrow \quad \begin{cases} \varepsilon' = n^2 - \kappa^2 \\ \varepsilon'' = 2n\kappa \end{cases} \tag{8}$$

The measured values of $n_c$ and the calculated values $\varepsilon_r$ are shown in Fig. 43 for the frequency band 9.375 ÷ 428.571 THz:

| λ (μm) | f (GHz) | f (THz) | $n$ | $\kappa$ | $\varepsilon'$ | $\varepsilon''$ |
|---|---|---|---|---|---|---|
| 32.000 | 9375.000 | 9.375 | 62.800 | 202.000 | -36860.160 | 25371.200 |
| 30.000 | 10000.000 | 10.000 | 56.600 | 192.000 | -33660.440 | 21734.400 |
| 28.000 | 10714.286 | 10.714 | 50.500 | 182.000 | -30573.750 | 18382.000 |
| 26.000 | 11538.462 | 11.538 | 44.600 | 171.000 | -27251.840 | 15253.200 |
| 24.000 | 12500.000 | 12.500 | 38.900 | 160.000 | -24086.790 | 12448.000 |
| 22.000 | 13636.364 | 13.636 | 33.400 | 148.000 | -20788.440 | 9886.400 |
| 20.000 | 15000.000 | 15.000 | 28.200 | 136.000 | -17700.760 | 7670.400 |
| 18.000 | 16666.667 | 16.667 | 23.300 | 124.000 | -14833.110 | 5778.400 |
| 16.000 | 18750.000 | 18.750 | 18.700 | 112.000 | -12194.310 | 4188.800 |
| 14.000 | 21428.571 | 21.429 | 14.500 | 98.600 | -9511.710 | 2859.400 |
| 12.000 | 25000.000 | 25.000 | 10.800 | 85.200 | -7142.400 | 1840.320 |
| 10.000 | 30000.000 | 30.000 | 7.620 | 71.500 | -5054.186 | 1089.660 |
| 8.000 | 37500.000 | 37.500 | 4.930 | 57.600 | -3293.455 | 567.936 |
| 7.000 | 42857.143 | 42.857 | 3.790 | 50.500 | -2535.886 | 382.790 |
| 6.000 | 50000.000 | 50.000 | 2.790 | 43.400 | -1875.776 | 242.172 |
| 5.000 | 60000.000 | 60.000 | 1.950 | 36.200 | -1306.638 | 141.180 |
| 4.000 | 75000.000 | 75.000 | 1.250 | 29.000 | -839.438 | 72.500 |
| 3.000 | 100000.000 | 100.000 | 0.704 | 21.800 | -474.744 | 30.694 |
| 0.950 | 315789.474 | 315.789 | 0.190 | 6.100 | -37.174 | 2.318 |
| 0.900 | 333333.333 | 333.333 | 0.180 | 5.720 | -32.686 | 2.059 |
| 0.800 | 375000.000 | 375.000 | 0.160 | 4.840 | -23.400 | 1.549 |
| 0.700 | 428571.429 | 428.571 | 0.170 | 3.970 | -15.732 | 1.350 |

Fig. 43. Measured values of complex refraction index and computed values of complex relative permittivity for gold at THz frequencies.

This turned out to be the most accurate way to characterize the metal by taking into account its lossy dispersive features. The resulting behavior of gold permittivity was in good agreement with the Drude model valid for metal dispersion characterization, with plasma frequency $\omega_p = 1.18 \times 10^{16}$ rad/sec and collision frequency $\upsilon_c = 1.11 \times 10^{14}$ Hz (which are typical values for gold). Fig. 44 shows the Drude curves for both $\varepsilon'$ and $\varepsilon''$ of gold in the band $77 \div 123$ THz, corresponding to a relative bandwidth of 40% (typical of bow–tie antennas) centered around the operating frequency of 100 THz. More in detail, Drude dispersion relation describes the characteristics of media with two kinds of charge carriers: one kind (usually fixed ions in metal or slow ions in a plasma) is assumed to be stationary while the other kind (usually electrons) is allowed to move freely. Damping is obtained by elastic collisions of the moving particles with the stationary particles, described with help of the collision frequency $\upsilon_c$. Considering the specific plasma frequency $\omega_p$ the correspondent relative permittivity is given as follows (where $\varepsilon_\infty$ is the high–frequency limit of relative permittivity):

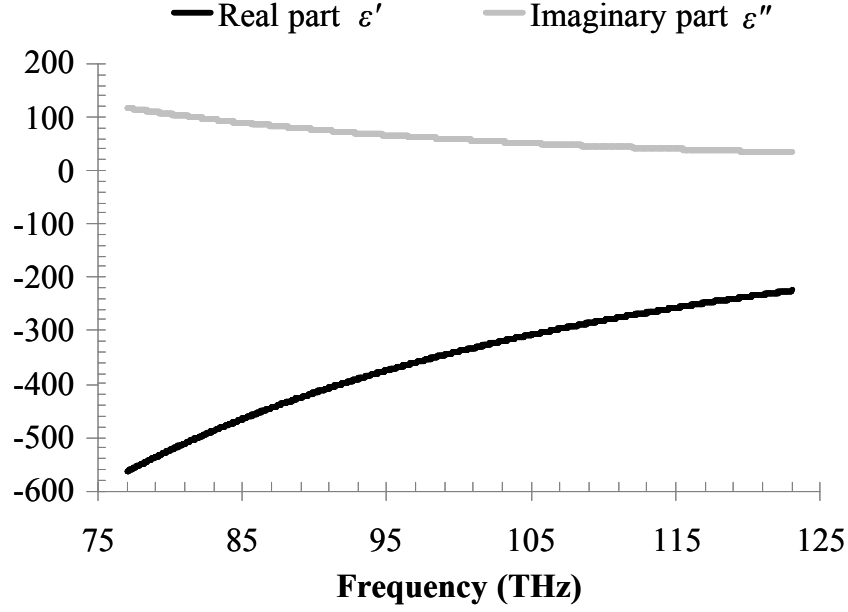$$\varepsilon_r(\omega) = \varepsilon_\infty - \frac{\omega_p^2}{\omega(\omega - j\upsilon_c)} \tag{9}$$

Fig. 44. Computed values of $\varepsilon_r$ for gold using the Drude model in the band $77 \div 123$ THz, corresponding to the 40%–relative bandwidth of a bow–tie antenna operating at 100 THz.

Finally, according to [10], the complex values of gold relative permittivity can be translated into complex values of conductivity and surface impedance as follows:

$$
\begin{aligned}
\sigma' &= \omega\varepsilon_0\varepsilon'' \\
\sigma'' &= \omega\varepsilon_0(1-\varepsilon') \\
Z_s &= (1+j)\sqrt{\frac{\omega\mu_0\mu_r}{2\sigma_c}} = (1+j)\sqrt{\frac{\omega\mu_0\mu_r}{2(\sigma'-j\sigma'')}}
\end{aligned}
\tag{10}
$$

In Eq. (10), $\varepsilon_0 = 8.854 \times 10^{-12}$ F/m is the vacuum permittivity, $\mu_0 = 4\pi \times 10^{-7}$ H/m is the vacuum permeability and $\mu_r$ is the metal relative permeability (usually set equal to 1). As will be shown in the next chapter, at THz frequencies $Z_s$ exhibits an imaginary (inductive) part greater than the resistive one which causes the afore–mentioned losses affecting the overall system performance.

First a bow–tie antenna whose monopoles are coplanar metallization printed on the $SiO_2$ substrate was designed, with the following dimensions: width W = 0.796 μm, length L = 0.675 μm and (fixed) flare angle α = 60°. With this data, the designed antenna resonates as a full–wavelength dipole according to the typical behavior of bow–ties, with an input impedance of about 400 Ω and a radiation efficiency of about 90%. As expected, the relative bandwidth has a value of approximately 35%. The most exploited solution so far is to use single antennas with printed coplanar monopoles and the MOM diodes grown between antenna arms, i.e. in the gap [11]. In the present PhD thesis, a new idea will be developed based upon the following requirements:

1. design of a geometrically–compact array, thus with closely–spaced antenna elements;
2. embedding inside the $SiO_2$ substrate: i) the block capacitances to avoid the DC component flowing back towards the antenna arms; ii) the MOM diode; iii) the DC circuitry;
3. exploitation of a multi–layer MOM diode or of a different type of THz diode (like a graphene–based one).

The latter requirements could be satisfied by implementing an antenna array with misaligned printed monopoles (i.e. on opposite sides of the substrate) and using a single (MOM) diode in the center of the array itself. This allows to always deploy the *array factor* for any angle of incidence of the solar radiation, hence to maximize the power transfer to the diode as will be explained in detail in the following. Fig. 45 shows a typical example of nano–bow–tie with printed coplanar arms and the MOM diode grown in the gap between monopoles.
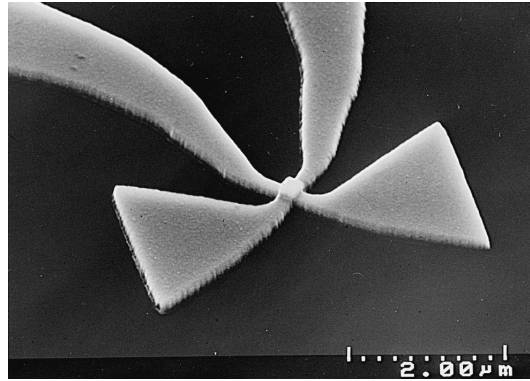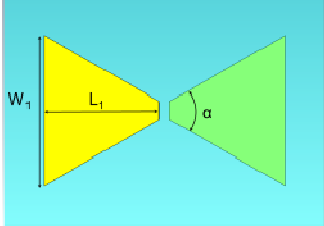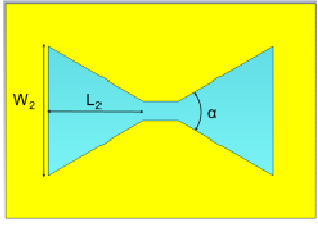


Fig. 45. Typical example of printed coplanar bow–tie nano–antenna with a MOM diode grown in the gap between monopoles.

Then, to put the new idea of misaligned printed monopoles into practice, the antenna layout had to be re–arranged by halving the $SiO_2$ thickness layer (i.e. from 200 nm to 100 nm), in order to keep the resonance frequency fixed at 100 THz. Without this change no resonance can be detected in the band of interest. Furthermore, it was observed that the same physical length corresponds to a shorter electrical length when misaligning antenna arms due to a different pattern of surface currents, which entails a higher resonance frequency.

In order to minimize the overall metallization losses and hence maximize the radiation efficiency, a further EM optimization led to a gold thickness of 60 nm. The final CAD project is shown in Table V (left side), where each monopole has width $W_1 \approx 1.15$ μm, length $L_1 = 0.875$ μm (about 30% longer than coplanar metallization), (fixed) flare angle $\alpha = 60°$ and gap between antenna arms of 0.08 μm (this will be referred to as "antenna 1"). Hence the full–wavelength dipole resonant behavior can be preserved with non–dramatic changes in the antenna input impedance and radiation efficiency values. In the left figure in Table V the $SiO_2$ substrate has been made partially transparent to bring out the monopole below.

For comparison purposes, a second solution with coplanar slots (Table V, right side) was also developed (namely "antenna 2"): in this case, a 35 nm–thick gold layer with bow–tie–shaped slots etched from the metallization was designed. The overall dimensions are: width $W_2 \approx 0.919$ μm, length $L_2 = 0.675$ μm, the same flare angle $\alpha$ as antenna 1 and gap between antenna arms of 0.25 μm. The arms gap is necessary since in an array configuration bow–ties need to be properly fed by a balanced transmission line (i.e. with specular strips on the opposite side of the substrate) if using antenna 1, and by a coplanar waveguide (CPW) if using antenna 2. Therefore, enough space is provided for connection to the feeding network. The MOM diode can be realized between the misaligned arms in the planar–strip realization, or between hot and ground metallization of the CPW.

Table V. Bow–tie antennas characteristics.

| | Bow–tie antenna | |
|---|---|---|
| | **Planar misaligned** | **Coplanar slot** |
| **Radiation Performance** |  |  |
| Directivity $D$ | $\approx 3$ dBi | $\approx 5.2$ dBi |
| Radiation efficiency $\delta$ | $\approx 93\%$ | $\approx 83\%$ |

## 3.3. OPTIMAL ARRAY DESIGN: PRELIMINARY THEORETICAL INVESTIGATION AND PROPOSED LAYOUT SOLUTIONS

The next step was the investigation of the optimal broadside planar array configuration to maximize the performance in terms of efficiency and radiation pattern. Indeed the deployment of an array allows to always exploit the array factor and, hence, maximize the power transferred to the diode through the as high as possible directivity: in fact, a *real* broadside array is made of antennas which are always fed in phase. This can be achieved only by means of a *corporate–feed* which guarantees the in–phase excitation for any angle of incidence of the EM radiation onto the array. Using singularly–excited antennas arranged in a pseudo array layout (namely "multi–element array") one can consider that the various elements give rise to an "array" only if the EM radiation impinges onto the antenna system in a direction perpendicular to the plane of the system itself. This entails a limited usage of a multi–element array, with which a comparison of the proposed nano–array will be shown.

From the uniform planar array theory, since the bi–dimensional array was designed on the xy plane, two *Array Factors* (*AFs*) need to be defined as follows:

$$AF_x = \frac{\left|\sin(nu_x)\right|}{\left|n\sin(u_x)\right|}, \quad AF_y = \frac{\left|\sin(mu_y)\right|}{\left|m\sin(u_y)\right|}$$

$$u_x = \pi \frac{L_x}{\lambda}\sin\theta\cos\phi, \quad u_y = \pi \frac{L_y}{\lambda}\sin\theta\sin\phi$$

(11)

where $m$ is the number of rows, $n$ is the number of columns, $L_x$ and $L_y$ are the element spacing along the x– and y–direction (respectively) and $(\theta,\phi)$ are the polar coordinates of the reference system in which the array is defined. Be $f_0(\theta,\phi)$ the radiation function of the single base–antenna, then the radiation function $f_{xy}(\theta,\phi)$ and the directivity $D_{xy}$ of the xy–array are, respectively:

$$f_{xy}(\theta,\phi) = f_0(\theta,\phi)\cdot AF_x \cdot AF_y$$

$$D_{xy} = 4\pi\left(\int_{4\pi} f_{xy}^{\,2}(\theta,\phi)\sin\theta\,d\theta\,d\phi\right)^{-1}$$

(12)

Starting from the theoretical (full–wavelength dipole analytical model) and simulated (antennas of Table V) radiation functions of the array element, assuming $L_x = L_y = L$, Eq. (12) was numerically evaluated in order to predict the optimum value of $L$ that maximizes the

array bi–dimensional directivity $D_{xy}$ with respect to $m$ and $n$. The latter were constrained to be ≤ 6 for layout–complexity reasons and for corporate–feed losses minimization. The chosen array topology was a 4 rows–by–2 columns matrix (this will be referred to as "solution 1") with a 0.8λ–spacing along the x and y directions. The importance of this initial investigation was confirmed by the corresponding behavior of a 2 rows–by–4 columns array with the same bi–dimensional $L$–spacing (this will be referred to as "solution 2"): Fig. 46a and Fig. 46b show the comparison between the theoretical and simulated $D_{xy}$ for solution 1 and for solution 2, respectively, as a function of the normalized wavelength $L/\lambda$. From these figures, the better performance in terms of directivity is clearly evident by choosing solution 1.
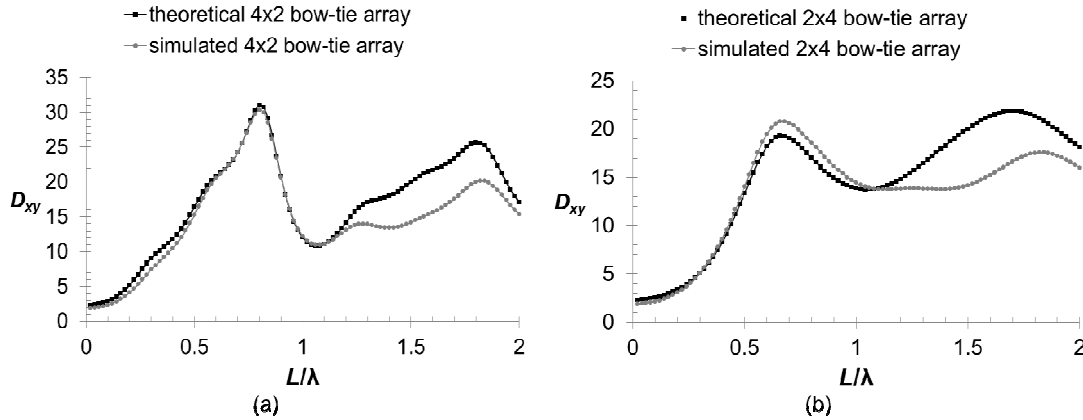


Fig. 46. Comparison between theoretical and simulated bi–dimensional directivity $D_{xy}$ (linear scale) as a function of the normalized element spacing $L/\lambda$ for (a) solution 1 and (b) solution 2.

Fig. 47a shows the layout for solution 1 together with the corporate–feed obtained by means of the balanced transmission line, with λ/4–adapters in correspondence of the 3 dB–dividers. The maximum predicted array efficiency is about 26%, with broadside radiation characteristic and the half–power beam width on the xz–plane ($\phi = 0°$) of approximately 35°. In Fig. 47b, the simulated 3D directivity (linear scale) at 100 THz is plotted. The overall broadside radiation is well preserved, with a directivity $D_{xy} \approx 27.5$ (14.4 dBi), which is very close to the value $D_{xy} \approx 30.3$ (14.8 dBi) corresponding to the maximum value numerically predicted of Fig. 46a for $L/\lambda = 0.8$. The considerable efficiency drop of the array assembly with respect to the single antenna is due to the corporate–feed losses in the THz region. Fig. 47c displays the simulated reflection coefficient $|S_{11}|$ dB normalized over the antenna array input port $Z_{port} = 65\ \Omega$ (this stems from the characteristic impedance of the designed balanced corporate–feed): a value less than −6 dB is guaranteed over the entire band of interest, which entails that more than 75% of the incident power goes into the diode. In fact, be $P_{inc}$ the incident power onto the antenna array input port and $P_r$ the reflected power at the same port, hence we have:

$$P_r = \left|S_{11}\right|^2 \cdot P_{inc} \tag{13}$$

and in Eq. (13) $|S_{11}| = -6$ dB means $|S_{11}|^2 = 0.25$.

In Fig. 47d the CST project of a 5–port corporate–feed is displayed to test the effective losses due to the gold metallization: it is apparent from Fig. 47e that in correspondence of port 2 and port 3 (where two bow–tie antennas need to be placed) the computed values of $|S_{21}|$ (green solid line) and $|S_{31}|$ (blue solid line) are about −14 dB and −13 dB at 100 THz, respectively, instead of −6 dB as should be due to the 3 dB–dividers (at port 1 and at the upper λ/4–adapter). This entails a power loss of 7–8 dB which reflects the above–mentioned efficiency drop of the entire array.
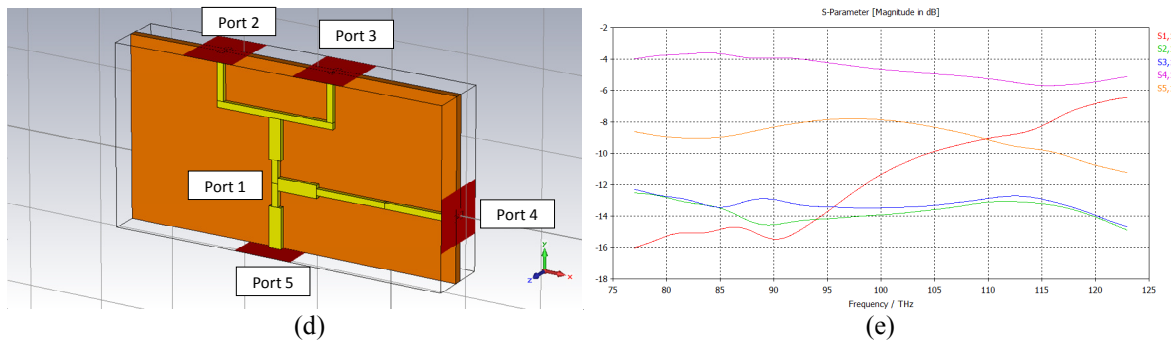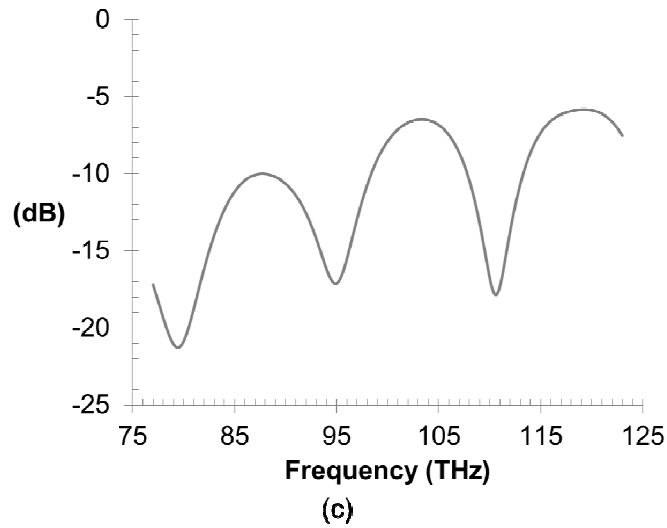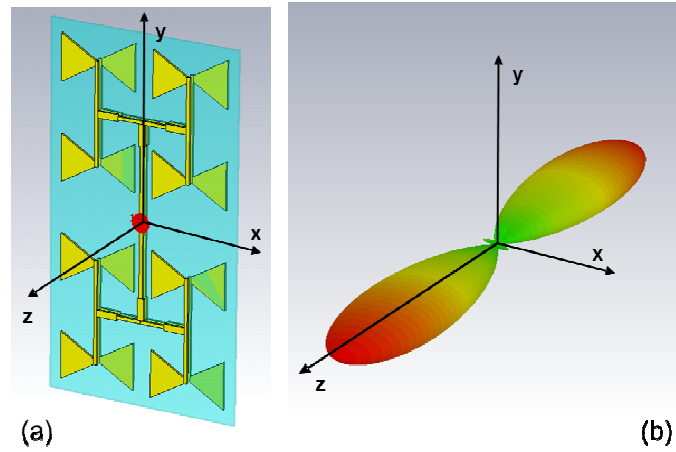
Fig. 47. (a) layout of the 4–by–2 misaligned bow–tie antenna array; (b) simulated directivity (linear scale) at 100 THz; (c) simulated reflection coefficient $|S_{11}|$ dB over the band of interest; (d) 5–port corporate–feed; (e) simulated $|S_{i1}|$ dB parameters of the 5–port corporate–feed (i = 1,2,3,4,5).

The total number of antenna elements used for the array design was set to be equal to 8 essentially for three reasons:

1. the more the number of array elements, the higher the bi–dimensional directivity $D_{xy}$;
2. an *even* number of array elements allows to design a geometrically–symmetric corporate–feed that guarantees an equal power partitioning among the various antennas;
3. the radiation efficiency is strongly influenced by the presence of long gold traces which introduce further losses in the signal propagation to/from the antennas.

Hence a trade–off among all the afore–mentioned requirements was reached to achieve the best overall performance of the array.

68

Fig. 48a and Fig. 48b show the layout topology and the simulated directivity of solution 2. In this case, the maximum predicted array efficiency is about 20%, with broadside radiation characteristic and the half–power beam width on the xz–plane ($\phi = 0°$) of approximately 16°. Again, the computed value for $D_{xy}$ is about 18.8 (12.7 dBi), hence it is almost identical to the value $D_{xy} \approx 18.7$ apparent in Fig. 46b for $L/\lambda = 0.8$.



(a)                    (b)
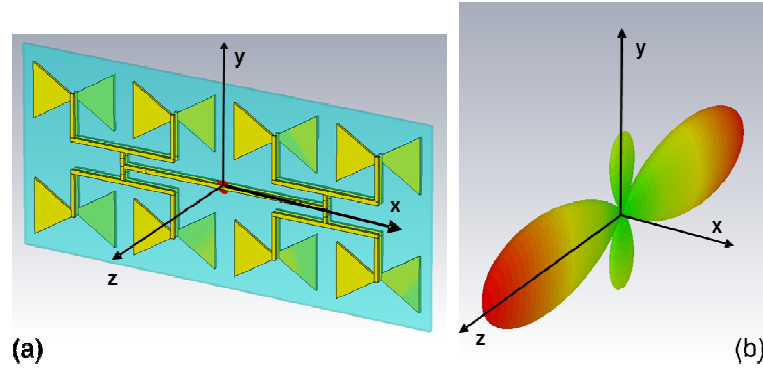
Fig. 48.  (a) 2–by–4 misaligned bow–tie antenna array; (b) simulated directivity (linear scale) at 100 THz.

The red dot in Fig. 47a and in Fig. 48a corresponds to the feed port used to excite the array: from a technological point of view, this is the exact point where the diode is placed. Hence in order to avoid mismatch phenomena and, thus, maximize the DC rectified power $P_{DC}$, the zero–bias differential resistance $R_{D0}$ of the diode must be equal to $Z_{port}$ (as will be explained in detail in the following).

The simulations of the IR arrays confirm the better radiation performance offered by solution 1 in terms of directivity, as predicted by the numerical evaluation of Eq. (12). For further investigation purposes, a 4x2 coplanar slot bow–tie array (which will be referred to as "solution 3") with a CPW corporate–feed was also designed, for a twofold purpose: i) to test if the better behavior of CPWs, with respect to losses, than their parallel–strip counterpart would be confirmed in the THz region; ii) to properly feed the slot antennas with a correctly–polarized electric field, based on the duality between the coplanar slot and coplanar printed bow–tie antennas (according to Babinet's principle). The final layout for solution 3 is shown in Fig. 49a, where the various ground layers have been joined by means of curved PEC bridges in correspondence of the excitation port (located by the red dot). The main shortcomings affecting this solution are:

1. at THz frequencies the feeding slots strongly contribute to the overall array radiation;
2. CPW 3 dB–dividers have to be used with parsimony for the same reason;
3. as a consequence in presence of a CPW corporate–feed Eq. (12) cannot be applied for maximum directivity prediction, as before.

As an alternative a "tree" topology for the slotted array was chosen: the spacing along the y–direction was established by the in–phase elements array condition (1.69 μm in the present case), whereas the x–spacing was chosen equal to 1.8 μm to avoid antenna arms overlapping. For the above–mentioned reasons, the computed efficiency is 24% (which is still a good result) but a 9–dBi maximum directivity (Fig. 49b) was computed with a less regular radiation surface than previous solutions.

A two–parallel line feed network, i.e. the dual of the slotted topology presented so far, could be deployed as substitute of the proposed solution and would be worth being investigated by further simulations.
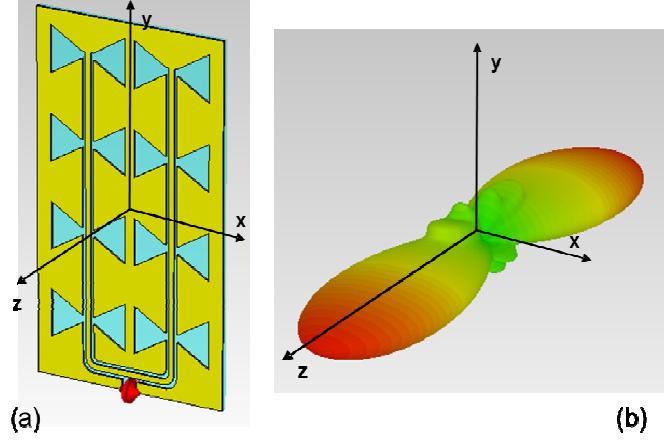
Fig. 49. (a) 4–by–2 coplanar slot bow–tie antenna array; (b) simulated directivity (linear scale) at 100 THz.

Finally, a rectenna topology was also considered for comparison with solution 1: the same 4x2 geometry was adopted in a multi–element structure, without corporate–feed and with eight ports (each of those in correspondence of the single bow–tie antenna port) and therefore with eight diodes for rectification ("solution 4"). Table VI summarizes the geometrical characteristics of all the considered antenna array topologies.

Table VI.  Geometrical characteristics of the various antenna array topologies.

| Solution | # of rows | # of columns | Technology | Corporate–feed |
|---|---|---|---|---|
| 1 (Fig. 47a) | 4 | 2 | Printed misaligned monopoles | Yes (balanced) |
| 2 (Fig. 48a) | 2 | 4 | Printed misaligned monopoles | Yes (balanced) |
| 3 (Fig. 49a) | 4 | 2 | Slot | Yes (CPW) |
| 4 | 4 | 2 | Printed misaligned monopoles | No |

The best conversion efficiency of the harvesting system should be achieved by choosing two different metals for misaligned antenna arms. In fact, the rectification properties of MOM diodes can be improved by resorting to an asymmetric structure to augment the diode potential barrier. This entails that antenna metallization, with which the diode electrodes are in contact, should be made of the same different materials as the diode metallic layers. However, this has no significant influence on array performance.

## 3.4.  MOM DIODE OVERVIEW

The device used to rectify the THz incident power is a Metal–Oxide–Metal (MOM) tunnel diode [11]. The most relevant parameters of such a diode are the average potential barrier height $\phi_0$, the barrier asymmetry factor $\alpha$, the junction area $A$ and the barrier (i.e. oxide) thickness (or channel length) $L$. According to *quantum mechanics*, be $E$ the energy of an electron $e$ impinging on metal 1 in the direction perpendicular to the barrier, then applying a voltage $V$ across the junction the tunneling probability $P_e(E,V)$ of the electron to pass through

the potential barrier of thickness $L$ and heights $\phi_1$ and $\phi_2$ (on the two sides of the barrier itself) is given by the WKB (= Wentzel–Kramers–Brillouin) approximation:

$$P_e(E,V) \propto \exp(-L) \tag{14}$$

According to [12], the oxide thickness $L$ must not be less than 2.27 Å as to not invalidate the WKB approximation. On the other hand, increasing $L$ reduces the tunneling probability and increases $R_D$, so that $L$ should never exceeds a few tens of Ångstrom.

Fig. 50 displays the schematic view of the energetic structure of a MOM diode: $E_F$ is the Fermi energy and "Metaloxide" is the potential barrier (which is very often made of metal oxide, like NiO).
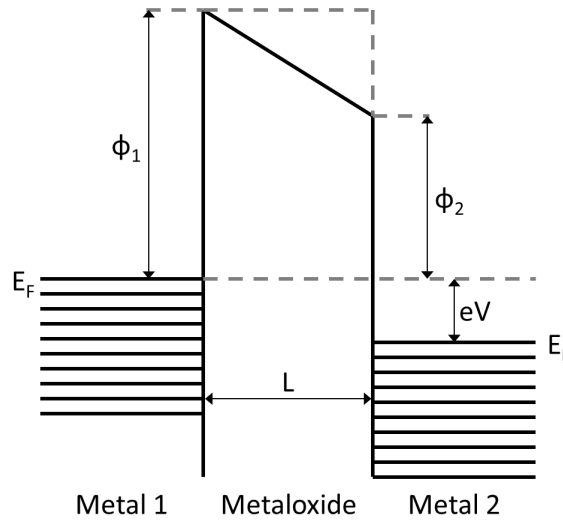


Fig. 50. Schematic view of the energetic structure of a MOM diode.

More in detail, the thin oxide layer between the two electrodes represents a potential barrier that, in a first–order approximation, is described by a rectangle function. The symmetry of a structure with two similar electrodes that possess the same Fermi level is distorted by applying a bias voltage $V$ on the contact. This gives rise to the diode characteristic of the MOM structure. Various effects contribute to the detection and mixing mechanisms in MOM diodes. The different electrical–conduction processes exhibit distinct properties and characteristic times. In most cases, several additive conduction mechanisms are active simultaneously. Therefore, it is difficult to decide which is predominant. For example, absorption of radiation increases the temperature of the MOM diode. Thermally excited electrons can therefore be emitted above the potential barrier. In the case of thin–film MOM diodes, absorption of the incoming radiation also occurs in the substrate. The thermal contribution is important for these devices, so that the heating of the diode is mainly caused by absorption of infrared radiation in the substrate and by dissipation of antenna currents. In the following only the conduction mechanisms will be considered.

According to Eq. (14), electrons in metals can tunnel through a high barrier with a probability which falls exponentially with its thickness. A first theoretical analysis was performed by Simmons and yielded an expression for the tunnel current as a function of the barrier height, its thickness and the oxide permittivity. In that calculation, the deformation of the rectangular potential barrier by image forces was taken into account. The tunneling effect is nonlinear and permits rectification and mixing of the infrared radiation coupled by the antenna to the diode. The theoretical calculation of the tunneling time remains an unsolved

71

problem: several different approaches were tried without success. Estimation of the tunneling time yields values in the range from $10^{-15}$ to $10^{-16}$ sec. In the visible range, photo–assisted tunneling seems to play an important role in the detection and mixing mechanism because the photo–energy gained by electrons is in the range of the barrier height of 1 to 2 eV. At infrared frequencies near 30 THz, however, this effect is negligible compared to field–assisted tunneling.

Let us now define the differential nonlinear resistance $R_D(V)$, where $V$ is the voltage across the junction, and the junction capacitance $C_J$. The simple equivalent circuit of the diode is set to be $R_D(V)$ in parallel with $C_J$ (as shown in Fig. 51, where $R_A$ is the antenna resistance). The I–V characteristic of the diode is given by the following series expansion up to the third order [12], according to the Stratton–Simmons model under the assumptions of no thermionic emission (hence barrier at 0 K) and trapezoidal potential barrier (which makes the tunneling of electrons possible even if the diode is unbiased):

$$I(V) = \frac{1}{R_{D0}}\left(V + mV^2 + nV^3\right)$$

$$R_D(V) = \left(\frac{dI}{dV}\right)^{-1} \qquad (15)$$

$$C_J = \frac{\varepsilon_0 \varepsilon_r A}{L}$$

where $m = m(\alpha, L, \phi_0)$, $n = n(L, \phi_0)$ and $R_{D0} = R_D(0)$ is the zero–bias differential resistance. The larger the coefficient $m$, the better the rectification properties of the diode, since the even–order harmonics contribute to the DC component as in any nonlinear device. This can be accomplished by increasing the value of the asymmetry factor $\alpha$: as it was demonstrated in [13] (where a "brute–force" approach allowed to fit experimental data to the BDR – Brinkman–Dynes–Rowell – theoretical model of MIM diodes), the exploitation of different metallization for the diode electrodes entails a trapezoidal potential barrier, which makes the tunneling of electrons possible even if the diode in unbiased. Moreover, the contact area $A$ has a predominant role on the value of $C_J$ (considering the junction as a small parallel–plate capacitor).
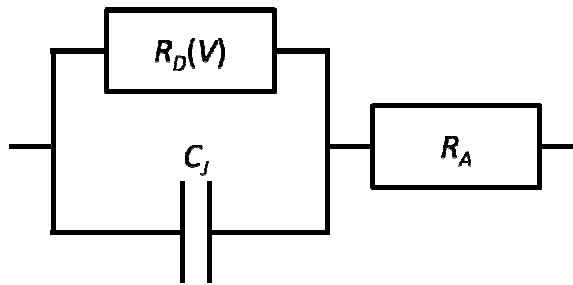


Fig. 51. Circuit schematic of an antenna–MOM diode system.

The cut–off frequency $f_{cut}$ of the diode at the operating (angular) frequency $\omega_{op}$ is defined a follows [12]:

$$f_{cut} = \frac{1}{\omega_{op} R_A C_J} \qquad (16)$$

In Eq. (16), $\omega_{op}$ is the operating (angular) frequency. The diode must operate below the cut–off frequency to have good rectification performance, which requires $f_{cut} > 100$ THz and, consequently, $C_J$ equal to some aF. A commonly adopted solution is the Ni–NiO–Ni MOM diode due to its fast response time in mid–infrared measurements. In such a diode both metallization are made of nickel and the tunnel junction is a nickel–oxide layer. As reported in [14,15], the Ni–NiO–Ni MOM diode has a weak nonlinear $I$–$V$ characteristic since $\alpha = 0.09$. Furthermore, in [15] the diode under test has $R_{D0} \approx 4600$ $\Omega$ and $C_J \approx 347$ aF. According to the theory presented in [12], such values do not provide a good impedance matching to the antenna input resistance, nor an optimal conversion efficiency below the cut–off frequency. On the contrary, in [16] a turn–on voltage $V_T$ of about 70 mV was defined as the transition point from a linear to a nonlinear behavior of the $I$–$V$ characteristic, thanks to the asymmetric structure of the diode, whose electrodes are made of nickel and gold. The greatest shortcoming of using MOM diodes is represented by their low conversion efficiency $\eta$, which can be even less than 0.1% in the far IR region [15]. In the following, a theoretical investigation on the rectification potentialities of MOM diodes will be carried out and a new model will be proposed, which could overcome the intrinsic limitations of conventional models and be thus more suitable for THz energy–harvesting system application.

## 3.5.  MOM DIODE CUSTOMIZED DESIGN

In order to deal with a realistic MOM diode model, a trade–off among the above–mentioned constraints has been reached, so that $R_{D0} \approx R_A \approx 65$ $\Omega$. The resulting optimized values for the MOM diode are listed in Table VII. These values were then exploited in a customized nonlinear simulation tool to predict the conversion capabilities of the whole harvester.

Table VII.  MOM diode customized characteristics.

| Parameter | $m$ (V$^{-1}$) | $n$ (V$^{-2}$) | $A$ (µm$^2$) | $L$ (Å) | $R_{D0}$ ($\Omega$) | $C_J$ (aF) |
|---|---|---|---|---|---|---|
| Value | 4 | 5 | 0.0001 | 20 | $\approx 65$ | $\approx 1.43$ |

The values chosen for $R_{D0}$, $A$ and $L$ allowed the following requirements to be simultaneously satisfied:

1. optimum impedance–matching to the antenna input resistance without the need of an *ad hoc* matching network, which would require a further technological complexity;
2. cut–off frequency well above the operating frequency (i.e. 100 THz), according to Eq. (16) from which it can be inferred that $R_A$ must not exceed 100 $\Omega$ to have the requested $f_{cut}$ at the desired operating (angular) frequency $\omega_{op}$.

The values of $m$ and $n$ resulted from an optimization process, which led to an alternative $I$–$V$ curve for the MOM diode, with a stronger nonlinearity than previously devices. First the typical values for tunneling barrier heights were investigated, taking into account some of the most exploited metals for diode electrodes: nickel (Ni), gold (Au) and aluminum (Al). Let the barrier height in eV be denoted by $\phi_x$ in a generic case (the subscript $x$ denotes the generic metal), then we have $\phi_{Ni} \approx 0.2$ eV [15], $\phi_{Au} \approx 4.2$ eV and $\phi_{Al} \approx 2.8$ eV [17]. For example, considering a Ni–NiO–Au diode [16], we have $\phi_0 = (\phi_{Ni}+\phi_{Au})/2 = 2.2$ eV and $\alpha = 0.9$. In the optimization process, $m$ and $n$ must undergo upper constraints (4 and 28, respectively), in order to obtain feasible DC characteristics and rectification performance. In Fig. 52 the $I$–$V$ characteristic of the optimum MOM diode, with $m = 4$ and $n = 5$, is shown. In agreement with [16], the target of the optimization was the research for a very nonlinear behavior by assuming that the electrodes are made of different metallization, so as to provide the afore–

mentioned values for *m* and *n*. In particular, from the Stratton–Simmons model we have, according to Fig. 50:

$\phi_1 \approx 4.71$ eV
$\phi_2 \approx -2.96$ eV
$\phi_0 = (\phi_1 + \phi_2)/2 \approx 0.88$
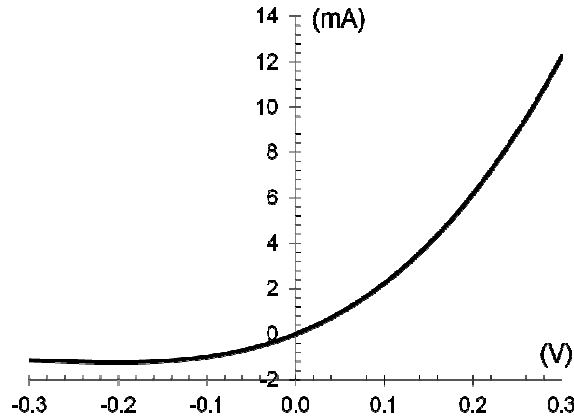$\alpha \approx 4.38$



Fig. 52. *I–V* characteristic of the optimum MOM diode with *m* = 4 and *n* = 5.

The proposed *I–V* characteristic shows very high values of the current in correspondence of the maximum available voltage (more than 12 mA), even if a value of 1 mA at 150 mV is reported in [14]. In fact, the typical MOM diode represents the real bottleneck of the overall system design, since it suffers from some intrinsic technological drawbacks, listed in the following:

1. weakly nonlinear behavior in the *I–V* characteristic which is apparent in all the state–of–the–art devices designed and measured so far;
2. the current has no exponential dependence on voltage such as in Schottky barriers;
3. high values of $f_{cut}$ require very small values of $C_J$, hence small values of the contact area *A* and/or high values of the channel length *L*;
4. according to Eqs. (14) and (15), increasing *L* reduces the tunneling probability and at the same time increases $R_D$;
5. as shown in Fig. 52 the voltage across the diode cannot exceed 300 mV to avoid the junction burnout [12].

The latter drawbacks can be partially tackled by properly designing the diode in order to achieve the following requirements, which led to the customized model proposed above:

1. augmentation of the asymmetry of the potential barrier by using different metals for the electrodes, which means to increase $\alpha$;
2. MIMIMIM stack [11], i.e. a multilayer diode, to enhance its nonlinearity and asymmetry characteristics (at the expense of bigger difficulties and higher costs in the manufacturing process);
3. trade–off between *A* and *L* to guarantee as small as possible values of both $C_J$ and $R_D$.

The curve in Fig. 52 represents a first attempt to overcome the constraints exhibited by MOM diodes, provided that the necessary technology shall be feasible in order to obtain the desired *I–V* characteristic.

74

## 3.6. PREDICTION OF THE EFFECTIVE PERFORMANCE OF THE PROPOSED IR– HARVESTER BY MEANS OF A RIGOROUS NONLINEAR/EM APPROACH

The overall performance of the entire harvesting system was predicted by using the Reciprocity Theorem [4] to calculate the Norton current sources equivalent to the (solar) electric field incident onto the bow–tie receiving system. It has to be stressed that, for the first time, a *quantitative* approach to predict the effective performance of an IR solar harvester was attempted, since in the literature scientific research focuses on the optimization of the single antenna–diode system neglecting the realistic levels of rectified power when exploiting the IR solar radiation. The application of the Reciprocity Theorem was done under the following prerequisites:

1. sun in the far–field region of the antenna system. This is sufficient to apply the theorem even if the antenna system is *not* in the far–field region of the sun;
2. *local* plane wave approximation. The spherical waves radiated by the sun can be approximated by means of plane waves when impinging onto the harvester;
3. by using Eq. (7) the real *emitting power* $E^{real}_{2.44,3.89}$ (subscript wavelengths are in μm) in the band of interest, i.e. $77 \div 123$ THz, was computed to be about 22 W/m$^2$. Multiplying $E^{real}_{2.44,3.89}$ by the area occupied by the bow–tie antenna array, the total power impinging onto the single harvester is $P_{inc} \approx 500$ pW.

Be $J_{solar,eq}$ the Norton current source equivalent to the incident solar electric field and $P_{av}$ the available power calculated from $P_{inc}$ by taking into account the array radiation efficiency $\delta$, so that $P_{av} = P_{inc} \cdot \delta$, then we have:

$J_{solar,eq} \approx 3$ μA for solution 1, $J_{solar,eq} \approx 826$ nA for solution 4
$P_{av} \approx 121$ pW for solution 1, $P_{av} \approx 25$ pW for solution 4

This approach led to one generator for solution 1 and eight generators for solution 4. In the latter case, eight MOM diodes were connected in series in order to sum all the DC power contributions coming from the multi–rectenna system. Two optimum values for the load resistance $R_L$ were obtained in the two cases, namely about 65 Ω (array with corporate–feed) and 2,900 Ω (multi–element system). Fig. 53 shows the circuit schematics for the two proposed solutions.
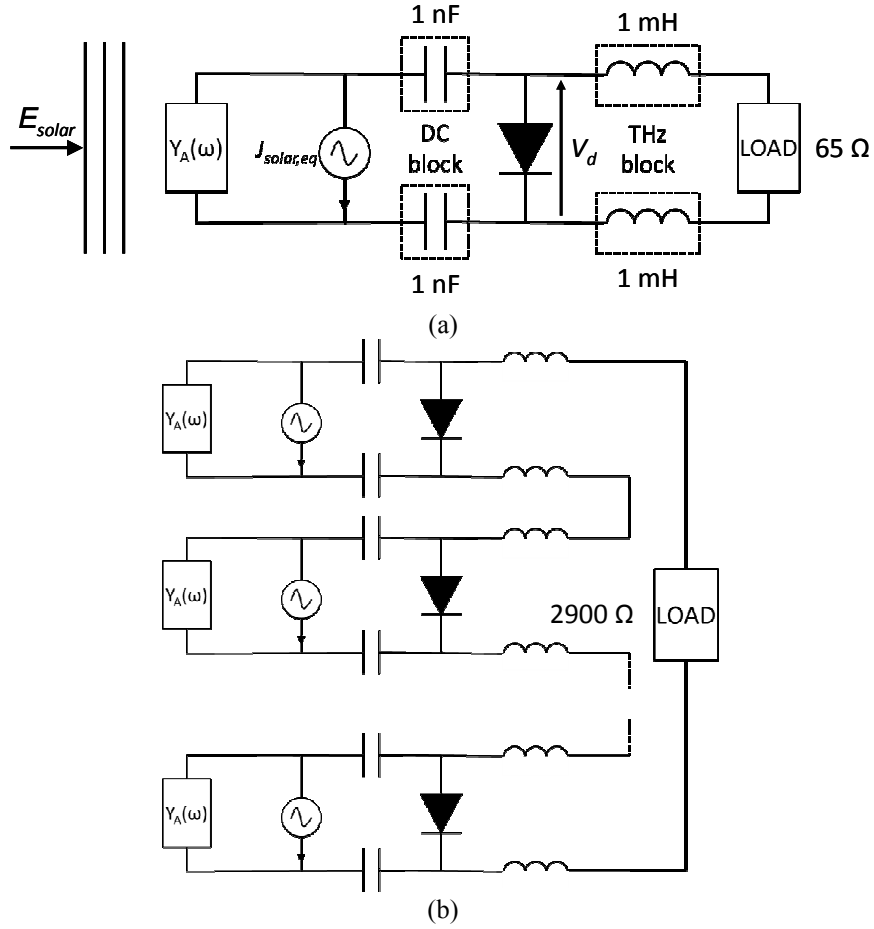
Fig. 53. Circuit schematics of the entire harvesters designed for (a) solution 1 and (b) solution 4. $Y_A(\omega)$ is the admittance matrix of the antenna array/single bow–tie, respectively.

In order to rigorously compute the resulting THz–DC conversion efficiency $\eta$, an HB analysis was carried out by means of a *customized* nonlinear simulation tool taking into account 3 harmonics. For the array case, $\eta$ is displayed in Fig. 54 as a function of the (incident) available power $P_{av}$. It is well–known that $\eta$ is defined as follows:

$$\eta = \frac{P_{DC}}{P_{av}} \tag{17}$$

The maximum value for $P_{av}$ was set equal to 0.7 mW since it corresponds to the maximum admissible voltage across the diode (i.e. 300 mV). The effective value for $\eta$ corresponding to the realistic value of 121 pW for $P_{av}$ is less than 0.1% due to the fact that the diode works around the origin of the *I–V* characteristics shown in Fig. 52.
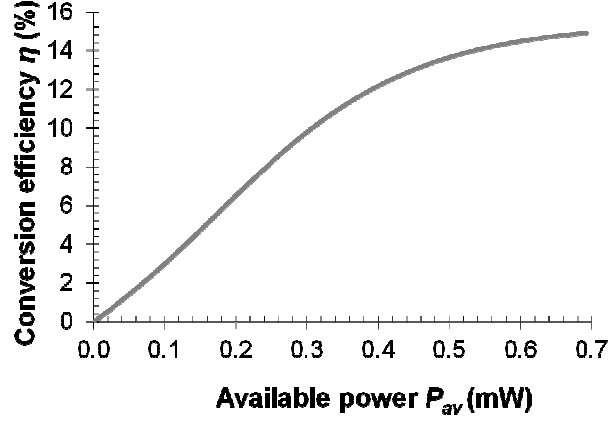
Fig. 54. Conversion efficiency $\eta$ (%) of the proposed array with corporate–feed (solution 1). The maximum predicted value for $\eta$ is about 15%.

Similar results were obtained for solution 4 because the advantage of highly–directive array behavior is lost due to THz corporate–feed losses.

In order to exploit the proposed THz harvester in a suitable wearable system, it was supposed to design a macro–system made of 1,230,000 arrays or multi–element systems arranged on an area of 1 cm$^2$, with a λ–spacing along the x– and y–direction to avoid EM interferences (the procedure could be iterated by combining various macro–systems with an even bigger area occupation, e.g. 1 dm$^2$). In these cases by setting $E_{2.44,3.89}^{real} \approx 22$ W/m$^2$ the following values for the total available power and for rectified power were obtained:

$P_{av} \approx 148$ μW, $P_{DC} \approx 5$ pW for solution 1
$P_{av} \approx 246$ μW, $P_{DC} \approx 7$ pW for solution 4

The latter results are very similar, since the highly–directive array behavior (solution 1) is damaged by the corporate–feed losses at THz frequencies as already stated above. However, very low values of $\eta$ pertain to these examples, due to the very weakly nonlinear behavior of the I–V characteristics for the available incident power level.

In conclusion, in spite of the MOM optimization process, poor rectification properties have to be taken into account for potential solar energy–harvesting applications. Hence the same design procedure could be much more profitably exploited by using a dedicated IR power source. Therefore, the proposed energy–harvester design can be conveniently adopted in embedded system applications with a dedicated IR source [15], e.g. an infrared laser with a beam section of 1 cm$^2$. For this purpose Fig. 55 shows the predicted $P_{DC}$ as a function of $P_{av}$ up to 100 mW for the macro–system made of 1,230,000 arrays (solution 1).
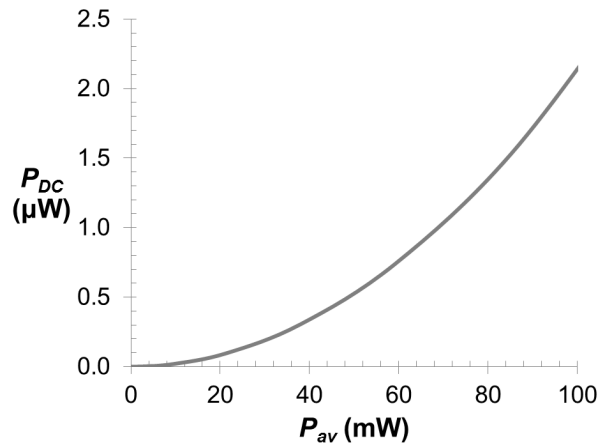
Fig. 55. Rectified power $P_{DC}$ as a function of the available power $P_{av}$ for a macro–array system arranged on 1 cm$^2$.


CONCLUSIONS

Environmental issues have become very important in these last years due to a pervasive pollution, which has spurred scientists to search for alternative energetic solutions. A largely–exploited technology is the photovoltaic one which suffers from some intrinsic limitations in spite of its maturity. Nevertheless solar radiation is an important source of "clean" energy that can be deployed in different ways to achieve the development of new low–consumption electronic devices. For the latter reason, a new solar harvester has been proposed thinking of a new family of miniaturized wireless systems able to work as power suppliers for wearable devices.

Goal of the presented research was the prediction of the *realistic* rectification capabilities offered by such IR harvesters by means of a rigorous nonlinear/EM approach. Even if the sun power density on earth is about 1,000 W/m$^2$ at ground level, it has to be stressed that it comprises the IR, the visible and the UV spectra, among which the first (IR) represents about the 40% of the total power emitted by the sun and neglected by conventional solar panels. A preliminary research on bow–tie antenna arrays has led to the optimal solution able to guarantee a high directivity and an acceptable value of radiation efficiency in spite of the unavoidable losses characterizing all metals at THz frequencies. Then, a customized model of a MOM diode was presented to emphasize its nonlinear characteristics and hence offer better rectification properties. The nonlinear simulation of the whole THz receiver was finally carried out by means of a customized tool: the results have shown that such an IR harvester has effectively low–rectification capabilities due to the low–level input power to the single nano–array. A possible countermeasure could be represented by the exploitation of several nano–harvester arranged in a certain desired area in order to augment the total rectified power. Furthermore, by using as a source a dedicated IR laser with appropriate emitted power and beam section, better performance could be reached for an off–the–shelf application.

Possible research future comprises:

1. conducting materials with low losses at THz frequencies;
2. MOM diodes with better rectification properties and higher values of the conversion efficiency;
3. usage of grahene devices (as will be shown in the next chapter);
4. search for alternative energy sources able to exploit the proposed technology with higher levels of the input power, like IR radiation at 31 THz emitted by the human

body.

In conclusions, the results presented so far aim at representing a starting point to stimulate new research in the field of "clean" energy deployment, even if the nowadays available technology has not yet reached a good maturity to offer satisfying performance of diodes with cut–off frequency in the THz frequency band and of low–cost superconducting materials to exploit as metallization for antenna design.

REFERENCES

[1] A. M. A. Sabaawi, C. C. Tsimenidis, B. S. Sharif, "Analysis and Modeling of Infra–Red Solar Rectennas", in press.

[2] A. M. A. Sabaawi, C. C. Tsimenidis, B. S. Sharif, "Bow–Tie Nano–Array Rectenna: Design and Optimization", *Proc. of EUCAP 2012*, pp. 1975–1978.

[3] M. Bareiβ et al., "Energy Harvesting using Nano Antenna Array", *Proc. of the 11th IEEE Int. Conf. on Nanotech. 2011*, pp. 218–221.

[4] A. Costanzo, A. Romani, D. Masotti, N. Arbizzani, V. Rizzoli, "RF–baseband co–design of switching receivers for multiband microwave energy harvesting", *Elsevier Journal on Sensors and Actuators A: Physical*, Vol. 179, No. 1, pp. 158–168, March 2012.

[5] M. Midrio, M. Romagnoli, S. Boscolo, C. De Angelis, A. Locatelli. D. Modotto, A.–D. Capobianco, "Flared monopole antennas for 10–μm radiation", *IEEE J. Quantum Elect.*, Vol. 47, No. 1, pp. 84–91, January 2011.

[6] W. Y.–Ming, L. L.–Wei, L. Bo, "Geometric effects in designing bow–tie nanoantenna for optical resonance investigation", *2010 APEMC*, pp. 1108–1111, 2010, Beijing, China, April 12–16.

[7] H. E. D. Palik, Handbook of Optical Constants of Solids, Vol. 1.

[8] CST Microwave Studio 2012, www.cst.com.

[9] M. A. Ordal, L. L. Long, R. J. Bell, S. E. Bell, R. R. Bell, R. W. Alexander Jr., and C. A. Ward, "Optical properties of the metals Al, Co, Cu, Au, Fe, Pb, Ni, Pd, Pt, Ag, Ti, and W in the infrared and far infrared", *Appl. Opt.*, Vol. 22, No. 7, pp. 1099–1120, 1 April 1983.

[10] Y. Poo, R. Wu, X. Fan, J. Q. Xiao, B. Jin, "An Experiment Study of Gold Nano–film's Conductivity at Microwave and Terahertz Frequencies", *Proc. of APMC 2010*, pp. 1452–1454.

[11] US Patent 6,534,784 B2, March 18, 2003.

[12] A. Sanchez, C. F. Davis, K. C. Liu, and A. Javan, "The MOM tunneling diode: theoretical estimate of its performance at microwave and infrared frequencies", *J. Appl. Phys.*, Vol. 49, No. 10, pp. 5270–5277, October 1978.

[13] E. N. Grossman, T. E. Harvey, and C. D. Reintsema, "Controlled barrier modification in Nb/NbOx/Ag metal insulator metal tunnel diodes", *J. Appl. Phys.*, Vol. 91. No. 12, pp. 10134–10139, June 2002.

[14] P. C. D. Hobbs, R. B. Laibowitz, and F. R. Libsch, "Ni–NiO–Ni tunnel junction for terahertz and infrared detection", *Applied Optics*, Vol. 44, No. 32, pp. 6813–6822, November 2005.

[15] P. C. D. Hobbs, R. B. Laibowitz, F. R. Libsch, N. C. LaBianca, and P. P. Chiniwalla, "Efficient waveguide–integrated tunnel junction detectors at 1.6 μm", *Optics Express*, Vol. 15, No. 25, pp. 16376–16389, December 2007.

[16] A. B. Hoofring and V. J. Kapoor, "Submicron nickeloxidegold tunnel diode detectors for rectennas", *J. Appl. Phys.*, Vol. 66. No. 1, pp. 429–437, July 1989.

[17] M. Bareiβ et al., "Nano antenna array for terahertz detection", *IEEE Trans. Microw. Theory Techn.*, Vol. 59, No. 10, October 2011.

# CHAPTER 4

## GRAPHENE–BASED TECHNOLOGY FOR REVOLUTIONARY APPLICATIONS AT MICROWAVE AND THZ FREQUENCIES

Graphene is in reason considered as the "silicon of the 21$^{st}$ century" for its unusual physical properties at MW and THz frequencies, together with the possibility of exploiting it in many engineering systems. In the field of materials science and condensed–matter physics, this two–dimensional (2D) material exhibits incredibly high crystal and electronic quality and is a promising candidate for new interesting applications. Due to its unique electronic spectrum, graphene can give rise to a conceptually new class of materials that are only one atom–thick and, hence, offer new inroads into low–dimensional physics.

Provided that the nowadays technology for MOM diodes presented in Chapter 3 does not exhibit a sufficient maturity to be profitably deployed in the THz band, during the third year of my PhD course I have been spending a research period of six months at the MIMOMEMS group of National Institute for Research in Microtechnologies – IMT – in Bucharest (RO) under the supervision of Prof. Mircea Dragoman. The main purpose of the collaboration between my research group in Bologna and the MIMOMEMS one was the investigation of new graphene–based technologies for THz applications, included energy–harvesting ones. In particular, owing to the manufacturing skills and facilities of the MIMOMEMS group, it was commonly agreed that the scientific activity during my stage would concern the development and characterization of graphene diodes at MW and THz frequencies.

First I received a basic training regarding micro– and nano–fabrication of electronic devices and characterization measurements.

At the beginning of my stay at IMT, I was involved in the design of a graphene patch antenna operating at 10 GHz and fed by a gold coplanar waveguide, with and without ground plane. By using a commercial 3D EM simulator (CST MWS®), I studied extensively the radiation properties of even and odd modes: this led to interesting results taking into account the unique properties of graphene at MW frequencies.

Then I designed three gold dipole antennas at 10, 20 and 30 GHz suspended over a graphene layer acting as a reflector. The research demonstrated that graphene behaves as a natural HIS (= High Impedance Substrate), thus allowing to put a dipole at a very close distance from the graphene reflector by keeping very good performance in terms of both radiation and matching properties with respect to classic metal reflectors, even in the presence of a thin low–loss dielectric substrate between the antenna and the ground plane. The results of the aforementioned research led to a paper (in which I am the first author) already published online in *Journal of Applied Physics*.

Finally I investigated antennas and diodes working in the THz frequency band, i.e. in the 0.3 ÷ 30 THz range. The research was very stimulating, since it relied upon the peculiar characteristics of graphene as a 2D material whose surface impedance changes dramatically according to the considered frequency band and the applied bias voltage. Moreover, the unique characteristics of metals (in this case, gold) in the THz range were considered to properly simulate the radiators by using the most accurate models for all materials inside CST MWS® (as already done for the IR harvester presented in Chapter 3). Interesting results were obtained, demonstrating that in the THz range graphene acts as a 2D material with highly–reactive (inductive) surface impedance, thus leading to a different design layout with respect to the MW range. Finally, a ballistic graphene diode (already characterized by IMT laboratories) was introduced in the project to predict the detection/rectification capabilities of the designed THz antennas with the above mentioned graphene diode. For this purpose, the

customized nonlinear simulator developed by my research group at DEI was exploited to carry out rigorous nonlinear simulations. The latter led to interesting results of the designed device in the THz range even in presence of low–power input signals. These results were used for the draft of a paper already published online in *Journal of Applied Physics*. Aim of the present chapter is the demonstration of the capabilities of graphene to act as a unique material for both enhanced linear (antennas) and nonlinear (diodes/transistors) applications in the MW range and in the field of imaging/harvesting techniques at THz frequencies.

## 4.1. GRAPHENE, A MATERIAL THAT SHOULD NOT EXIST: OVERVIEW OF ITS MAIN PHYSICAL PROPERTIES

Graphene is a flat monolayer of carbon atoms tightly packed into a two–dimensional (2D) honeycomb lattice and is a basic building block for graphitic materials of all other dimensionalities. It can be wrapped up into 0D fullerenes, rolled into 1D nano–tubes or stacked into 3D graphite. Graphene (or "2D graphite") has been theoretically studied for almost seventy years and is widely used for describing properties of several carbon–based materials. About thirty years ago it was realized that graphene provides an excellent condensed–matter analogue of (2+1)–dimensional Quantum Electro–Dynamics (QED), too. Nevertheless graphene was supposed not to exist in the free state and, hence, was described as an "academic" material (in fact, almost eighty years ago Landau and Peierls argued that strictly 2D crystals were thermodynamically unstable and could not exist) and was believed to be unstable with respect to the formation of curved structures such as soot, fullerenes and nano–tubes. A turning point was about ten years ago, when free–standing graphene was unexpectedly found and the subsequent experiments confirmed that its charge carriers were mass–less Dirac fermions. In graphene, charge carriers can travel thousands of inter–atomic distances without scattering (ballistic regime); furthermore, the strong inter–atomic bonds ensure that thermal fluctuations cannot lead to the generation of dislocations or other crystal defects even at elevated temperature [1].

From a physical point of view, graphene is a 2D crystal consisting of a single atomic plane, whose electronic structure approaches at ten layers the 3D limit of graphite. Moreover, (bilayer) graphene is a zero–gap semiconductor with one type of electron and one type of hole, but electronic spectra become even more complicated with three or more layers. Fig. 56 shows the graphene in the upper part and, in the lower one, other carbon materials that can be obtained from graphene by "geometrical manipulation" of its honeycomb lattice structure.
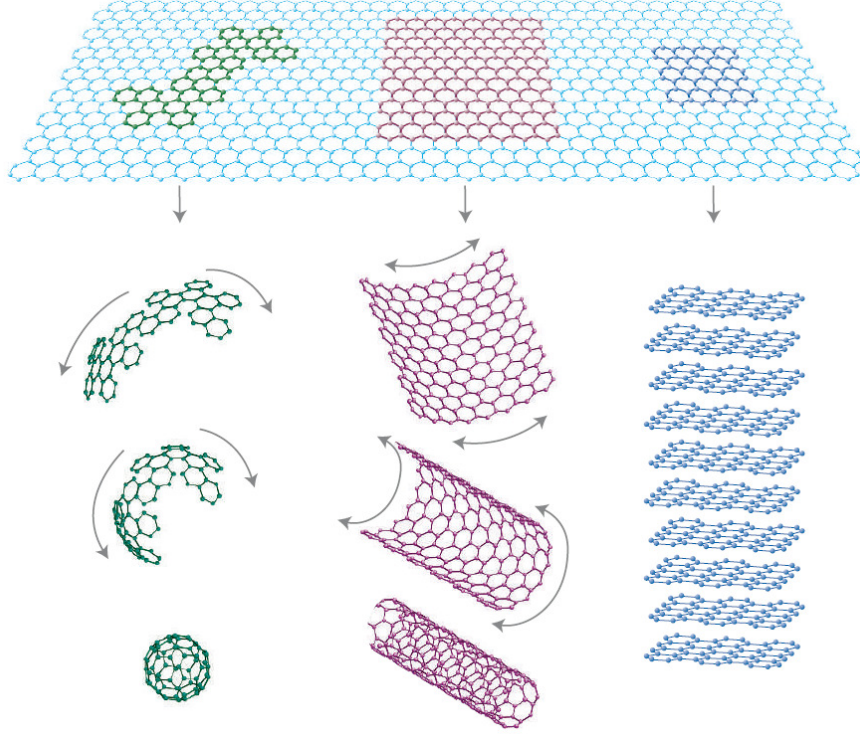
Fig. 56. Graphene (upper part) and its derived carbon materials: i) 0D buckyball (lower–left part); ii) 1D nano–tube (lower–central part); iii) 3D graphite (lower–right part) [1].

Graphene is characterized by a remarkable ambipolar electric field effect (displayed in Fig. 57): charge carriers can be tuned continuously between electrons and holes in concentration $n$ as high as $10^{13}$ cm$^{-2}$ and their mobility $\mu$ can exceed 15,000 cm$^2 \cdot$V$^{-1} \cdot$s$^{-1}$ even under ambient conditions. Furthermore, the observed $\mu$ weakly depends on temperature $T$, which entails that the mobility is still limited by impurity scattering at 300 K and therefore can be improved significantly, even up to about 100,000 cm$^2 \cdot$V$^{-1} \cdot$s$^{-1}$. In graphene, $\mu$ remains high even at a high concentration value of its charge carriers ($n > 10^{12}$ cm$^{-2}$) in both electrically and chemically doped devices, which translates into ballistic transport on the sub–micrometre scale. The electronic quality of graphene is further proved by the so–called Quantum Hall Effect (QHE) that can be observed even at room temperature. The unique nature of graphene's charge carriers gives rise to another important result: in condensed–matter physics, the Schrödinger equation is usually exploited to sufficiently describe the electronic properties of materials. Graphene is an exception, since its charge carriers mimic relativistic particles and are more easily and naturally described by the Dirac equation rather than by the Schrödinger equation. The interactions of graphene's electrons, moving around carbon atoms, with the periodic potential of graphene's honeycomb lattice give rise to new quasi–particles that at low energies $E$ are accurately described by the (2+1)–dimensional Dirac equation with an effective speed of light (Fermi velocity) $v_F \approx 10^6$ m·s$^{-1}$. These quasi–particles, called mass–less Dirac fermions, can be seen as electrons that have lost their rest mass $m_0$ or as neutrinos that have acquired the electron charge $e$.

As stated above, graphene is a zero–gap semiconductor such that low–energy quasi–particles (mass–less Dirac fermions) can be described by the following Dirac–like hamiltonian:

$$\hat{H} = \hbar v_F \begin{pmatrix} 0 & k_x - i k_y \\ k_x + i k_y & 0 \end{pmatrix} = \hbar v_F \, \underline{\sigma} \cdot \bar{k} \tag{1}$$

In Eq. (1) $\hbar = h/2\pi \approx 1.055\text{x}10^{-34}$ J·s is the reduced Planck's constant, $\underline{\sigma}$ is the 2D Pauli matrix and $\overline{k}$ is the quasi–particle momentum. Eq. (1) stems directly from graphene's crystal symmetry: in fact, its honeycomb lattice is made up of two equivalent carbon sub–lattices $A$ and $B$, and cosine–like energy bands associated with the sub–lattices intersect at zero–energy $E$ near the edges of the Brillouin zone. This produces the conical sections of the energy spectrum for $|E| < 1$ eV as shown in Fig. 57.
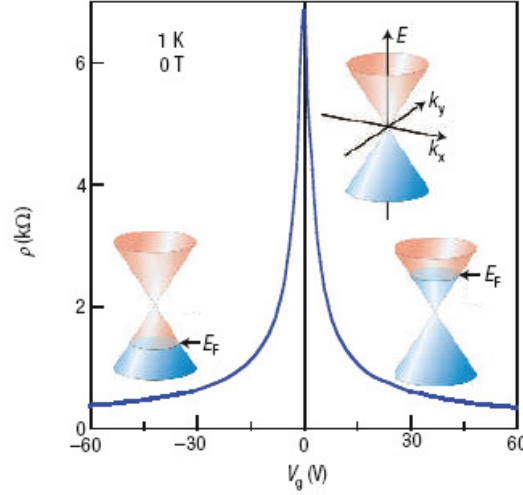


Fig. 57.  Band structure in graphene. The insets show the conical low–energy spectrum $E(k)$: changes in the position of the Fermi energy $E_F$ occur when changing the applied gate voltage $V_g$. Positive or negative values of $V_g$ induce electrons or holes, respectively, in concentrations $n = \alpha \cdot V_g$ where $\alpha \approx 7.2\times10^{10}$ cm$^{-2}$·V$^{-1}$ for field–effect devices with a 300 nm–thick $SiO_2$ layer used as a substrate. The decrease in graphene surface resistivity $\rho$ (kΩ) when augmenting $|V_g|$ indicates the high mobility of charge carriers (in this case, $\mu \approx 5{,}000$ cm$^2$·V$^{-1}$·s$^{-1}$) which is not significantly affected by increasing the temperature up to 300 K [1].

Graphene's electronic states near zero–value of $E$ (where bands intersect, as can be seen in Fig. 57) comprise states that belong to the different sub–lattices and their contributions in the generation of mass–less Dirac fermions have to be considered as well, e.g. by means of *spinors* (i.e. two–components wave–functions). In a way similar to QED (where spin indexes *up* and *down* are used), graphene's sub–lattices $A$ and $B$ are denoted by a pseudo–spin index, hence in Eq. (1) $\underline{\sigma}$ refers to this pseudo–spin rather than to the real spin of electrons.

Phenomena that can be described by QED are often inversely proportional to the speed of light in vacuum $c$: this entails that they are enhanced in graphene by a factor $c/v_F \approx 300$. Therefore, pseudo–spin related effects should generally dominate those due to the real spin. By analogy with QED, one can also introduce a quantity called "chirality" can be introduced, which is formally a projection of $\underline{\sigma}$ on the direction of motion $\overline{k}$ and is positive or negative for electrons or holes, respectively. In graphene, chirality means that $k$ electron and $-k$ hole states are intricately connected because they originate from the same carbon sub–lattices. The two concepts of chirality and pseudo–spin are important because many electronic processes in graphene can be understood as due to conservation of these quantities.

## 4.2.  UNIQUE CHARACTERISTICS OF GRAPHENE'S CONDUCTIVITY

Graphene has very interesting chemical, thermal, mechanical, electronic and optical properties, which have been exploited mostly for field–effect transistors and frequency multipliers [2,3]. Aim of the present chapter is to present the unique properties of graphene's

conductivity for potential antenna applications.

From an EM point of view, since graphene is a 2D one atom–thick material, it can be modeled inside an EM simulation tool by means of an equivalent zero–thickness surface with assigned values of its complex surface impedance $Z_s$ or surface conductivity $\sigma$. In particular, $\sigma$ depends on the chemical potential $\mu_c$: this quantity can be tuned by changing the initial doping of graphene (hence type and density of charge carriers) or by applying an external field. As regards the latter possibility, a distinction has to be made between a DC bias (i.e. electrostatic field) and a magnetic field:

4. a DC bias gives rise to a tunable isotropic $\sigma$;
5. a magnetic field provides a tunable anisotropic $\sigma$ due to the Hall Effect (which entails a change in the Hall resistance).

When no magnetic field is applied, $\sigma$ may be calculated by means of the Kubo formula [4]:

$$\sigma(\omega) = \sigma_1(\omega) + \sigma_2(\omega)$$

$$\sigma_1(\omega) = -j \frac{e^2 K_B T}{\pi \hbar^2 (\omega - j2\Gamma)} \left( \frac{\mu_c}{K_B T} + 2\ln\left( e^{-\frac{\mu_c}{K_B T}} + 1 \right) \right)$$

$$\sigma_2(\omega) = -j \frac{e^2}{4\pi\hbar} \ln\left( \frac{2|\mu_c| - (\omega - j2\Gamma)\hbar}{2|\mu_c| + (\omega - j2\Gamma)\hbar} \right)$$

$$\Gamma = \frac{1}{\tau}, \tau = \frac{\mu E_F}{e v_F^2}, \mu_c \approx e\alpha V_b$$

(2)

In Eq. (2) $\sigma_1$ is the intraband contribution and $\sigma_2$ is the interband one, $e$ is the electron charge, $K_B$ is the Boltzmann's constant, $T$ is the temperature, $\Gamma$ is the scattering rate independent of energy, $\tau$ is the scattering time (which is related to the slope between the imaginary and the real part of the surface impedance), $\mu$ is the charge carriers mobility, $E_F$ is the Fermi energy, $\alpha$ is a constant depending on the geometry of the graphene device and $V_b$ is the bias (gate) voltage. In the case of graphene the Fermi velocity $v_F$ equals the propagating speed of the electrons (holes). Furthermore, $\Gamma$ is in the order of some THz (because $\tau$ is in the order of some psec) or, equivalently, some meV (by using an appropriate scale factor).

The minimum value of graphene's conductivity or, equivalently, the maximum of its resistivity $\rho$, occurs at the so–called *Dirac point* (or charge neutrality point), due to the occurrence of electron–hole puddles [5]. In correspondence of the *Dirac point* conduction and valence bands meet (in the absence of doping) and the 2D energy spectrum of graphene is linear, thus the electrons always move at a constant speed. The afore–mentioned minimum value of $\sigma$ may be theoretically expressed as follows:

$$\sigma_{\min}(\omega) = \sigma_{Dirac}(\omega) = -j \frac{e^2 K_B T \, 2\ln 2}{\pi\hbar^2(\omega - j2\Gamma)}$$

(3)

$\sigma_{Dirac}$ is reached at a bias voltage $V_b = V_{Dirac}$, around which the curve representing graphene's resistivity is largely symmetric and, as stated before, shows a maximum since the carrier concentration $n = 0$. The fact that $V_{Dirac} \neq 0$ suggests that there exists a doping of the graphene samples under test, whose origin may be electrostatic or caused by charged impurities. In synthesis, the higher $|V_b|$, the higher the carrier concentration, hence graphene behaves more like a metal for increasing values of $|V_b|$ and more like a PMC (= Perfect Magnetic Conductor) at $V_b = V_{Dirac}$. It has to be stressed that graphene possesses a positive

85

dielectric constant which changes according to the substrate (dielectric or metallic) attached to it. This kind of "dielectric" behavior entails that a complex relative permittivity can be defined:

$$\varepsilon_r(\omega) = \varepsilon'(\omega) - j\varepsilon''(\omega) = \varepsilon'(\omega) - j\frac{\sigma}{\omega\varepsilon_0} = \varepsilon'(\omega)(1 - \tan\delta) \tag{4}$$

The real part of the intraband term of conductivity in graphene dominates over an ultra–wideband range of frequencies, from DC up to $2 \div 3$ THz. In the same range of frequencies, the imaginary part is very small and the interband contribution is negligible.

The expression in Eq. (2) for the intraband contribution $\sigma_1$ is valid for $\omega < \mu_c$. In particular, by expressing $\mu_c$ in K, according to the Fermi–Dirac statistics $\mu_c$ undergoes the following constraints:

$$\begin{aligned} \mu_c &\gg T \\ \mu_c &\propto T^{-1} \end{aligned} \tag{5}$$

Typical values of $\mu_c$ are comprised in the interval $0 \div 1$ eV but $\mu_c$ changes according to the applied bias voltage $V_b$, which makes the carrier concentration $n$ change:

$$n = \frac{(\mu_c/\hbar v)^2}{\pi} \tag{6}$$

where $v$ is the speed of carriers (which coincides with the Fermi velocity $v_F$).

Eq. (6) expresses a unique property of graphene: its surface conductivity (surface impedance) changes with $V_b$, which means that graphene's electrical properties can be tuned by applying the proper bias voltage.

As regards the surface impedance $Z_s$, it is defined as follows:

$$Z_s(V_b) = \frac{1}{\sigma(\omega)} = R_s(V_b) + jX_s(V_b) \tag{7}$$

$Z_s$ depends on $V_b$, which can tune it, since both $R_s$ and $X_s$ can be changed by an applied voltage. According to Eq. (7), increasing $Z_s$ decreases $\sigma$: this means that, by referring to Eq. (4), the imaginary part of $\varepsilon_r$ decreases and consequently $\tan\delta$ decreases, i.e. graphene starts to effectively act as a low–loss thin dielectric.

## 4.3. GRAPHENE'S CONDUCTIVITY IN THE MW FREQUENCY BAND: FIRST ANTENNA APPLICATION

By means of an *ad hoc* Matlab script, the complex values of $\sigma$ and $Z_s$ expressed by Eq. (2) and Eq. (7) can be computed according to the desired values of $T$, $\Gamma$ and $\mu_c$ in the band of interest. This way, according to the experimental measurements, at micro– and millimeter–waves it can be seen that $Z_s$ is characterized by a small *inductive* reactance, i.e.:

$$Z_s(V_b) = R_s(V_b) + j\omega L_s(V_b) \tag{8}$$

and the scattering time $\tau$ can be calculated as follows [6]:

$$\tau = \frac{L_s(V_b)}{R_s(V_b)} \qquad (9)$$

As stated before, applying $V_b$ allows to tune $R_s$ and $L_s$ in Eq. (8) within the ranges of 50 Ω ÷ 2 kΩ and 0.2 ÷ 3 Ω, respectively. Moreover, The most important consequence of such a result is that graphene is a natural HIS (= High Impedance Surface) because it exhibits a relative high surface resistance in an ultra–wide band that reaches THz without the need of texturing, contrary to metallic HISs.

Graphene antennas are now subject of several studies [7] and seem to have special properties not encountered in any other antenna, in particular the tuning of the antenna resonance in a large bandwidth through the variation of graphene's surface impedance via an applied DC voltage. It is also known that electromagnetic propagation in graphene is nonlinear [8]. The interaction between graphene and optical electromagnetic fields is nowadays better understood and exploited [9]. Although the surface resistance of graphene is high at $V_b = 0$ V and becomes lower when $V_b$ increases, the high graphene's surface resistance at 0 V bias, in the order of 500 Ω ÷ 4 kΩ [6,10,11] remains the same up to THz frequencies [12]. Apparently, this is a detrimental effect in propagation/radiation in comparison with metals, which have surface impedances (resistances) in the range of 0.2 ÷ 0.3 Ω.

In the following, the design of a 10 GHz coplanar patch antenna (CPA) in graphene fed by means of a 400 nm thick–gold CPW will be presented and its overall performance will be discussed with a detailed comparison of the different results obtained by means of the graphene's surface impedance tuning. In the case of the CPA, the physical properties of graphene are well preserved [13], i.e.: i) high electrical conductivity; ii) high thermal conductivity for rapid heat evacuation.

Fig. 58 shows the first proposed layout of the graphene CPA operating at the frequency $f_0 = 10$ GHz. Be W the graphene's width along the x–direction and L its length along the y–direction. S the gap width between the graphene layer and the gold electrodes along both the x– and y–direction, A the width of the hot wire of the CPW and B the gap width between the hot wire and the ground electrodes of the CPW in correspondence of the excitation port, then we have:

1. $f_0 = 10$ GHz, hence $\lambda_0 = 30$ mm. According to the technological constraints, the graphene is grown on a 300 nm–thick $SiO_2$ layer which is deposited on a 500 μm–thick High–Resistivity (HR) silicon substrate with $\varepsilon_r = 12.9$. This way, the effective relative permittivity is $\varepsilon_{eff} = 2.7$, hence the guided wavelength is $\lambda_g = \lambda_g / \sqrt{\varepsilon_{eff}} = 18$ mm. This way, W = $0.5\lambda_g = 9$ mm and L = $0.1\lambda_g = 1.8$ mm;
2. S = 100 μm;
3. A = 100 μm;
4. B = 50 μm.
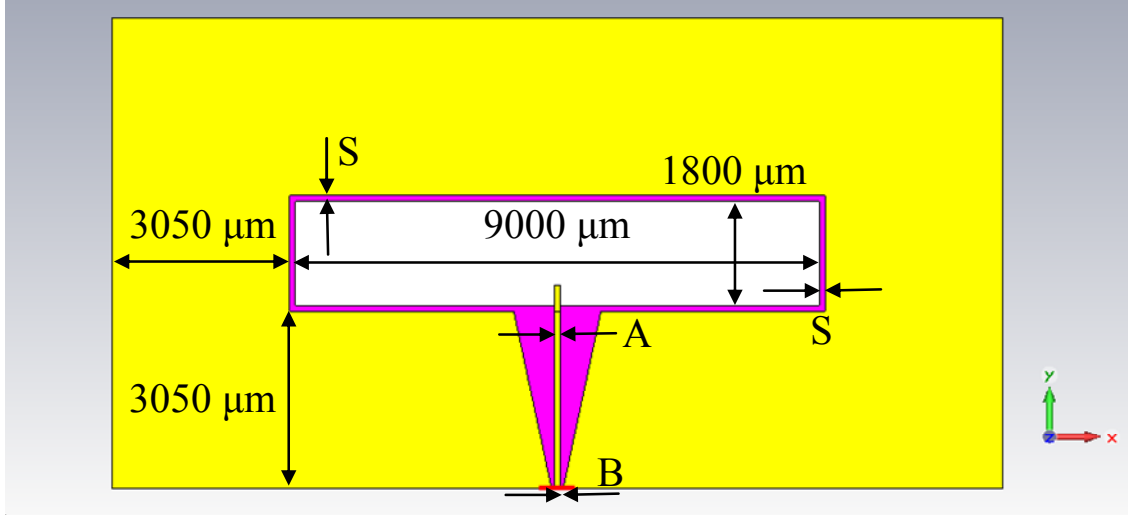
Fig. 58. First layout of the graphene CPA fed by a gold CPW and operating at 10 GHz. All measures are expressed in μm.

In order to reduce the simulation time and increase the accuracy of the results at the same time, the following assumptions were made:

1. the graphene layer was modeled as a zero–thickness "ohmic sheet" with a specific value for $R_s$ and $X_s$ in Eq. (7) at the desired operating frequency;
2. the sheet was considered "transparent", i.e. it has the same electric field on both sides (nevertheless fields do not penetrate solid ohmic sheet bodies);
3. loss tangent of $SiO_2$ was taken into account as well. This choice does not affect the resonance frequency and the impedance matching;
4. "open (add space)" boundary conditions were considered in every direction of the bounding box for proper radiation pattern simulation;
5. it was observed that varying the hot wire length attached to the graphene does not affect the overall antenna performance.

The initial value for $R_s$ was set equal to 250 Ω, whereas the value for $X_s$ can be chosen in the range 0 ÷ 4 Ω (it does not have a significant effect on the performance due to the already stated properties of graphene's surface impedance at MW frequencies).

The main result of the present investigation was the great difference in the antenna performance when choosing to excite it by either the *even* or the *odd* mode (see Fig. 59).
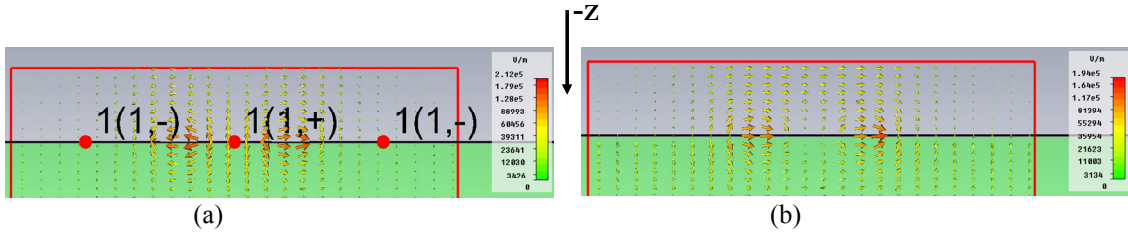


Fig. 59. (a) Even and (b) odd mode for the CPW excitation of the graphene CPA antenna. It is evident the field distribution along the CPW metallization (the hot wire is the central one).

Table VIII summarizes the main radiation performance of the graphene CPA antenna: input impedance $Z_{port}$, resonance frequency $f_{res}$, the frequency at which the best matching (i.e. the minimum value for $|S_{11}|$ dB) is obtained $f_{best}$, the radiation efficiency $\eta_{rad}$ and the bandwidth at

−10 dB BW$|_{-10dB}$ (i.e. the bandwidth over which $|S_{11}| \leq -10$ dB). It has to be stressed that the minimum of $|S_{11}|$ dB does not necessarily corresponds to the real resonance frequency, instead it is a measure of the matching to the value of $Z_{port}$.

Table VIII. CPA performance by considering *even* and *odd* mode excitation.

| Mode | *Even* | *Odd* |
|---|---|---|
| $Z_{port}$ | ~ 50 Ω | ~ 119 Ω |
| $f_{res}$ | ~ 10.3 GHz | ~ 9.5 GHz |
| $f_{best}$ | ~ 10.8 GHz | ~ 9.1 GHz |
| $\eta_{rad}$ | ~ 0.7% | ~ 50% |
| BW$|_{-10dB}$ | ~ 4 GHz | > 4 GHz |

It is apparent from Table VIII that the excitation of the *odd* mode gives an outstanding improvement in terms of radiation efficiency. Nevertheless in both cases there is a relevant enhancement of the relative bandwidth RBW$|_{-10dB}$, which is equal to about 40% (instead of the classical 4% typical for standard patch antennas) due to the peculiar characteristics of graphene. Moreover, the impedance matching to $Z_{port}$ is very good in both cases, as can be seen in Fig. 60 where the values of $|S_{11}|$ dB for the two types of excitation is shown.

Table IX displays the CPA performance when considering the layout of Fig. 58 with the following characteristics and dimensions:

1. $R_s = 250$ Ω;
2. S = 450 μm;
3. A = 100 μm;
4. B = 50 μm.

The main effect of increasing the dimension S (i.e. the distance between the graphene layer and the ground plane) is the decreasing of the capacitive coupling between antenna and CPW, thus a reduction of the EM energy stored by the near–field can be observed. This entails (as shown in Table IX) that an increasing in the radiation efficiency is possible.

Table IX. CPA performance by considering *even* and *odd* mode excitation with S = 450 μm.

| Mode | *Even* | *Odd* |
|---|---|---|
| $Z_{port}$ | ~ 50 Ω | ~ 119 Ω |
| $f_{res}$ | ~ 10.4 GHz | ~ 10.7 GHz |
| $f_{best}$ | ~ 11 GHz | ~ 9.5 GHz |
| $\eta_{rad}$ | ~ 2.4% | ~ 66% |
| BW$|_{-10dB}$ | ~ 4 GHz | ~ 4 GHz |
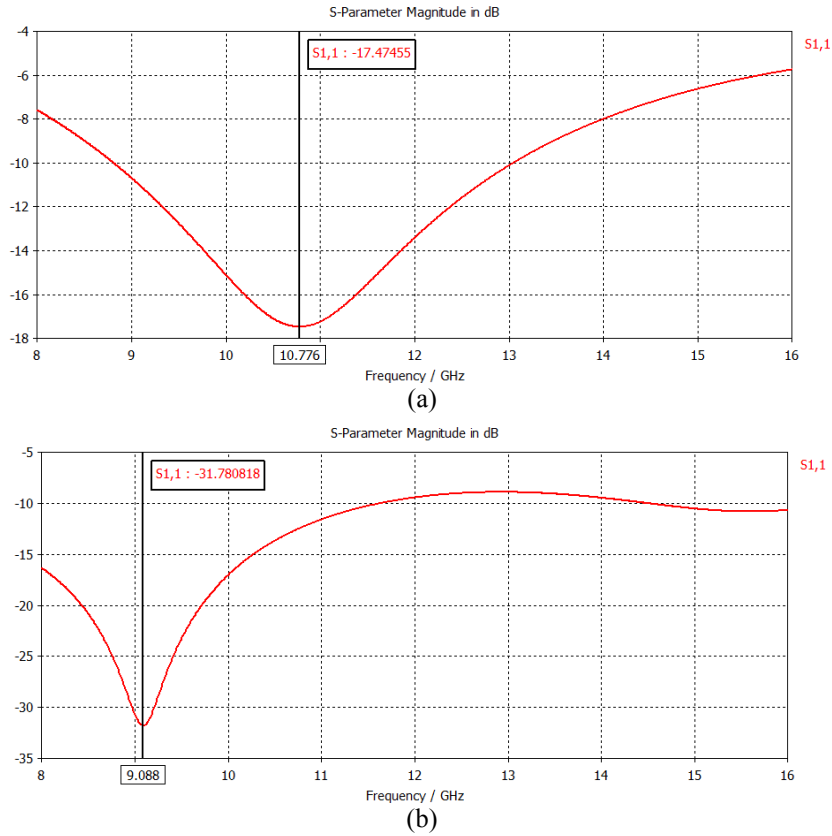
Fig. 60. $|S_{11}|$ dB for the graphene CPA operating at 10 GHz and excited by: (a) an even mode; (b) an odd mode. The scattering parameters are automatically normalized over the antenna input port $Z_{port}$ calculated by the EM simulation tool CST MWS®.

Fig. 61a and Fig. 61b display the radiation patterns of the E–field at 10.8 GHz (*even* mode) and at 9.1 GHz (*odd* mode), respectively. Radiation characteristics change dramatically when choosing either the *even* or the *odd* mode to excite the patch: this can be considered a very interesting result, since it allows to select the most appropriate mode according to the requested overall performance.
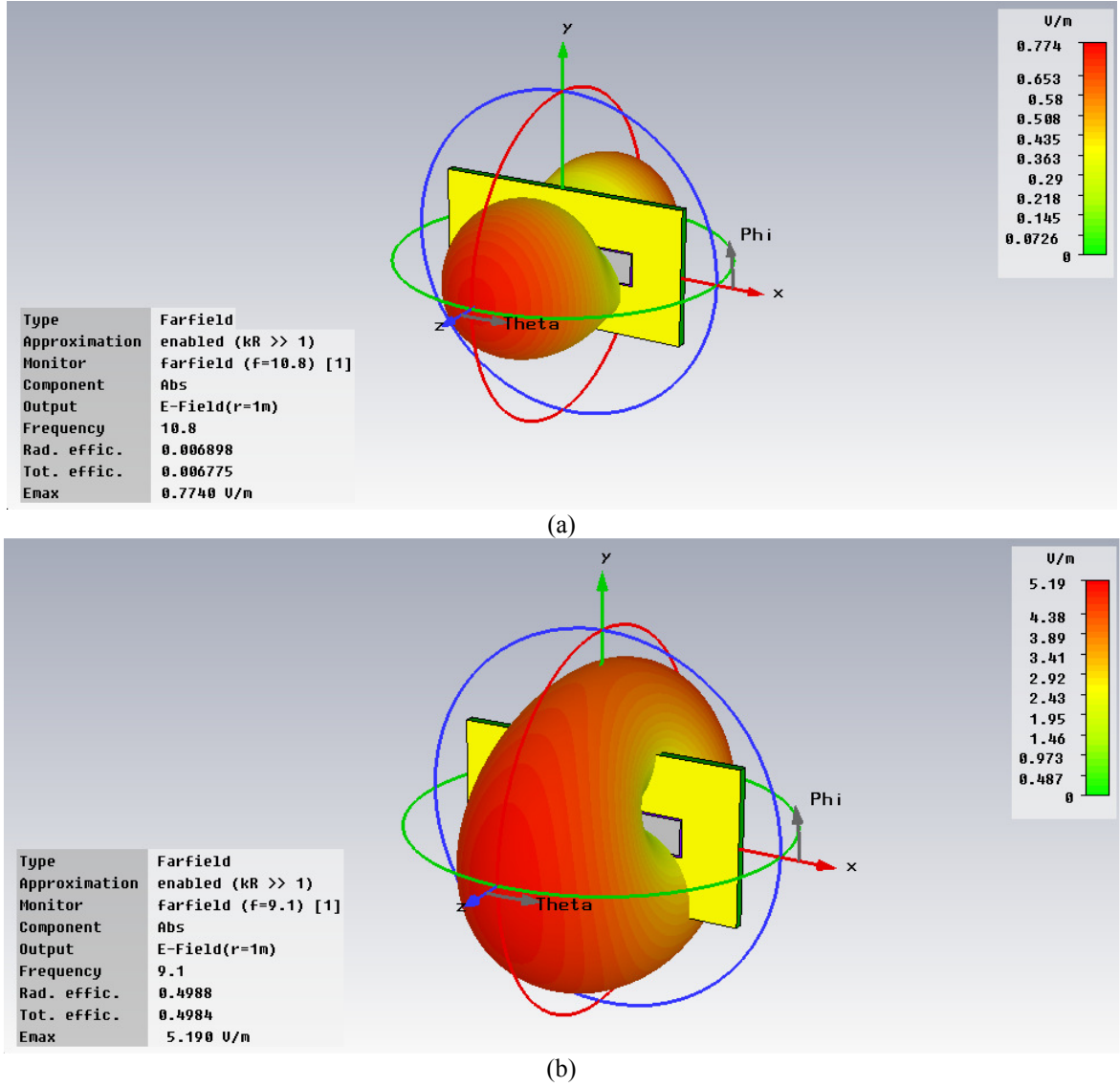
Fig. 61.  Simulated radiation pattern of the E–field in the case of (a) *even* and (b) *odd* mode excitation for the graphene CPA operating at 10 GHz.

The electric $\mathbf{J}_s$ and magnetic $\mathbf{J}_{ms}$ surface currents are expressed as follows:

$$\begin{cases} \mathbf{J}_s = \hat{\mathbf{n}} \times \mathbf{H} \\ \mathbf{J}_{ms} = \mathbf{E} \times \hat{\mathbf{n}} \end{cases} \quad \left(\hat{\mathbf{n}} \equiv \hat{\mathbf{k}}\right) \tag{10}$$

The same results as Fig. 61a were obtained using for the EM simulations a *magnetic* yz–symmetry plane, i.e.:

$$\begin{cases} J_{s,x}(-x) = -J_{s,x}(x) \\ J_{ms,x}(-x) = J_{ms,x}(x) \end{cases} \tag{11}$$

whereas an *electric* yz–symmetry plane was used to obtain the same results as Fig. 61b:

$$\begin{cases} J_{s,x}(-x) = J_{s,x}(x) \\ J_{ms,x}(-x) = -J_{ms,x}(x) \end{cases} \qquad (12)$$

The exploitation of the afore–mentioned symmetry planes through Eqs. (11) and (12) gave the proof of the correct excitation of the graphene CPA by means of the *even* and *odd* mode, respectively. Fig. 62 shows the amplitude of the surface currents on the graphene CPA for the two types of excitations; in particular, in the case of the *odd* mode the graphene layer acts a $1.5\lambda_g$–dipole as is evident from Fig. 61b and Fig. 62b.



(a)



(b)
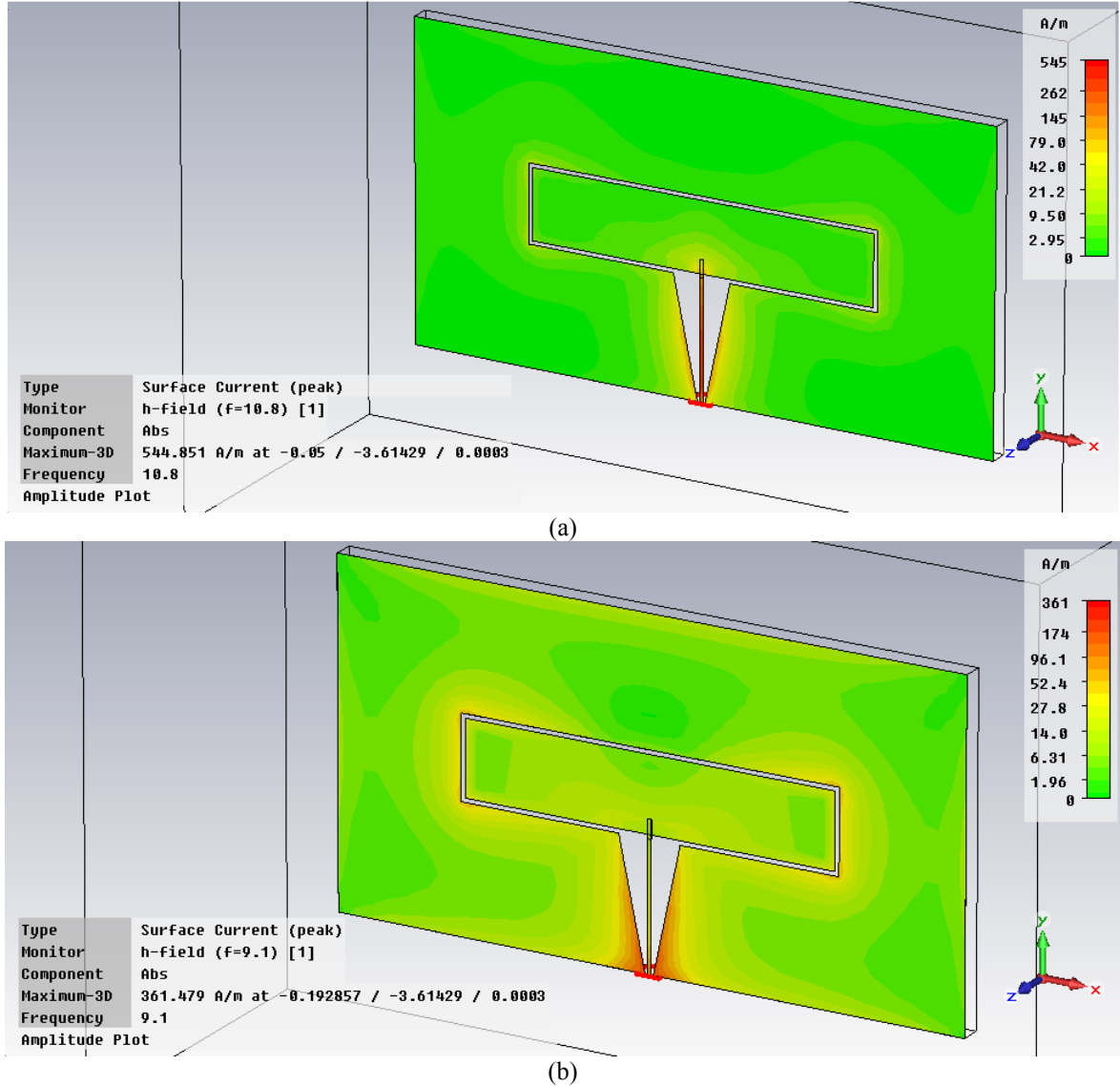
Fig. 62. Surface current distributions on the graphene CPA at 10 GHz for the: (a) *even* mode excitation; (b) *odd* mode excitation. The *odd* mode case corresponds to a $1.5\lambda_g$–dipole.

Let us now consider the same graphene CPA but with a 400 nm–thick gold ground plane attached at the HR silicon layer. In this case, three modes can excite the structure:

1. *even* (as before);
2. *odd* (as before);
3. *quasi–TEM*.

Each mode has its own characteristic impedance and the *quasi–TEM* one resonates at different frequencies with respect to the *even/odd* modes (which have more or less the same resonance frequency, as shown in Table VIII).

From the Z–matrix (Fig. 63a and Fig. 63b) it can be inferred that there are "spurious" resonances which do not appear without the ground plane, hence they are due to the ground plane itself. In fact the energy decay in the structure is very low, which gives a direct proof of the presence of undesired resonances (which affect the resonance frequencies, the matching, the bandwidth and the radiation efficiency).



(a)



(b)
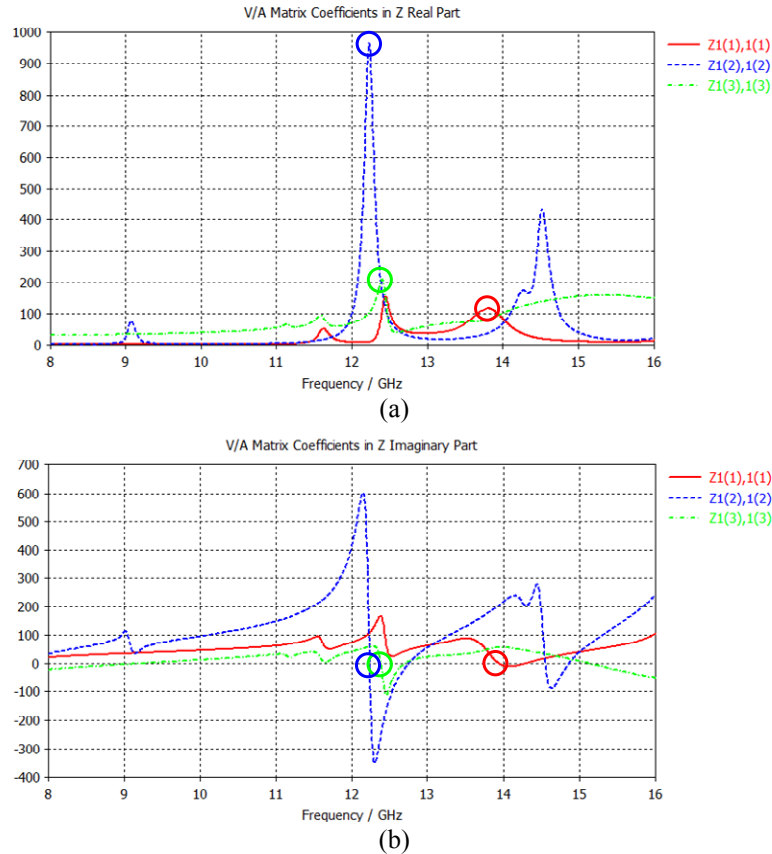
Fig. 63. (a) real and (b) imaginary part of the input impedance $Z_{11}$ of grounded graphene CPA at 10 GHz. The solid red line refers to the *quasi–TEM* mode, the green dash–dotted line to the *even* mode and the blue dashed line to the *odd* mode. The circles indicate the real resonances of the structure for each mode.

Fig. 64a shows the values of $|S_{11}|$ dB for the three modes and in Fig. 64b the radiation pattern of the E–field in the case of *quasi–TEM* excitation is displayed.
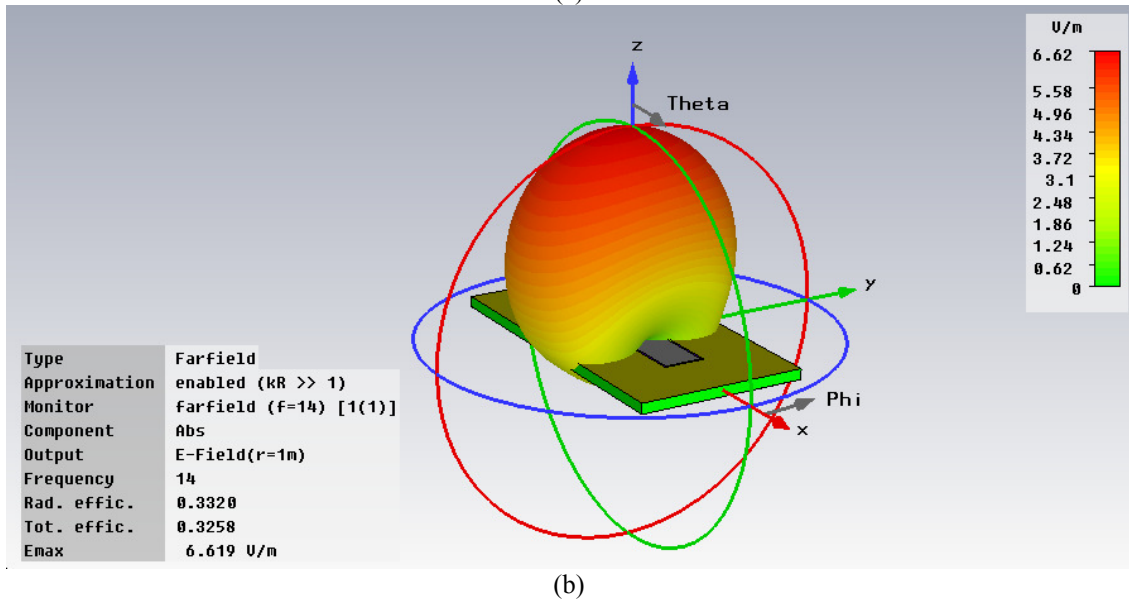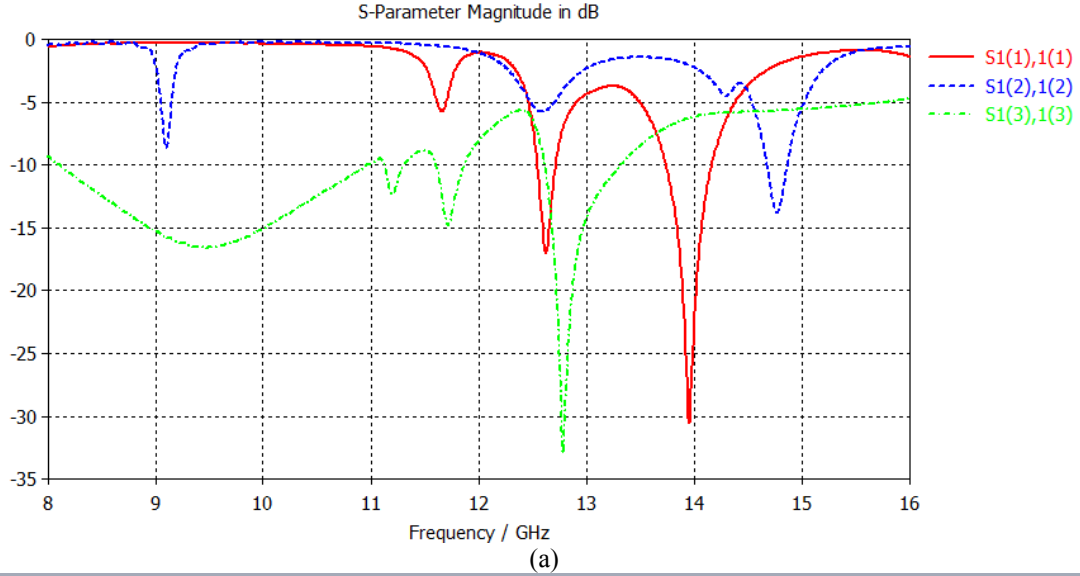
Fig. 64. (a) $|S_{11}|$ dB for the three excitation modes of the grounded graphene CPA at 10 GHz. The solid red line refers to the *quasi–TEM* mode, the green dash–dotted line to the *even* mode and the blue dashed line to the *odd* mode; (b) simulated radiation pattern of the E–field in the case of *quasi–TEM* excitation.

From Fig. 63a and Fig. 63b it is evident that the resonance due to the *quasi–TEM mode* is at 14 GHz, whereas Fig. 64a shows that the best impedance matching is at the same frequency. Fig. 64b demonstrates that the radiation efficiency is about 33%, hence a good value with respect to state–of–the–art graphene antennas, and the radiation pattern is broadside in the z–direction. Moreover, *odd* mode radiation efficiency (about 39%) is always better than *even* mode radiation efficiency (about 1.8%). This has been verified by placing several farfield monitors in the simulated frequency band. Nevertheless *odd* and *even* mode radiation patterns are very irregular due to the presence of the ground layer.

In conclusion, when using a grounded Si–layer, the *quasi–TEM* mode is the best trade–off, since it is characterized by a stable radiation pattern (*always* broadside radiation) over the entire frequency band of interest, with a maximum value of the front–to–back ratio of about – 6 dB and an acceptable maximum value of the radiation efficiency of about 33%.

It is important to understand how varying $Z_s$ affects antenna performance. For this reason,

let us consider the *even* mode excitation with $R_s = 250 \div 2000\ \Omega$ and $X_s = 0 \div 4\ \Omega$ for the ungrounded graphene CPA.
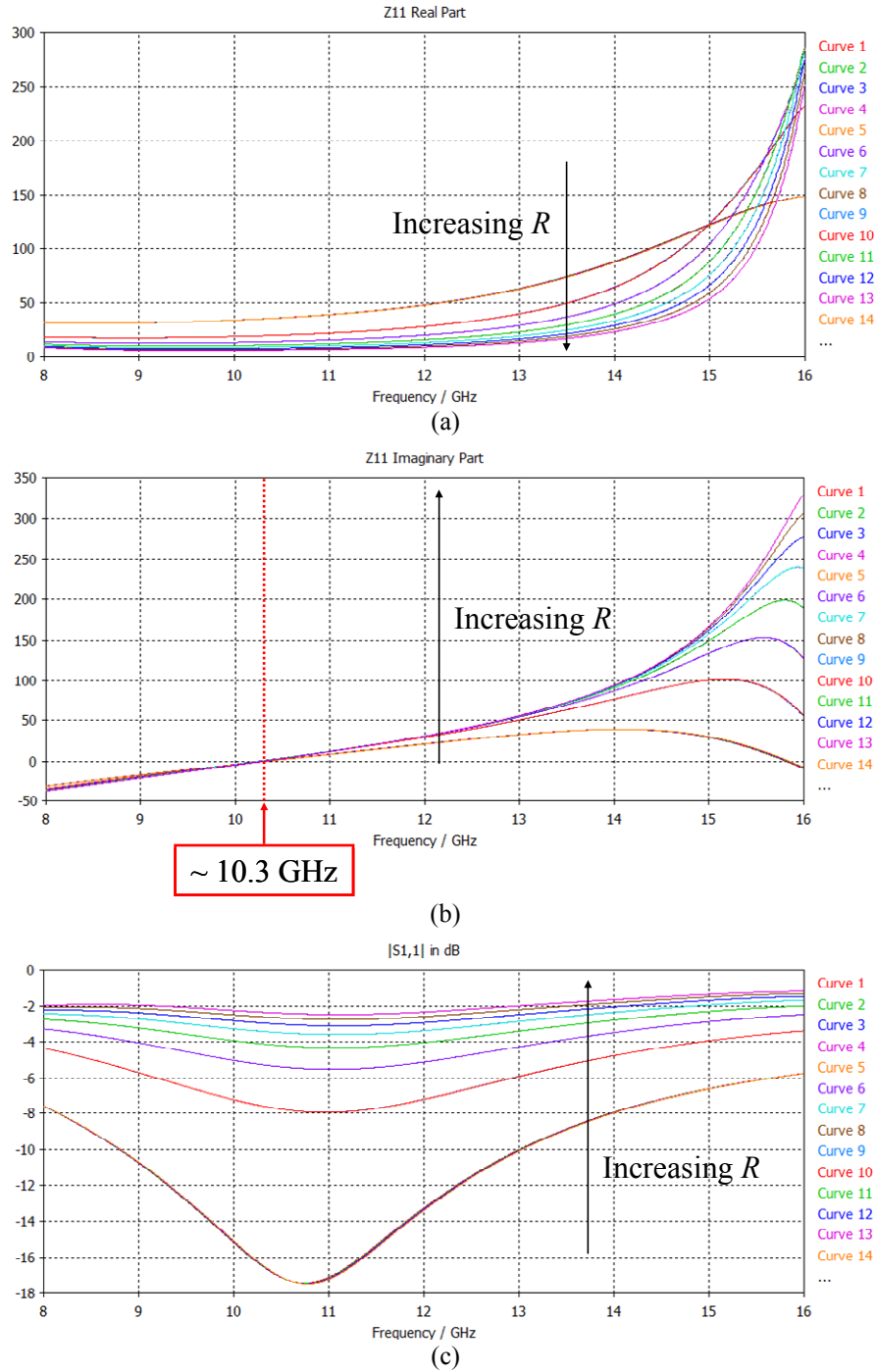


Fig. 65. Effect of varying $Z_s$ for the graphene CPA operating at 10 GHz with the *even* mode excitation: (a) real and (b) imaginary part of the antenna input impedance; (c) $|S_{11}|$ dB.

From Fig. 65 three main effects can be inferred:

1. increasing $R_s$ decreases the value of $\mathrm{Re}\{Z_{11}\}$;
2. increasing $R_s$ keeps the resonance fixe at around 10.3 GHz;
3. increasing $R_s$ worsens matching to CPW port impedance (i.e. about 50 Ω).

Finally, Fig. 66 shows the main radiation characteristics of varying $Z_s$, in particular:

1. increasing $R_s$ increases the radiation efficiency (up to about 4.5%);
2. increasing $R_s$ increases the E–field intensity (in Fig. 66 the $\phi = 90°$ plane is displayed).



(a)



(b)
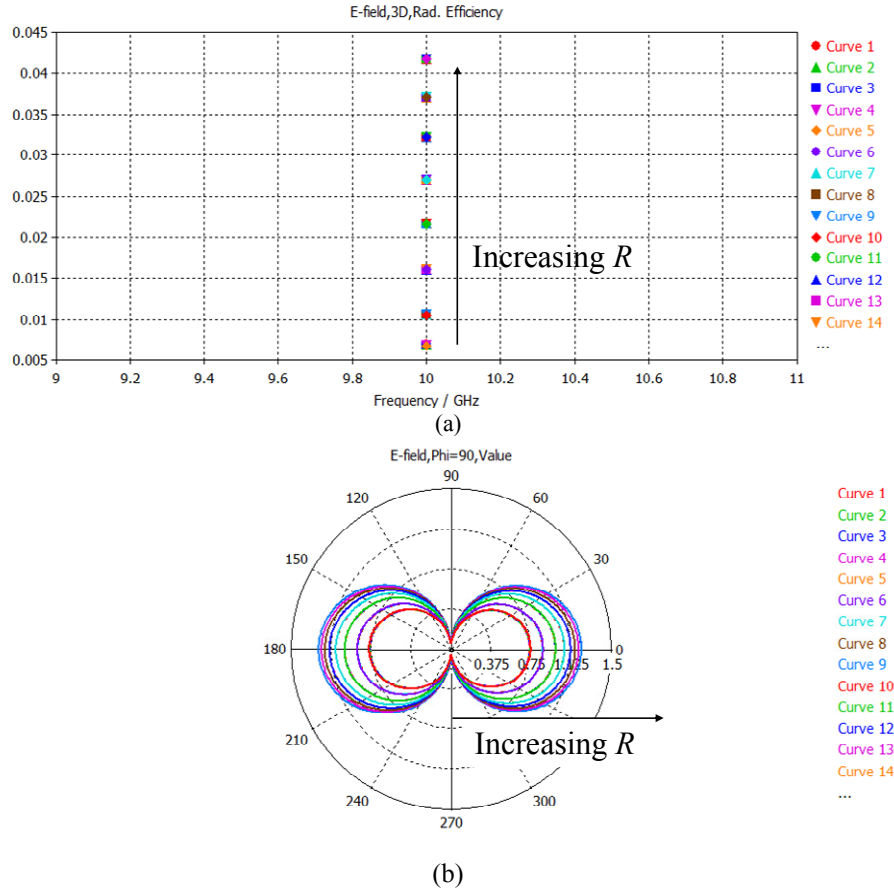
Fig. 66. Effects of varying $Z_s$ on the (a) radiation efficiency and (b) the E–field on the $\phi = 90°$ plane for the ungrounded graphene CPA operating at 10 GHz with the *even* mode excitation.

A possible explanation for the efficiency increasing can be inferred from the fact that, as already specified, graphene does not behave like a metal, since its dielectric constant is positive and changes according to the substrate (dielectric or metallic) attached to it. This kind of "dielectric" behavior entails that a complex relative permittivity can be defined as shown in Eq. (4). Since $Z_s = 1/\sigma$ as stated by Eq. (7), increasing $R_s$ decreases $\sigma$, hence the imaginary part of $\varepsilon_r$ decreases and $\tan\delta$ decreases. This means that radiation efficiency $\eta_{rad}$ increases, since it depends only on the radiated and dissipated power: if the latter decreases, $\eta_{rad}$ increases.

Let us now consider the *odd* mode excitation by varying $Z_s$ at the same time. In this case, for the sake of simplicity, $R_s = 250 - 500 - 750$ Ω and $X_s = 4$ Ω. Fig. 67 and Fig. 68 show the main results obtained by the simulations.
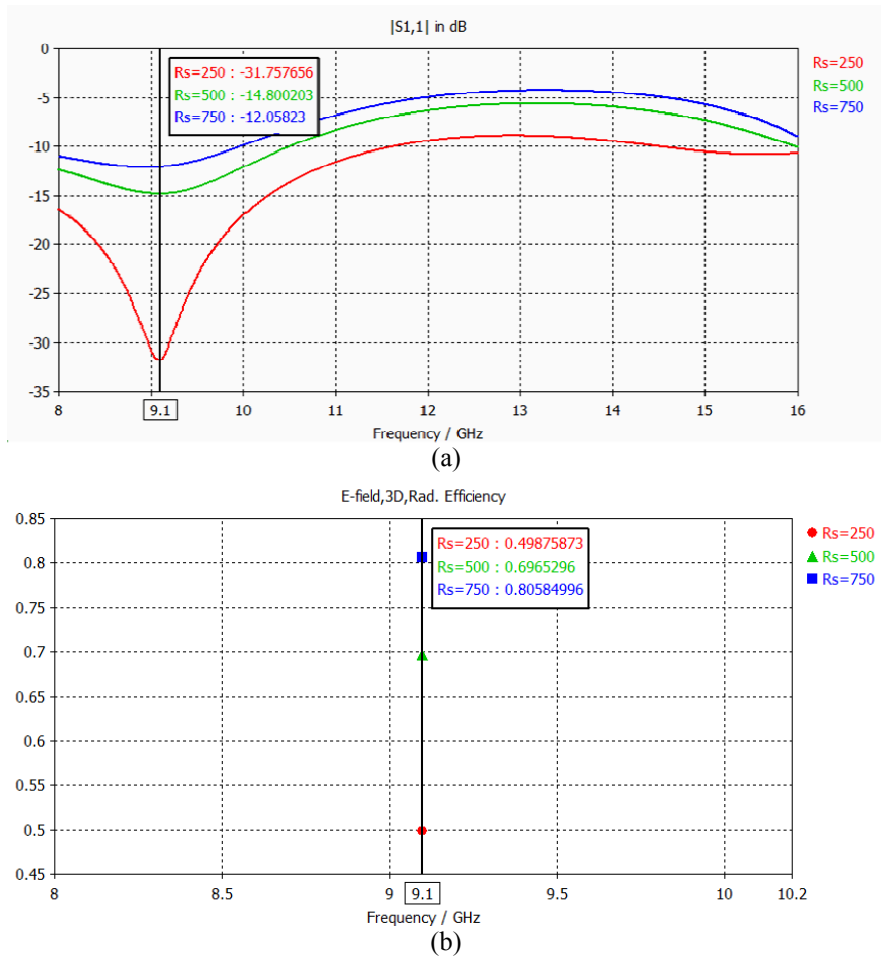
Fig. 67. Effects of varying $Z_s$ on the (a) $|S_{11}|$ dB and (b) the radiation efficiency for the ungrounded graphene CPA operating at 10 GHz with the *odd* mode excitation.

E-field, Phi=0.0, Value



(a)

E-field, Phi=90, Value

(b)
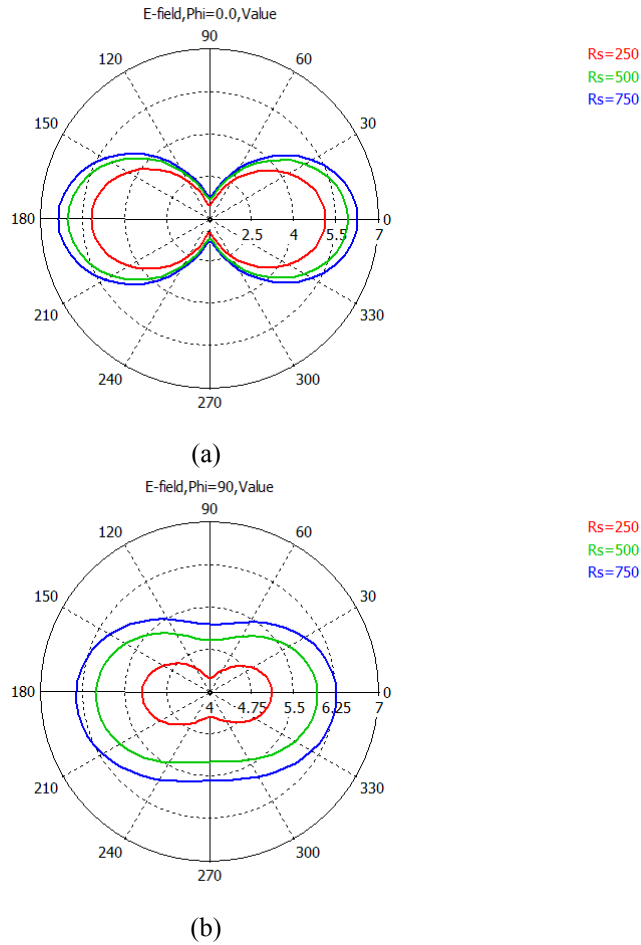
Fig. 68. Effects of varying $Z_s$ on the (a) E–field on the $\phi = 0°$ plane and (b) E–field on the $\phi = 90°$ plane for the ungrounded graphene CPA operating at 10 GHz with the *odd* mode excitation.

From Fig. 67 and Fig. 68 it is evident how the *odd* mode excitation always guarantees better performance in terms of both impedance matching to the port characteristic impedance and radiation efficiency enhancement (up to about 81% for $R_s = 750$ $\Omega$) with respect to the *even* mode. This can be explained by the fact that in CPWs *even* mode and *odd* mode have different characteristic impedances $Z_{even}$ and $Z_{odd}$, respectively, as shown in Table VIII. In particular (at least at mm waves) $Z_{odd} > Z_{even}$. As a consequence, since the *odd* mode has a higher characteristic impedance, it is easier to match the CPW to the surface impedance of the graphene layer.

*A posteriori* I extensively searched in literature for a proof of the advantage in using *odd* mode excitation for CPAs and, in fact, *odd* mode seems to be the most appropriate for CPAs feeding, whereas the *even* mode seems to be suitable for resonators. This result can be also justified by the fact that one may potentially consider the graphene CPA as a folded slot antenna.

In conclusion, it would be more convenient to excite the *odd* mode to obtain better overall performance with the proposed graphene CPA and this could be accomplished by means of proper feeding techniques. Moreover, as apparent from Table VIII, the graphene CPA under study exhibits a very high relative bandwidth of about 40%, which can be considered a great advantage in a practical wireless application at 10 GHz.

## 4.4. GRAPHENE AS A HIGH–IMPEDANCE SURFACE FOR ULTRA–WIDEBAND APPLICATIONS IN THE MW FREQUENCY RANGE

In the frequency range spanning from MW up to THz, conventional metals are regularly used as reflectors of EM fields emitted by antennas. In order to enhance reflection and thus the gain of the antenna, metallic HISs are used. HIS is a planar array of continuous metallic periodic cell surfaces able to suppress surface waves causing multipath interference and backward radiation in a narrow bandwidth near the resonance of the cell. The image currents are reduced as well and therefore the antenna can be placed near the HIS itself. In the following it will be demonstrated that graphene can act as a high HIS in a very large bandwidth from MW to THz and hence suppress the radiation leakages better than a metal.

First, the EM properties of graphene in RF, microwave and millimeter waves are not well known yet. Coplanar metallic lines deposited on graphene transferred on Si/SiO$_2$ were studied and it was demonstrated that graphene is working as a DC–voltage–tunable matching device [14], and that the contact resistance – a serious issue in graphene – is shorted beyond few GHz, since the graphene devices behave contactless at measurements up to 110 GHz [10]. Graphene antennas are now extensively studied [7 and the references therein] and exhibit unique properties not encountered in any other antenna such as the variation of surface impedance via an applied DC voltage (as already stated) tuning the antenna resonance in a large bandwidth. It is also known that EM propagation in graphene is nonlinear [8]. Nowadays, the interaction between graphene and optical electromagnetic fields is better understood and exploited [9].

It is well known that the surface resistance of graphene is high at a gate voltage $V_b = 0$ V and becomes lower when the $V_b$ is increasing. However, the graphene surface resistance is high being in the order of 500 $\Omega$ ÷ 4 k$\Omega$ [6,11,15] at $V_b = 0$ V and these high values are the same up to THz frequencies [12]. Apparently, this is a detrimental effect in propagation/radiation in comparison with metals having surface impedances of 0.2–0.3 $\Omega/\square$. However, the enhancing of the reflection of the EM fields of metal reflectors positioned below an EM radiator (antenna) is done through the high impedance of a HIS [15]. A HIS is modeled as a 2D array of circuits, in which the real part of the surface impedances takes high values near the resonance, of $10^2 \div 10^4 \, \Omega$, depending on the geometry of metal cells and their dimensions. As a result the reflection coefficient ($|S_{11}|$) becomes very high and the efficiency of the antennas places over such a structure can be increased by suppression of the side lobes due the suppression of surface modes' propagation and the suppression of phase reversal of the image currents. So, it is necessary to adjust periodically a metallic surface to enhance the reflection properties and to transform it from a low–impedance surface into a HIS in a narrow bandwidth, not exceeding few hundreds of MHz.

Due to its intrinsic physical properties, graphene has a relatively–high resistance, hence it can be considered as a natural HIS which does not need any texture keeping this property in an ultra–wideband reaching THz. Furthermore, state–of–the–art synthesis methods allow to produce large graphene flakes, with widths of 30 inc. [16], therefore it possible to use graphene as HIS over large surfaces.

As demonstrated by Eq. (2), the Kubo formula gives the surface conductivity of graphene, in particular:

$$\sigma_1(\omega) = -j \frac{e^2 K_B T}{\pi \hbar^2 (\omega - j2\Gamma)} \left( \frac{\mu_c}{K_B T} + 2\ln\left( e^{-\frac{\mu_c}{K_B T}} + 1 \right) \right) \tag{13}$$

is the intraband contribution, whose real part dominates over an ultra–wideband range of frequencies, from DC up to 2 ÷ 3 THz. In the same range of frequencies, the imaginary part of $\sigma_1$ is very small and the interband contribution is negligible.

L = 0.45$\lambda_0$ = 13.5 mm

W = 500 μm

Gap = 50 μm

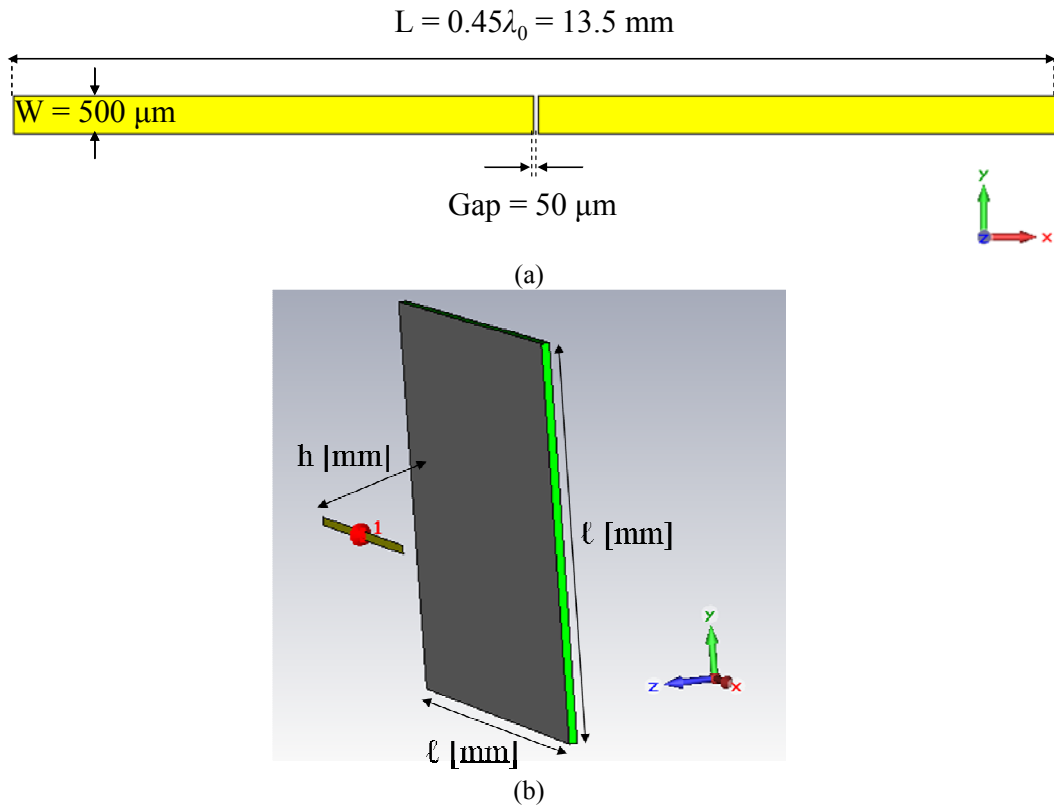(a)



h [mm]

ℓ [mm]

1

ℓ [mm]

(b)

Fig. 69. (a) Gold dipole antenna geometry; (b) layout of the CST design project with the dipole at distance h [mm] over a square graphene reflector of length ℓ [mm].

By using CST MWS®, a gold dipole operating at 10 GHz and suspended over a graphene flake was designed, as it is indicated in Fig. 69. Gold thickness is 2 μm, the dipole length is 0.45$\lambda_0$ = 13.5 mm being $\lambda_0$ = 30 mm, and the graphene film is a square of length ℓ = 0.78 $\lambda_0$ = 23.4 mm deposited over 300 nm of $SiO_2$ ($\varepsilon_r$ = 3.9, tan$\delta$ = 0.001) grown on high–resistivity silicon ($\varepsilon_r$ = 12.9, tan$\delta$ = 0.00025) with a thickness of 500 μm. The distance h between the dipole and the ground is $\lambda_0/4$ = 7.5 mm. Thus, the image current are disabled, but the surface waves at the interface of graphene/air are still present and they reach the boundaries of graphene, thus radiating into free–space and producing interferences and ripples on the radiation pattern, which downgrade the efficiency of any antenna. It has to be stressed that graphene was initially modeled as a zero–thickness sheet with complex surface impedance $Z_s$ = $R_s$+j$X_s$ = 250+j0.25 $\Omega$ (since real part of $Z_s$ is predominant). In this case, the bandwidth in correspondence of |$S_{11}$| = −10 dB is more than 1.5 GHz, which means a relative bandwidth of more than 15% with a value of |$S_{11}$| ≈ −25 dB at 10 GHz. Fig. 70 shows that the graphene flake effectively acts as a reflector by suppressing the back–radiation and guarantees at the same time a good radiation efficiency (about 64%) with a good value of the directivity (3.68 in linear scale or, equivalently, about 5.7 dBi). For comparison, by using as reflector a 2 μm–thick gold layer, since gold is a very good conductor at MW ($\sigma$ = 4.561x10$^7$ S/m) ohmic losses are low, hence radiation efficiency is high (more than 99%) and the computed directivity exhibits a value of about 5.9 (linear scale or, equivalently, 7.7 dBi).
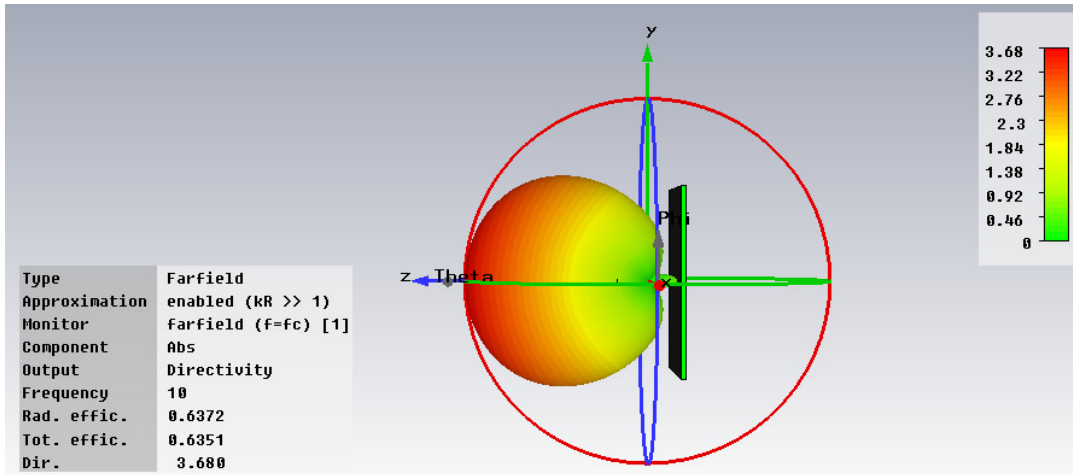
Fig. 70. Farfield at 10 GHz of the gold dipole suspended over a graphene HIS.

Fig. 71 displays the frequency–dependence of the real (a) and imaginary (b) parts of the antenna input impedance for several surface resistance values, whereas Fig. 72 shows the reflection coefficient ($|S_{11}|$ dB) of the antenna in the frequency range $8 \div 12$ GHz. The surface resistance is considered to be 950 $\Omega$ at $V_b = 0$ V in agreement with the experimental results [6,15] and close to the value of this parameter provided by commercial companies for CVD (= Chemical Vapour Deposition) grown graphene. The value can be decreased progressively up to 50 $\Omega$ applying on graphene (via a gate) voltages which do not exceed 5 V.



(a)



(b)
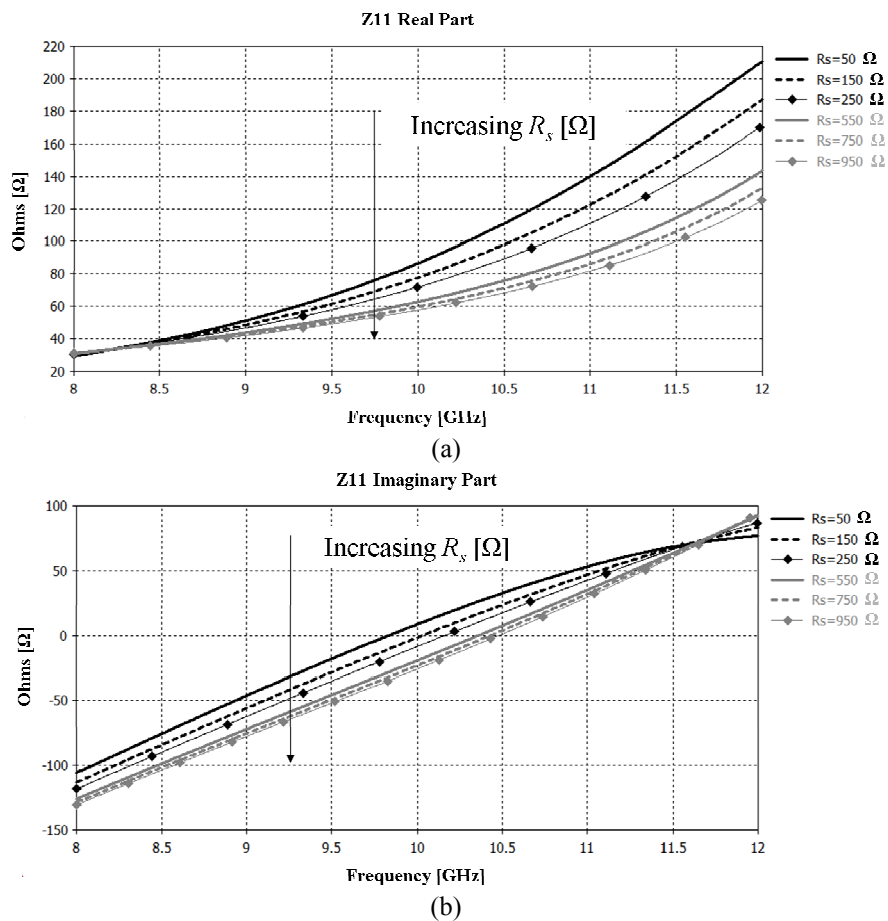
Fig. 71. Frequency–dependence of (a) real and (b) imaginary part of the input impedance of the gold dipole over graphene for different $R_s$ values.

101
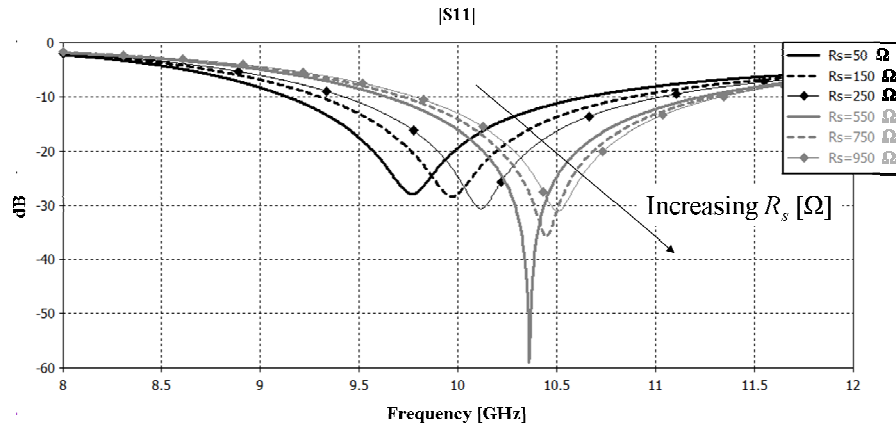
Fig. 72. Frequency–dependence of the reflection coefficient $|S_{11}|$ dB of the gold dipole over graphene for different $R_s$ values.

From Fig. 71a and Fig. 71b, respectively, it can be inferred that the real part of the input impedance of the antenna decreases from its value at 50 Ω, which is a reference surface resistance for any RF measurement. At 10 GHz (i.e. in correspondence of the dipole resonance frequency), for $R_s$ = 950 Ω a real part of antenna input impedance equal to 57 Ω and an imaginary part of –25 Ω were obtained, with a very good voltage standing wave ratio VSWR = 1.57, according to the results shown in Fig. 72. Better results were obtained for $R_s$ = 150 Ω, since the imaginary part of the antenna input impedance is zero and the real part is equal to 77 Ω, which can be easily matched to a standard 50 Ω–impedance, while the VSWR = 1.094. Fig. 73 shows the E–field radiation pattern on the $\phi$ = 0° plane for increasing values of $R_s$.
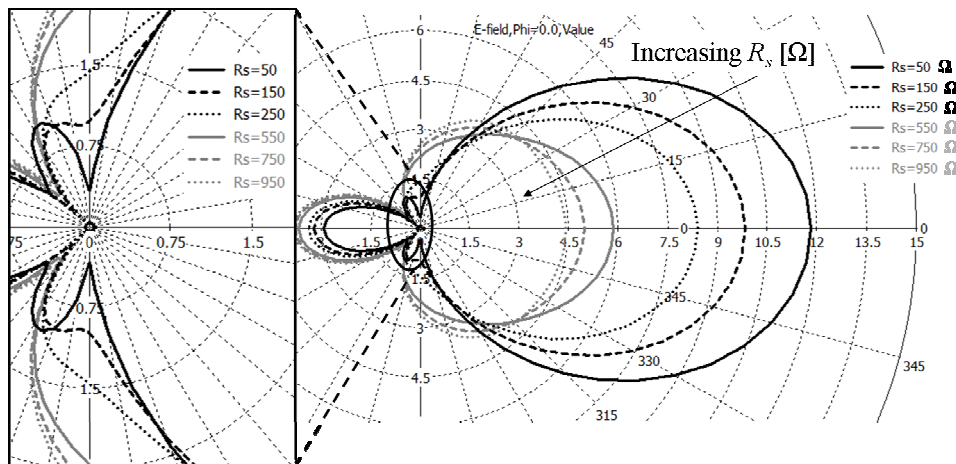


Fig. 73. E–field horizontal radiation pattern of the gold dipole antenna over graphene for different values of $R_s$. The magnification in the inset shows the reduction of the side lobes due to the graphene flake.

From Fig. 73 it is apparent that that the sides lobes can be significantly reduced by increasing $R_s$ until they completely disappear. The radiation efficiency $\eta_{rad}$ was also computed: it is equal to about 85% when $R_s$ = 50 Ω (i.e. when graphene's behavior is more close to that of an electric conductor) and this value decreases up to about 64% when $R_s$ = 950 Ω.

The influence of different h values on the side lobes of the radiation pattern is displayed in Fig. 74.
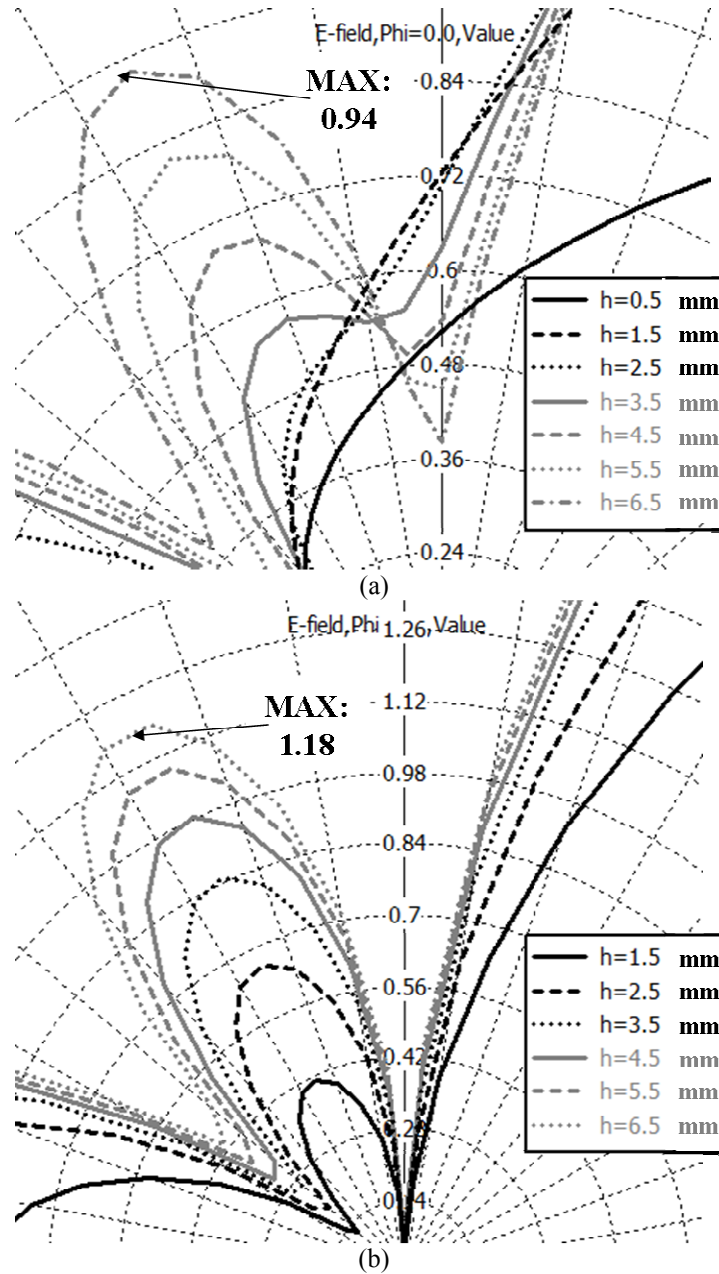
Fig. 74. Comparison between the E–field (on the φ = 0° plane) side lobe amplitude reduction due to: (a) a graphene reflector and (b) a 2 μm–thick gold reflector at various values of the distance h.

Simulations were made for graphene (with $R_s$ = 50 Ω) in Fig. 74a and for a 2 μm–thick gold reflector in Fig. 74b. The results demonstrate that graphene reduces the side lobes and the back–radiation better than a metal, for all the considered values of the distance h of the antenna from the reflector itself. By keeping, for example, $R_s$ = 250 Ω, there are no side lobes for each value of the parameter h, thus giving a direct proof of the advantage in exploiting high–resistance graphene layers as HIS reflectors for better radiation performance. It has to be stressed that a graphene layer used as a HIS under an EM radiator can also allow a better matching to the antenna input impedance, as shown in Fig. 75a for the graphene reflector and in Fig. 75b for the gold reflector: in fact, impedance matching is more difficult when using a metal layer because the real part of the antenna input impedance becomes very small (e.g. about 5 Ω for h = 1.5 mm vs. about 41 Ω in the graphene case for the same value of h) and the imaginary part increases (in modulus). Moreover, Fig. 76 displays the radiation efficiency in

the two cases of graphene and gold reflector, respectively. Again, very good values pertaining to the graphene layer can be observed and it is clear how they increase by increasing $R_s$.
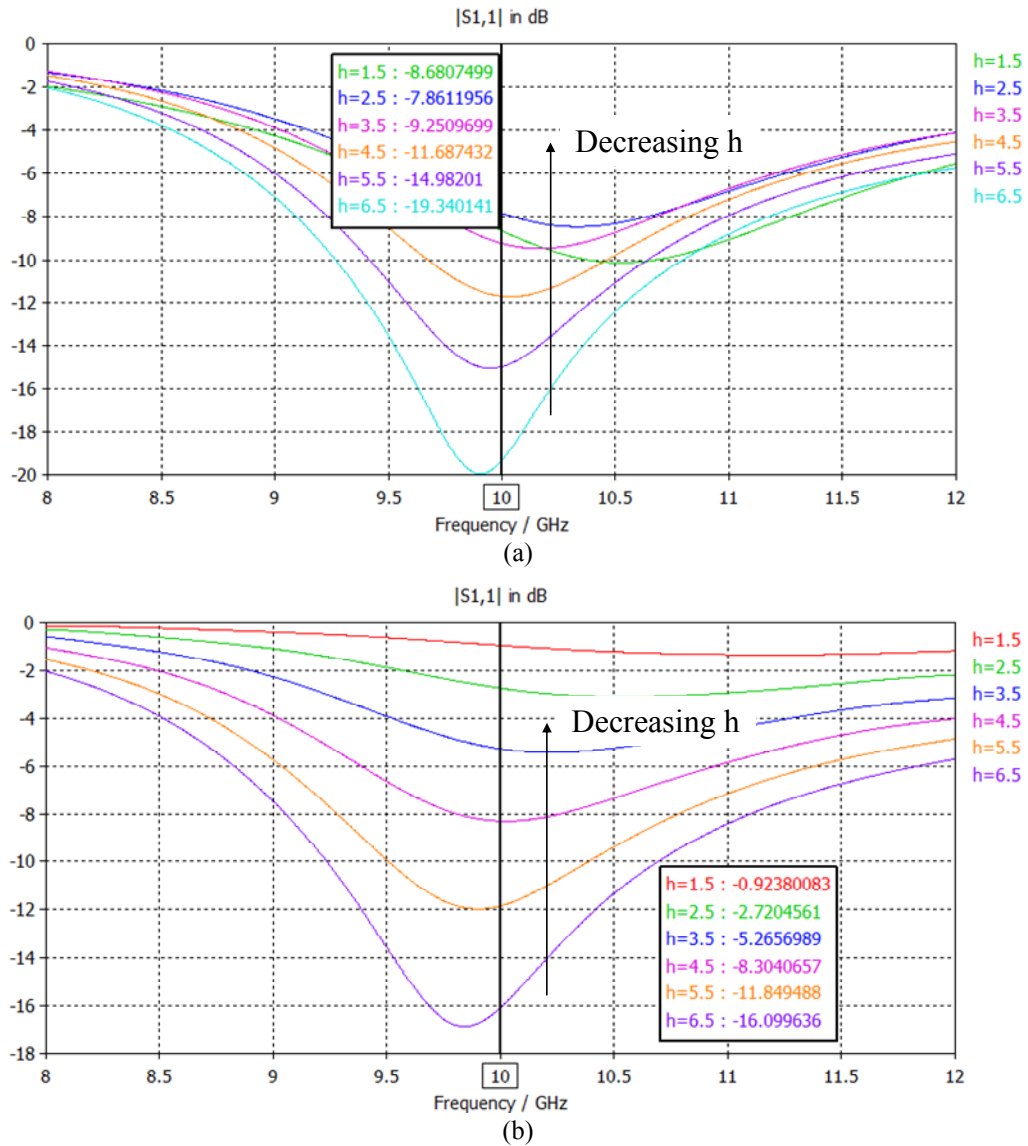


Fig. 75. $|S_{11}|$ dB at various distances h of the gold dipole antenna from: (a) the graphene reflector; (b) the gold reflector. It is apparent how the graphene layer guarantees better matching conditions even in correspondence of the minimum value of h.
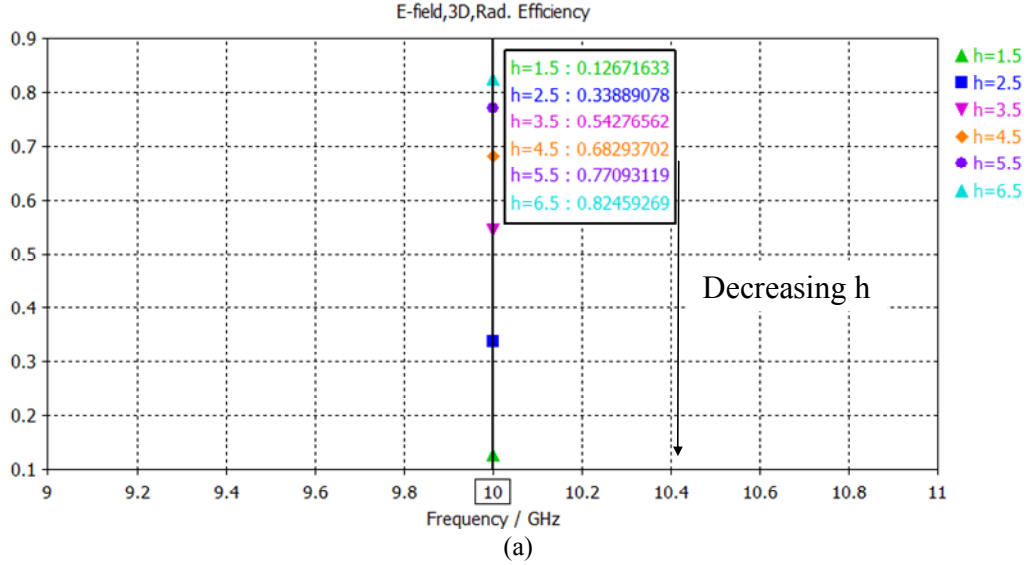
E-field,3D,Rad. Efficiency

h=1.5 : 0.12671633
h=2.5 : 0.33889078
h=3.5 : 0.54276562
h=4.5 : 0.68293702
h=5.5 : 0.77093119
h=6.5 : 0.82459269

Decreasing h

▲ h=1.5
■ h=2.5
▼ h=3.5
◆ h=4.5
● h=5.5
▲ h=6.5

(a)

E-field,3D,Rad. Efficiency

h=1.5 : 0.94940978
h=2.5 : 0.97996551
h=3.5 : 0.99134365
h=4.5 : 0.99601265
h=5.5 : 0.99749238
h=6.5 : 0.99788402

Decreasing h

● h=1.5
▲ h=2.5
■ h=3.5
▼ h=4.5
◆ h=5.5
● h=6.5

(b)
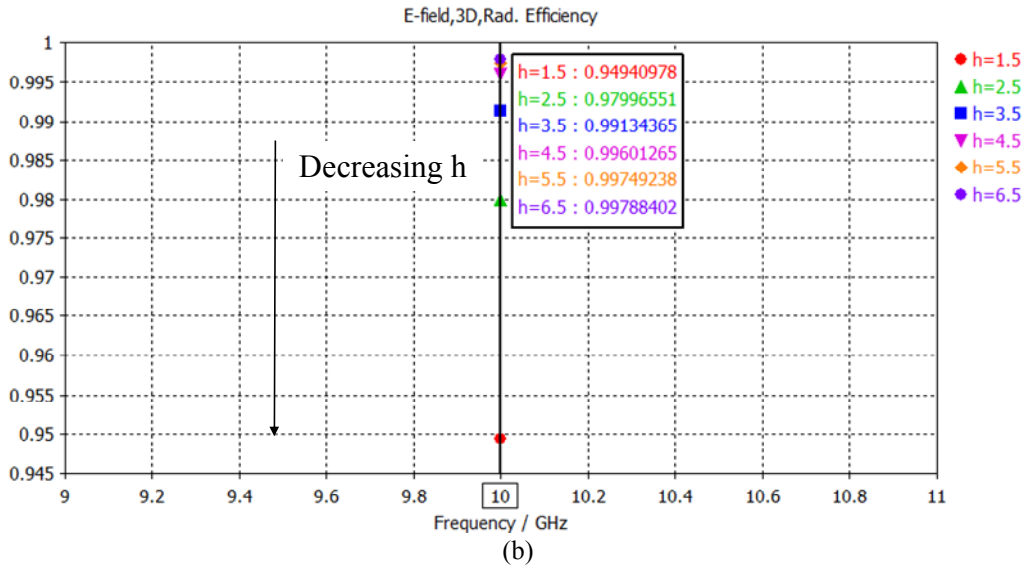
Fig. 76.  Radiation efficiency $\eta_{rad}$ at various distances h of the gold dipole antenna from: (a) the graphene reflector; (b) the gold reflector. At h = 1.5 mm the graphene reflector still guarantees an acceptable value of

A simulation at 10 GHz by keeping fixed the value for $R_s$ = 1 kΩ (which is the typical value for the unbiased case) and decreasing the distance h between the gold dipole and the graphene reflector from 6.5 mm (i.e. about $\lambda_0/5$) to 0.5 mm (i.e. about $\lambda_0/60$) was performed as well. As displayed in Fig. 77a, worst impedance matching occurs at h = 0.5 mm due to the strongly capacitive behavior of the antenna input impedance, but as stated before the high value of graphene's surface impedance provides broadside radiation with no side lobes and reduced back–radiation for all values of h (see Fig. 77b). Furthermore, at $\lambda_0/60$ radiation efficiency still exhibits a remarkable value around 27%, whereas at $\lambda_0/5$ it is 64%. This is a proof of the advantage in using graphene as HIS, since metal antennas can be placed at a distance from the reflector also well below $\lambda_0/12$, thus providing at the same time good radiation performance and low–profile design for compact devices.
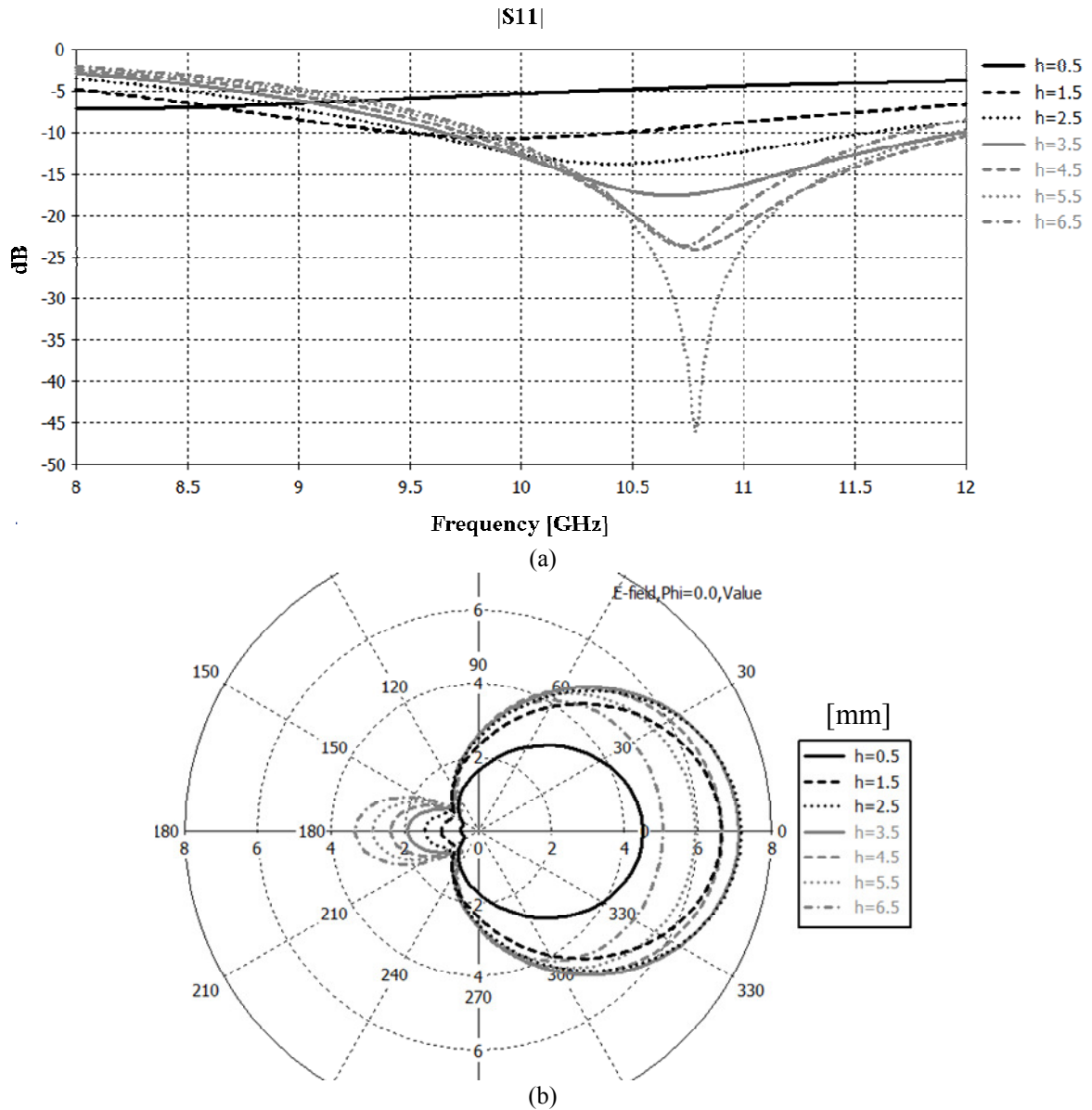
Fig. 77. Performance of the gold dipole over graphene for a fixed value of surface resistance $R_s$ = 1 kΩ at various distances h from the reflector: (a) frequency–dependence of the reflection coefficient $|S_{11}|$ dB; (b) E–field radiation pattern on the $\phi$ = 0° plane. No side lobes are apparent due to graphene's properties as HIS.

In order to practically exploit the technology presented so far, in the following it will be proposed an off–the–shelf solution to realize a gold dipole antenna operating at 10 GHz and placed over a squared graphene flake to use as HIS reflector. In particular, the antenna dipole is deposited over a dielectric layer which is backed by a graphene monolayer. A commercial laminate Nelco N9000 PTFE plays the role of the dielectric thanks to its very good performance at 10 GHz: $\varepsilon_r$ = 2.08, tan$\delta$ = 0.0006. The total length of the gold dipole is L = 11.4 mm = $0.38\lambda_0$, its width W = 500 μm, the dipole gap is 50 μm, the gold thickness is 2 μm and the laminate thickness is 3.175 mm, i.e. about $\lambda_0/9$. The final layout is shown in Fig. 78.
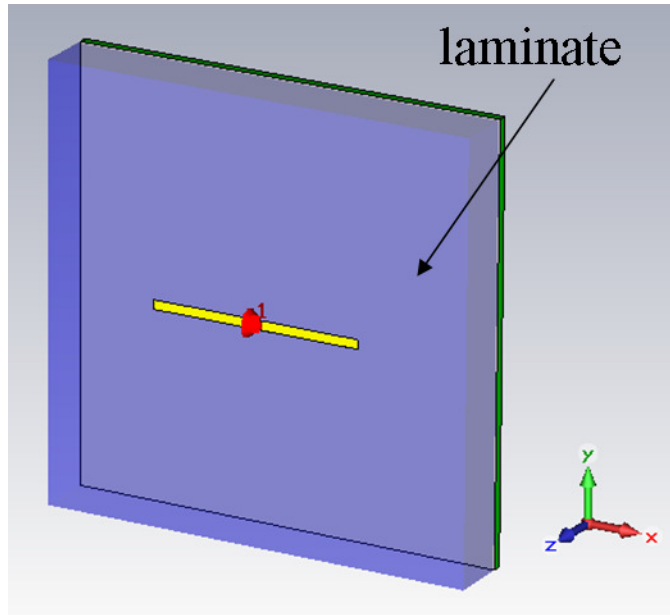
Fig. 78. Layout of a gold dipole over a graphene–backed dielectric layer of laminate NELCO N9000 PTFE.

The frequency–dependent behavior of the reflection coefficient of the antenna, $|S_{11}|$ dB, is depicted in Fig. 79 for different values of the surface resistance $R_s$ (in the inset of the same figure). It can be seen that the worst reflection corresponds to $R_s = 50\ \Omega$, whereas in the nonbiased case ($R_s = 950\ \Omega$) the minimum value of $|S_{11}|$ is about –22 dB, which means VSWR = 1.173, hence a very good value of the voltage standing wave ratio.
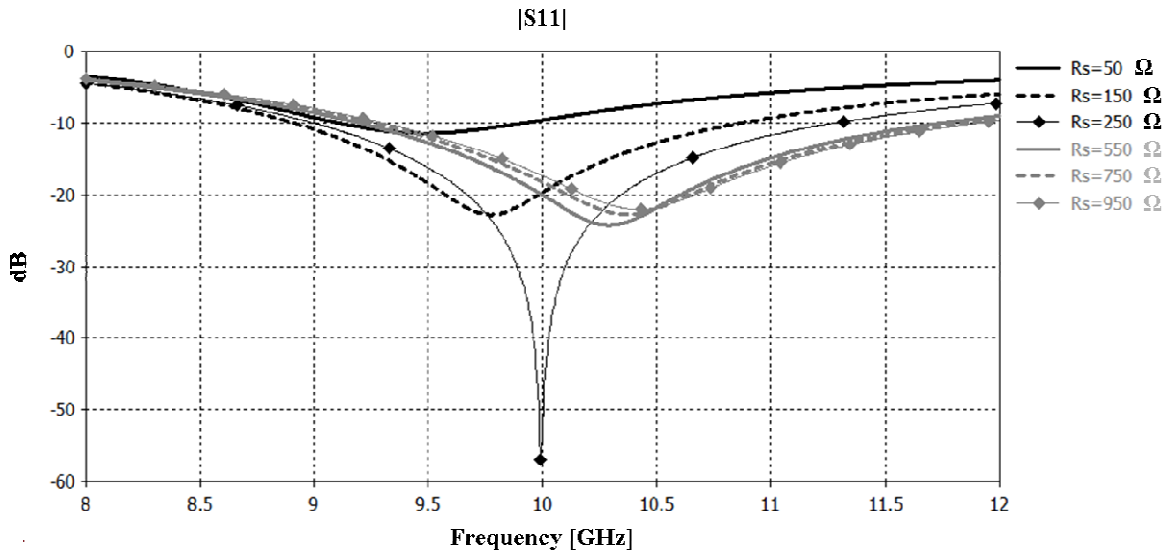


Fig. 79. Frequency–dependence of the reflection coefficient $|S_{11}|$ dB for the gold dipole printed on the graphene–backed NELCO substrate for different values of the surface resistance $R_s$.

Finally, in Fig. 80 the horizontal and vertical dipole radiation patterns are displayed, respectively, for different values of the surface resistance $R_s$. From these figures it follows that the dipole has no side lobes, the backward radiation is drastically reduced and no ripples are detected. The best and worst radiation patterns are marked with solid black and dotted grey line, respectively, corresponding to $R_s = 50\ \Omega$ and $R_s = 950\ \Omega$. The computed value of the radiation efficiency $\eta_{rad}$ is about 47% for the best case, whereas in the worst situation the efficiency value is about 25%: in both cases, $\eta_{rad}$ exhibits pretty good values. In conclusion, it

can be stated that tuning the surface resistance $R_s$ allows to obtain the desired trade–off between impedance matching, bandwidth, directivity and radiation efficiency.
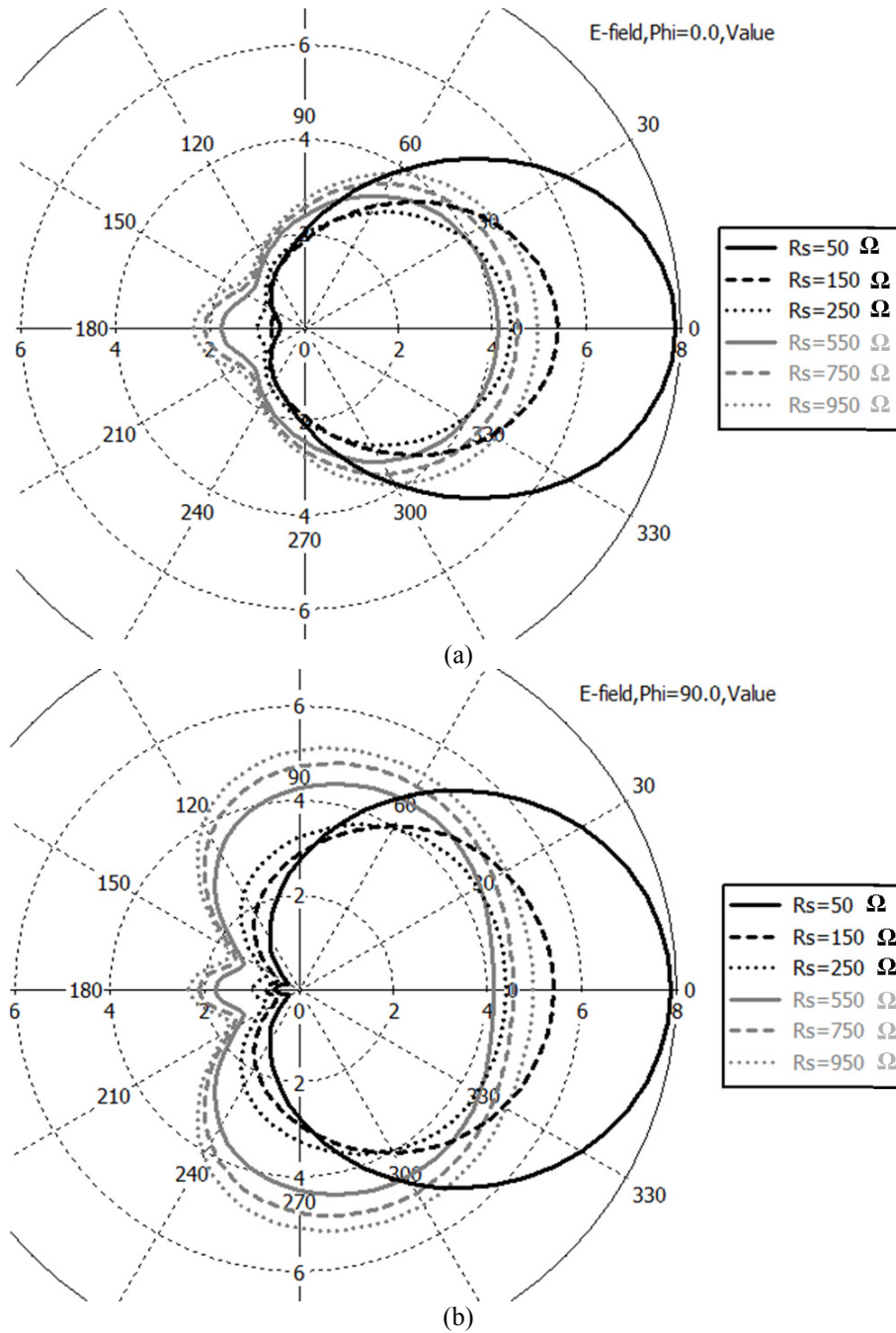


(a)



(b)

Fig. 80. E–field radiation pattern of the gold dipole printed on the graphene–backed NELCO substrate for increasing values of the surface resistance $R_s$: (a) $\phi = 0°$ (horizontal) plane; (b) $\phi = 90°$ (vertical) plane.

Let us denote with (a) the gold dipole antenna suspended over the graphene layer and with (b) the configuration with the antenna deposited on a thin graphene–backed dielectric. Therefore, two different optimum working conditions can be defined with respect to the distance h from the graphene HIS:

1. in situation (a), for $R_s = 1$ kΩ the best working condition is at 10.8 GHz at h = 5.5 mm, in fact $|S_{11}| < -45$ dB (the minimum value). This means that the graphene flake is bias–free, thus no additional energy needs to be consumed to get a very low value of the

108

reflection coefficient;

2. in situation (b), $|S_{11}| \approx -58$ dB at 10 GHz for $R_s = 250\ \Omega$, whereas in the unbiased situation ($R_s = 950\ \Omega$) $|S_{11}| \approx -20$ dB at 10 GHz which is still a very good value. In this case, a little amount of energy has to be necessarily consumed in order to tune $R_s$ to desired value.

Nevertheless in both configurations (a) and (b) the best working conditions are when $|S_{11}|$ is low enough in an unbiased condition. If such best working conditions cannot be found in the frequency range of interest, graphene's surface resistance must be biased until $|S_{11}| < -20$ dB at the operating frequency of the device.

As demonstrated throughout the present paragraph, a graphene monolayer can be exploited to suppress surface waves, which produce multipath interferences and backward radiation, and that the image currents are reduced. This way, an antenna can be placed even directly above the graphene flake. No texture is necessary for graphene as in the case of metals. Comparing graphene with metals used as HISs, graphene can work in a very large bandwidth. Simulations for gold dipoles with resonance frequencies of 20 GHz and 30 GHz were performed as well and the results (not shown for the sake of conciseness) are similar to those reported so far for a 10 GHz–resonant antenna. Furthermore, it has been shown that graphene works well as HIS even when no bias is applied to it. These results could be of paramount importance for future reflectors for antennas due to the unique properties of graphene.

In particular, dipoles over a graphene layer take the advantage of working as antennas shielded with a PEC layer, with the following characteristics:

1. broadside radiation;
2. good values of the maximum directivity $D_{\max}$: $D_{\max} > 7$ dBi;
3. good values of the radiation efficiency $\eta_{rad}$: $60\% < \eta_{rad} < 90\%$;
4. good impedance matching at the operating frequency, even at distances well below $\lambda_0/4$ from the graphene layer (due to easy–to–match values of antenna input impedance);
5. good relative bandwidth RBW for each value of $R_s$: RBW > 15%;
6. side lobe suppression with an appropriate value of $R_s$.

## 4.5. Theoretical and Experimental Study of a Terahertz Direct Receiver based on Graphene up to 10 THz

In the present paragraph, a theoretical and experimental study of a graphene–based THz receiver will be discussed for its exploitation in detection/energy–harvesting devices. First, dipole and bow–tie THz antennas on graphene will be presented, followed by the on–wafer fabrication of a graphene diode matched to the antenna and an estimation of the *Responsivity* of the receiver up to 10 THz. The obtained results show that the antenna and the diode behaviors are very different compared to semiconductor devices working at THz. These important differences are caused by the unique physical properties of graphene.

As THz technology has attained maturity, THz spectroscopy, imaging, and other various applications have grown considerably in the last decade. THz spectrometers and imaging systems are the main techniques adopted in THz technology and have a plethora of applications, spanning from explosive and concealed weapon detection up to bio–molecule detection, pharmacy and medical applications [17].

However, THz devices are still the subject of intensive research involving the most advanced micro– and nano–electronic materials and devices, such as plasma channel FETs [18], Si–FETs [19], mesocrystal microspheres [20], quantum cascade lasers [21] and graphene [22]. In spite of these efforts, the miniaturization of THz circuits and devices still exhibits

some drawbacks: for example, THz imaging is challenging since a single detector is scanning the entire image and the data rate of the image acquisition is slow, but graphene–based electro–absorption modulators as electrically reconfigurable patterns for THz cameras are investigated and promise fast data acquisition [23].

In order to enhance the miniaturizing capabilities for devices operating in the THz frequency range, graphene is an excellent candidate since it is characterized by:

1. a high mobility $\mu$ that can be improved significantly up to about 100,000 cm$^2$·V$^{-1}$·s$^{-}$1. As already stated in paragraph 4.1, $\mu$ remains high even at a high concentration value of its charge carriers ($n > 10^{12}$ cm$^{-2}$) in both electrically and chemically doped devices, which translates into ballistic transport on the sub–micrometer scale;
2. a high mean–free carrier path, of 400 nm up to 1 μm at room temperature, when encapsulated with a hexagonal boron nitride substrate [24] that matches the graphene lattice. Even for unmatched substrates, like SiO$_2$, the graphene mobility is in the range 9,000–15,000 cm$^2$·V$^{-1}$·s$^{-}$1, much higher than that of Si [25].

As a consequence, ballistic transport in graphene–based devices plays a key role in THz electronics. Nevertheless graphene devices have not yet attained their ultimate performance in the THz domain. For example, the recently reported graphene THz receiver [22] has a *Responsivity* of only ±0.04 V/W at 0.3 THz. Aim of the present paragraph is to demonstrate that a further increase of the *Responsivity* is possible, in order to be comparable with that of THz Schottky diodes, by extending at the same time the working frequency to reach 10 THz (and above).

Moreover, the unique physical properties of graphene will be further used to design new antennas and diodes with properties which do not exist in classical semiconductor–based THz devices.

First, Eq. (2) states that graphene's conductivity has two components: an intraband contribution and an interband contribution [11], which overall give rise to a complex conductivity:

$$\sigma = \sigma_{\text{intra}} + \sigma_{\text{inter}} = \sigma' + j\sigma'' \tag{14}$$

The imaginary part of conductivity $\sigma''$ plays an important role in the propagation of surface waves guided by the graphene sheet.

The intraband term is given by:

$$\sigma_{\text{intra}}(\omega) = -j\frac{e^2 K_B T}{\pi\hbar^2(\omega - j2\Gamma)}\left(\frac{\mu_c}{K_B T} + 2\ln\left(e^{-\frac{\mu_c}{K_B T}} + 1\right)\right) \tag{15}$$

whereas the interband term is expressed as follows:

$$\sigma_{\text{inter}}(\omega) = -j\frac{e^2}{4\pi\hbar}\ln\left(\frac{2|\mu_c| - (\omega - j2\Gamma)\hbar}{2|\mu_c| + (\omega - j2\Gamma)\hbar}\right) \tag{16}$$

The real part of the intraband contribution dominates over an ultra–wideband range of frequencies, from DC up to 2 ÷ 3 THz. In the same range of frequencies, the imaginary part is very small and the interband contribution is negligible.
Taking into account the following classification:

1. THz–frequency band: $0.3 \div 30$ THz;
2. IR–frequency band: $30 \div 400$ THz.

it has to be stressed that in the THz–frequency band the intraband contribution predominates and surface impedance exhibits and inductive–type imaginary part. In particular, according to Eq. (7) in the range $3 \div 30$ THz we have:

$$X_s \gg R_s \tag{17}$$

On the contrary, in the IR–frequency band the interband contribution predominates and surface impedance exhibits a capacitive–type imaginary part.

Graphene's complex conductivity, as expressed by Eq. (14), can be specified in detail as regards both the intraband and interband terms:

$$\begin{aligned} \sigma'_{intra} &\geq 0 \\ \sigma''_{intra} &< 0 \end{aligned} \tag{18}$$

For $\Gamma = 0$ and $2|\mu_c| > \hbar\omega$ we have:

$$\begin{aligned} \sigma_{inter} &= j\sigma''_{inter} \\ \sigma''_{inter} &> 0 \end{aligned} \tag{19}$$

while for $\Gamma = 0$ and $2|\mu_c| < \hbar\omega$ the interband term can be expressed as follows:

$$\begin{aligned} \sigma_{inter} &= \sigma'_{inter} + j\sigma''_{inter} \\ \sigma'_{inter} &= \frac{\pi e^2}{2h} = \sigma_{min} = 6.085 \times 10^{-5} \, [S] \\ \sigma''_{inter} &> 0 \quad for \ \mu_c \neq 0 \end{aligned} \tag{20}$$

In [26,27] negative values of the (total) imaginary part of graphene's conductivity in the THz–frequency band are reported, giving a proof of the predominant role played by the intraband term at such frequencies. Moreover, in [28] a relation between temperature and behavior of graphene's total conductivity is apparent, so that the higher the temperature the more positive the imaginary part of $\sigma$.

One of the most interesting properties of graphene is its ability to support transverse magnetic (TM) *surface plasmonic modes* with unprecedented properties. Specifically, in the THz–frequency band $\sigma$ can take a highly inductive behavior, leading to very slow TM plasmonic modes that open the way to miniaturized and low–loss devices, as well as interesting sensing applications.

The general resonance and radiation mechanisms of the antenna are similar to those of standard metallic dipoles, except for the important difference that the standing wave on the dipole corresponds to the propagation of plasmonic modes along graphene. In most cases of interest these modes are much slower than light, hence the resulting radiator is at the same time resonant and electrically very small.

Surface plasmons (SPs) are electromagnetic EM waves that propagate along the boundary surface of a metal and a dielectric. More in detail, these are transverse magnetic TM modes

accompanied by collective oscillations of surface charges, which decay exponentially in the transverse directions.

Close to the SP resonance ($\omega = \omega_{SP}$), the SP wave vector is much larger than the wave vector of the same frequency excitation in the bulk. As a result, a localized SP wave packet can be much smaller than a same–frequency wave packet in a dielectric. Moreover, this "shrinkage" is accompanied by a large transverse localization of plasmonic modes. These features are considered very promising for enabling nano–photonics, as well as high field–localization and field–enhancement.

Fig. 81 shows the typical propagation method of a TM (SP) mode along the z–direction.
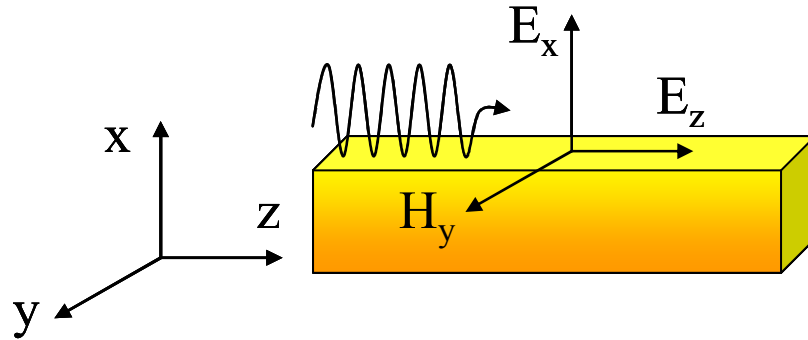


Fig. 81. Example of a TM (SP) mode propagation along the z–direction.

In the simulations carried out to compute Eq. (14), the following set of parameters was chosen, since they are typical values for graphene:

1. $T = 300$ K;
2. $\Gamma = 0.11$ meV;
3. $\mu_c = 0.13$ eV.

Although the intraband conductivity is much larger than the interband term in the THz range, both terms were taken into account for the calculation of the surface impedance.

The simulation results, illustrated in Fig. 82, show that the surface impedance is (as expected) predominantly reactive (inductive), $R_s$ having values below 52 Ω, while $X_s \gg R_s$ attains 17 ÷ 18 kΩ.

**Real part of graphene surface impedance Re{$Z_S$}**



(a)

**Imaginary part of graphene surface impedance Im{$Z_S$}**
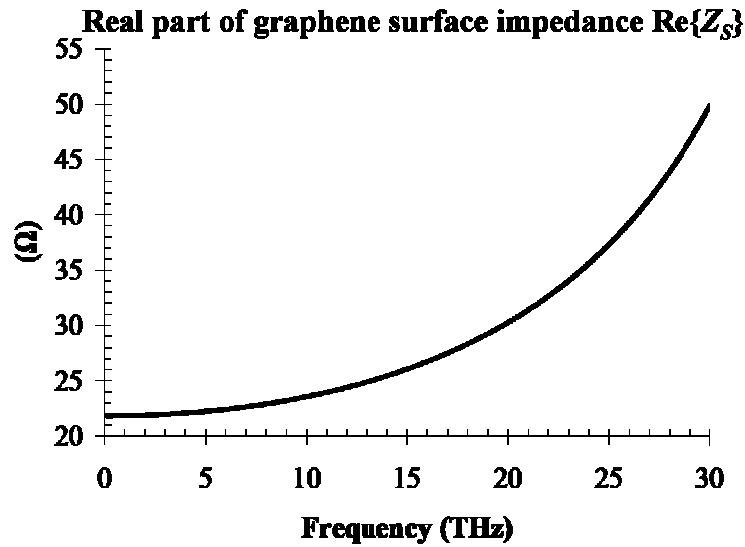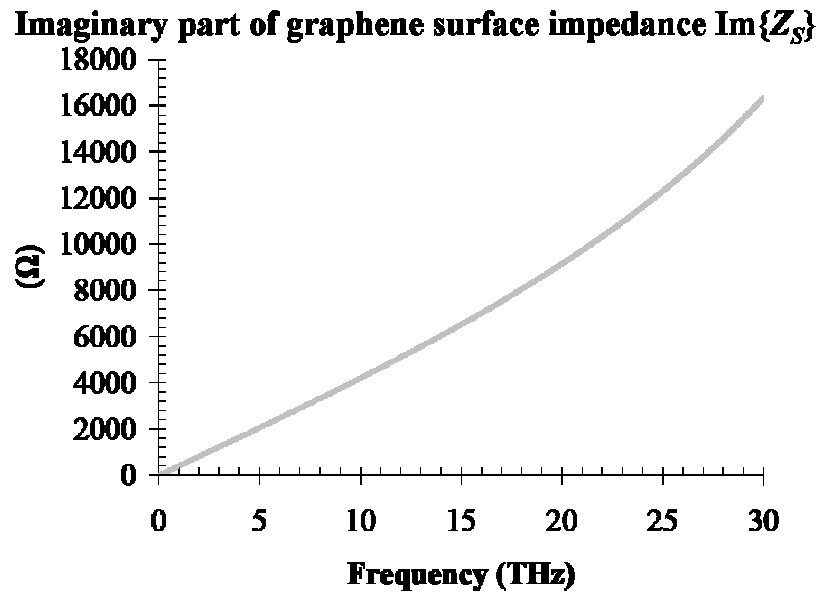


(b)

Fig. 82. Computed frequency–dependent surface impedance of graphene in the range 1 ÷ 30 THz: (a) real part of $Z_s$; (b) imaginary part of $Z_s$.

This means that graphene is a highly–Reactive Impedance Surface (RIS), which is able to reduce the lateral lobes, to enhance the front–to–back ratio of radiated power, to minimize the coupling between antenna and its image, to achieve impedance matching in possibly a wider band and to assure antenna miniaturization [29]. Furthermore, since both conductivity components depend on an applied DC electric field, the surface impedance can be modified by changing this field, since graphene is a natural tunable high RIS.

In Fig. 83 the layout of a gold dipole antenna operating at 10 THz and placed directly over a graphene monolayer deposited on a Si/SiO$_2$ substrate, where the SiO$_2$ layer has a thickness of 300 nm, is illustrated. The length of the dipole is L = 0.38$\lambda_0$ = 11.25 μm, its width is W = 1 μm, the gap is of 100 nm and the gold thickness is 200 nm. It has to be stressed that nowadays 4 inch–wafers of graphene monolayers CVD grown on Si/SiO$_2$ are commercially available.

In this case, for the EM simulations carried out by CST MWS® the following assumptions were made:

1. graphene is modeled as a realistic 3 Å–thick layer by using a table of simulated values for $Z_s$, according to Fig. 82;
2. gold is modeled as a realistic 200 nm–thick layer by using the computed dispersive values of complex permittivity/surface impedance, as done in paragraph 3.2;
3. only a SiO₂ layer was considered, otherwise simulations were not possible due to the high aspect ratio which would stem from the thick HR–Si substrate (i.e. 500 µm).

A very important characteristic of the present design is that the antenna can be directly attached to the graphene layer without being suspended as done in the previous paragraph, e.g. by means of a low–permittivity dielectric substrate. This is due to the highly–inductive behavior of graphene's surface impedance.
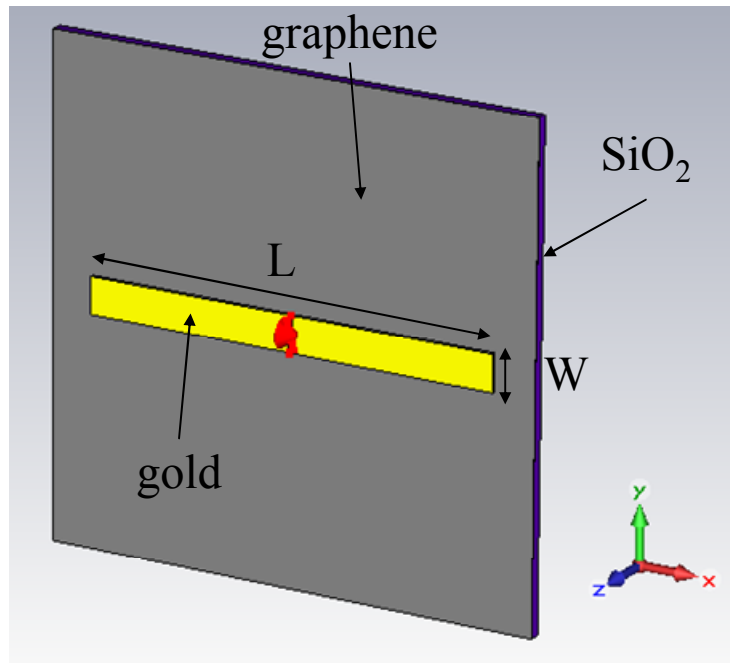


Fig. 83.  Layout of a 10 THz–resonant gold dipole antenna attached to a graphene layer.

By means of Eq. (10) of Chapter 3, the complex conductivity and surface impedance of gold were computed in the THz–frequency range, as shown in Fig. 84 for the 10 ÷ 30 THz band: Fig. 84a shows the frequency–dependence of gold's complex conductivity $\sigma_c$, whereas in Fig. 84b and Fig. 84c the real and imaginary part of gold's surface impedance $Z_s$ are depicted.
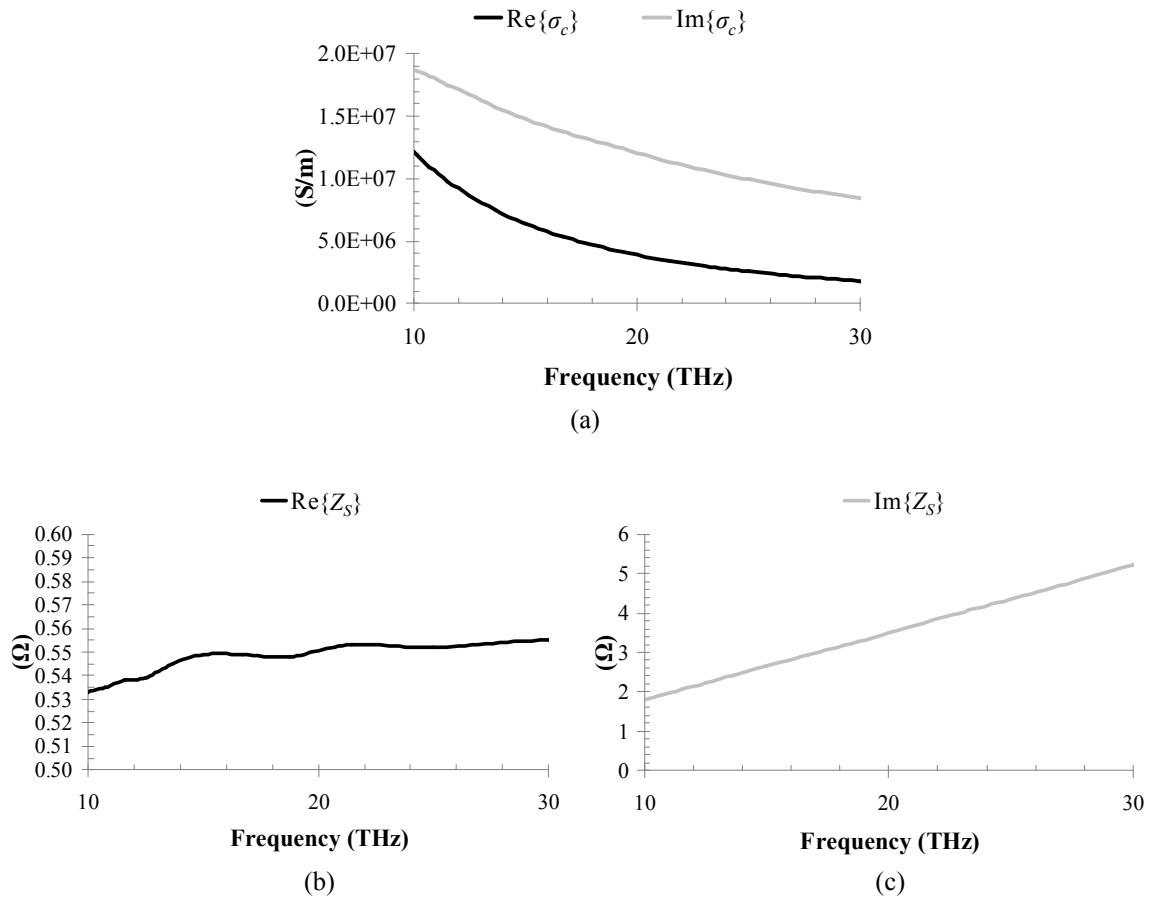
Fig. 84. EM properties of gold in the 10 ÷ 30 THz frequency range: (a) real and imaginary part of complex conductivity $\sigma_c$; (b) real part of complex surface impedance $Z_s$; (c) imaginary part of $Z_s$.

The real Re$\{Z_{11}\}$ and imaginary Im$\{Z_{11}\}$ parts of the input impedance of the THz dipole on graphene, obtained using the complex conductivity of gold in the THz region from [30], are displayed in Fig. 85a and Fig. 85b, respectively. The simulations show that there are 11 frequency points where Im$\{Z_{11}\}$ is zero, points which allow perfect matching according to the RIS theory [29], an entire frequency region existing over which Im$\{Z_{11}\}$ is small.

V/A Matrix Coefficients in Z Real Part

(a)



V/A Matrix Coefficients in Z Imaginary Part

(b)
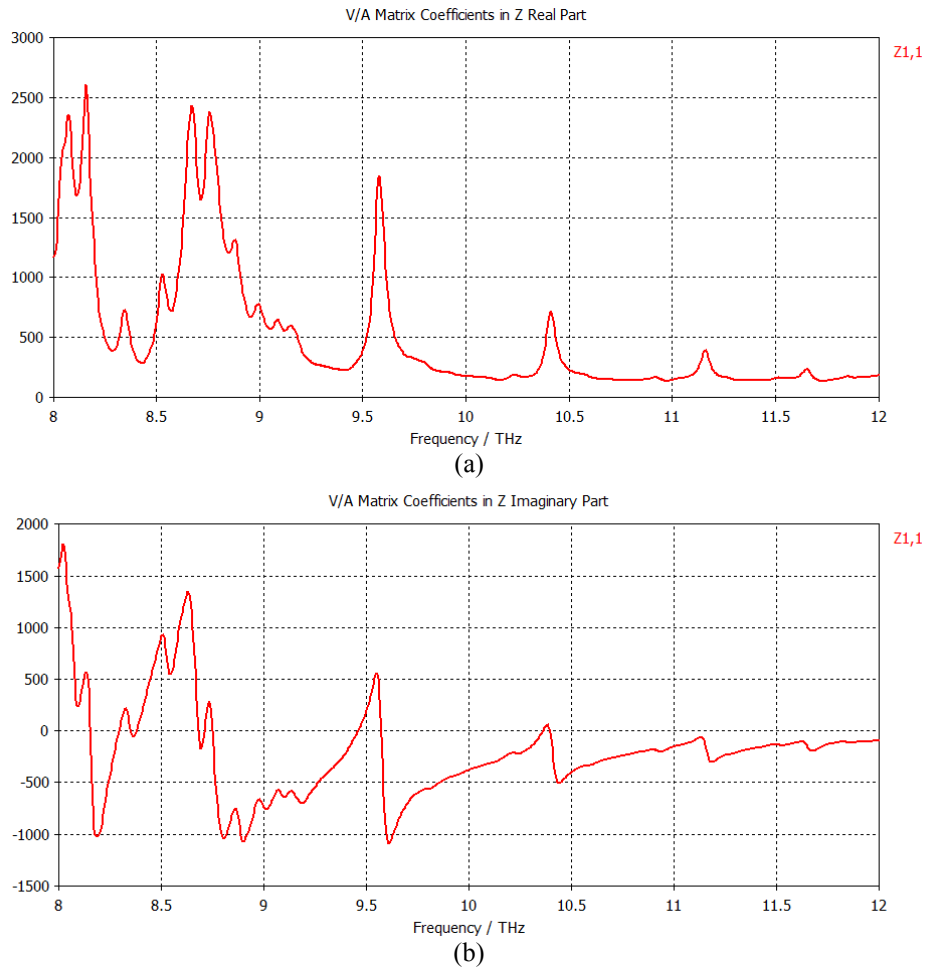
Fig. 85. The input impedance of the THz dipole antenna on graphene: (a) real part; (b) imaginary part.

The radiation pattern at the frequency of 10 THz was computed via CST and is displayed in Fig. 86, from which it can be inferred that the radiation pattern has a high front–to–back ratio of radiated power and no side lobes. The directivity of the antenna is about 6 dBi and its total efficiency is almost 15%, as can be seen from the inset in Fig. 86. The efficiency can attain up to 82% if antenna matching is improved. This is a remarkable result at such a high frequency.
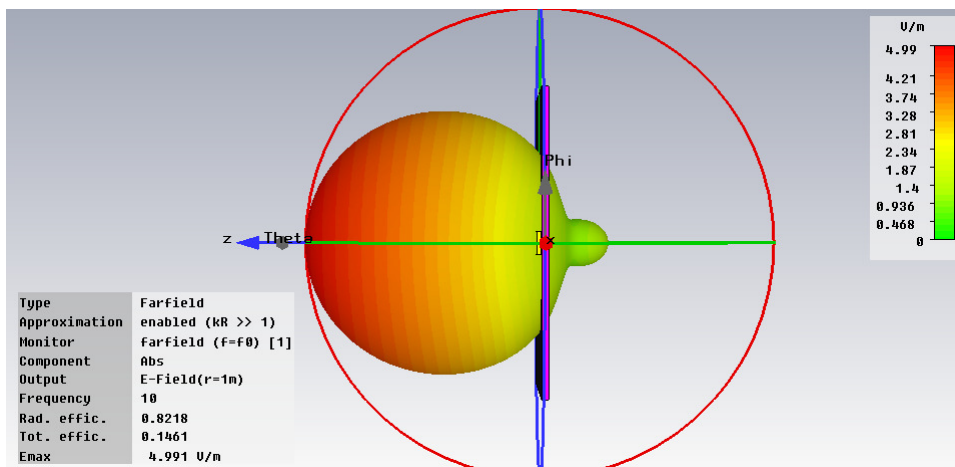


Fig. 86. Radiation pattern of the 10 THz–resonant gold dipole antenna.

In Fig. 87, another configuration of a THz antenna on graphene is presented: a gold bow–tie with $L = 0.76\lambda_0 = 22.55$ μm, $W = 13$ μm, a gap of 100 nm and gold thickness of 200 nm. The real and imaginary parts of the input impedance are represented in Fig. 88a and Fig. 88b. It is apparent that, in contrast to the dipole impedance, zero values of the imaginary part of antenna input impedance appear only at a smaller number of points (3 in Fig. 88b), at frequencies larger than 11 THz. From the radiation pattern at 10 THz illustrated in Fig. 89 it follows that the total efficiency reaches about 34%, the directivity being of about 8 dBi. Although it is well known that the bow–tie antenna has two lobes, a single lobe with a high directivity, able to collimate alone the THz radiation without any lens, is evident from the simulation in Fig. 89. This dramatic change in the radiation pattern is due to the RIS–like behavior of graphene.
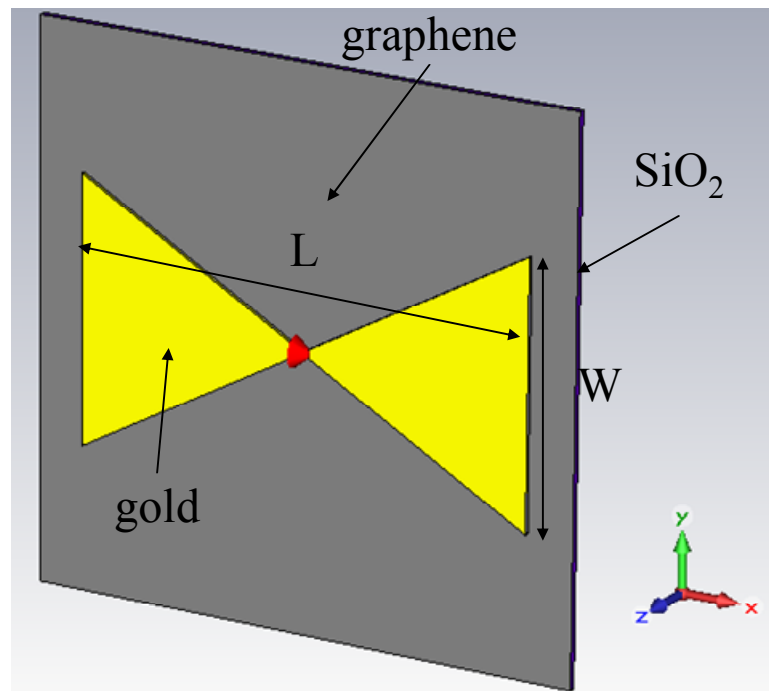


Fig. 87.  Layout of a 10 THz–resonant gold bow-tie antenna attached to a graphene layer.

V/A Matrix Coefficients in Z Real Part

(a)

V/A Matrix Coefficients in Z Imaginary Part

(b)
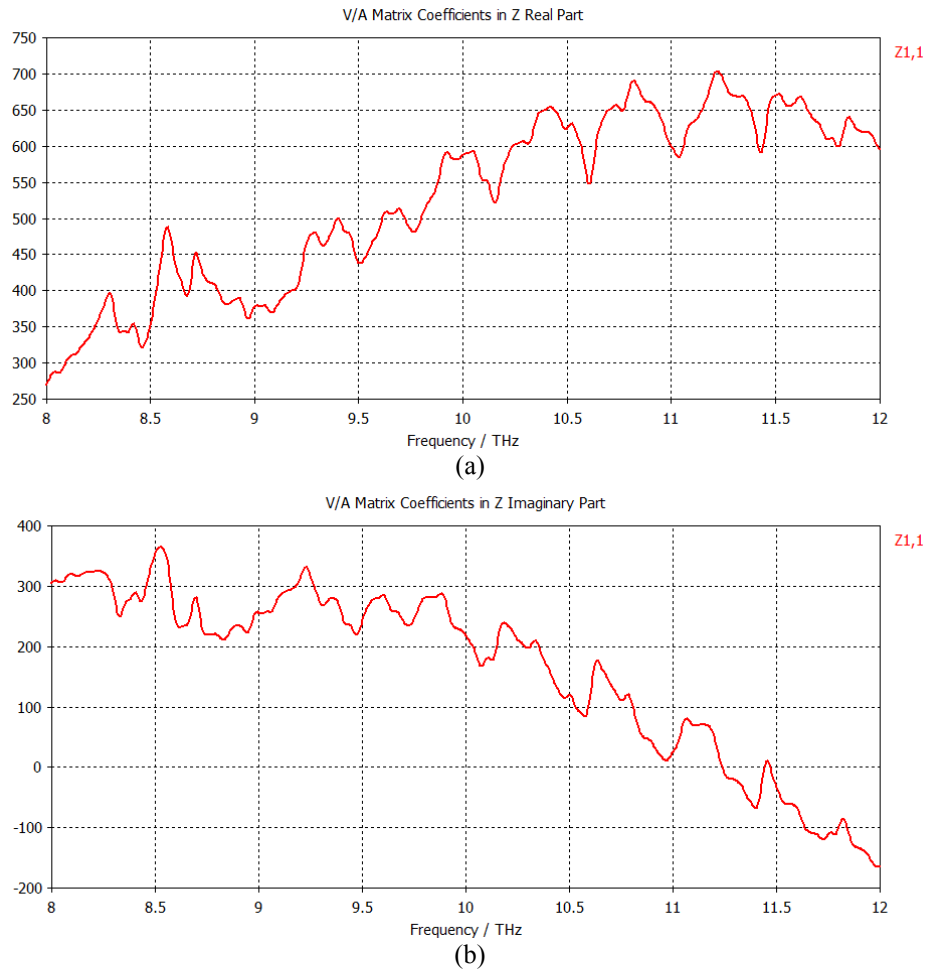
Fig. 88. The input impedance of the THz bow–tie antenna on graphene: (a) real part; (b) imaginary part.
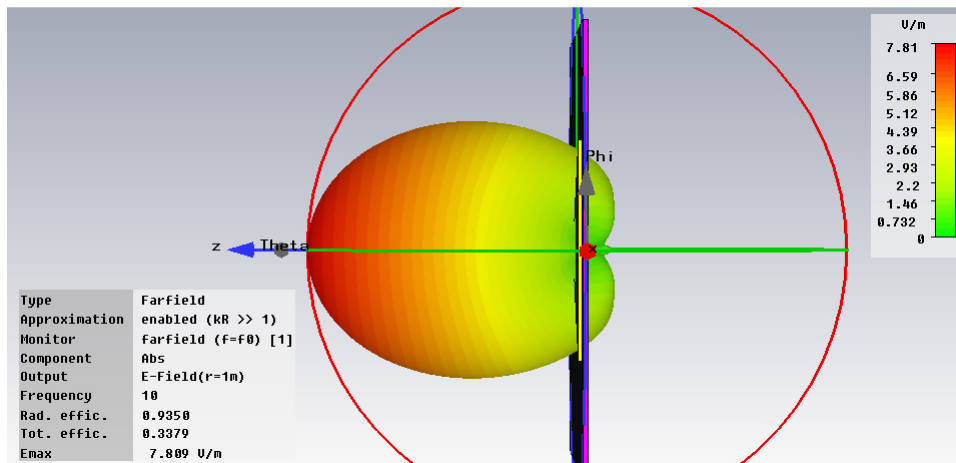


Fig. 89. Radiation pattern of the 10 THz–resonant gold bow–tie antenna.

More computational experiments reveal the fact that both the real and imaginary parts of the antenna input impedance decrease when increasing $R_s$ via a DC voltage, such that the radiation efficiency decreases. On the contrary, when $X_s$ increases, the real and imaginary parts of the input impedance become almost constant over the entire frequency band of interest, the antenna can be easily matched, its radiation efficiency increases and the back–radiation is always negligible, with no side lobes. It thus becomes possible to match the

118

antenna to a rectifying diode positioned at its end by changing the DC voltage on the antenna. Fig. 90 and Fig. 91 refer to the case $R_s$ =10 Ω and $X_s$ = 4 − 7 − 10 kΩ, whereas Fig. 92 and Fig. 93 refer to the case $R_s$ =50 Ω and $X_s$ = 4 − 7 − 10 kΩ. It has to be stressed that the latter values considered for $R_s$ and $X_s$ are quite reasonable according to the data reported in the literature.
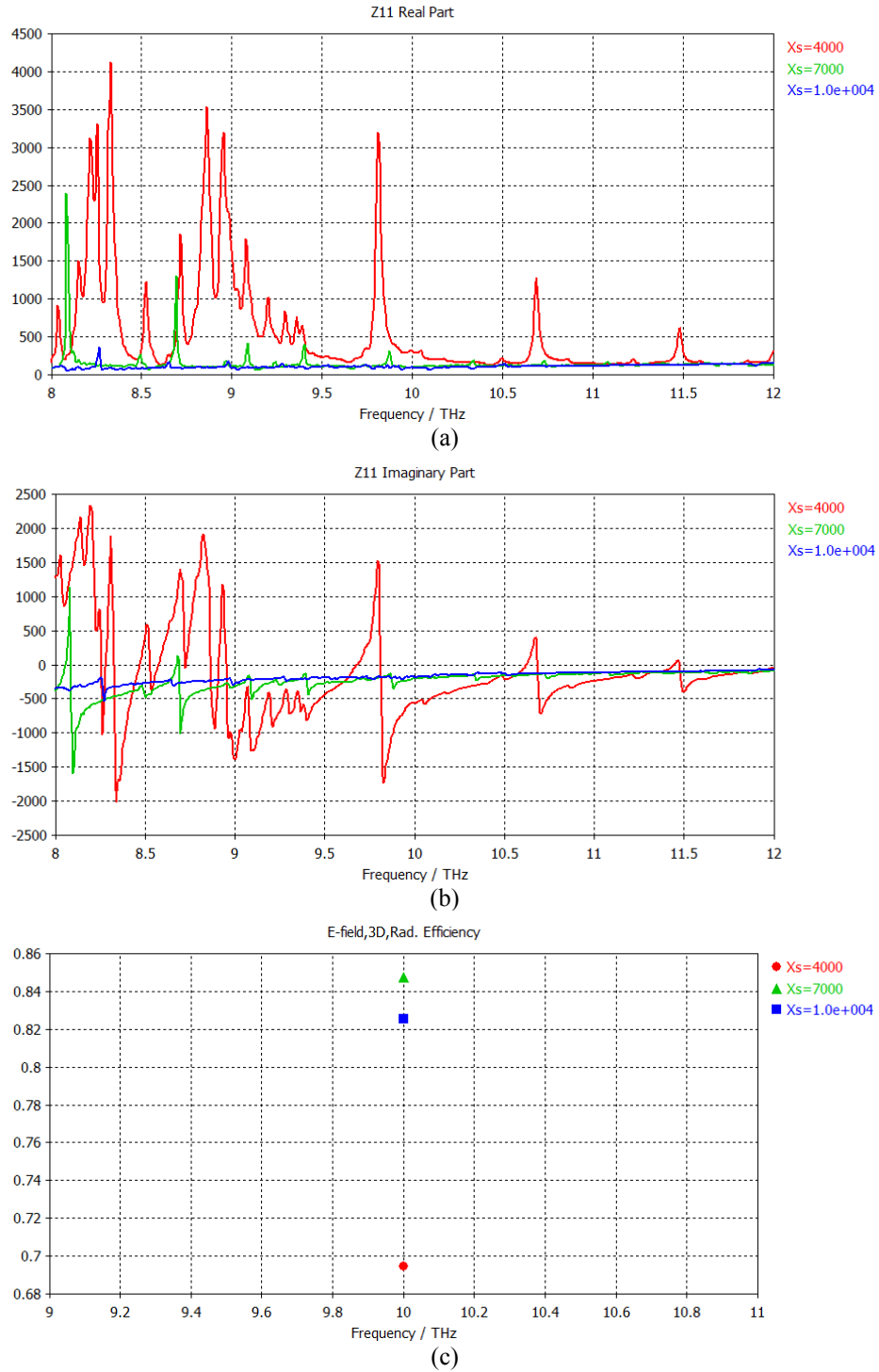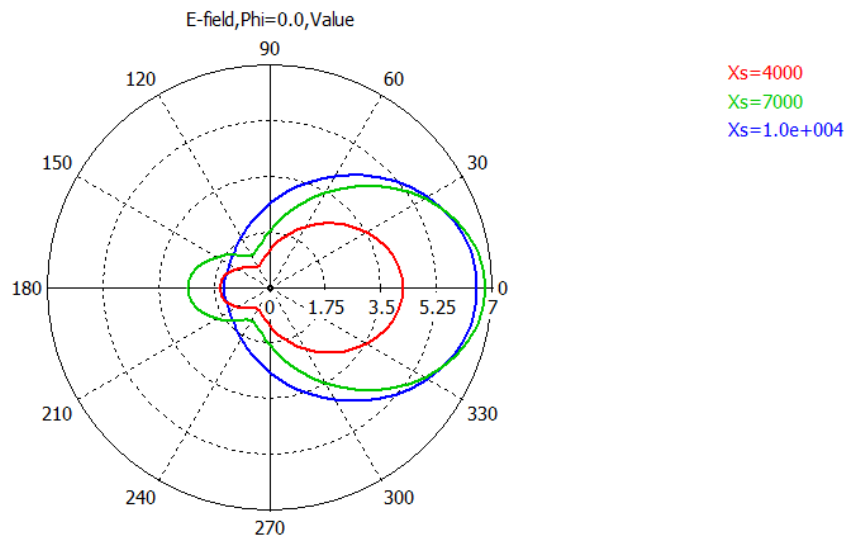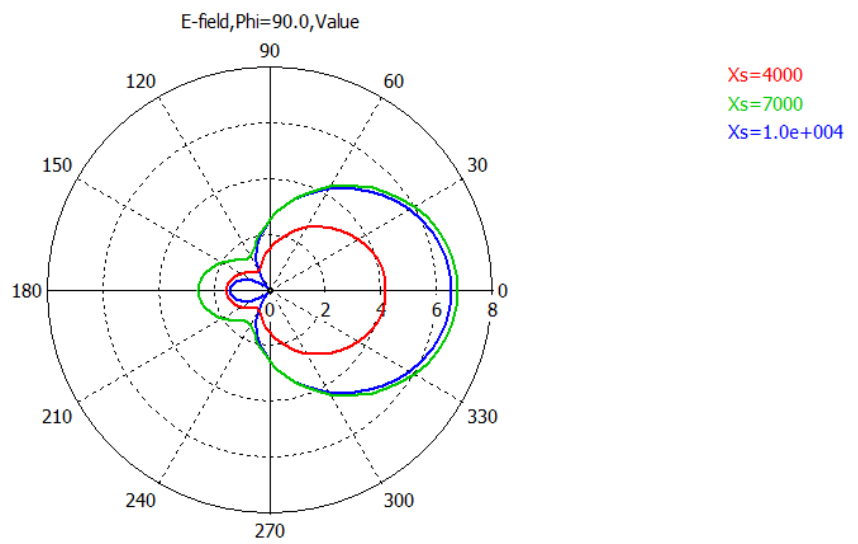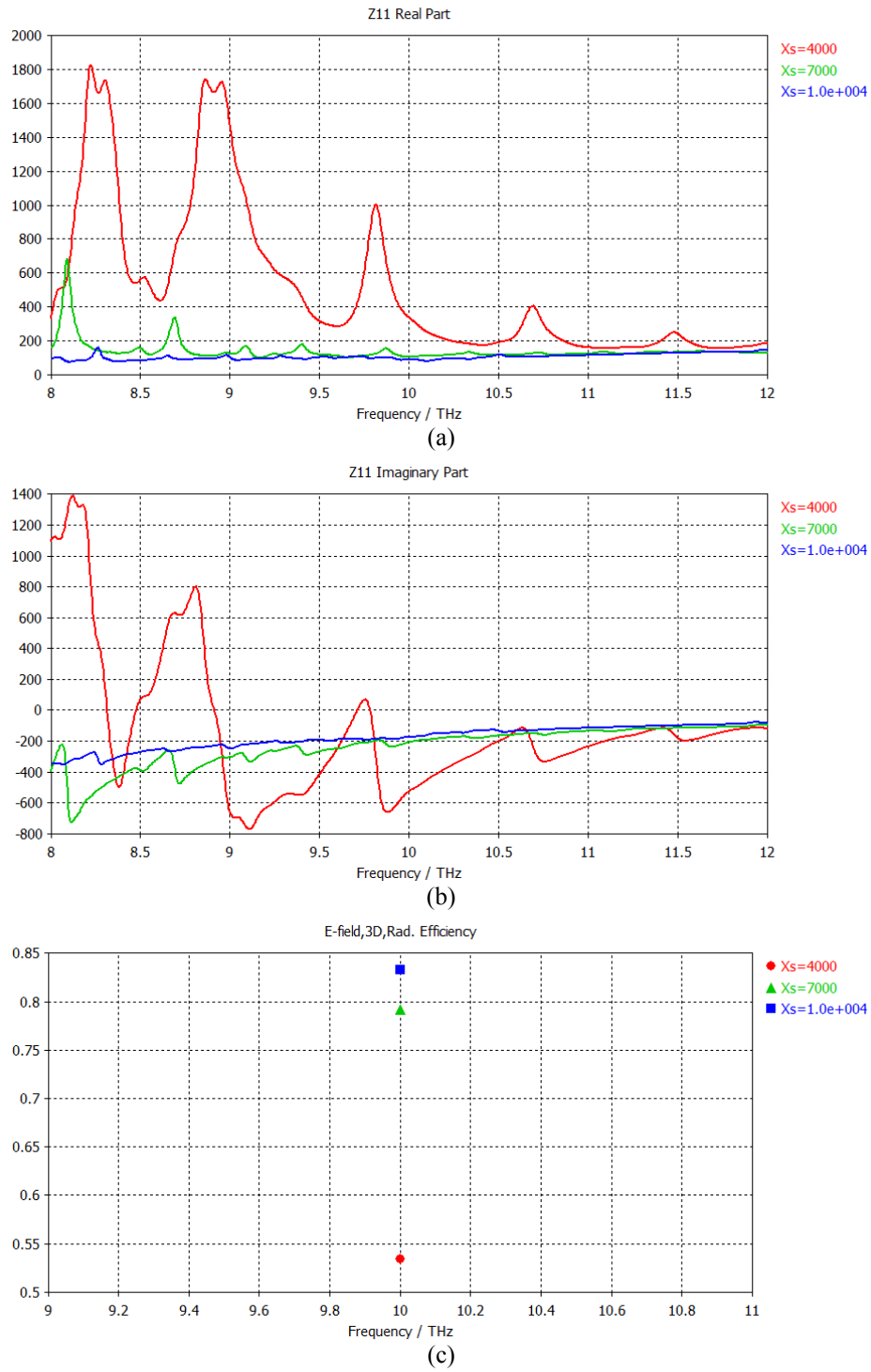


(a)



(b)



(c)

Fig. 90.  EM properties of the 10 THz–resonant gold dipole antenna for $R_s$ = 10 Ω and $X_s$ = 4 − 7 − 10 kΩ: (a) real part of input impedance; (b) imaginary part of input impedance; (c) radiation efficiency.

E-field,Phi=0.0,Value

Xs=4000
Xs=7000
Xs=1.0e+004

(a)



E-field,Phi=90.0,Value

Xs=4000
Xs=7000
Xs=1.0e+004

(b)

Fig. 91. E–field radiation patterns of the 10 THz–resonant gold dipole antenna for $R_s$ = 10 Ω and $X_s$ = 4 – 7 – 10 kΩ: (a) ϕ = 0° (horizontal) plane; (b) ϕ = 90° (vertical) plane.

120

Fig. 92. EM properties of the 10 THz–resonant gold dipole antenna for $R_s$ = 50 Ω and $X_s$ = 4 – 7 – 10 kΩ: (a) real part of input impedance; (b) imaginary part of input impedance; (c) radiation efficiency.

E-field,Phi=0.0,Value
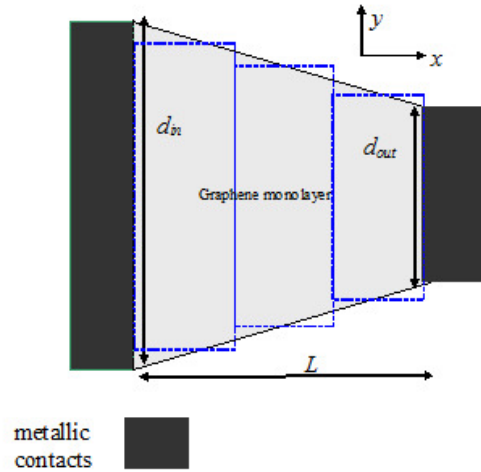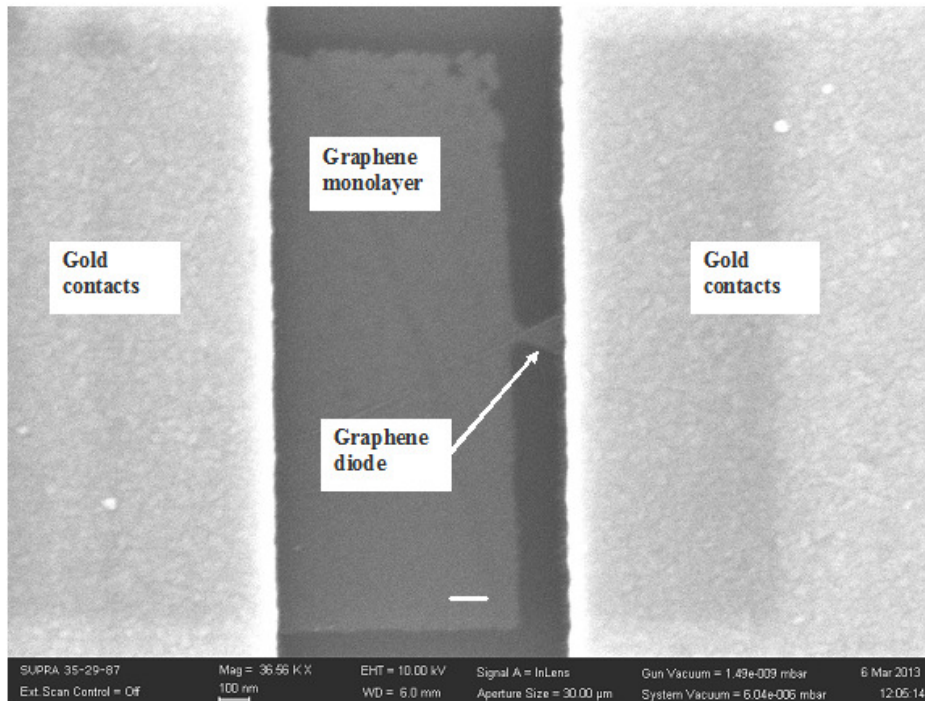


(a)

E-field,Phi=90.0,Value



(b)
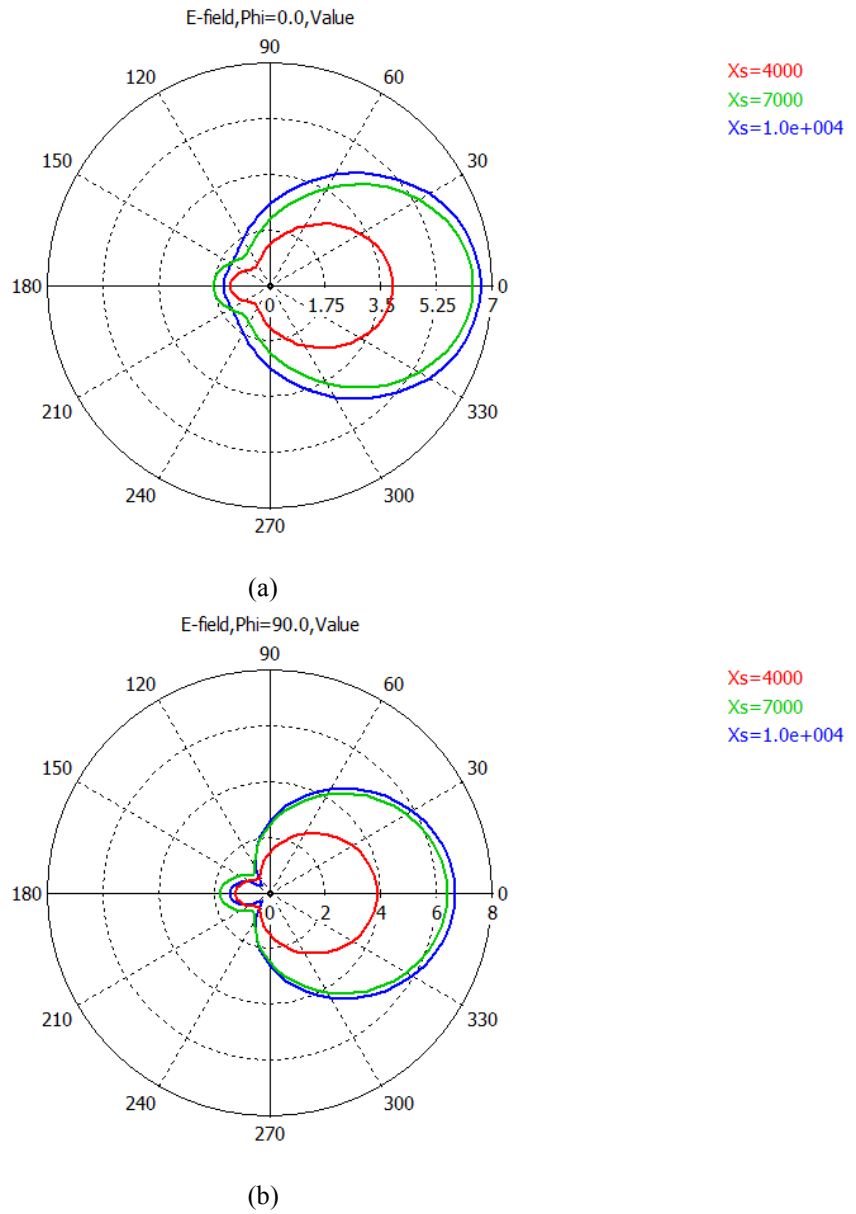
Fig. 93. E–field radiation patterns of the 10 THz–resonant gold dipole antenna for $R_s$ = 50 Ω and $X_s$ = 4 – 7 – 10 kΩ: (a) $\phi$ = 0° (horizontal) plane; (b) $\phi$ = 90° (vertical) plane.

The next device needed for a THz receiver is a graphene diode. The graphene monolayer rectifier is schematically represented in Fig. 94a, while a SEM photo of the fabricated device is shown in Fig. 94b.

Fig. 94. THz graphene geometric diode: (a) diode schematic; (b) SEM photo of the diode (the bar scale is 100 nm).

This geometrically–rectifying graphene diode works up to $20 \div 30$ THz. In the following the fabrication of the graphene diode with a length of around 100 nm will be reported, so that it is able to work in the ballistic regime at room temperature.

For the sake of clarity, a brief description of the basics of geometric graphene diode operation will be now provided.

Geometric graphene diode is modeled as a *two–dimensional electron gas* (2DEG) *device*. According to the *Ballistic Theory*, no reflections occur within the graphene used as a conductor between two contacts. At room temperature, the ballistic transport in graphene occurs for a mean–free path $L_m$ of 0.4 µm ($L_m$ is distance that an electron travels until its initial momentum is destroyed), reaching an intrinsic mobility of 44,000 cm$^2 \cdot$V$^{-1} \cdot$s$^{-1}$.

The theoretical *I–V* dependence of the graphene diode was calculated using the *Landauer formula* [31] and was found by dividing the total area of the diode in a certain number of regions (see Fig. 94a), solving the Dirac equation in each region and imposing the continuity conditions at each interface for the spinorial solutions of the Dirac equation. It was found that the diode has a certain region of width $\pi\hbar v_F/d_{out}$, with $v_F$ the Fermi velocity in graphene, where the current is nearly zero. So, the diode exhibits rectifying capabilities in this region and its *I–V* characteristic is strongly dependent on the Fermi energy, which can be tuned by a gate voltage.

The *Landauer formula* requires some assumptions:

1. reflection–less contacts. The current flowing from the conductor to the contact(s) is not reflected;
2. ballistic conductor;
3. low temperatures.

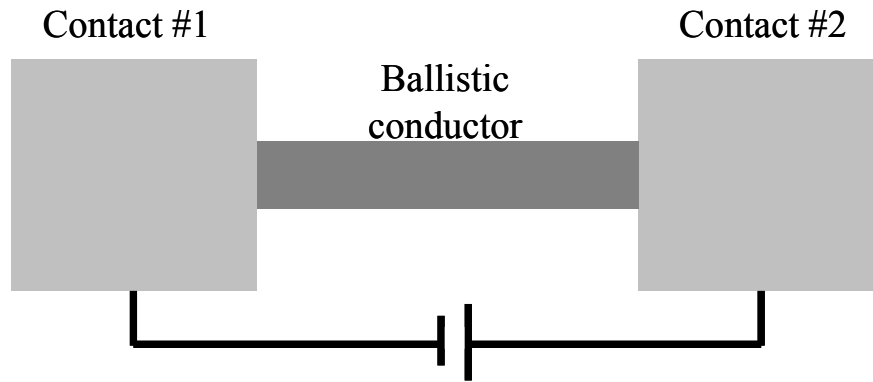Fig. 95 shows a schematic of a geometric graphene diode in ballistic regime.



Fig. 95. Schematic of a graphene geometric diode in ballistic regime.

Let us now define the following quantities:

1. be $k_F$ the Fermi wavenumber;
2. be $\lambda_F = 2\pi/k_F$ the Fermi wavelength. A realistic value is $\lambda_F = 50$ nm;
3. be $L$ the graphene conductor length, hence (in ballistic regime) we have $\lambda_F < L < L_m$. If we denote with $W$ the graphene conductor width, it results that $L \leq W$;
4. be $v_{pr}$ the propagating velocity of charge carriers. As already stated, for graphene $v_{pr} = v_F = c/300$ being $c$ the light speed in vacuum;
5. be $f_c$ the cut–off frequency of the diode. In the case of a geometric graphene diode, it is defined as $f_c = v_{pr}/L$. Hence in order to have $f_c = 10$ THz, $L$ must be equal to 100 nm;
6. be $G_q$ the quantum unit of the quantized conductance;
7. be $M$ the number of transverse modes propagating in the diode;
8. be $T(V)$ the voltage–dependent transmission coefficient in the graphene layer.

Finally, the *Landauer formula* can be expressed as follows:

$$I(V) = G_q \cdot M \cdot T(V) \cdot V$$

$$G_q = \frac{2e^2}{h} = \frac{1}{12.9\,[k\Omega]}$$

$$M = Int\left[\frac{k_F W}{\pi}\right]$$

(21)

In Fig. 96a and Fig. 96b the typical behaviors of $G_q$ and $T(V)$ are depicted, respectively, as a function of the (gate) voltage.
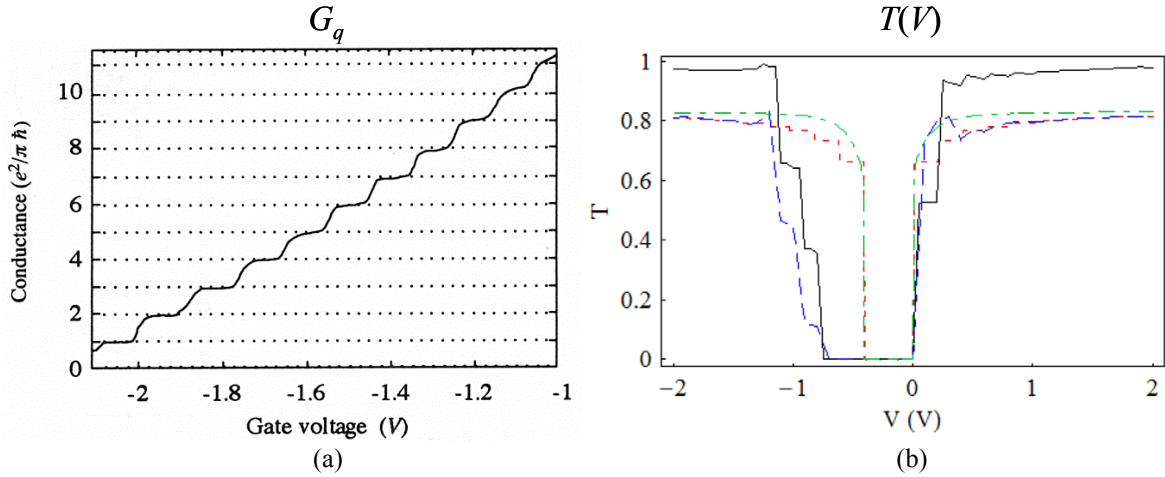


Fig. 96. Typical behavior for a ballistic graphene diode of: (a) the quantized conductance; (b) the transmission coefficient as a function of the (gate) voltage.

The geometric diode was fabricated in the laboratories of IMT on a graphene monolayer wafer deposited on a 4 in–wafer purchased from Graphene Supermarket. The graphene monolayer is grown by CVD and is deposited on 285 nm of $SiO_2$ grown on $p$–doped Si. Raman spectroscopy was used to map the graphene area and to identify the eventual cracks, as well as the graphene bi–layer, tri–layer and multilayer regions. It was discovered that 80% of the graphene wafer area consists of graphene monolayers. The regions where graphene monolayers were not present were marked by e–beam lithography, this procedure allowing the fabrication of tens of graphene diodes on the same wafer. Subsequently, PMMA 950 K Az was spin coated over the graphene wafer at 3000 rpm with a thickness of 70 nm, the geometric diode was further patterned with an e–beam tool–Raith e–Line, and a RIE equipment was used to cut the graphene in trapezoidal shapes. Then, the PMMA coating and e–beam lithography were again employed to obtain the metallic contact patterning. The metal deposition was done in a highly directional e–gun evaporation chamber (Temescal) and the lift–off process was performed in acetone. The SEM photo in Fig. 94b shows a graphene diode with a length of 100 nm, a shoulder of $d_{in}$ = 100 nm and a neck of only $d_{out}$ = 30 nm. A Keithley 4200 was used to measure several diodes on the same wafer, as illustrated in Fig. 97a. A typical $I$–$V$ dependence is presented in Fig. 97b. A region of about 140 mV around 0 V exists where the current is very small. By applying a gate voltage it was observed that at small gate voltages ($\pm$ 10 V) the current is increasing and the region where the current is zero is preserved, but at high gate voltages ($-40$ V $\div$ $-60$ V) the current is almost linear and shows a saturation region, the $I$–$V$ dependence being similar to that of a FET transistor. The results in Fig. 97b show that it is possible to build a graphene monolayer FET with a bandgap. The saturation region occurs because large gate voltages produce large densities of carriers, but only a limited number of carriers can flow through the neck of the diode, which is very small

(30 nm is about 300 atoms in width) and thus the current is saturated. The disappearance of the rectifying region at large gate voltages can be attributed to the progressive decrease of the mean–free path as the carrier concentration and their energy increase, which can lead to non–ballistic transport at large gate voltages. When the back gate is −60 V, the current at 0 V is 0.2 nA, while at +1 V increases about $8 \times 10^3$ times and reaches 15 µA, which is a remarkably large current for such a small device.
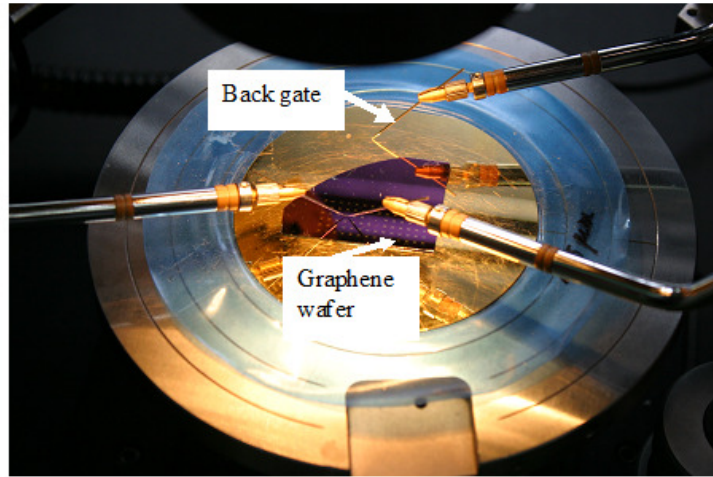


(a)
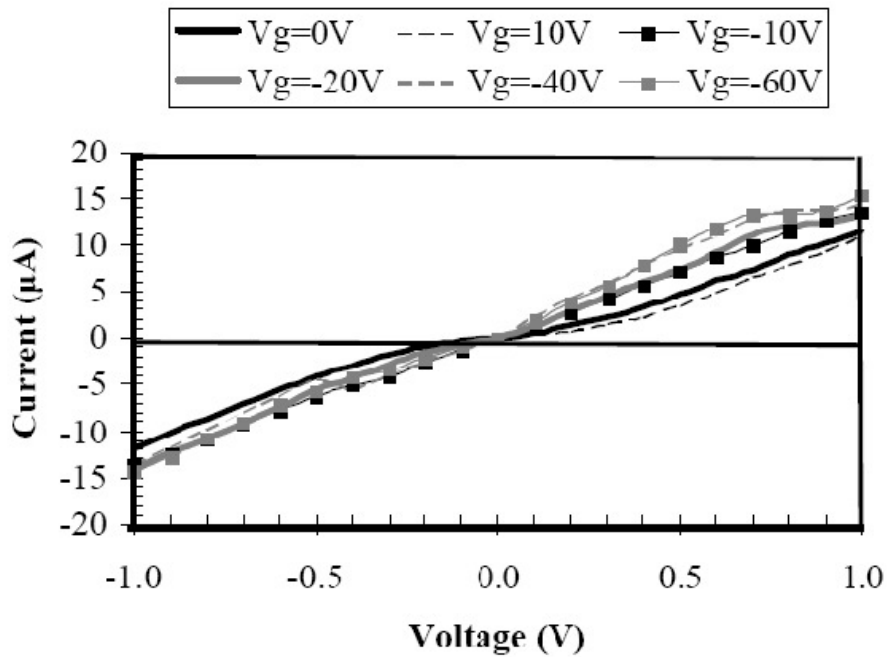


(b)

Fig. 97. The *I–V* measurement: (a) set–up, (b) measurement results for some values of the gate voltage.

Exploiting the 10 THz–resonant dipole on graphene of Fig. 83 and the graphene diode described above, the results obtained by the simulations of an entire THz receiver on graphene can ne now presented. For this purpose, the same approach adopted in Chapter 3 was used, hence the simulations were carried out by means of the NONLIN software developed by my research group at the University of Bologna. The NONLIN model takes into account the

Norton current source $J_{eq}$, equivalent to the incident EM field, using the Reciprocity Theorem of EM fields. The whole admittance matrix $\underline{Y}_A(\omega)$ of the considered antenna was used all over the band of interest. An inductance of 1 μH was used inside the circuit topology to simulate a filter that avoids a high–frequency output power: the chosen value provides very low–power levels of the higher harmornics (the total number set for the nonlinear simulations is 3). Series capacitors may be also necessary to block the DC current going into the antenna (as this is the "classical" harvester topology), but the miniaturized characteristics of the system and the fact that the diode is put in the gap of the dipole antenna suggested to not consider the afore–mentioned capacitances. By the way, at THz frequencies only transmission line components could be used to create lumped elements. The graphene diode was modeled as a voltage–dependent current source (whose equation is given by the *Landauer formula* expressed in Eq. (21)) in parallel with a (static) junction capacitance $C_J$ of 1 aF. The load is considered to be 50 Ω. The modeling structure of the THz receiver on graphene is depicted in Fig. 98.
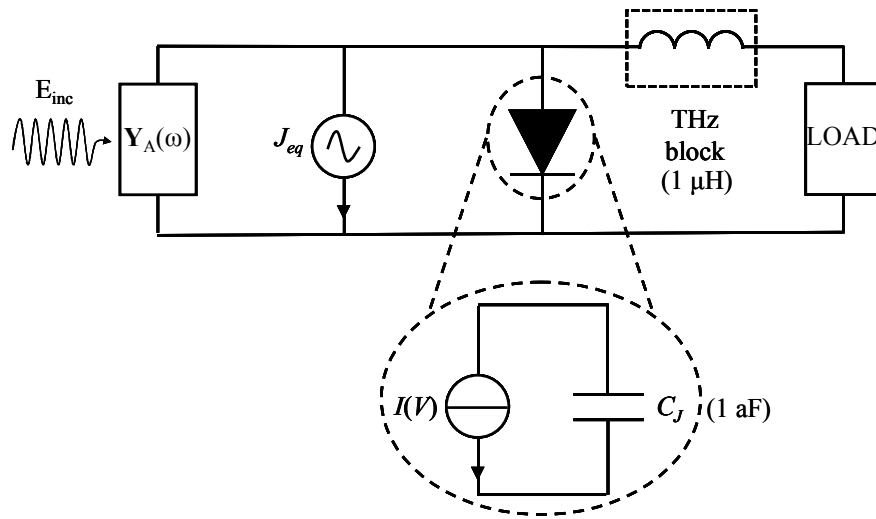


Fig. 98. NONLIN model of the circuit topology for the THz receiver on graphene.

The *Voltage Responsivity $R_V$* can be defined as follows:

$$R_V = \frac{V_{DC}}{P_{in}} \quad [V/W] \tag{22}$$

where $V_{DC}$ is the rectified voltage and $P_{in}$ is the input power.

According to the literature, a reference value for $P_{in} = 1$ μW was chosen. It has to be stressed that $P_{in}$ represents the power level assigned to the source inside the nonlinear simulator and does not represent necessarily the effective power incident onto the diode. This assumption is mandatory to make homogeneous comparisons among the various cases of study.

In the following, the graphs of the *Voltage Responsivity $R_V$* and of the rectified power $P_{DC}$ as a function of the frequency are shown, for 17 values of THz frequencies: 0.2, 0.3, 0.4, 0.5, 0.6, 0.7, 0.8, 1, 2, 3, 4, 5, 6, 7, 8, 9 and 10 THz. As stated above, a reference value of 50 Ω for the LOAD displayed in Fig. 98 was used for all the nonlinear simulations.

The EM simulations of the THz antennas at the afore–mentioned frequencies were carried out by using an excitation port with fixed impedance $Z_{port} = 75$ Ω. This assumption affects only the behavior of the reflection coefficient $|S_{11}|$, since no prediction of the effective antenna input impedance was possible due to the presence of the graphene layer under the

gold metallization. In any case, for the subsequent nonlinear simulations, the admittance matrix $\underline{Y}_A$ was exploited, which is independent of the normalization impedance used for the scattering matrix $\underline{S}$.

The EM simulations of the THz antennas highlighted that the antenna input impedance $Z_A = R+jX$ is mostly reactive (inductive) up to 3 THz with $R < X$, hence gold radiators act like reactive (inductive) antennas. Starting from 4 THz, antennas behave as dipoles with multiple resonances (in correspondence of which $X = 0$ $\Omega$) over the band of interest.

Fig. 99 shows the behavior of the absolute value of the THz voltage $|V_{THz}|$ on the diode when varying the frequency, since it gives a preliminary idea of the rectification/detection capabilities of the graphene diode.



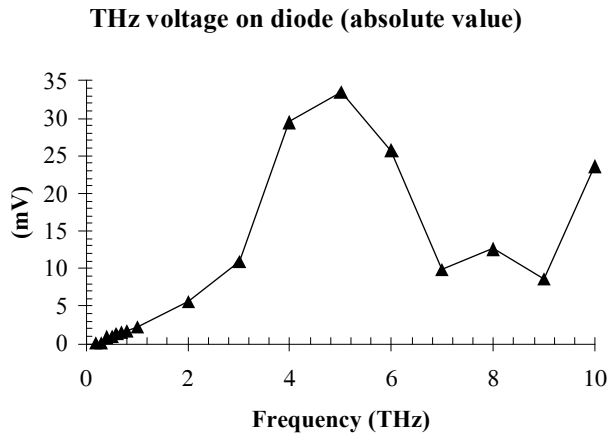**THz voltage on diode (absolute value)**

Fig. 99.  Absolute value of the THz voltage on the graphene diode as a function of the frequency.

Fig. 99 demonstrates that the lowest value of $|V_{THz}|$ is reached at 0.2 THz ($\approx$ 0.173 mV), whereas the highest one is reached at 5 THz ($\approx$ 33.414 mV). This means that the maximum THz voltage applied to the graphene diode is very low, hence we can expect low rectification/detection capabilities due to the fact that the diode itself works around the origin of the $I$–$V$ characteristics.

Nevertheless, as will be demonstrated in the following, reasonable values of the *Voltage Responsivity $R_V$* were obtained in despite of the afore–mentioned low applied THz voltages.

Now let us show the behavior (in Fig. 100) of the absolute value of the THz current flowing in the diode $|I_{THz}|$ when varying the frequency. For the sake of comparison, two values of the applied gate voltage $V_g$ were considered, i.e. $V_g = 0$ V (unbiased case) and $V_g = -20$ V.
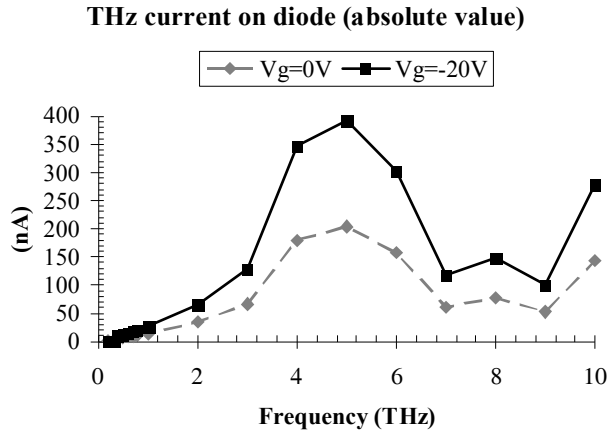
**THz current on diode (absolute value)**



Fig. 100.  Absolute value of the THz current flowing in the graphene diode as a function of the frequency.

The two values of $V_g$ correspond to two *I–V* characteristics: $V_g = 0$ V is the specific case for the graphene diode acting as a real rectifier, hence without bias.

It is evident how the curve trend is the same in the two cases, but with much higher values of $|I_{THz}|$ for $V_g = -20$ V. In fact, the peak value (in correspondence of 5 THz) is about 200 nA for $V_g = 0$ V and about 400 nA (hence doubled) for $V_g = -20$ V.

In Fig. 101, the THz power absorbed by the graphene diode is shown.

**THz power absorbed by diode**



(a)

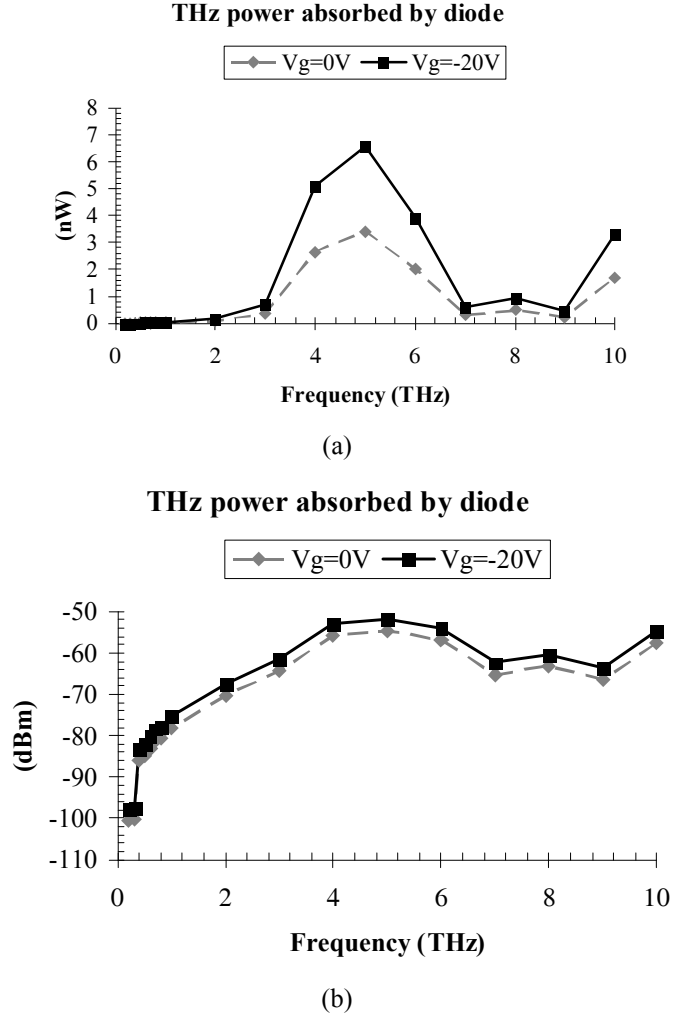**THz power absorbed by diode**



(b)

Fig. 101. THz power absorbed by the graphene diode: (a) linear scale; (b) logarithmic scale.

The *Voltage Responsivity* $R_V$ is represented in Fig. 102 when the input power is 1 μW and the back gate is 0 V (a) and −20 V (b), respectively. The nonlinear performance of the graphene diode guarantees a *Voltage Responsivity*:

1. $R_{V,Vg=0V} > 6.6$ V/W
2. $R_{V,Vg=-20V} > 21.3$ V/W

hence $R_{V,Vg=-20V} > 3 \cdot R_{V,Vg=0V}$.

The difference is due to the different nonlinearity of the *I–V* characteristics according to the applied gate voltage.

The dynamic range of the variations in the $R_V$ curves (in both cases) is not very wide because the reference values of the applied THz voltage $|V_{THz}|$ are low, i.e. do not exceed about 33 mV. In any case, the values obtained for $R_V$ are with orders of magnitude larger than the present state–of–the–art values of THz receivers based on graphene.

**Responsivity: Vg = 0 V, Pin = 1 μW**



(a)

**Responsivity: Vg = -20 V, Pin = 1 μW**
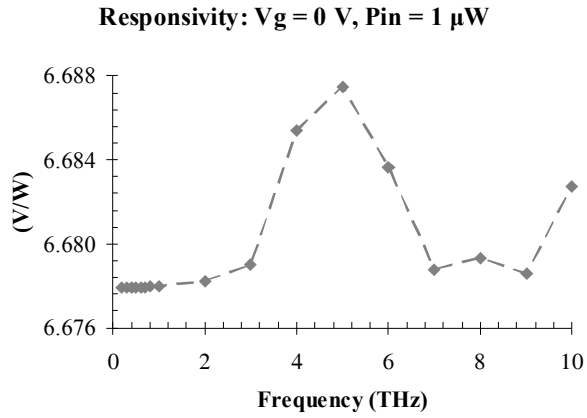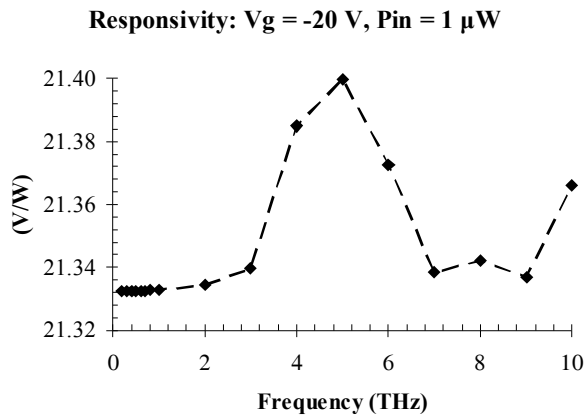


(b)

Fig. 102. *Voltage Responsivity $R_V$ of the graphene diode (as a function of frequency) for two different values of the applied gate voltage $V_g$: (a) $V_g = 0$ V; (b) $V_g = -20$ V.*

Finally, the computed results for the rectified power $P_{DC}$ are depicted in Fig. 103. In this case, a difference of 10 dB is apparent in the values of $P_{DC}$ for the two cases $V_g = 0$ V and $V_g = -20$ V. As stated before regarding the results for $R_V$, the dynamic range of the variations in the $P_{DC}$ curves (in both cases) is not very wide because the reference values of the applied THz voltage $|V_{THz}|$ are low, i.e. do not exceed about 33 mV.
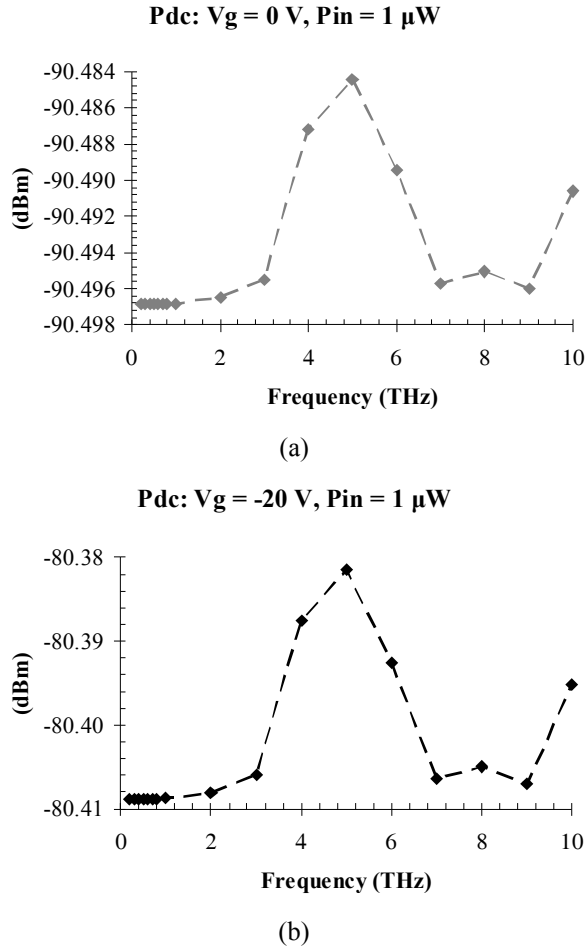
**Pdc: Vg = 0 V, Pin = 1 μW**



(a)

**Pdc: Vg = -20 V, Pin = 1 μW**



(b)

Fig. 103. Rectified power $P_{DC}$ of the graphene diode (as a function of frequency) for two different values of the applied gate voltage $V_g$: (a) $V_g = 0$ V; (b) $V_g = -20$ V.

A last issue addressed in the present research is the matching problem of the diode with the antenna, taking into account that the resistance series of the diode is around 64 kΩ. Indeed such a matching can be achieved because also the dipole on graphene has a large reactive part, in the order of 5 kΩ ÷ 10 kΩ. To match the 10 THz–resonant dipole antenna to the graphene diode around 8 ÷ 10 THz we need the AWR circuit topology shown in Fig. 104: since the operating frequency is very high, very small transmission lines are needed for the two parallel inductances of 0.5 nH connected to the antenna, ended by a capacitor of 0.5 fF which in turn is in parallel with the 64 kΩ–diode. For the AWR design, the graphene diode is modeled as an RC–parallel circuit with R_diode = 64 kΩ and C_diode = 1 aF. The design exploits the scattering matrix of the antenna and the above–mentioned parallel circuit equivalent to the graphene diode.

Finally, in Fig. 105 the |S₁₁| dB parameter at the diode output is represented, from which it can be inferred that at 8.1 THz and 8.8 THz a very good value for the reflection coefficient of −13.3 dB can be obtained (corresponding to a VSWR = 1.53).
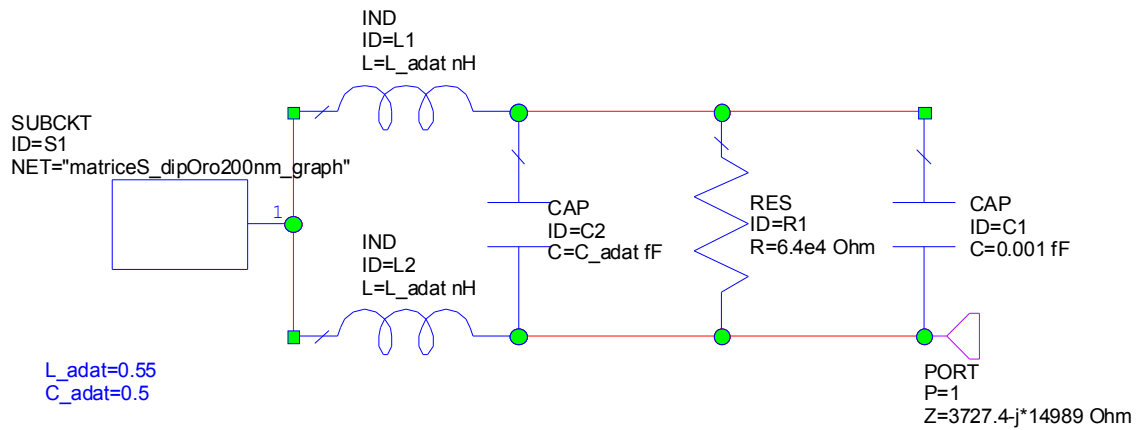
Fig. 104. AWR design of the circuit topology for the impedance matching between the 10 THz–resonant dipole and the graphene diode with a series resistance of 64 kΩ.
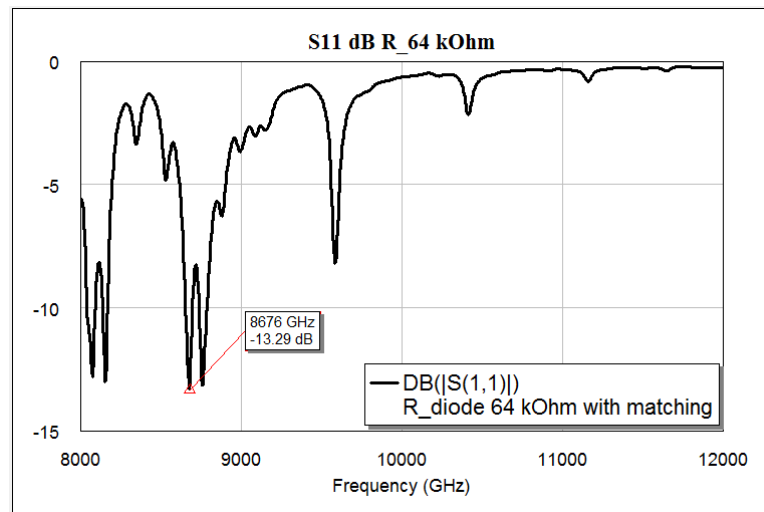


Fig. 105. Frequency–dependence of $|S_{11}|$ dB for the matching between the dipole antenna and the graphene

## CONCLUSIONS

In the present chapter a detailed description of the research activity carried out throughout the six months spent at IMT, Bucharest (RO), in the last year of my PhD course has been presented. A scientific exchange between my research group at University of Bologna and the MIMOMEMS group at IMT has led to interesting results in the field of innovative MW and THz applications. In particular, starting from the peculiar physical properties of graphene, it has been demonstrated that a new family of high–performance receivers in the THz frequency range can be developed by means of a low–cost integration of a metal antenna (dipole or bow–tie) with a graphene RIS and a geometric graphene diode. The results obtained so far show that it is possible to design THz devices for a twofold purpose: i) "classical" spectroscopy/imaging techniques; ii) energy–harvesting applications. This can be achieved by applying or not a bias gate to the graphene RIS that acts as a reflector, providing excellent performance in terms of both radiation characteristics (reduced back–radiation, absence of side lobes, good values of the radiation efficiency) and impedance matching to the antenna

133

input impedance. Nowadays, the technological constraints allow to design geometric graphene diodes with a cut–off frequency of maximum few tens of THz but with rectification properties better than those provided by the MOM diodes presented in Chapter 3.

Thanks to the expertise of the people with whom I collaborated at IMT, I could design and study the properties of the proposed devices with a strong technological approach: the most important consequence of such a method is that the CAD design presented in each paragraph can be considered as a good representation of the real working conditions of the device itself, thus providing reliable results which I expect to test in the next future by synthesizing all the receivers described above.

Finally, the combination of an EM simulation tool with the nonlinear simulator developed by my research group has represented so far an extraordinary instrument to accurately predict the performance of various devices in a realistic operating situation.

## REFERENCES

[1] A. K. Geim and K. S. Novoselov, "The rise of graphene", *Nature Materials*, Vol. 6, pp. 183–191, March 2007.

[2] K. S. Novoselov, A. K. Geim, S. V. Morozov, et al., "Electric field effect in atomically thin carbon films", *Science*, Vol. 306, pp. 666–669, 2004.

[3] H. Wang, D. Zenich, J. Kong, and T. Palacios, "Graphene frequency multipliers", *IEEE Electron Device Lett.*, Vol. 30, pp. 547–549, 2009.

[4] V. P. Gusynin, S. G. Sharapov, and J. P. Carbotte, "Magneto–optical conductivity in graphene", *Journal of Physics: Condensed Matter*, Vol. 9, No. 2, p. 026222, 2007.

[5] J. Martin, N. Akerman, G. Ulbricht, T. Lohmann, J. H. Smet, K. von Klitzing, and A. Yacoby, "Observation of electron–hole puddles in graphene using a scanning single–electron transistor", *Nat. Phys.*, Vol. 4, pp. 144–148, 2007.

[6] J. S. Gómez–Díaz, J. Perruisseau–Carrier, P. Sharma, and A. Ionescu, "Non–contact characterization of graphene surface impedance at micro and millimeter waves", *J. Appl. Physics*, Vol. 111, p. 114908, 2012.

[7] D. Mencarelli, M. Dragoman, L. Pierantoni, T. Rozzi, and F. Coccetti, "Design of a coplanar graphene–based nano–patch antenna for microwave application," *Proc. of the Internal Microwave Symposium*, Tampa, Florida, USA (2013).

[8] S. A. Mikhailov, "Electromagnetic response of graphene: Non–linear effects," *Physica E*, Vol. 40, pp. 2626–2629, 2008.

[9] Q. Bao and K. P. Loh, "Graphene photonics, plasmonics, and broadband optoelectronic devices", *ACS Nano*, Vol. 6, pp. 3677–3694, 2012.

[10] H. S. Skulason, H. V. Nguyen, A. Guermoune, V. Sridharan, M. Siaj, C. Caloz, and T. Szkopek, "110 GHz measurement of large–area graphene integrated in low–loss microwave structures", *Appl. Phys. Lett.*, Vol. 99, p. 153504, 2011.

[11] G. W. Hanson, "Dyadic Green's function and guided surface waves for a surface conductivity model of graphene", *J. Appl. Phys.*, Vol. 103, p. 064302, 2008.

[12] B. S. Rodríguez, R. Yen, L. Liu, D. Jena, and H. G. Xiang, "Graphene for reconfigurable terahertz optoelectronics", *Proc. IEEE*, Vol. 101, pp. 1705–1716, 2013.

[13] A. Eldek et al., "Wideband antennas for radar applications", *IEEE MTT–S*, p. 79, 2003.

[14] M. Dragoman, D. Neculoiu, A. Cismaru, A. A. Müller, G. Deligeorgis, G. Konstantinidis, D. Dragoman, and R. Plana, "Coplanar waveguide on graphene in the range 40 MHz – 110 GHz", *Appl. Phys. Lett.*, Vol. 99, p. 033112, 2011.

[15] D. Sievenpiper, L. Zhang, R. F. J. Broas, N. G. Alexópolous, and E. Yablonovitch, "High–impedance electromagnetic surfaces with a forbidden frequency band", *IEEE Trans. Antenna and Prop.*, Vol. 47, pp. 2059–2074, 1999.

[16] H. Ahn, B. H. Hong, S. Bae, H. Kim, Y. Leo, X. Xu, J. S. Park, K. S. Kim, B. Ozyilmaz, and S. Iijima, "Roll–to–roll production of 30 graphene film for transparent electrodes", *Nat. Nanotechnology*, Vol. 5, p. 574, 2010.

[17] J. Federici and L. Moeler, "Review of terahertz and subterahertz wireless communications", *J. Appl. Phys.*, Vol. 107, p. 111101, 2010.

[18] W. Knap, S. Rumyantsev, M. S. Vitiello, D. Coquillat, S. Blin, N. Dyakonova, M. Shur, F. Teppe, A. Tredicucci, and T. Hagarsua, "Nanometer size field effect transistors for terahertz detectors", *Nanotechnology*, Vol. 24, p. 214002, 2013.

[19] D. Glaab, S. Boppel, A. Lisauskas, U. Pfeiffer, E. Öjerfors, and H.G. Roskos, "Terahertz heterodyne detection with silicon field transistors", *Appl. Phys. Lett.*, Vol. 96, p. 042106, 2010.

[20] X. L. Wu, S. J. Xiong, Z. Liu, J. Chen, J. C. Shen, T. H. Li, P. H. Wu, and P. K. Chu, "Green light stimulated terahertz emission, from mesocrystal microspheres", Nature *Nanotechnologies*, Vol. 6, pp. 103–106, 2011.

[21] M. C. Wanke, E. W. Young, C. D. Norquist, M. J. Cich, A. D. Grine, C. T. Fuller, J. L. Reno, and M. Lee, "Monolithically integrated solid–state terahertz transceivers", *Nature Photonics*,Vol. 4, pp. 565–569, 2010.

[22] L. Vicarelli, M. S. Vitiello, D. Coquillat, A. Lombardo, A. C. Ferrari, W. Knap, M. Polini, V. Pellegrini and A. Tredicuci, "Graphene field–effect transistors as room temperature terahertz detectors", *Nature Materials*, Vol. 11, pp. 865–871, 2012.

[23] B. Sensale–Rodriguez, S. Rafique, R. Yan, M. Zhu, V. Protasenko, D. Jena, L. Liu, and H. G. Xing, "Terahertz imaging employing graphene modulator arrays", *Optics Express*, Vol. 21, pp. 2324–2330, 2013.

[24] A. S. Mayorov, R. V. Gorbachev, S. V. Morozov, L. Britnell, R. Jail, L. A. Ponomarenko, K. S. Novoselov, K. Watanabe, T. Taniguchi, and A. K. Geim, "Micrometer–scale ballistic transport in encapsulated graphene at room temperature", *Nano Letters*, Vol. 11, pp. 2396–2399, 2011.

[25] J.–H. Chen, C. Jang, S. Xiao, M. Ishigami, and M. S. Fuhrer, "Intrinsic and extrinsic performance limits of graphene devices on $SiO_2$", *Nature Nanotechnology*, Vol. 3, p. 206, 2008.

[26] J. Perruisseau–Carrier in "Graphene for Antenna Applications: Opportunities and Challenges from Microwaves to THz", *Loughborough Antennas & Propagation Conference*, 2012, UK.

[27] J. S. Gómez–Díaz, J. Perruisseau–Carrier, "Microwave to THz Properties of Graphene and Potential Antenna Applications, *Proc. of ISAP2012*, Nagoya, Japan, pp. 239–242, 2012.

[28] L. A. Falkovsky, "Optical properties of graphene", *Journal of Physics: Conference Series*, Vol. 129, p. 012004, 2008.

[29] H. Mosallaei and K. Sarabandi, *IEEE Trans. Antennas and Prop.*, Vol. 52, pp. 2403–2414, 2004.

[30] M. A. Ordal, L. L. Long, R. J. Bell, S. E. Bell, R. R. Bell, R. W. Alexander Jr., and C. A. Ward, "Optical properties of the metals Al, Co, Cu, Au, Fe, Pb, Ni, Pd, Pt, Ag, Ti, and W in the infrared and far infrared", *Appl. Opt.*, Vol. 22, No. 7, pp. 1099–1120, 1 April 1983.

[31] D. Dragoman and M. Dragoman, "Geometrical–induced rectification in two–dimensional ballistic nanodevices", *J. Phys. D*, Vol. 46, p. 055306, 2013.

# FINAL CONCLUSIONS

The present PhD thesis is the results of three years of studies carried out at the Faculty of Engineering of University of Bologna, Bologna (I).

Thanks to the scientific skills of my tutors and of several other people who have contributed to my scientific growth, I was involved in deep investigations regarding the design and manufacturing of energy–harvesting devices at MW and THz/IR frequencies.

This is an outstanding research field due to energetic issues which have become even more important in the last decades. In the literature a huge amount of papers can be found about harvesters exploiting various natural/artificial energy sources, but the main purpose of my personal research was to offer an alternative way to design such devices by means of:

1. uncommon CAD techniques (Chapter 1);
2. new materials (Chapter 2);
3. an innovative approach to deploy natural energy–sources (Chapter 3);
4. completely new applications based on revolutionary materials and their unique physical properties (Chapter 4).

The design of an energy–harvesting system is a formidable problem that faces a plethora of different EM/nonlinear issues. An accurate prediction of the overall performance is a desirable target to which I have tried to propose a solution.

Some applications, like the MIMO transceivers, have reached their technological maturity as regards the hardware but still encounter problems when exploiting these devices in modern wireless networks. To overcome the latter drawbacks a rigorous approach to the prediction of the realistic performance of a MIMO system has been proposed.

Other technologies are widely deployed but need a further improvement for their usage in comfortable body–centric systems: this is the case of *BANs*, for which research is still in progress in many engineering fields. Among the latter, materials science has a great importance since it can give rise to a new family of high–performance substrates for antenna miniaturization, as explained in detail for the proposed MD patch antenna.

No need to speak about the potentialities offered by the solar radiation, to which the scientific activity dedicates a lot of efforts in order to better use the most abundant source of "clean" energy on earth. In this frame, some portions of the solar spectrum are not properly exploited due to the lack of appropriate devices, hence an alternative way to harvest the IR radiation has been presented with an as rigorous as possible prediction of the real rectifying capabilities provided by state–of–the–art MOM diodes with cut–off frequency in the IR region.

Finally, aiming to propose an alternative to MOM diodes, the last part of the present PhD thesis deals with a new family of graphene–based devices that can be potentially deployed for traditional THz applications and (in prospect) new low–cost and easy–to–embed energy–harvesting systems.

The results obtained in these last three years, from a theoretical and experimental point of view, show that the path towards the "optimal" wearable/implantable device is characterized by a set of different issues that need to be merged focusing on the best trade–off for each of the constituent elements. For example, for a wearable application the proposed MD antenna of Chapter 2 can be used together with a power supply based on a solar (IR) or graphene (THz) energy–harvester; the whole system can be then studied as regards the link performance by using the EM/nonlinear techniques described in Chapter 1.

Science is made of successes and failures: I hope to have given a little contribution to improve the future life of all human beings.

# LIST OF PUBLICATIONS

**Conferences:**
[1] Masotti, Diego; Aldrigo, Martino; Costanzo, Alessandra; "Integrated design of antenna and PCB layers for back–radiation free RFID–enabled mobile devices," Microwave Conference (EuMC), 2011 41st European, 717–720, 2011, IEEE.
[2] Masotti, Diego; Costanzo, Alessandra; Mastri, Franco; Aldrigo, Martino; Rizzoli, Vittorio; "Nonlinear/electromagnetic co–design of MIMO and UWB radio links," Computational Electromagnetics International Workshop (CEM), 2011, 47–52, 2011, IEEE.
[3] Aldrigo, Martino; Bianchini, Davide; Costanzo, Alessandra; Masotti, Diego; Galassi, Carmen; Mitoseriu, Liliana; "New broadband button–shaped antenna on innovative magneto–dielectric material for wearable applications," Radar Conference (EuRAD), 2012 9th European, 397–400, 2012.
[4] Aldrigo, Martino; Costanzo, Alessandra; Masotti, Diego; Rizzoli, Vittorio; "A wearable UHF small patch antenna on a new magneto–dielectric material," XIX Riunione Naz. Elettromagnetismo (RiNEm), 301–304, 2012.
[5] Aldrigo, Martino; Masotti, Diego; Costanzo, Alessandra; Rizzoli, Vittorio; "Numerical analysis of an innovative energy–harvesting system in the infrared region," Wireless Power Transfer (WPT), 2013 IEEE, 123–126, 2013, IEEE.
[6] Aldrigo, Martino; Costanzo, Alessandra; Masotti, Diego; Trevisan, Riccardo; "Theoretical and Numerical Investigation of a Mid–infrared Energy–harvesting System," Session 4P5a SC4: Wireless Energy Transmission and Harvesting 2, 1574, 2013.
[7] Masotti, Diego; Costanzo, Alessandra; Del Prete, Massimo; Aldrigo, Martino; Trevisan, Riccardo; "Compact Design of a Flexible and Wearable Tri–band Rectenna," Session 4AK, 1480, 2013.
[8] Aldrigo, Martino; Masotti, Diego; Costanzo, Alessandra; Rizzoli, Vittorio; "Design rules for innovative nano–rectennas in the infrared region," 43rd European Microwave Conference (EuMC), 2013.

**Journals:**
[1] Rizzoli, Vittorio; Costanzo, Alessandra; Masotti, Diego; Aldrigo, Martino; Donzelli, Francesco; Esposti, Vittorio Degli; "Integration of non–linear, radiation, and propagation CAD techniques for MIMO link design," International Journal of Microwave and Wireless Technologies, 4, 2, 223–232, 2012, Cambridge University Press.
[2] Aldrigo, Martino; Costanzo, Alessandra; Masotti, Diego; Galassi, Carmen; "Exploitation of a novel magneto–dielectric substrate for miniaturization of wearable UHF antennas," Materials Letters, 87, 127–130, 2012, North–Holland.
[3] Aldrigo, Martino; Costanzo, Alessandra; Masotti, Diego; Baldisserri, Carlo; Dumitru, Ioan; Galassi, Carmen; "Numerical and experimental characterization of a button–shaped miniaturized UHF antenna on magneto–dielectric substrate," International Journal of Microwave and Wireless Technologies, 1–9, 2013, Cambridge University Press.
[4] Aldrigo, Martino; Dragoman, Mircea; Costanzo, Alessandra; Dragoman, Daniela; "Graphene as a high impedance surface for ultra–wideband electromagnetic waves," Journal of Applied Physics, 114, 184308, 2013.
[5] Dragoman, Mircea; Aldrigo, Martino; Dinescu, Adrian; Dragoman, Daniela; Costanzo, Alessandra; "Towards a terahertz direct receiver based on graphene up to 10 THz," Journal of Applied Physics, 115, 044307, 2014.

Web: http://scholar.google.com/citations?user=l0QbHDcAAAAJ&hl=en